# Development of a predictive kinematic model for the small overlap crash for obtaining force deformation solution spaces of grouped structural components

*BMW AG*
*Special Concepts Passive Safety*

Author:
Robbert Heuijerjans

Tutors:
Dr. Sergio Tuteltaub, MSc (TU Delft)
Iván Cuevas Salazar, MSc (BMW AG)
Lennart Keuthage, MSc (BMW AG)
Dr. Johannes Fender, MSc (BMW AG)

Master Thesis


TU Delft Delft University of Technology

Faculty of Aerospace Engineering

July 29, 2016

*This page is intentionally left blank.*

The image on the front cover can be found online under: `https://techdata.iihs.org/`. Consulted on July 29, 2016.

BMW
GROUP

BMW MINI Rolls-Royce Motor Cars Limited

## Agreement on the Application of a Blocking Notice

The degree thesis by

Mr Robbert Heuijerjans

on the subject of Development of a predictive kinematic model for the small overlap crash for obtaining force deformation solution spaces of grouped structural components

is supervised within the BWM Group by

Mr Lennart Keuthage

department EG-330

The following notice has to be inserted in the degree thesis on the first page after the cover sheet specifying the finish date:

### Blocking Notice

This degree thesis contains confidential information about the BMW Group which is subject to non-disclosure or confidentiality obligations. For this reason, the degree thesis may not be published or duplicated without the prior written consent of the BMW Group. This reservation of consent ends on: 31.07. 2021

This above mentioned date is mutually agreed.

Munich, 25.07.2016
Place, Time

Munich, 25.07.2016
Place, Time

R. Heuijerjans
Author

Supervisor

**Firma**
Bayerische Motoren Werke Aktiengesellschaft

**Postanschrift**
BMW AG
80788 München

**Hausanschrift**
Petuelring 130

**Hausanschrift**
Forschungs- und Innovationszentrum (FIZ)
Knorrstraße 147

**Telefon**
Zentrale
+4989 382-0

**Fax**
+49 89 382-25858

**Internet**
www.bmwgroup.com

**Bankkonto**
BMW Bank GmbH
Konto 5 100 940 940
BLZ 702 203 00

IBAN DE02 7022 0300 5100 9409 40

SWIFT(BIC)
BMWBDEM1

*This page is intentionally left blank.*

# Development of a predictive kinematic model for the small overlap crash for obtaining force displacement solution spaces of grouped structural components

Master of Science Thesis

For obtaining the degree of Master of Science in Aerospace Engineering
at Delft University of Technology

Robbert Heuijerjans

August 17, 2016

Faculty of Aerospace Engineering · Delft University of Technology

The work in this thesis was supported by BMW AG. Their cooperation is gratefully acknowledged.

Delft University of Technology
Faculty of Aerospace Engineering
Department of Aerospace Structures and Materials

**GRADUATION COMMITTEE**

Dated: August 17, 2016

Chair holder:

Dr. Sergio Turteltaub, MSc

Committee members:

Iván Cuevas Salazar, MSc

Dr. Derek Gransden, B. Eng.

Dr. Roeland de Breuker, MSc

*This thesis is dedicated to my loved ones.*

# Preface

Before you lies the thesis 'Development of a predictive kinematic model for the small overlap crash for obtaining force deformation solution spaces of grouped structural components'. The thesis is the final milestone for obtaining the Master of Science degree in Aerospace Engineering at Delft University of Technology. The project was performed in cooperation with the research and development center of BMW AG located in Munich in Germany from November 2015 until July 2016.

The conducted research deals with the determination of the influence of the most relevant structural components on the response of passenger vehicles subjected to the small overlap crash test of the Insurance Institute for Highway Safety (IIHS) and the development of a predictive kinematic model which is used to determine the force deformation solution spaces for the most relevant structural components. The type of crash test under investigation was introduced in 2012 to improve the crashworthiness of passenger vehicles and challenges automotive companies to develop profound design solutions to manufacture safer cars. Two approaches have been used in the thesis to perform the above mentioned research. The first approach uses full vehicle finite element method simulations performed with Abaqus/Explicit in which changes to structural components are made to investigate the influence on the response. In the second approach, an analytical tool to predict the kinematics of the vehicle subjected to the small overlap crash test is developed. The analytical tool is combined with an optimizer tool in order to obtain the desired force deformation solution spaces of the grouped components.

The research was challenging, but also very rewarding and my supervisors at TU Delft and BMW AG were always eager to help me and answer my questions. Without them, the outcome of the thesis would have not been the same and I am very grateful and thankful for their supervision.

*Robbert Heuijerjans*
*July 29, 2016*
*Munich, Germany*

# Acknowledgements

Now that the master thesis has been finished, the author would like to express his gratitude to particular individuals. Because of their insights, guidance, tips and commitment, the results shown in the thesis could been achieved.

First of all, I would like to thank my supervisor at TU Delft, Dr. Sergio Turteltaub for guiding me through the master thesis project. His large amount of knowledge, valuable feedback and experience in supervising a Master of Science thesis at TU Delft was very helpful. A lot has been learned from Sergio, especially in the field of multibody dynamics, and I am very thankful for his supervision.

Next, I would like to thank Lennart Keuthage, my first supervisor at BMW AG for giving me the opportunity to write my thesis at BMW AG and for the experience of working as a professional engineer in the passive safety department of one of the most successful premium car manufacturers in the world. His large amount of knowledge in finite element method simulations and understanding crash tests of passenger cars proved to be very valuable for the master thesis.

Many thanks go out to Ivàn Cuevas Salazar, my second supervisor at BMW AG, for helping me with the technical parts of my thesis. His help in the creation of simplified predictive models was very valuable. In addition, his engineering, as well as programming skills, are astonishing and he helped me to achieve the results shown in this thesis.

Furthermore, many thanks go to Dr. Johannes Fender, my third supervisor at BMW AG. His tremendous amount of knowledge in the development of simplified models and optimization for automotive crashworthiness applications, as well as his strong academic background helped me to complete the master thesis.

In addition, I would like to thank Dr. ir. Gillian Saunders-Smith, my master track coordinator at the faculty of Aerospace Engineering of TU Delft, for assisting me with the administrative processes.

Further, I would like to thank my colleagues at BMW AG who always helped me whenever I had a question during my time at BMW AG and made my experience so valuable.

Finally, I would like to thank my friends for supporting and motivating me during the nine month project. Especially I would like to thank my parents, my brother and my girlfriend for their patience and support. They were always there for me and especially in the challenging times of the project, they believed in me for which I am extremely thankful.

# Contents


**1 Introduction** **1**

**2 Literature review** **3**
2.1 Significance of crashworthiness for road users . . . 3
2.2 The small overlap crash test according to the IIHS . . . 4
2.2.1 Overview of the small overlap crash test . . . 5
2.2.2 Response modes of the vehicle . . . 6
2.3 Design strategies for crashworthiness . . . 7
2.3.1 Structural components of passenger vehicles . . . 7
2.3.2 Main load paths of structural components . . . 8
2.3.3 Main load paths of structural components for the small overlap crash . . . 9
2.3.4 Main structural design strategies for the small overlap crash test . . . 10
2.4 Simulation methods used for crashworthiness analysis . . . 10
2.4.1 Multibody system simulations . . . 11
2.4.2 Finite element method simulations . . . 14
2.4.3 Macro element method simulations . . . 15
2.4.4 Hybrid model formulation simulations . . . 17

**3 Finite element method for crashworthiness applications** **18**
3.1 Fundamental principles of FEM . . . 18
3.2 Time integration schemes . . . 20
3.3 Elements used in crashworthiness applications . . . 20
3.3.1 Solid elements . . . 21
3.3.2 Shell elements . . . 21
3.3.3 Beam elements . . . 21
3.3.4 Truss and cable elements . . . 21
3.3.5 Cohesive elements . . . 22
3.3.6 Discrete elements . . . 22
3.4 Modeling characteristics in crashworthiness applications . . . 22
3.4.1 Contact definition . . . 22
3.4.2 Friction definition . . . 22
3.4.3 Boundary conditions . . . 22
3.4.4 Loading conditions . . . 23
3.4.5 Failure mechanisms . . . 23
3.5 Simulation process . . . 23
3.5.1 Assembly process . . . 24
3.5.2 Solution process . . . 24
3.5.3 Post process . . . 24

**4 Force deformation solution spaces for crashworthiness design** **25**
4.1 Systems engineering . . . 25
4.2 Concept of solution spaces . . . 26
4.2.1 Solution spaces for crashworthiness design . . . 26
4.2.2 Importance of solution spaces for early stage crashworthiness design . . . 26
4.2.3 Force deformation solution spaces for crash structures . . . 26
4.3 Fundamental principles of solution spaces for crashworthiness design . . . 27

4.3.1 Monte Carlo sampling method . . . 27
4.3.2 Objective function . . . 28

**5 Numerical study on the most relevant structural components** **30**
5.1 Methodology . . . 30
5.1.1 Energy study . . . 30
5.1.2 Output variables . . . 31
5.1.3 Monitoring of output variables . . . 32
5.1.4 Variation of parameters . . . 33
5.1.5 Determination of the structural components of interest . . . 33
5.2 Trolley FEM simulation model . . . 34
5.2.1 Overview . . . 34
5.2.2 Energy study . . . 36
5.2.3 Output variables . . . 37
5.2.4 Monitoring of output variables . . . 37
5.2.5 Variation of parameters . . . 37
5.2.6 Determination of structural components of interest . . . 38
5.2.7 Discussion of results . . . 41
5.3 Reduced full vehicle FEM simulation model . . . 42
5.3.1 Overview . . . 42
5.3.2 Energy study . . . 44
5.3.3 Output variables . . . 46
5.3.4 Monitoring of output variables . . . 46
5.3.5 Variation of parameters . . . 46
5.3.6 Determination of structural components of interest . . . 46
5.3.7 Discussion of results . . . 50
5.4 Discussions and conclusions . . . 50

**6 Predictive kinematic model** **52**
6.1 Motivation . . . 52
6.2 Methodology of predictive kinematic model for two springs . . . 53
6.2.1 Overview . . . 53
6.2.2 Mathematical formulation . . . 55
6.2.3 Interpolation of force deformation curve . . . 60
6.2.4 Simulation process . . . 61
6.3 Methodology of predictive kinematic model for multiple springs . . . 62
6.3.1 Overview . . . 62
6.3.2 Mathematical formulation . . . 63
6.3.3 Interpolation of force deformation curve . . . 65
6.3.4 Simulation process . . . 65

**7 Verification and validation of the predictive kinematic model** **66**
7.1 Verification of predictive kinematic model . . . 66
7.2 Validation of predictive kinematic model . . . 66
7.2.1 Methodology . . . 67
7.2.2 Validation of predictive kinematic model with two springs . . . 70
7.2.3 Validation of predictive kinematic model with 18 springs . . . 74
7.2.4 Validation of predictive kinematic model with 80 springs . . . 77
7.2.5 Summarized results and discussion . . . 79

**8 Force deformation solution corridors obtained with the predictive kinematic model** **82**
8.1 Methodology . . . 82
8.1.1 Inputs . . . 82
8.1.2 Constraint variables . . . 82
8.1.3 Pre-processing . . . 84
8.2 Force deformation corridors with two springs kinematic model . . . 84
8.2.1 Input parameters . . . 84

8.2.2 Optimization parameters . . . 84
8.2.3 Force deformation corridors . . . 84
8.2.4 Discussion . . . 85
8.3 Rotational response force deformation corridors with two springs kinematic model . . 85
8.3.1 Input parameters . . . 85
8.3.2 Optimization parameters . . . 86
8.3.3 Force deformation corridors . . . 86
8.3.4 Discussion . . . 87
8.4 Glancing-off response force deformation corridors with two springs kinematic model . 87
8.4.1 Input parameters . . . 87
8.4.2 Optimization parameters . . . 87
8.4.3 Force deformation corridors . . . 87
8.4.4 Discussion . . . 88
8.5 Force deformation corridors with ten springs kinematic model . . . 88
8.5.1 Input parameters . . . 89
8.5.2 Optimization parameters . . . 89
8.5.3 Force deformation corridors . . . 90
8.5.4 Discussion . . . 92
8.6 Rotational response force deformation corridors with ten springs kinematic model . . . 92
8.6.1 Input parameters . . . 92
8.6.2 Optimization parameters . . . 93
8.6.3 Force deformation corridors . . . 93
8.6.4 Discussion . . . 95
8.7 Glancing-off response force deformation corridors ten springs kinematic model . . . 95
8.7.1 Input parameters . . . 95
8.7.2 Optimization parameters . . . 95
8.7.3 Force deformation corridors . . . 95
8.7.4 Discussion . . . 98
8.8 Summarized results and discussions . . . 98
8.8.1 Two springs configuration . . . 98
8.8.2 Ten springs configuration . . . 99

**9 Discussions and conclusions** **100**
9.1 Numerical study . . . 100
9.2 Predictive kinematic model . . . 101
9.3 Force deformation solution spaces . . . 102

**10 Recommendations** **103**
10.1 Numerical study . . . 103
10.2 Predictive kinematic model . . . 103
10.3 Force deformation solution spaces . . . 104

# List of Figures


2.1 Overview of the global road traffic fatalities by type of road user in 2013. . . . . . . . 3
2.2 Illustration of the small overlap crash test at the moment of contact. . . . . . . . . . 5
2.3 Top, rear, front and isometric view of the barrier of the small overlap crash test. . . . 5
2.4 Rotational response mode of a vehicle subjected to the small overlap crash. . . . . . . 6
2.5 Lateral translational response mode of a vehicle subjected to the small overlap crash. 6
2.6 Main structural components of a passenger vehicle. . . . . . . . . . . . . . . . . . . . 7
2.7 Generic main load paths for a passenger vehicle. . . . . . . . . . . . . . . . . . . . . . 8
2.8 Structural components relevant for the small overlap crash test load-case. . . . . . . . 9
2.9 Location of the longitudinal framerails in a passenger vehicle. . . . . . . . . . . . . . 10
2.10 Idealized representation of a vehicle used for the lumped mass model. . . . . . . . . . 11
2.11 Components which are idealized by the lumped mass model. . . . . . . . . . . . . . . 12
2.12 Complete lumped mass model for the frontal car structure. . . . . . . . . . . . . . . . 12
2.13 Representation of elastoplastic collapse element. . . . . . . . . . . . . . . . . . . . . 13
2.14 Nonlinear force displacement curve of a crushed tube. . . . . . . . . . . . . . . . . . . 13
2.15 Piecewise linear representation of the elastoplastic collapse element. . . . . . . . . . . 14
2.16 Example of FEM crash simulation of a passenger vehicle. . . . . . . . . . . . . . . . . 15
2.17 Assumed 'concertina' collapse mode of an axially loaded cylindrical shell. . . . . . . . 16
2.18 Deformation mode represented by the Superfolding element. . . . . . . . . . . . . . . 16
2.19 Illustration of the Superbeam element. . . . . . . . . . . . . . . . . . . . . . . . . . . 16
2.20 Comparison between FEM and macro element crash simulation of passenger vehicle. . 17

3.1 Discretized element in global and local reference coordinate system. . . . . . . . . . . 18
3.2 Typical element types used in FEM. . . . . . . . . . . . . . . . . . . . . . . . . . . . 21

4.1 V-diagram from systems engineering for the development of a vehicle. . . . . . . . . . 25
4.2 Force deformation corridors of structural components of a passenger vehicle. . . . . . 27
4.3 Feasible and infeasible design regions. . . . . . . . . . . . . . . . . . . . . . . . . . . 28

5.1 Normalized forces as a function of normalized time. . . . . . . . . . . . . . . . . . . . 33
5.2 Isometric view of the trolley FEM simulation model. . . . . . . . . . . . . . . . . . . . 35
5.3 Overview of the trolley FEM simulation model. . . . . . . . . . . . . . . . . . . . . . 35
5.4 Result of the energy study of trolley FEM simulation model. . . . . . . . . . . . . . . 36
5.5 Trolley FEM simulation model before and after impact. . . . . . . . . . . . . . . . . . 38
5.6 Normalized displacement as a function of normalized time of the trolley model. . . . 39
5.7 Normalized angle as a function of time of the trolley model. . . . . . . . . . . . . . . 39
5.8 Normalized force as a function of normalized time of the trolley model. . . . . . . . . 40
5.9 Normalized force as a function of normalized x displacement of the trolley model. . . 40
5.10 Normalized energy as a function of normalized time of the trolley model. . . . . . . . 41
5.11 Deformation due to the small overlap crash test load-case. . . . . . . . . . . . . . . . 42
5.12 Isometric view of the reduced FEM simulation model. . . . . . . . . . . . . . . . . . . 43
5.13 Overview of the reduced FEM simulation model. . . . . . . . . . . . . . . . . . . . . . 44
5.14 Result of the energy study of FEM trolley model. . . . . . . . . . . . . . . . . . . . . 45
5.15 Reduced FEM simulation model before and after impact. . . . . . . . . . . . . . . . . 47
5.16 Normalized displacement as a function of normalized time for the reduced model. . . 47
5.17 Normalized angle as a function of time of the reduced model. . . . . . . . . . . . . . . 48
5.18 Normalized force as a function of normalized time of the reduced model. . . . . . . . 48
5.19 Normalized force as a function of normalized time for the reduced model. . . . . . . . 49

5.20 Normalized energy as a function of normalized time for the reduced model. . . . . . . 49

6.1 Idealization of the small overlap crash test using a mass spring system. . . . . . . . . 53
6.2 Overview of the predictive kinematic model using two springs. . . . . . . . . . . . . . 54
6.3 Idealization of predictive kinematic model using two springs. . . . . . . . . . . . . . . 55
6.4 Force deformation curve. . . . . . . . . . . . . . . . . . . . . . . . . . . . . . . . . . 60
6.5 Force deformation curve divided into two segments. . . . . . . . . . . . . . . . . . . . 61
6.6 Overview of the predictive kinematic model using multiple springs. . . . . . . . . . . 62
6.7 Idealization of predictive kinematic model using multiple springs. . . . . . . . . . . . 63

7.1 Overview of patches on barrier for 18 springs and glance-off concept. . . . . . . . . . 69
7.2 Overview of patches on barrier for 18 springs and rotational concept. . . . . . . . . . 69
7.3 Model using two springs compared to SUV FEM model with glance-off concept. . . . 71
7.4 Model using two springs compared to SUV FEM model with rotational concept. . . . 71
7.5 Model using two springs compared to mid-size sedan FEM model with glance-off concept. 72
7.6 Model using two springs compared to mid-size sedan FEM model with rotational concept. 72
7.7 Model using two springs compared to sports car FEM model with glance-off concept. 73
7.8 Model using two springs compared to sports car FEM model with rotational concept. 73
7.9 Model using 18 springs compared to SUV FEM model with glance-off concept. . . . . 74
7.10 Model using 18 springs compared to SUV FEM simulation with rotational concept. . 74
7.11 Model using 18 springs compared to mid-size sedan FEM model with glance-off concept. 75
7.12 Model using 18 springs compared to mid-size sedan FEM model with rotational concept. 75
7.13 Model using 18 springs compared to sports car FEM model with glance-off concept. . 76
7.14 Model using 18 springs compared to sports car FEM model with rotational concept. . 76
7.15 Model using 80 springs compared to SUV FEM model with glance-off concept. . . . . 77
7.16 Model using 80 springs compared to SUV FEM model with rotational concept. . . . . 77
7.17 Model using 80 springs compared to mid-size sedan FEM model with glance-off concept. 78
7.18 Model using 80 springs compared to mid-size sedan FEM model with rotational concept. 78
7.19 Model using 80 springs compared to sports car FEM model with glance-off concept. . 78
7.20 Model using 80 springs compared to sports car FEM model with rotational concept. . 79

8.1 Force deformation corridors of predictive kinematic model with two springs. . . . . . 85
8.2 Force deformation corridors of kinematic model with two springs for rotational response. 86
8.3 Comparison of force deformation corridors of two springs model for rotational response. 86
8.4 Force deformation corridors of kinematic model with two springs for glancing-off response. 87
8.5 Comparison of force deformation corridors of two springs model for glancing-off response. 88
8.6 Boxes to determine the grouped components. . . . . . . . . . . . . . . . . . . . . . . 89
8.7 Force deformation solution corridors for the wheel. . . . . . . . . . . . . . . . . . . . 90
8.8 Force deformation solution corridors for the shotgun. . . . . . . . . . . . . . . . . . . 90
8.9 Force deformation solution corridors for the lower framerail. . . . . . . . . . . . . . . 91
8.10 Force deformation solution corridors for the upper framerail. . . . . . . . . . . . . . . 91
8.11 Force deformation solution corridors for the springdome. . . . . . . . . . . . . . . . . 92
8.12 Force deformation solution corridors of the wheel for rotating response. . . . . . . . . 93
8.13 Force deformation solution corridors of the shotgun for rotating response. . . . . . . . 93
8.14 Force deformation solution corridors of the lower framerail for rotating response. . . . 94
8.15 Force deformation solution corridors of the upper framerail for rotating response. . . 94
8.16 Force deformation solution corridors of the springdome for rotating response. . . . . . 95
8.17 Force deformation solution corridors of wheel for glancing-off response. . . . . . . . . 96
8.18 Force deformation solution corridors of shotgun for glancing-off response. . . . . . . . 96
8.19 Force deformation solution corridors of lower fraimerail for glancing-off response. . . . 97
8.20 Force deformation solution corridors of upper framerail for glancing-off response. . . . 97
8.21 Force deformation solution corridors of springdome for glancing-off response. . . . . . 98

A.1 Kinematic model compared to SUV FEM model with glance-off concept. . . . . . . . 109
A.2 Kinematic model compared to SUV FEM model with rotational concept. . . . . . . . 109
A.3 Kinematic model compared to mid-size sedan FEM model with glance-off concept. . . 110
A.4 Kinematic model compared to mid-size sedan FEM model with rotational concept. . 110

A.5 Kinematic model compared to FEM sports car model with glancing-off concept. . . . 110
A.6 Kinematic model compared to FEM sports car model with rotational concept. . . . . 111
B.1 Force deformation solution corridors of wheel for rotational response. . . . . . . . . . 112
B.2 Force deformation solution corridors of shotgun for rotational response. . . . . . . . . 112
B.3 Force deformation solution corridors of lower framerail for rotational response. . . . . 113
B.4 Force deformation solution corridors of upper framerail for rotational response. . . . . 113
B.5 Force deformation solution corridors of springdome for rotational response. . . . . . . 114
B.6 Force deformation solution corridors of wheel for glancing-off response. . . . . . . . . 114
B.7 Force deformation solution corridors of shotgun for glancing-off response. . . . . . . . 115
B.8 Force deformation solution corridors of lower framerail for glancing-off response. . . . 115
B.9 Force deformation solution corridors of upper framerail for glancing-off response. . . . 116
B.10 Force deformation solution corridors of springdome for glancing-off response. . . . . . 116

# List of Tables

5.1 Thickness ratios of structural components of the trolley FEM simulation model variants. 37
5.2 Thickness ratios of structural components of reduced FEM simulation model variants. 46

7.1 Mean absolute error of output variables. . . . . . . . . . . . . . . . . . . . . . . . . . . 80

# List of Abbreviations

| | |
|---|---|
| AG | Aktiengesellschaft |
| ALLIE | All internal energy in Abaqus/Explicit |
| ALLKE | All kinetic energy in Abaqus/Explicit |
| ANSA | Automatic net generation for structural analysis |
| ANSYS | Analysis System |
| ASIRT | Association for Safe International Road Travel |
| BMW | Bayerische Motoren Werke |
| CCW | Counter clockwise |
| CF | Contact force output in Abaqus/Explicit |
| CF1 | Contact force output in the 1 direction in Abaqus/Explicit |
| CF2 | Contact force output in the 2 direction in Abaqus/Explicit |
| CF3 | Contact force output in the 3 direction in Abaqus/Explicit |
| CFORCE | Contact force in Abaqus/Explicit |
| CNORMF | Contact normal force in Abaqus/Explicit |
| CP | Position output in Abaqus/Explicit |
| CP1 | Position output in the 1 direction in Abaqus/Explicit |
| CP2 | Position output in the 2 direction in Abaqus/Explicit |
| CP3 | Position output in the 3 direction in Abaqus/Explicit |
| CPU | Central Processing Unit |
| COG | Center of gravity |
| CSHEARF | Frictional shear force in Abaqus/Explicit |
| CW | Clockwise |
| DOF | Degree of freedom |
| EOM | Equation of motion |
| FEA | Finite Element Analysis |
| FEM | Finite Element Method |
| GDP | Gross Domestic Product |
| IIHS | Insurance Institute for Highway Safety |
| MAE | Mean absolute error |
| MATLAB | Matrix Laboratory |
| MPC | Multi-Point Constraints |
| MRE | Mean relative error |
| NHTSA | National Highway Traffic Safety Administration |
| PID | Property identifier |
| SUV | Sports utility vehicle |
| TNO | Netherlands Organization for Applied Scientific Research |
| VCS | Visual Crash Studio |
| WHO | World Health Organization |

# List of Symbols

| | | |
|---|---|---|
| $a$ | Magnitude for auxiliary vector | $m$ |
| $\alpha$ | Slope of elastoplastic force | $N/m$ |
| $AbWAP$ | Ratio of A-Pillar movement over overlap width | $-$ |
| $AbWP$ | Ratio of projected A-Pillar point movement over overlap width | $-$ |
| $AP_x$ | x distance of A-Pillar to COG | $m$ |
| $AP_y$ | y distance of A-Pillar to COG | $m$ |
| $b$ | Magnitude for auxiliary vector | $m$ |
| $\beta$ | Elastoplastic force stiffness correction factor | $N$ |
| $\underline{\underline{B}}$ | Strain displacement matrix | $-$ |
| $d$ | Displacement | $m$ |
| $dir$ | Direction value of spring | $m$ |
| $c$ | Wave propagation velocity | $m/s$ |
| $\underline{\underline{C}}$ | Damping matrix | $Ns/m$ |
| $\underline{\underline{D}}$ | Stress strain constitutive relation matrix | $N/m^2$ |
| $E$ | Young's Modulus | $N/m^2$ |
| $h$ | Shape function | $-$ |
| $\underline{\underline{H}}$ | Displacement interpolation matrix | $-$ |
| $I_{zz}$ | Mass moment of inertia | $kgm^2$ |
| $FS$ | Elastoplastic force | $N$ |
| $F$ | Force | $N$ |
| $F_x$ | Force in x | $N$ |
| $F_y$ | Force in y | $N$ |
| $\underline{\underline{F}}_{local}$ | Force in local coordinate system | $N$ |
| $F_{x,local}$ | Force in x in local coordinate system | $N$ |
| $F_{y,local}$ | Force in y in local coordinate system | $N$ |
| $\underline{\underline{F}}_{global}$ | Force in global coordinate system | $N$ |
| $F_{x,global}$ | Force in x in global coordinate system | $N$ |
| $F_{y,global}$ | Force in y in global coordinate system | $N$ |
| $\underline{\underline{K}}$ | Stiffness matrix | $N/m$ |
| $k_x$ | Spring stiffness in x | $N/m$ |
| $k_y$ | Spring stiffness in y | $N/m$ |
| $k_\theta$ | Rotational stiffness | $Nm/rad$ |
| $\kappa$ | Damping property parameter | $Ns/m$ |
| $\underline{L}$ | Lagrangian | $N$ |
| $l$ | Element length | $m$ |
| $M$ | Mass | $kg$ |
| $\underline{\underline{M}}$ | Mass matrix | $kg$ |
| $M_z$ | Moment around z axis | $Nm$ |
| $m$ | Mass | $ton$ |
| $N$ | Number of points | $-$ |
| $n$ | Number of points | $-$ |
| $O_i$ | Observed value | $m, rad$ |
| $\Omega$ | Element domain | $-$ |
| $P_i$ | Predicted value | $m, rad$ |

| | | |
|---|---|---|
| $\underline{p}_1$ | Point in space | $m$ |
| $\underline{p}_2$ | Point in space | $m$ |
| $\underline{p}_3$ | Point in space | $m$ |
| $q$ | Node | $-$ |
| $\underline{q}$ | Degrees of freedom vector | $m, rad$ |
| $\underline{\ddot{q}}$ | Second derivative of degrees of freedom vector | $m/s^2, rad/s^2$ |
| $\rho$ | Mass density | $kg/m^3$ |
| $\underline{\underline{R}}$ | Rotation matrix | $rad$ |
| $\underline{r}_{COG}$ | Vector of COG location | $m$ |
| $\underline{r}_{AP}$ | Vector of A-Pillar location | $m$ |
| $\underline{r}_{AP,B}$ | Vector of projected A-Pillar location on the barrier | $m$ |
| $\underline{r}_w$ | Vector of $w$ location | $m$ |
| $\underline{r}_{y,1}$ | Vector of first point of y spring location | $m$ |
| $\underline{r}_{y,2}$ | Vector of second point of y spring location | $m$ |
| $\underline{r}_{P,1}$ | Vector of first point of axial spring location | $m$ |
| $\underline{r}_{P,2}$ | Vector of second point of axial spring location | $m$ |
| $S$ | Elastoplastic force | $N$ |
| $s_x$ | Deformation of spring in x | $m$ |
| $s_y$ | Deformation of spring in y | $m$ |
| $s_L$ | Final length of spring | $m$ |
| $T$ | Kinetic energy | $J$ |
| $t$ | Time | $s$ |
| $t_{crit}$ | Critical time step | $s$ |
| $t_{baseline}$ | Thickness of baseline model | $m$ |
| $t_{medium\ stiff}$ | Thickness of medium stiff model | $m$ |
| $t_{very\ stiff}$ | Thickness of very stiff model | $m$ |
| $t_{strong}$ | Thickness of strong model variant | $m$ |
| $t_{weak}$ | Thickness of weak model variant | $m$ |
| $\Delta t$ | Time step | $s$ |
| $\theta$ | Angle of center of gravity | $rad$ |
| $\dot{\theta}$ | First derivative of angle of COG | $rad/s$ |
| $\ddot{\theta}$ | Second derivative of angle of COG | $rad/s^2$ |
| $u$ | Displacement | $m$ |
| $\dot{u}$ | Velocity | $m/s$ |
| $\ddot{u}$ | Acceleration | $m/s^2$ |
| $u_{x,COG}$ | x displacement of COG | $m$ |
| $u_{y,COG}$ | y displacement of COG | $m$ |
| $\dot{u}_{x,COG}$ | x velocity of COG | $m/s$ |
| $\dot{u}_{y,COG}$ | y velocity of COG | $m/s$ |
| $\ddot{u}_{x,COG}$ | x acceleration of COG | $m/s^2$ |
| $\ddot{u}_{y,COG}$ | y acceleration of COG | $m/s^2$ |
| $u^{t+\Delta t}$ | Displacement at next time step | $m$ |
| $u^{t-\Delta t}$ | Displacement at previous time step | $m$ |
| $u^t$ | Displacement at current time step | $m$ |

| | | |
|---|---|---|
| $V$ | Potential energy | $J$ |
| $v$ | Displacement | $m$ |
| $v_0$ | Initial velocity of the vehicle | $m$ |
| $\underline{v}_a$ | Unit vector | $m$ |
| $\underline{v}_b$ | Unit vector | $m$ |
| $\underline{v}_{r_{y,1}r_w}$ | Unit vector | $m$ |
| $\underline{v}_1$ | Auxiliary vector | $m$ |
| $\underline{v}_2$ | Auxiliary vector | $m$ |
| $\nu$ | Poisson's ratio | $-$ |
| $w$ | Displacement | $m$ |
| $w_y$ | y distance of lateral spring location | $m$ |
| $x$ | Coordinate | $m$ |
| $x_B$ | x distance of barrier | $m$ |
| $x_{COG,0}$ | Initial x location of COG | $m$ |
| $x$ | Displacement | $m$ |
| $\ddot{x}$ | Acceleration | $m/s^2$ |
| $y$ | Coordinate | $m$ |
| $y_B$ | y distance of barrier | $m$ |
| $y_{COG,0}$ | Initial y location of COG | $m$ |
| $z$ | Coordinate | $m$ |

Since the early days of the automobile, crashworthiness has been of large importance. Nowadays, with the introduction of common vehicle architectures across the model range, stricter requirements regarding active, as well as passive safety, and with the introduction of new crash tests, automotive manufacturers are facing an increased challenge in designing passenger vehicles. One of these new crash tests is the small overlap crash test, introduced in 2012 by the Insurance Institute for Highway Safety (IIHS), a non profit organization founded in 1959 and funded by auto insurers and insurance associations. In this type of frontal crash test, the passenger vehicle impacts a rigid barrier with an overlap of 25% traveling at a velocity of 64.4 km/h, resulting into an asymmetrical load-case of the frontal structure. From studying relevant literature in academia and industry, two different main response modes to the small overlap crash test are identified, being the lateral translational response mode where the vehicle 'glances-off' from the barrier and the rotational response mode where the vehicle experiences a significant amount of deformation of the frontal structure and sub-sequentially a large rotation around the barrier.

In order to reduce the number of required crash tests and to improve the understanding of the load-case, it is of special interest to investigate the influence of the most relevant structural components on the response of the passenger vehicle subjected to the small overlap crash test and to develop a simplified model which is capable to predict the kinematics of the vehicle. The outcome allows the designers and engineers to improve the structural design and increase the crashworthiness. This is particularly of interest at an early development phase, as it allows to make early adoptions and enables the possibility to collaborate from an early start point on with other design departments. In this thesis, the research is performed by following two approaches: a bottom up approach and a top down approach.

In the bottom up approach, a numerical study on the most relevant structural components is performed with detailed Finite Element Method (FEM) simulations of two different vehicle models of the Bayerische Motoren Werke (BMW) Aktiengesellschaft (AG) product line analyzed with Abaqus/Explicit. The first FEM simulation model is a trolley model which is normally used at an early development phase of a passenger vehicle to investigate and test the structural performance of the load carrying structural components for frontal crashes without having the necessity to build the complete vehicle. The second FEM simulation model is a full vehicle model, except for the fact that all elements behind the A-Pillar are deleted. Following the bottom up approach, the influence of the most relevant structural components on the response of the passenger vehicle is analyzed by changing the wall thickness of these components. Specifically, it has been found that a tendency of required force levels in x and y is seen for obtaining a certain response. A higher level of y force increases the tendency of the vehicle model to glance-off from the barrier, while a higher level of x force increases the tendency of the vehicle model to rotate around the barrier. In addition, the importance of the wheel and the surrounding structure has been identified by using the bottom up approach. After performing several different sets of changes to the wall thickness of the relevant components, it was not possible to evoke the two different responses for both models.

Following the top down approach, a simplified predictive kinematic model has been developed which is on a higher hierarchical level than the FEM simulations and which is capable of predicting the response of a passenger vehicle when subjected to the small overlap crash test using the force deformation characteristics of relevant structural components. After showing that the predictive kinematic model is able to accurately predict the response of any vehicle to the load-case, by validating the predictive kinematic model with three different full vehicle FEM simulation models of the BMW AG product line, each with the two different responses, the predictive kinematic model is used to obtain force deformation

solution spaces of the grouped main load carrying components. Basically, the force deformation solution space describes the feasible design area in the force deformation domain constraint by the upper and lower force level. Following the principle of the V-diagram of systems engineering, components which fall inside the solution space bounds also meet the higher level design goals. By decoupling the design targets of the groups of components, the specific method gives the freedom to achieve those targets to the responsible design departments. These design targets of the grouped components inherently fulfill the top level design goals of the system.

The outcome of the thesis is helping the crashworthiness design of passenger vehicles to a large extend, especially at an early development phase where the exact geometry of the vehicle is unknown, but design targets are required by the engineers of design departments who can use the outcome of the force deformation solutions spaces of the grouped components.

# CHAPTER 1

## Introduction

Since the early days of the automobile, crashworthiness has been of large importance. Nowadays, several improvements have been made in the area of crashworthiness, driven by manufactures, government and insurance companies of passenger cars. Nevertheless, the ninth frequent cause of death across all age groups is still due to a fatal car crash [1, 2]. Over 1.24 million people died and approximately 20 million people suffered from non-fatal injuries as a consequence of traffic accidents in 2013. Out of these 1.24 million people, approximately 31% are occupants of passenger vehicles. It is predicted that car crashes will be the seventh leading cause of death in 2030 [3]. Several studies indicated that a large portion of today's frontal crashes are without the involvement of the main frontal load paths resulting in large deformations of the striking side of the vehicle. As much as 27% of all crashes have no engagement of the main frontal load paths of the car [4]. Similar numbers were determined by an investigation conducted in Sweden by Lindquist, Hall and Björnstig which showed that approximately one-third of all fatal car crashes were without affecting the main frontal load path of the structure [5]. These crashes, which have no involvement of the main frontal load path, are commonly categorized as small overlap crashes. In this type of impact, large deformations on the striking side of the vehicle occur along with large rotations of the vehicle. Small overlap car crashes are not only frequent, but also pose a great injury risk to occupants and account for the largest number of fatalities in frontal collisions. To increase the safety of passenger cars for this type of load-case, the Insurance Institute for Highway Safety (IIHS), a non profit organization founded in 1959 and funded by auto insurers and insurance associations, introduced the so called small overlap crash test in 2012 [6]. In this type of frontal crash test, the car impacts a rigid barrier with an overlap of 25% traveling at a velocity of 64.4 km/h, resulting into an asymmetrical load-case of the frontal crash structure [6].

In order to enhance the crashworthiness of vehicles subjected to this load-case, a detailed understanding of the different load paths and the structural interaction of components is of vital importance. In addition to the need of adapting the structure to the requirements of the new load-case, automotive manufacturers make use of an increased modularity and use similar components throughout their complete model line. Due to the fact that the vehicle's structure is a highly nonlinear system with multiple interactions, the best design of a specific component is dependent on the design of each sub-component [7]. Therefore, it is of special interest for industry to develop a simplified predictive model for the small overlap crash test load-case of the IIHS for passenger cars which incorporates relevant structural interactions of components in order to derive requirements for each structural component. Based on this background, the modeling of the dynamics and the response of the vehicle which gives an indication of the crashworthiness of the passenger car subjected to the small overlap crash, without the necessity to perform expensive experimental crash tests or computationally expensive detailed Finite Element Method (FEM) simulations, is of special interest. This is particularly the case at an early development phase of a passenger car where the level of detail and therefore the knowledge of the topology and dimensions of the crash structure is limited.

A long history of research in academia and industry exists for the formulation of simplified predictive models for simulating car crashes [8], however, due to the stricter requirements, which require more accurate models, and new load-cases, such as the small overlap crash test of the IIHS, this research field remains a challenging and popular research area. Recent developments in academia and industry showed an increased interest in understanding and predicting the structural response of passenger cars for the small overlap crash test using experimental, analytical and numerical methods. Experimental tests are performed according to the IIHS standard for performing and rating the crash test [6, 9]. These tests are helping to understand the structural interactions and their influence on the vehicle response to a great extend. Due to the increased computational power, detailed FEM simulations predicting the vehicle's response to the small overlap crash test load-case are performed. Especially in the development of simplified predictive models for the small overlap crash test load-case, an increasing need is observed. For this, a profound insight into the structural interactions of components is required in order to establish the relevant and mostly loaded components. Several studies investigated the response of the vehicle to the small overlap crash test and the relevant load paths [10, 11]. The response of the vehicle to the small overlap crash is dependent on the individual components and their interactions along the different load paths. Over the past years, the rapid increase in FEM simulation models increased the insight into the interaction of components and helped in the formulation of simplified predictive models for means of impact modeling of passenger cars. Nevertheless, most of the work focuses on symmetrical load-cases, in contrast to the small overlap crash test. The consequence of this is a gap in the research field, which can be closed by expanding the existing knowledge to the small overlap crash test of the IIHS.

In order to close this gap, two approaches, being the bottom up approach and the top down approach are used in this thesis. In the bottom up approach, the interaction of the main components of the front structure of the vehicle and influence on the response is investigated by performing a numerical study. This is done by using FEM simulations models of passenger cars of the Bayerische Motoren Werke (BMW) Aktiengesellschaft (AG) product line. The intention of the numerical study is to quantify the influence of the most relevant components along the load path on the vehicle's response to the small overlap crash. In the top down approach, a simplified predictive kinematic model is developed which is capable of predicting the vehicle's response when subjected to the small overlap crash test load-case using the force deformation characteristics of relevant structural components. After showing that the predictive simplified model is able to accurately predict the response of the vehicle, the model is used to obtain force deformation corridors of the main load carrying components, for obtaining a certain response of the vehicle. This allows to generate force deformation solution spaces of the components at an early development phase of the vehicle, greatly helping the passive safety development of passenger vehicles.

Summarized, the main research objective of the thesis is formulated as follows:

*The objective of the project is to determine the influence of the most relevant structural components on the response of the vehicle subjected to the small overlap crash of the IIHS and to develop a predictive kinematic model which is capable of modeling the response of the vehicle to the small overlap crash in order to obtain force deformation solution spaces of grouped structural components. On the one hand, this is achieved by performing FEM simulations in Abaqus/Explicit and, following the bottom up approach, by investigating the changes in wall thicknesses of the most relevant components on the vehicle's response. On the other hand, this is achieved by following the top down approach where a predictive kinematic model is created which is on a higher hierarchical level than FEM simulations and is able to predict the response of the vehicle to the small overlap crash test by incorporating the force deformation curves for the grouped components of interest.*

The thesis is structured in the following way. First, in Chapter 2, a condensed literature review of the research area is presented. Next, in Chapter 3, a short introduction and theory behind to the FEM simulations used for crashworthiness applications is given. Then, the concept of the force deformation solution space for crashworthiness applications is discussed in Chapter 4. Further, in Chapter 5, the numerical study of the most relevant structural components for the small overlap crash test load-case is provided. Chapter 6 presents the description of the predictive kinematic model. In chapter 7, the verification and validation of the predictive kinematic model is discussed. Next, in chapter 8, the resulting force deformation corridors are presented. Finally, in chapter 9 and 10, discussions and conclusions, as well as recommendations about the research project are presented.

# CHAPTER 2

## Literature review

This chapter presents a condensed literature review of the relevant research areas of crashworthiness which are of importance for the thesis. The topics of the literature review are divided into four main areas, being: the significance of crashworthiness for road users, the description of the small overlap crash test load-case, the design strategies used for crashworthiness and the simulation methods available for crashworthiness analysis. These four topics are discussed in more detail in Sections 2.1, 2.2, 2.3 and 2.4, respectively.

### 2.1 Significance of crashworthiness for road users

Fatal car crashes have a long history and are of major concern in the automotive industry. In 1889, already three years after the invention of the automobile, the first known motor vehicle fatality occurred [12]. Arguably, therefore, since the early days of the automobile, the safety of passenger cars is of vital importance.

In 2013, over 1.2 million people died as a result of road traffic accidents and around 50 million were injured [2, 3]. In Fig. 2.1, an overview of the global road traffic deaths by the type of road user in 2013 is shown.

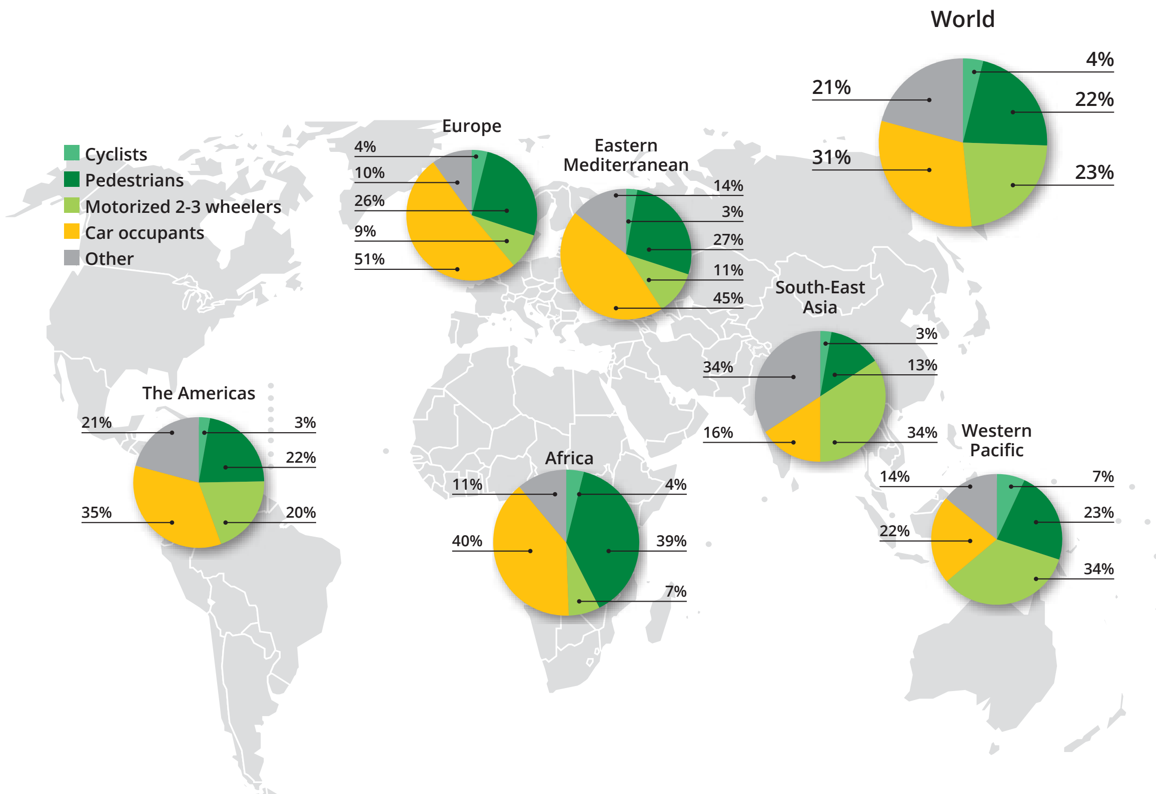


Figure 2.1: Overview of the global road traffic fatalities by type of road user in 2013. Source [2].

Referring to Fig. 2.1, out of the 1.2 million people that died in 2013, around 31% are occupants of a passenger vehicle [3]. According to the Association for Safe International Road Travel (ASIRT) and the World Health Organization (WHO) [1, 2], the ninth frequent cause of death across all age groups is due to a fatal car crash. It is predicted that this will be the seventh leading cause in 2030 [13]. For young people (15 to 29 years), a fatal car crash is the leading cause of death [2]. In the United States of America alone, almost 30000 people died due to a car crash in 2007 [14]. Looking at Europe, approximately 240000 car occupants were killed in the EU 27 countries between 2001 and 2012 [15]. The number of killed car occupants decreased from 27700 in 2001 to 12345 in 2012 [15]. Referring to Lund [16], the death rate decreased from 55 deaths per billion miles of travel in 1966 to 11.3 deaths per million miles of travel in 2009. Specifically, for the countries which are investigated by the Road Safety Annual Report [17], among which are Germany, the Netherlands, Sweden and the United States of America, the number of road fatalities decreased by 42% between 2000 and 2013. Economically, it is important to mention that the low and middle income countries in the world lose as much as 3% of their gross domestic product (GDP) as a result of road traffic crashes [2].

Part of the reduction in number of road fatalities is due to the constant strive of automotive manufacturers, as well as the constant push from insurance companies and government, to increase the safety of passenger cars. Generally, a distinction is made between two different types of safety in the automotive industry, being active and passive safety [18]. Active safety is mainly concerned with measures to avoid any crash, while passive safety is concerned with the reduction of risk of injuries by improving the structural integrity of the vehicle [18]. Specifically, the passive safety is improved by enhancing the capability of structural components to protect the occupants in survivable crashes [12]. This term is known as the crashworthiness of a passenger car [12]. According to Lindquist, Hall and Björnstig [19], the term crashworthiness is the ability to protect the occupants of the car in a crash. Referring to Wei, Karimi and Robbersmyr [20], the analysis of crashworthiness is based on the crash responses which are the displacement, velocity and acceleration of critical parts of a vehicle during the crash [20]. The authors Zu, Pan, Chen and Zhang, state that the performance of crashworthiness is based on safety parameters such as peak acceleration, energy absorption capacity, maximum crush force and maximum firewall intrusion [21].

Several studies suggest that a large portion of road fatalities is due to a small overlap of the vehicle during impact with the object which means that the main absorbing crash structure is not loaded. Lindquist, Hall and Björnstig determined in their research that of all frontal crashes in Sweden, approximately 34% are without engaging the main longitudinal beams (also called framerails) of the vehicle. In addition, 48% of the crashes occurring in Sweden are without involvement of the drivetrain and have less than 30% of structural involvement [5]. Similar results were confirmed by Hobbs [4] who found out that 27% of all the fatalities in car crashes have a small frontal overlap. Referring to Lenard et. al. 20% of the frontal crashes have an overlap of less than 25% [22].

The aforementioned scenarios, in which no or little involvement of the main longitudinal framerails is occurring, are commonly categorized as so called small overlap crashes. In this type of crash, the main energy absorbing structure at the front of the car is not active and thus large deformations on the striking side of the vehicle occur. Small overlap crashes are not only frequent but also pose a greater injury risk to occupants. When compared with large overlap impacts, occupants in small overlap crashes have a 'demonstrated increased incidence of head, chest, spine, and hip/pelvis injuries' [23]. Furthermore, according to Iraeus and Lindquist, frontal crashes, such as the small overlap crash test, are responsible for a large number of fatalities [24].

## 2.2 The small overlap crash test according to the IIHS

In order to increase the safety of passenger cars for crashes where a small overlap of the frontal structure with the impacting object occurs, the IIHS introduced the small overlap crash test in 2012 which puts a large demand on the structure of the vehicle and its occupants and imposes a challenge for automotive manufacturers to adapt their existing vehicles to the new load-case [6]. The main goal behind the introduction of the small overlap crash test of the IIHS is to increase the safety for passenger cars when the outboard part of the vehicle collides with another vehicle or when impacting an object, for example a tree or a pole [11]. In this section, an overview of the small overlap crash test is given, along with the vehicle's response to this type of crash.

### 2.2.1 Overview of the small overlap crash test

In the small overlap crash test performed by the IIHS, the vehicle is accelerated with an average acceleration of 0.3 g using a propulsion system until the speed of the car is equal to 64.4 km/h. Roughly 25 cm before the barrier, the vehicle is uncoupled from the propulsion system. The vehicle hits then the barrier with a 25% offset (± 1% offset) measured from the widest part of the car without mirrors, flexible mud flaps and marker lamps. Currently, the test is such that the striking side of the vehicle is always on the driver's side. Exactly 1.5 s after releasing the vehicle from the propulsion system, the braking system of the vehicle is activated [6]. A schematic illustration of the small overlap crash test just at the moment of contact with the barrier is shown in Fig. 2.2.

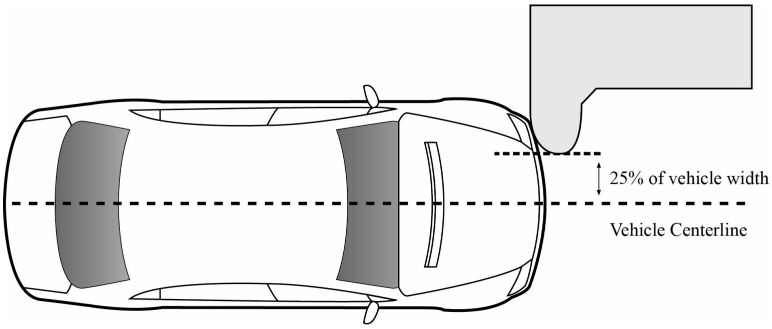


Figure 2.2: Illustration of the small overlap crash test at the moment of contact. Source [6].

Note that the small overlap crash test, as shown in Fig. 2.2, is for a passenger car which has the driver position on the left hand side of the car. The illustration in Fig. 2.2 shows that the contour of the barrier impacted by the vehicle is curved and it shows how the overlap of 25% is measured with respect to the barrier.

The barrier which is impacted by the vehicle during the small overlap crash test must be rigid and must be sized according to the specifications of the IIHS. A schematic drawing of the barrier in the top, rear, front and isometric view is given in Fig. 2.3.

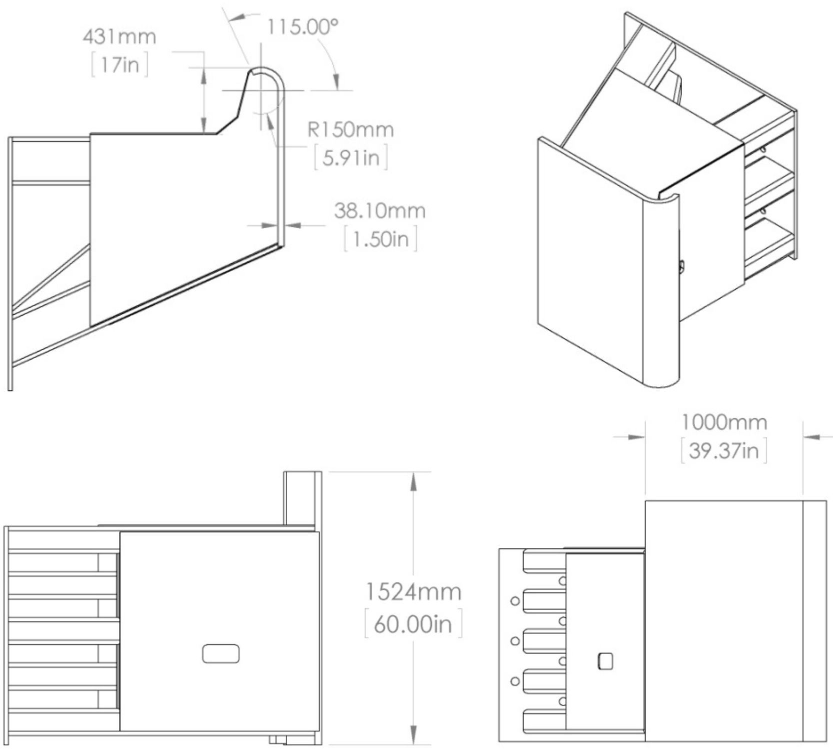


Figure 2.3: Top, rear, front and isometric view of the barrier of the small overlap crash test. Source [6].

Looking at the top and front view in Fig. 2.3, it can be seen that the shape of the barrier consists out of a constant radius arc of 150 mm connected to a flat surface with a width of 1000 mm. The height of the barrier is equal to 1524 mm, as shown in the rear view. The barrier is attached to a base unit which is 1840 mm high, 3660 mm wide and 5420 mm deep [6]. The base unit is made out of laminated steel and reinforced concrete and has a total mass of 145150 kg [6].

### 2.2.2 Response modes of the vehicle

Due to the asymmetrical loading of the crash structures in the small overlap crash test, the response of the vehicle is of special interest. According to Mueller, Brethwaite, Zuby and Nolan, a vehicle exhibits three different responses when subjected to the small overlap crash test [10]. These responses are categorized according to the lateral translation and rotation of the vehicle [10] which is discussed in the following.

**Rotational response mode**

The rotational response of the vehicle is visualized in Fig. 2.4.

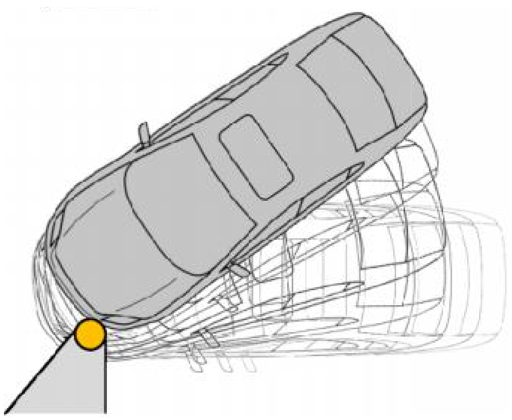

Figure 2.4: Rotational response mode of a vehicle subjected to the small overlap crash. Source [10].

In this response, the main part of the initial kinetic energy of the vehicle is absorbed by deformation of the frontal structure which is impacted by the rigid barrier [11]. At the point when structure of the vehicle does not deform anymore, the car rotates around the barrier, as shown in Fig. 2.4. Mueller, Brethwaite, Zuby and Nolan state that this rotation is often larger than 10 degrees during the first 200 ms of the crash [10].

**Lateral translational response mode**

Another possible response of the vehicle to the small overlap crash test is a significant lateral translation with respect to the initial lateral position of the vehicle [10], as shown in Fig. 2.5.

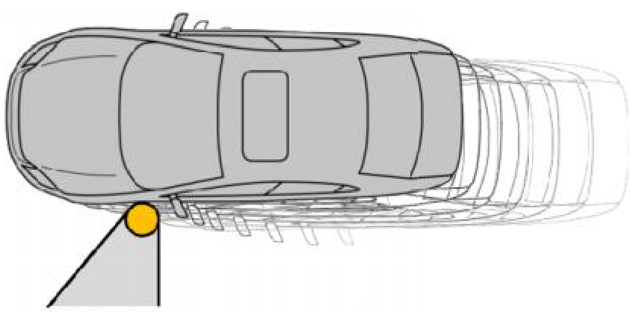

Figure 2.5: Lateral translational response mode of a vehicle subjected to the small overlap crash. Source [10].

In this response, the structure of the vehicle interacts with the rigid barrier such that the car 'glances-off' the barrier and a significant amount of the initial kinetic energy is dissipated by sliding [11]. According to Mueller, Brethwaite, Zuby and Nolan, the lateral translation response is observed in the first 150 ms where a lateral translation of approximately 350 mm occurs [10].

**Rotational and lateral translational response mode**

A combination of rotational and lateral translational response modes is also possible, as stated by Mueller, Brethwaite, Zuby and Nolan [10]. In this combined response mode, one part of the kinetic energy of the car is dissipated by deformation of the frontal structure and subsequently rotation around the rigid barrier and the other part of the kinetic energy is dissipated by sliding away from the rigid barrier. Therefore, this response can neither be classified in a rotational response nor a lateral translational response.

## 2.3 Design strategies for crashworthiness

In this section, the current design strategies for crashworthiness of passenger cars are discussed. First, the structural components for maintaining structural integrity are shown, followed by the general main load paths of structural components. Then the main load paths for the small overlap crash are described. Finally, the main design strategies for the small overlap crash test are discussed.

### 2.3.1 Structural components of passenger vehicles

Every load-case for a passenger vehicle puts certain demands and requirements on the different components of a passenger car. Over the years, the requirements on the structural integrity of the passenger car have been increasing and more safe structures are designed. Most of the modern vehicles have the following structural components to protect the occupants in case of a crash, as shown in Fig. 2.6.

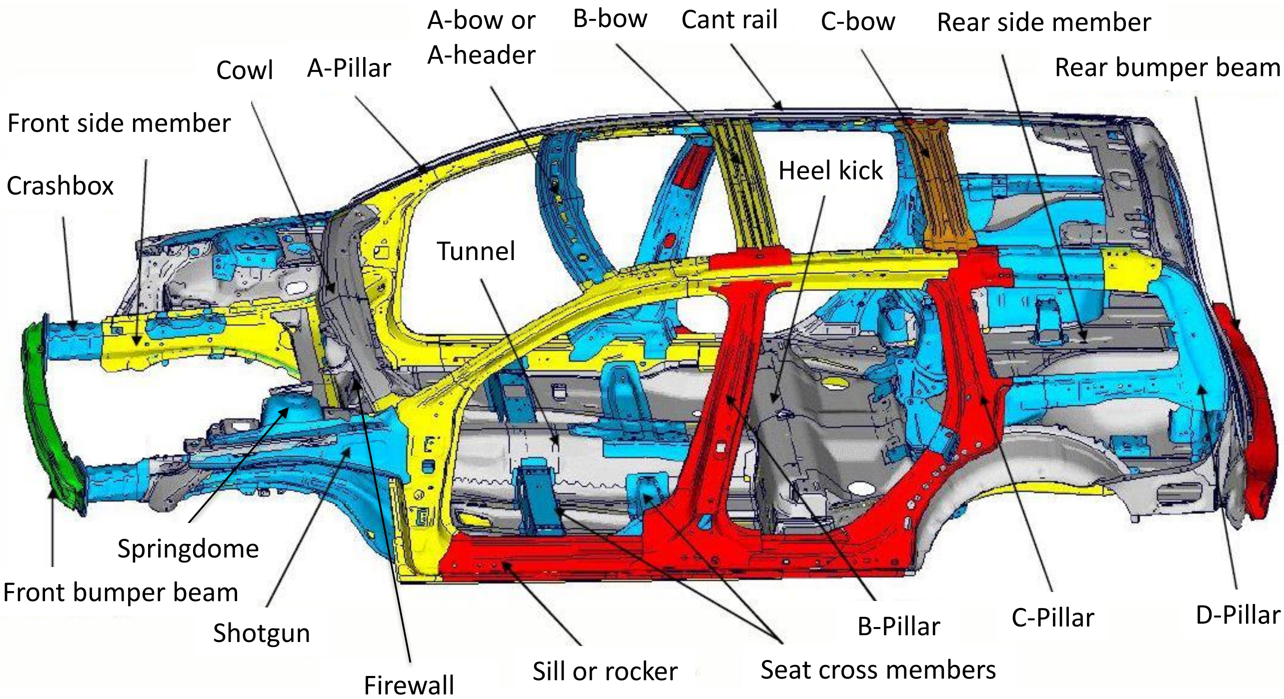


Figure 2.6: Main structural components of a passenger vehicle. Source [18].

These components shown in Fig. 2.8 have the main purpose to ensure the structural integrity of the car in the case of a crash and therefore ensure the safety of the occupants. Specifically, for frontal crashes, the main structural components are:

- Front bumper beam.
- Crashbox.
- Front side member (also called main framerail or longitudinal beam).
- Shotgun.

· Cowl.
· Rocker.
· A-Pillar.
· Tunnel.
· Firewall.

Note that Fig. 2.8 should be understood as as example. Other vehicles may have slightly different structural components and/or have slightly different locations of these components.

### 2.3.2 Main load paths of structural components

The load paths of a structure are defined as the parts of the vehicle which are able to produce restrictive forces during a crash event [19]. According to Wei, Karimi and Robbersmyr [20], three main load paths in a vehicle exist in order to transmit the load during a frontal crash:

1. Accessories - front bumper and crashbox - front longitudinal beam - engine - firewall [20].
2. Upper wing beam - A-pillar - rocker panels [20].
3. Sub-frame - dill beam [20].

These three load paths are the most general [20]. It is interesting to mention that there is small variation in the design of the vehicle body-in-white construction between different car manufacturers. Lindquist, Hall and Björnstig [19] found out that a generic car structure might be used which represent all car models studied. The generic car structure consists out of beams, such as longitudinals, sills and A-Pillars which are connected by joint connections, and plate areas, such as the floor and dash panels [19]. According to Lindquist, Hall and Björnstig [19], nine generic load paths exists which can be seen in Fig. 2.7.

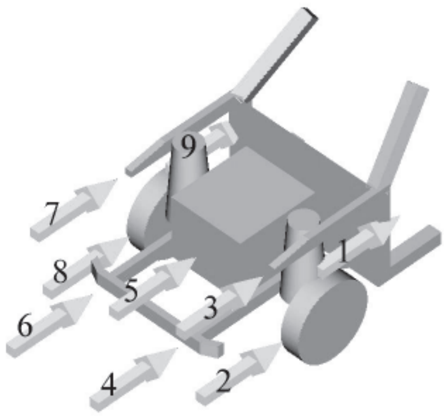


Figure 2.7: Generic main load paths for a passenger vehicle. Source [19].

These load paths have the following description, as shown below [19].

1. 'Direct load to the left side structure (hinge pillar, door, A-Pillar)' [19].
2. 'Load on left front wheel transmitted to front sill and hinge pillar' [19].
3. 'Load on left shot gun beam/shock tower transmitted to hinge pillar and side structure' [19].
4. 'Load on left longitudinal transmitted to compartment floor and dash panel/hinge pillar area' [19].
5. 'Load on drive-train transmitted to the dash panel and compartment floor' [19].
6. 'Load on right longitudinal transmitted to compartment floor and dash panel/hinge pillar area' [19].
7. 'Load on right shot gun beam/shock tower transmitted to hinge pillar and side structure' [19].
8. 'Load on right front wheel transmitted to front sill and hinge pillar' [19].
9. 'Direct load to right side structure (hinge pillar, door, A-Pillar)' [19].

Referring to Lindquist, Hall and Björnstig [19], the load paths of the structure are typically restricted by the packaging constraints of the vehicle, such as the engine and gearbox integration into the vehicle. In addition, the incompatibility condition, where the load is not directed through the primary crash structure, results into secondary load paths of the vehicle [19] which are of great interest for the small overlap crash test load-case.

### 2.3.3 Main load paths of structural components for the small overlap crash

The small overlap crash test, as defined by the IIHS puts severe loads on the structure of the vehicle and its occupants. Due to the small frontal offset of the vehicle with respect to the barrier, the main longitudinals of the front structure are often not, or at most partially, loaded in the crash. This means that the remaining structure must dissipate the kinetic energy of the car. Commonly, the energy dissipation path of the small overlap crash test is categorized as a secondary load path [19], since there is a minimal engagement of the main crash structure. In the small overlap crash, the cabin of the occupants becomes the first substantial load path during the small overlap crash [19]. Normally, the main crash absorbing structure is not active and therefore the load must be carried by other components [10]. Looking at the main load paths for a frontal crash test from the previous section, some major differences are found for the small overlap crash test. First, it is looked at the main structural components which are relevant for the small overlap crash test, as shown in Fig. 2.8.

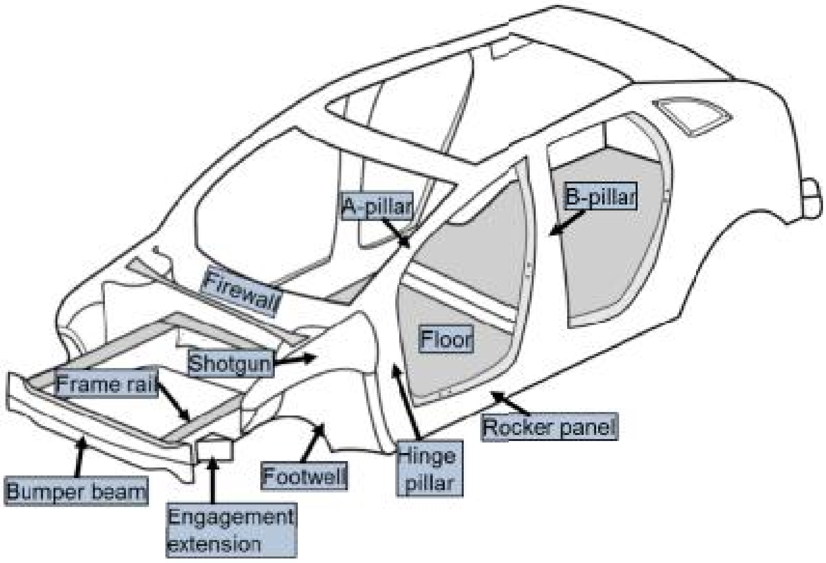


Figure 2.8: Structural components relevant for the small overlap crash test load-case. Source [10].

Comparing Fig. 2.8 to Fig. 2.6, we see that most structural components relevant for frontal crashes are also of importance for the small overlap crash. However, normally, the load which is transferred through the crashbox, longitudinal beam or engine is relatively low [5]. This leaves one of the main load paths, the longitudinal beam, without considerable load-transfer. Therefore, the kinetic energy from the car must be carried by other structures. One of the structural components which increases the energy dissipation of the structure is a so called engagement structure shown in Fig. 2.8. According to Kikuchi et. al. the forces occurring in the small overlap crash test are occurring on the front suspension, at the left front wheel and at the base of the A-Pillar [25]. Referring to Sherwood et. al. , contrary to existing crash tests, the two longitudinal framerails, designed to support the engine and to absorb the crash energy, are not highly loaded in the small overlap crash test [26]. According to Scullion et. al. the direct damage on the structure of the car, as a result of the small overlap crash, is located entirely outside the longitudinal framerails [27]. Further, when referring to Yadav and Pradhan, only 15 to 20% of the total front structure normally designed for crashworthiness is involved in the small overlap crash [28]. This is confirmed by Sherwood et. al. who state that approximately 20% of the total width is without energy absorbing structures such as the longitudinal rails [26]. This can be seen in Fig. 2.9.

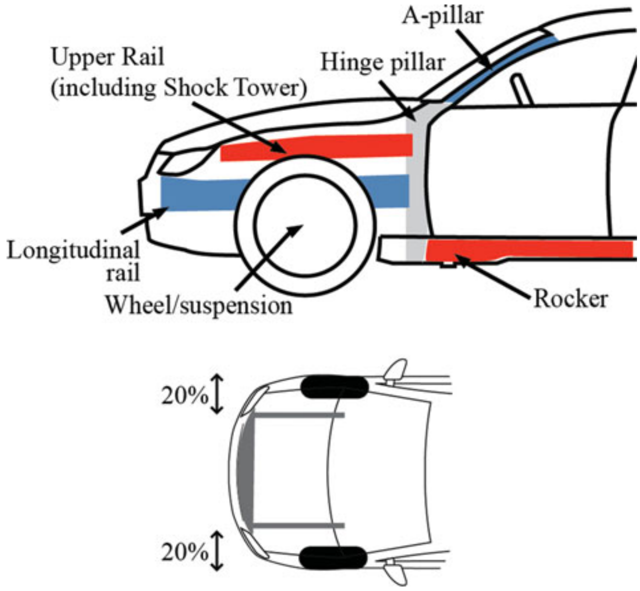


Figure 2.9: Location of the longitudinal framerails in a passenger vehicle. Source [26].

In an analysis performed by Nguyen et. al. the most sensitive parts of the vehicle to the small overlap crash test are determined [29]. The authors found that the rocker panel, the A-Pillar and the lower hinge pillar are the most sensitive to the crash response of the vehicle. In a similar study performed by Sen, Jikuang and Zihua, it has been identified that the main energy absorbing structures of the vehicle in a small overlap collision are the upper rails [30]. Referring to Sherwood et. al. the small overlap crash primarily loads the wheel, suspension system and the hinge pillar [26].

### 2.3.4 Main structural design strategies for the small overlap crash test

Referring to Thomas, three main structural design strategies are used to improve the performance of passenger vehicles to the small overlap crash test [31]. Similar strategies are found by looking at current industry practices of their passenger vehicles, as discussed by Nguyen et. al. and also by Mueller, Brethwaite, Zuby and Nolan [10, 29].

The first strategy is to use components which push the vehicle laterally away from the rigid barrier, thus achieving the translational response mode, as discussed in Section 2.2. This reduces the required dissipation energy of the structure of the passenger vehicle, because more energy is dissipated by sliding away from the barrier. An example of this type of component is the engagement component shown in Fig. 2.8. The second strategy makes use of structures in the proximity of the outside of the main longitudinal framerails and forward of the wheel well. These structural components help to absorb energy and force the vehicle to rotate around the barrier, thus achieving the rotational response mode. The third design strategy follows the usage of a reinforced safety cage structure which helps to maintain the structural integrity. Similar to the second design strategy, this concept results into a large energy absorption of the structure and sub-sequentially large rotation of the vehicle around the barrier [31].

## 2.4 Simulation methods used for crashworthiness analysis

Since the early days of crash testing, the ability to model the crash of a passenger car is of great interest. A model which is able to provide accurate results of the response of the vehicle quickly in an early phase of the design is very valuable [12]. Specifically, the formulation of mathematical models to simulate the crash response of a car reduces development time and costs due to less cars being tested in a crash test and less numerical simulations performed [32]. In this section, the main simulation methods used for crashworthiness analysis are discussed. First, a description of multibody system simulations methods is given, followed by the presentation of the macro element method. Next, the Finite Element Method (FEM) simulation is briefly discussed. Finally, hybrid model formulation simulations are elaborated on.

### 2.4.1 Multibody system simulations

According to Ambrosio [8], multibody systems are 'generally complex arrangements of structural and mechanical subsystems with different design purposes and mechanical behavior'. Depending on the application, small or large deformations may occur to the multibody system which lead to a change of the performance of the system [8]. Generally said, structures behave like multibody systems due to their large rotations and their mechanisms of deformation. These phenomena can be observed in crashes of automobiles, making multibody system simulations very suitable for purposes of predicting the response of vehicles for crashes [8]. In the following, three different models are discussed, being: lumped mass models, rigid multibody models and elastoplastic collapse element models.

#### Lumped mass models

In 1970, Kamal introduced the lumped mass model to simulate the impact of a vehicle [33]. The main idea of this system is to divide the overall mass of the front structure of the car into different lumped masses. The structure is divided into the major sub-components relevant for the structure to absorb the kinetic energy of the crash. The stiffness of these sub-components are idealized by multiple springs. Generally, the lumped mass system model is a common way of modeling the crash test of a vehicle [34]. Bois et. al. make a similar statement regarding the common usage of lumped mass models for simulating crash tests of vehicles [12]. A recent study which compares the result of the lumped mass model with finite element data, as well as real test data for the side impact crash test of the National Highway Traffic Safety Administration (NHTSA), shows that the lumped mass spring model is still current practice in industry [35, 36]. The best model is chosen according to the kinematic response and the energy distribution [37].

According to Kamal [33], the front structure can be divided from the elastic model of the body which can be seen in Fig. 2.10, resulting in a lumped mass model for the frontal car structure of a passenger car.

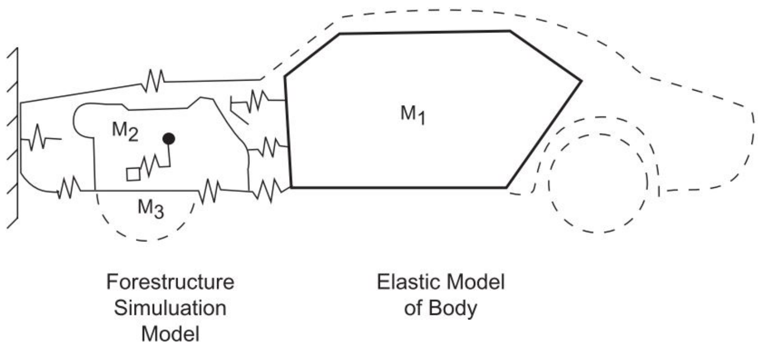


Figure 2.10: Idealized representation of a vehicle used for the lumped mass model. Source [33].

In the lumped mass model, every major component of the front structure takes up a certain force, as illustrated in Fig. 2.11.

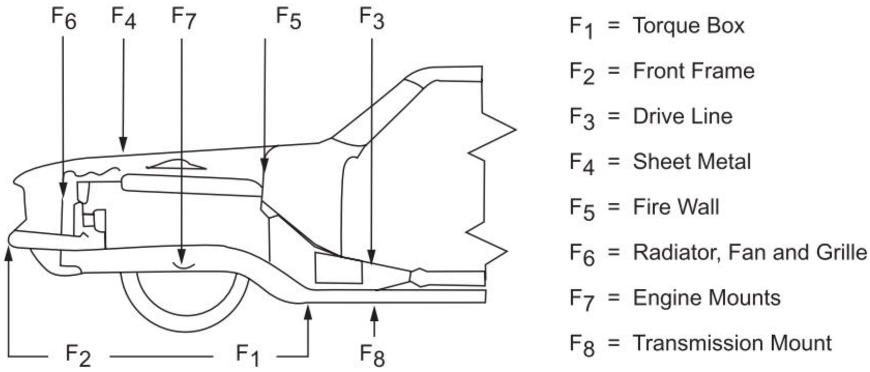


Figure 2.11: Components which are idealized by the lumped mass model. Source [33].

Depending on the stiffness, damping and the deformation of each component, the force by which it is loaded can be computed [38]. Applying this principle to the complete car, one obtains the following result, as shown in Fig. 2.12.

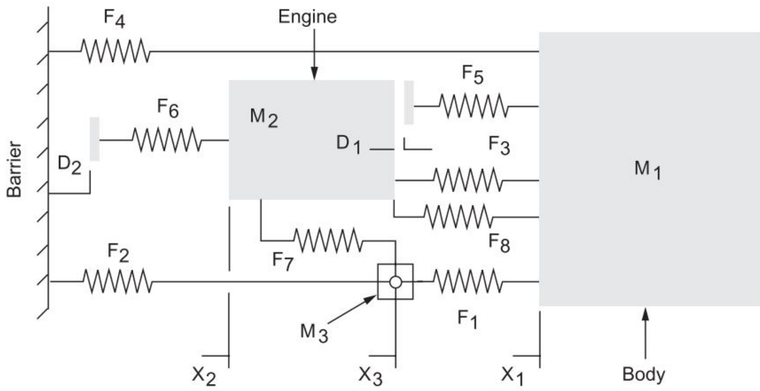


Figure 2.12: Complete lumped mass model for the frontal car structure. Source [33].

Note that the idealization of the frontal structure of the car shown in Fig. 2.12 is only an example. Depending on the type of load-case, the idealization may be different from Fig. 2.12.

**Rigid multibody models**

Another type of simplified models used in crash testing are rigid multibody models. These models are often used for the simulation of the kinematic connections, for example of the dummy or the suspension system and steering assembly. According to Bois et. al. [12], the main difference between a lumped mass model and a rigid body model is the connection of the elements of the rigid body model. For the rigid multibody model, the degrees of freedom between the elements is determined by the used joints. The first rigid multibody model was developed in 1963 by Mc Henry [39]. In this model, the dummy kinematics together with the restraint system were simulated. However, the use of rigid multibody models to simulate the structural behavior of a passenger car performing the small overlap crash test is very limited.

Referring to Bois et. al. [12], two simulation models exist which are MVMA2D and CAL3D. These models were validated using multiple simulation models and are still in use. A more recent program which is a multibody/finite element program, called MADYMO, developed by the automotive division of the Netherlands Organization for Applied Scientific Research (TNO) in Delft, can be used for crash analysis. In this program, the equation of motion is computed including the contribution of the inertia of the bodies in the model [12].

**Elastoplastic collapse element models**

In an analogy to the lumped mass spring model, another possible method to simulate the response of the vehicle in a crash event is to use elastoplastic collapse elements. These elements act as a connector between the mass and the rigid barrier to dissipate the kinetic energy [40]. Referring to Kim, the main idea of this concept is based on the concept of modeling the progressive dynamic plastic collapse of tubes [40]. Here a new element, the so called elastoplastic collapse element, is defined in the displacement domain. A series of elements which act in sequence are used to capture the progressive dynamic collapse behavior of the tube. This means that at a certain displacement domain a specific elastoplastic collapse element is activated. The characteristics of the nonlinear force elements are described using a piecewise linear force displacement curve. The approach allows to represent the typical force displacement curve of a tube along with its failure behaviors, such as buckling [40]. The governing equation for this system is described in Eq. 2.1 [40].

$$M\ddot{x}(t) + FS(x(t)) = 0 \tag{2.1}$$

In Eq. 2.1, $M$ is the mass and $x(t)$ is the displacement of the mass at time $t$ [40]. The force $FS(x(t))$ represents a series of elastoplastic collapse elements which are active depending on the time dependent displacement, as shown in Fig. 2.13.

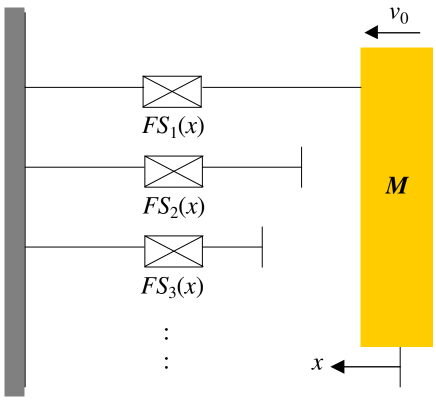


Figure 2.13: Representation of elastoplastic collapse element. Source [40].

As proposed by Kim [40], the concept of the elastoplastic collapse element can be used to represent the force displacement curve of a tube crushed by a moving mass. A typical force displacement curve of a tube crushed by a moving mass is shown in Fig. 2.14.

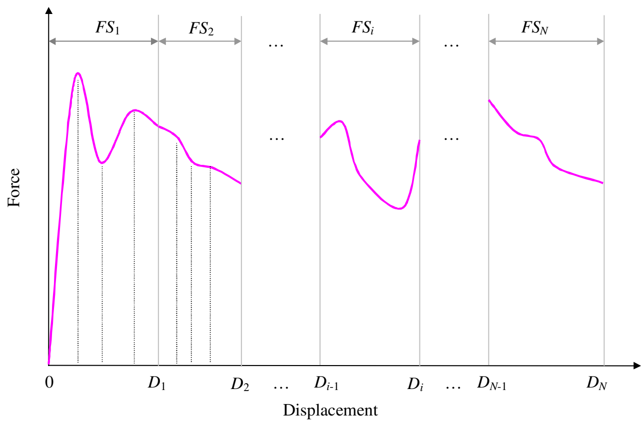


Figure 2.14: Nonlinear force displacement curve of a crushed tube. Source [40].

In order to represent the stiffness of each segment on the force displacement curve of the elastoplastic collapse concept, a piecewise linear representation of the segments is used, see Fig. 2.15. The main idea behind the elastoplastic collapse elements is to have only one element active depending on the current displacement of the segment, as shown in Fig. 2.13.

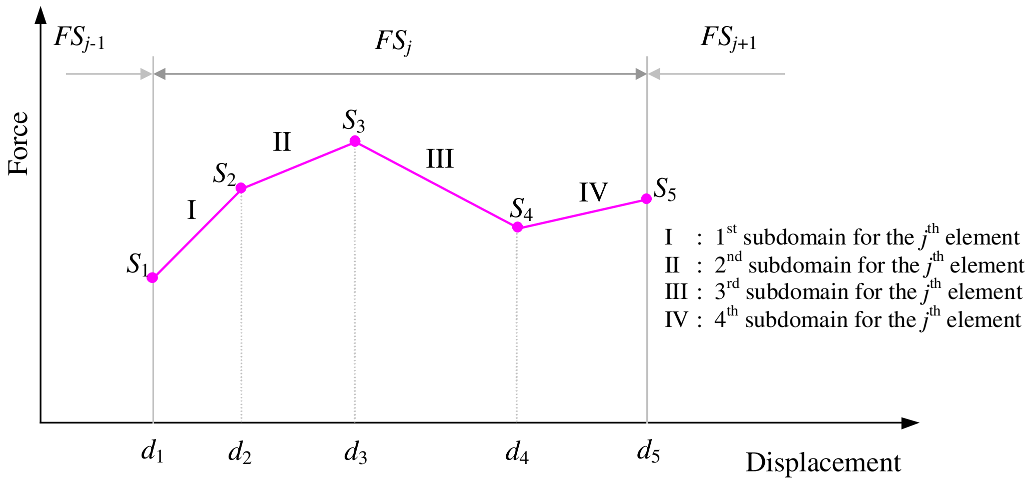


Figure 2.15: Piecewise linear representation of the elastoplastic collapse element. Source [40].

Looking at Fig. 2.15, the term $FS(x)$ is the sum of each individual representation of the force connector elements, see Eq. 2.2 [40].

$$FS(x) = \sum_{j=1}^{N} FS_j(x_j) \tag{2.2}$$

Using the piecewise linear representation of the force displacement curve, the mathematical definition of $FS(x)$ can be found, as shown by Eq. 2.2 [40].

$$FS_i(x(t)) = \alpha_i x_i(t) - \beta \tag{2.3}$$

In Eq. 2.2, $\alpha$ and $\beta$ are defined as follows, see Eq. 2.4 and Eq. 2.5 [40].

$$\alpha_i = \frac{S_{i+1} - S_i}{d_{i+1} - d_i} \tag{2.4}$$

$$\beta = \alpha_i d_i - S_i \tag{2.5}$$

Here, $S$ is the force value of the segment $j$ at the $i^{th}$ increment, $d$ is the $i^{th}$ displacement of the $j^{th}$ segment of the force displacement curve [40]. Mathematically, the term $\beta$ is used to correct for the offset of the value of the stiffness of the elastoplastic collapse element with respect to the origin.

### 2.4.2 Finite element method simulations

According to Schweizerhof, Nilsson and Hallquist [41], the crashworthiness simulation suffers from the complexity of crash analysis because of large nonlinearities. These nonlinear phenomena are due to the large deformations, large rotations, high dynamic behavior, localization of plastic flow, tearing of material, local and global buckling and due to the contact with the impacting object [12, 18, 42, 43, 44]. However, the rapid increase in computer hardware resulted into new technologies of simulations such as the finite element method.

FEM simulations are widely used in the automotive industry for a wide range of applications, such as crash analysis, forming process analysis of sheet metal components and strength tests. Already in the mid 1950s the linear finite element method became known through the work of the Boeing Company [45]. Soon, in the early 1960s, the extension of the method to nonlinear problems was performed by engineers at many universities and research laboratories. Generally said, the root of invention goes back to three research groups: mathematicians, physicists and engineers [42]. Although FEM was first used in structural applications only, soon the method was applied to a variety of applications such as heat transfer [42]. In 1969, the first nonlinear commercial finite element program called MARC was released. Soon, in 1969 the program ANSYS, a commercial FEM program was introduced to the market, followed by Abaqus in 1972. Nowadays several numerical packages exists, such as: Abaqus, ANSYS, LS-DYNA and PAM-Crash [45].

The FEM is based on solid mechanics and structural mechanics and currently, it is the most precise method to simulate any crash test numerically [41]. In addition, the growing complexity of transport vehicles requires huge finite element method models to simulate the crash behavior accurately [46]. According to Drazetic, Markiewicz and Ravalard [46], fully blown finite element methods are only used when the design of the structure is well advanced.

Referring to Bois et. al. [12], the system in a finite element model is divided into a number of finite elements which are connected by a discrete number of nodes and form together the complete model. The divisions of the system into a number of finite elements are called finite elements [47]. The method of dividing the system is named discretization [47]. The collection of nodes and finite elements is named finite element mesh [47]. At each node, so called shape functions exist which describe the displacement of the nodes [47]. In addition, boundary conditions and loading conditions are imposed on the nodes. Using the constitutive relations of the material together with the known displacement, the stress can be computed at each node [12, 42, 43].

In Fig. 2.16, a frontal crash test simulation with FEM for a passenger vehicle is shown as an example.

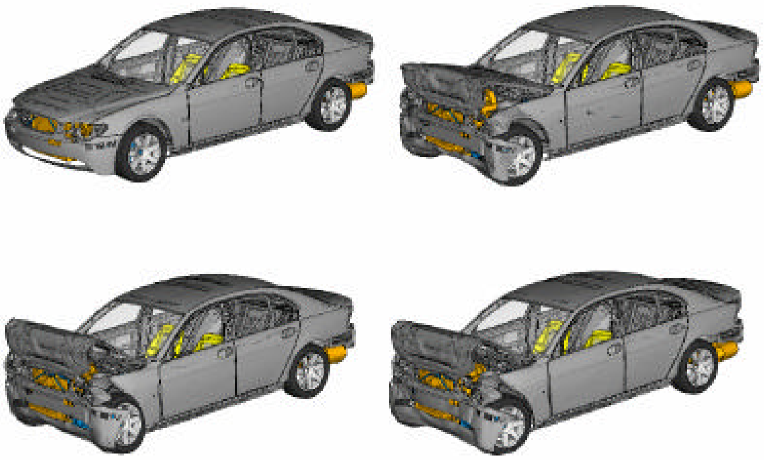

Figure 2.16: Example of FEM crash simulation of a passenger vehicle. Source [48].

Looking at Fig. 2.16, it can be seen that the crash mechanisms during a full frontal crash test are represented reasonably accurate with the FEM simulation.

### 2.4.3 Macro element method simulations

In order to design crash structures of passenger vehicles which are able to protect the occupants while keeping the deceleration loads low during the crash, several simulation models are available [49]. The previously discussed multibody system simulation models are very useful for an early development stage of the design of crashworthy structures. For very detailed design stages, finite element method simulations are well established and commonly used methods. However, for intermediate design stages, where more detailed information is required when compared to the outcome of multibody system simulation models, the so called macro element method developed by Abramowicz can be used [49]. This method is particularly useful when large deformations of thin walled components are occurring which is the case of automotive crash structures [49]. The method is implemented using the object oriented formulation into the software package called Visual Crash Studio (VCS) which was released in 2006 [50].

The main idea behind the macro element method is to assume the kinematics of the element instead of calculating them from the equilibrium equations [44, 49]. Referring to Abramowicz, the governing theory behind the macro element method are the kinematic method of plasticity and the energy method of classic elasticity [49]. The idea of assuming the kinematics of thin walled sheets goes back to Alexander who assumed shape functions to describe the kinematics of shells based on experimental observations in 1960 [51]. In his study on the collapse of a thin walled cylindrical shell, 'concertina' collapse modes were assumed for the structure, as shown in Fig. 2.17 [51].

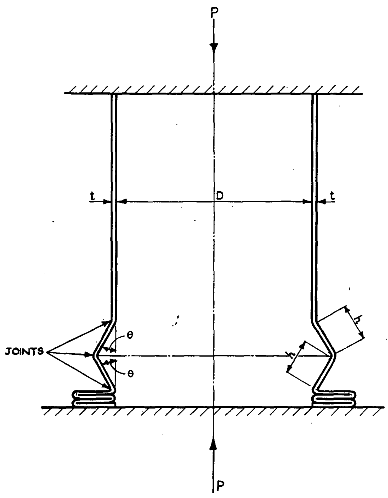


Figure 2.17: Assumed 'concertina' collapse mode of an axially loaded cylindrical shell. Source [51].

This main idea is extended for the macro element method. Studies have shown that the folding principle of structural components made out of steel follows a deformation pattern which can be represented by one characteristic deformation mode [44]. This characteristic deformation mode is described by using a so called Superfolding element [44], as shown in Fig. 2.18.

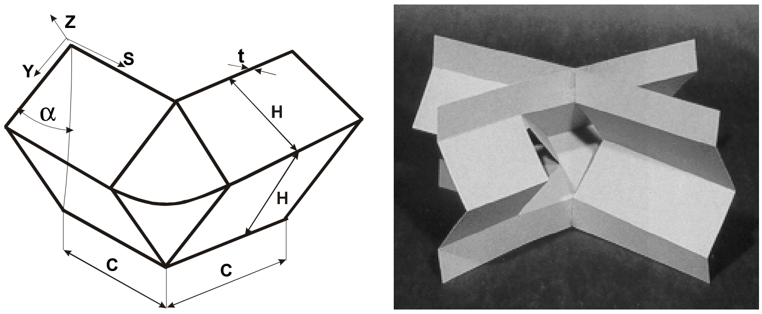


Figure 2.18: Deformation mode represented by the Superfolding element. Source [44].

These Superfolding elements are used to build up so called Superbeam elements where each Superbeam element consists out of two Superfolding elements at the ends of the beam and a deformable cell placed between them, as shown in Fig. 2.19 [49, 50].

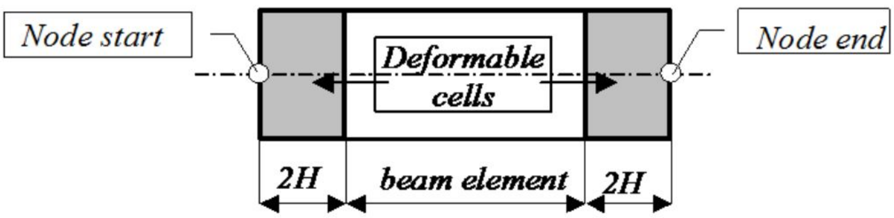


Figure 2.19: Illustration of the Superbeam element. Source [50].

These elements are then implemented into commercial finite element method programs by following the object orientated programming principle [49]. Due to the 'unambiguous definition of all entities' which are described by objects, the macro element can be implemented into the finite element approach [49]. Here the nodes are the objects that ensure the global equilibrium of the simulation while the elements are the objects that introduce the loading conditions into the nodes [49].

Lasek, Bohm and Schindler compared in their study the macro element method to the FEM for a crash simulation of a passenger vehicle, as shown in Fig. 2.20.

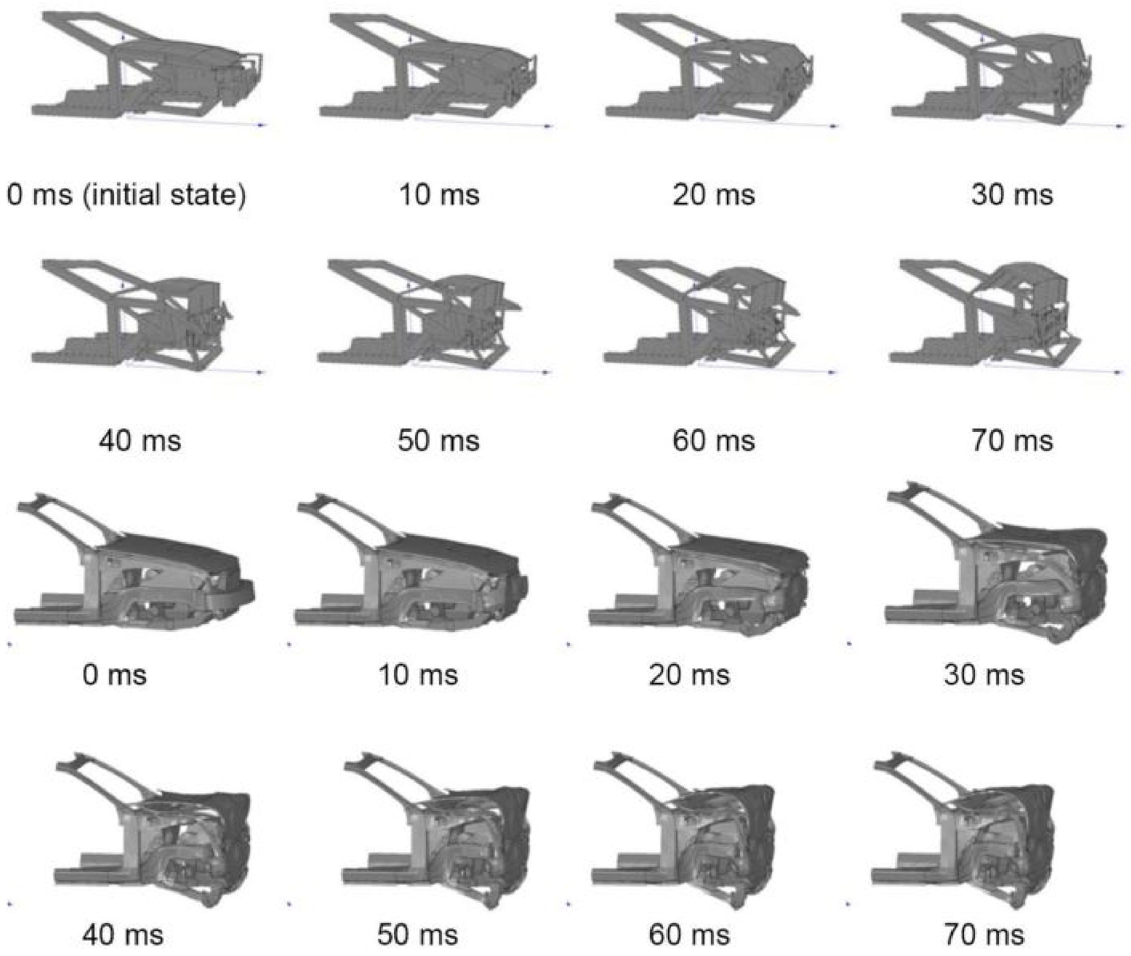


Figure 2.20: Comparison between FEM and macro element crash simulation of passenger vehicle. Source [52].

Looking at Fig. 2.20, the upper two rows show the result of the macro element method while rows three and four show the result using the FEM simulation. Investigating the crash mechanisms for the full overlap crash, it can be seen that they are reasonably similar. In addition, in their study, the velocity and displacement over time curves of the macro element method match quite well with the FEM results, showing the potential of the method [52].

### 2.4.4 Hybrid model formulation simulations

Referring to Bois et. al. [12], so called hybrid models are used in the simulation of crashworthiness in order to reduce the limitations of the lumped mass spring models. Also, since full FEM simulations for the complete vehicles require a large number of degrees of freedom [53], it is advantageous to reduce the number of elements by combining lumped mass spring models with FEM simulation models.

The first hybrid models were introduced in 1974 by Mc Ivor [54]. In these models, lumped mass models are combined with FEM simulation models with the intention of having the simplicity of the lumped mass models with the precision and iteration convenience of FEM simulations [12].

In the study of Kim and Aurora [55], similar hybrid model formulations were discussed where some structural components were modeled as nonlinear spring elements and other structural components were modeled using FEM simulations.

CHAPTER 3

# Finite element method for crashworthiness applications

Part of the thesis deals with a numerical study using FEM crash simulations performed with the Finite Element Analysis (FEA) package Abaqus/Explicit. Therefore, this chapter discusses some fundamental aspects of FEM simulations, with special emphasis on crash applications. First, in Section 3.1, the fundamental principles of FEM are described. Second, in Section 3.2, the commonly used time integration schemes for FEM are shown. Section 3.3 deals with the common element types used for crashworthiness applications. Then, in Section 3.4, important modeling characteristics for FEM crash simulations are described. Finally, in Section 3.5, the simulation process of Abaqus/Explicit consisting out of the assembly, solution and post processes are presented.

## 3.1 Fundamental principles of FEM

In FEM, a distinction is made between the explicit and implicit method [42]. Explicit methods use calculation schemes where the calculations are based on the current time step of the simulation. Implicit methods are based on calculation schemes which involve the current, as well as the next time step of the simulation [43, 45]. For crash simulations, the explicit method is used due to the stability of the solution and the power in solving highly nonlinear problems without having convergence problems [56]. For that reason, the FEM crash simulations shown in this thesis use the explicit method and therefore only the explicit method for FEM is discussed in this chapter.

The FEM is based on solid mechanics and structural mechanics. Referring to Bois et. al. , the finite element model is divided into a number of finite elements which are connected by a discrete number of nodes [12]. Any node has a set of degrees of freedom (DOF), depending on the boundary conditions and type of analysis. The process of dividing the model into a number of finite elements is called discretization [47]. The collection of nodes and finite elements is named finite element mesh [47]. An example of a discretized two dimensional element in global and local representation is shown in Fig. 3.1.

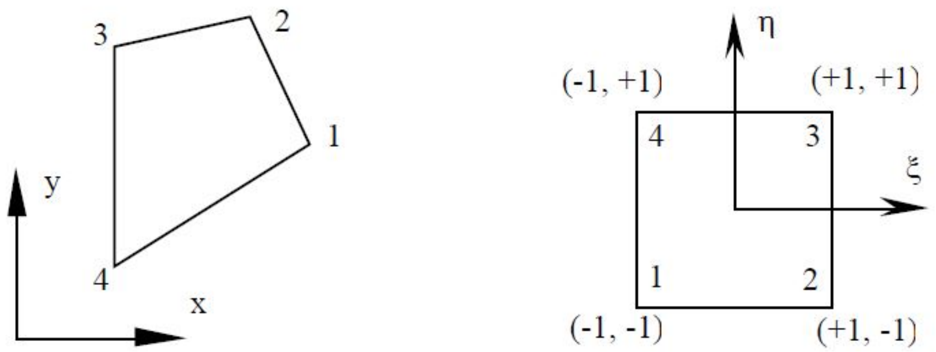


Figure 3.1: Discretized element in global and local reference coordinate system. Source [57].

The local coordinates of any point on the element are determined by interpolating between the coordinates using a shape function $h$ at the the element nodes $q$, as shown in Eq. 3.1, Eq. 3.2 and Eq. 3.3 [42, 43, 45].

$$x = \sum_{i=1}^{q} h_i(x_i) \tag{3.1}$$

$$y = \sum_{i=1}^{q} h_i(y_i) \tag{3.2}$$

$$z = \sum_{i=1}^{q} h_i(z_i) \tag{3.3}$$

In a similar fashion, the local displacements are determined using the shape functions describing the displacements between the element nodes, see Eq. 3.4, Eq. 3.5 and Eq. 3.6 [42, 43, 45].

$$u = \sum_{i=1}^{q} h_i(u_i) \tag{3.4}$$

$$v = \sum_{i=1}^{q} h_i(v_i) \tag{3.5}$$

$$w = \sum_{i=1}^{q} h_i(w_i) \tag{3.6}$$

The shape functions are polynomials of any order and used to interpolate between the nodes in order to describe the assumed solution. The strain is determined using the derivative of the displacements with respect to the local coordinates. Following this approach for all elements, the overall solution is determined [42, 43, 45]. The guiding principle in the explicit FEM is to solve the governing equation which is shown in Eq. 3.7 [42, 43, 45].

$$\underline{\underline{M}}\ \underline{\ddot{u}} + \underline{\underline{C}}\ \underline{\dot{u}} + \underline{\underline{K}}\ \underline{u} = \underline{\underline{F}} \tag{3.7}$$

In order to obtain the displacements $u$ at nodes, Eq. 3.7 must be solved. The variables $\dot{u}$ and $\ddot{u}$ are the velocities and the accelerations of the nodes, respectively [42, 43, 45]. The mass, damping and stiffness matrices are given in Eq. 3.8, Eq. 3.9 and Eq. 3.10 [42, 43, 45].

$$\underline{\underline{M}} = \int_{\Omega} \underline{\underline{H}}^T \rho \underline{\underline{H}} d\Omega \tag{3.8}$$

$$\underline{\underline{C}} = \int_{\Omega} \underline{\underline{H}}^T \kappa \underline{\underline{H}} d\Omega \tag{3.9}$$

$$\underline{\underline{K}} = \int_{\Omega} \underline{\underline{B}}^T \underline{\underline{D}}\ \underline{\underline{B}} d\Omega \tag{3.10}$$

The matrix $B$ is the strain displacement matrix, the matrix $H$ is the displacement interpolation matrix containing the interpolation functions $h$ and the matrix $D$ contains the stress strain constitutive relations. The variable $\Omega$ is the element domain, $\kappa$ is the damping property parameter of the element and $\rho$ is the mass density of the element [42, 43, 45].

Using the imposed boundary conditions and loading conditions on the nodes, along with the constitutive relations of the material together with the known displacement, the stress can be computed at each node [42, 43, 45].

## 3.2 Time integration schemes

The velocity and the acceleration are dependent on the time which requires a discretization of the problem in time. Several time integration schemes are available, such as: the central difference method, the Houbolt method, the Wilson method and the Newmark method [43, 45]. In the following, the commonly used central difference scheme is discussed.

The central difference scheme is derived using the Taylor series expansion of the displacement centered around the chosen time step. In the final form of the scheme, the velocity and the acceleration are computed by using Eq. 3.11 and Eq. 3.12 [58]. Note that for the sake of simplicity, in the following it is only looked at the one dimensional case.

$$\dot{u} = \frac{u^{t+\Delta t} - u^{t-\Delta t}}{2\Delta t} \tag{3.11}$$

$$\ddot{u} = \frac{u^{t+\Delta t} - 2u^{t} + u^{t-\Delta t}}{\Delta t^2} \tag{3.12}$$

Note that in Eq. 3.11 and Eq. 3.12, the variable $\Delta t$ describes the chosen time step, $u$ the displacement, $\dot{u}$ the first derivative of the displacement, so the velocity, and $\ddot{u}$ the second derivative of the displacement, hence the acceleration. Substituting Eq. 3.11 and Eq. 3.12 back into Eq. 3.7, the following result is obtained for computing the displacement at the next time increment [58].

$$u^{t+\Delta t} = \left(\frac{1}{\frac{C}{2\Delta t} + \frac{M}{\Delta t^2}}\right)\left[F + u^{t}\left(\frac{2M}{\Delta t^2} - K\right) + u^{t-\Delta t}\left(\frac{C}{2\Delta t} - \frac{M}{\Delta t^2}\right)\right] \tag{3.13}$$

Note that Eq. 3.13 is also known as the recurrence formula [58]. With Eq. 3.13, the displacement at the next time step is calculated using the displacement from the previous time step along with the mass, damping and stiffness values, as well as with the force $F$.

Explicit methods, however, are only conditionally stable. In order to ensure convergence, the time step must be controlled and must be smaller than some critical value. Besides increasing the stability, a smaller time step also increases the accuracy of the results. However, the choice of the time step should not be too small as this would increase the computational time unnecessarily [42, 56]. The time step is computed as follows, see Eq. 3.14 [45, 59].

$$t_{crit} = \frac{l}{c} \tag{3.14}$$

Where in Eq. 3.14, $l$ is the length of the element and $c$ is the wave propagation velocity [42]. For a 3D solid element, the wave propagation velocity is determined using Eq. 3.15 [45, 59].

$$c = \sqrt{\frac{E(1-\nu)}{(1+\nu)(1-2\nu)\rho}} \tag{3.15}$$

In Eq. 3.15, $E$ is the Young's Modulus, $\nu$ is the Poisson's ratio and $\rho$ is the specific mass density. Referring to Svensson and Bärgman [18], so called mass scaling can be performed by increasing the specific mass density $\rho$ which increases the time step in order to reduce the computational time.

## 3.3 Elements used in crashworthiness applications

In FEM, several different element types for the mesh exist, along with several options in choosing the number and location of integrations points. Each element type has its own advantages and limitations in terms of its application. More and more efficient element types are developed by research performed in industry and academia. Due to the advantages and limitations, not all types of elements are equally well suited for representing a certain part of the structure. According to Hora [41] and Drazetic, Markiewicz and Ravalard [46], automotive structures consist out of several types of elements:

- Solid elements.

· Shell elements.
· Beam elements.
· Truss and cable elements.
· Cohesive elements.
· Discrete elements.

Some of the listed element types are shown in Fig. 3.2.

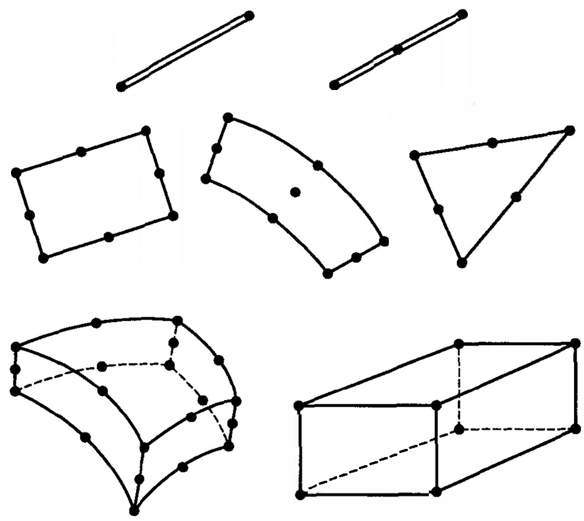

Figure 3.2: Typical element types used in FEM. Source [42].

The first row in Fig. 3.2 illustrates truss and cable elements, the second row shows two dimensional elements (shell elements) and the last row presents three dimensional elements (solid and beam elements) [42]. In the following, each of the listed elements types are discussed along with their characteristics.

### 3.3.1 Solid elements

These elements are used to represent solid parts of the structure, for example the engine [41, 46]. Mostly, these solid elements use linear shape functions and are used due to their simplicity and efficiency, especially in contact situations [41].

### 3.3.2 Shell elements

Shell elements are used to represent the body-shell of the car and the bumpers [41]. For shell elements, the stress through the thickness is zero [42]. Referring to Drazetic, Markiewicz and Ravalard [46], the special types of Mindlin-Reissner shells, an extension of the Kirchoff plate theory, are often used for FEM crash simulations due to their ability to include shear effects [42].

### 3.3.3 Beam elements

Beam elements are used in the FEM crash simulation for slender parts, for example the steering column or longitudinal framerails of the frontal crash structure, as they account for bending deformations [41, 42]. In general, most structural components of the front structure are characterized as beam-like structures. Drazetic, Markiewicz and Ravalard [46] mention in their study that several parts of the crash structure of passenger vehicles are modeled by beam elements.

### 3.3.4 Truss and cable elements

Truss elements take up only axial loads (truss elements) or tension (cable elements) and are therefore used as an idealization of the structure which reduces the computational effort [42]. Therefore, they are not the elements of choice when accuracy is much more important compared to the computational time.

### 3.3.5 Cohesive elements

These elements are used in Abaqus/Explicit to model adhesive joints between two surfaces. These special type of elements are often modeled using a zero thickness and they allow to specify a certain damage evaluation characteristic [60].

### 3.3.6 Discrete elements

These elements are used to model springs and dampers which have constant stiffness or damping [41]. Similar to truss and cable elements, for full vehicle FEM crash simulations, discrete elements are rarely used due to their limited accuracy.

## 3.4 Modeling characteristics in crashworthiness applications

In this section, some aspects which require special attention in full vehicle FEM crash simulations, are discussed. These aspects are important to elaborate on in order to understand the simulation results. First, the contact and friction definitions are described, followed by the boundary and loading conditions and finally the failure modeling mechanisms used in full vehicle FEM crash simulations are presented.

### 3.4.1 Contact definition

The contact definition is crucial for automotive crash FEM simulations. First of all, contact is a non-linear phenomenon where the boundary conditions are changing through the analysis [42, 43, 45]. For FEM crash simulations, contact situations are occurring at several locations through the simulation time. Besides the contact between the structure of the vehicle and the barrier, the self contact of the deforming structure needs attention when setting up the model [43]. Most prominent, the self contact is important for buckling which is the deformation mode of crash structures by which most of the energy is dissipated.

The contact phenomena in FEM are solved numerically using so called search algorithms. These algorithms are required in each time step, since the exact boundaries of the contact regions are unknown. Often, contact search algorithms can take up a significant part of the analysis [43]. In FEM crash simulations, the contact definition is modeled by establishing the master and the slave surface, where the master surface contains the set of test nodes and the slave surface contains the set of surface nodes which are checked for penetration with the master surface. In crash simulations, the master surface consists out of the barrier nodes and the slave surface which are checked for penetration consists out of the nodes of the vehicle. Central to this scheme is the minimization of the total potential energy functional which is subjected to contact constrains. Common solution methods for contact in FEM are the Lagrange multiplier method, the penalty method and the mortar methods [43, 61]. On top of that, Abaqus/Explicit offers the possibility of having a general contact function in which the contact surfaces do not have to be defined manually. In this case, the contact algorithm does not know beforehand which elements do belong to the barrier and which elements do belong to the vehicle.

### 3.4.2 Friction definition

Besides the contact phenomenon itself, the friction definition is relevant. The friction between the barrier and the vehicle is of large importance and sensitive in terms of the results obtained from the simulation. Generally said, determining the friction between all structural elements of the vehicle which are in contact with the barrier is quite difficult to do. Therefore, the choice of the frictional coefficient must be done carefully and requires validation with real crash testing and/or previous simulations.

### 3.4.3 Boundary conditions

In order to solve the governing equation of the FEM simulation problem, boundary conditions can be described on the nodes. For the small overlap crash, the displacement and rotation of the barrier nodes are constrained in all directions, since the impacted barrier is assumed to be rigid, as described in Chapter 2. Similar constraints are used for the road on which the vehicle is traveling on.

### 3.4.4 Loading conditions

In order to initialize the FEM simulation, load conditions are applied on the relevant nodes. The gravity load can be applied to all vehicle elements. Just at the start of the simulation, the elements describing the ground are moved upwards to contact the wheel elements. The simulation problem itself in the FEA is initialized by introducing the initial velocity as an initial condition of the adequate vehicle nodes.

### 3.4.5 Failure mechanisms

As the small overlap crash involves large deformation and rotation of the vehicle and severe failure of the structure, the modeling of failure mechanisms is of vital importance. In the following, some of the most relevant failure mechanisms which are the material failure, fastener failure and tire failure, are briefly described.

#### Material failure

The material failure is implemented according to the stress strain curve of the used material. In the FEA analysis program Abaqus/Explicit, for every used material, a material model is used. This can be elastic, plastic, inelastic, as well as non perfectly plastic behavior.

#### Fastener failure

Vehicle structures following the unibody design concept are made out of several sheets which are assembled together using mechanical fastening methods. Larger components are attached to the structure using bolts of different size and strength. The connections of the structure (such as bolts, sport welds and adhesive) require also special interest in the FEA modeling. For crashworthiness applications, the failure mechanisms of fasteners are done such that after a certain load, the fastener fails and does not transfer any load to the surrounding structure. The principle is comparable to the material modeling approach where the user is allowed to define the elastic and plastic region of the material/fastener.

Spot welds are commonly modeled using beam elements, joint elements or connectors in Abaqus/Explicit. This allows to bond surfaces together while using a master-salve formulation to prevent the slave nodes from separating of the master nodes.

Bolts are modeled using beam formulations which allows to specify a tension/compression failure load, as well as a failure shear load for the bolt. Alternatively, bolts can be modeled using connectors to simulate the characteristics of the fastener.

Adhesive joints are modeled using adhesive elements in Abaqus/Explicit. Studies show that by using these elements, accurate results are obtained [60].

#### Tire failure

The failure of the tires requires special attention. Any tire consists out of rubber which experiences some kind of hysteresis, i. e. a different loading and unloading condition in the stress strain domain. In addition, the material behavior is highly nonlinear. Next to that is the modeling aspect that after rupture, the elements are deleted, since the plastic flow is extremely high. Finally, the volume inside the tire, which contains the pressurized air, is modeled using the fluid cavity definition of Abaqus/Explicit which is the negative of the work done by all fluid cavities [61].

## 3.5 Simulation process

The simulation process within the FEA program Abaqus/Explicit for crashworthiness applications consists outs of three major steps. These are: the assembly process, the solution process and the post process which are described in more detail in Subsection 3.5.1, 3.5.2 and 3.5.3.

### 3.5.1 Assembly process

Often, full vehicle models are very large and require quite a decent amount of storage space. Therefore, larger models in Abaqus/Explicit consist out several include files which form together the complete FEM model. Generally, an include file can for example contain a certain component, a material description, a measurement kit or the modeling parameters. This type of set up of the model allows the engineer to efficiently change a part in a model without having the necessity to set up a complete new model. It is important to mention that the last include file must contain the modeling parameters, such as the explicit time integration scheme, the simulation time, as well as the desired field and history output variables. This include file is often called the step file in Abaqus/Explicit. By assembling all include files, the complete model is created and stored as an input file. Before solving the model, the pre-processing step is performed which involves the generation of the mesh and all constraints and DOFs of the model.

### 3.5.2 Solution process

After assembling the complete model, the input file is interpreted by Abaqus/Explicit and solved using the selected properties. Often, in crashworthiness applications, it is too time consuming to solve the model using only one Central Processing Unit (CPU). Therefore, the model is divided into several smaller regions which can be solved in parallel to some extend. However, all degrees of freedom at the boundary nodes between two domains have to be exchanged in every time step. The outcome of the smaller domains are combined in the end to obtain the final result. This allows to obtain the required results faster, since the regions can be solved separately by the CPU. Often the FEM simulations are performed on a high performance cluster which reduces the computational time even further, since this allows to split the problem into even more regions.

### 3.5.3 Post process

After the simulation has been solved, the results can be retrieved. In case of the FEA application software Abaqus/Explicit, the results are given in an .odb file. The .odb file contains all the outcome results information and can be loaded in using for example the software Animator 4 or Abaqus viewer for means of visualization. By loading the simulation into one of the post-processing software, one can see the simulation over all time steps at the selected time intervals and how the vehicle is reacting to the load-case. The .odb file can be opened with Python for post processing the results and evaluating the simulation data.

# CHAPTER 4

## Force deformation solution spaces for crashworthiness design

This chapter presents the concept of force deformation solution spaces for means of crashworthiness design. In order to introduce the topic, the systems engineering approach used in the safety development in the automotive industry is discussed in Section 4.1. Next, in Section 4.2, the concept of the force deformation solution spaces is presented. Finally, in Section 4.3, the fundamental principles and governing theory used for finding the required solution space in crashworthiness design are provided.

### 4.1 Systems engineering

The development process of passenger vehicles in the automotive industry follows the principle of the so called V-diagram, derived from systems engineering. During the development of a passenger vehicle, the system is broken into subsystems. The sub-systems are broken down one level further to the detailed level. As presented in the work of Song, Fender and Duddeck [62], the process of designing the structure of the vehicle is divided into several different phases. This process follows the V-diagram, which shows the different levels of a system along with their individual design goals [62]. An illustration of the safety development process for passenger cars following the V-diagram appraoch of systems engineering is shown in Fig. 4.1 [53].

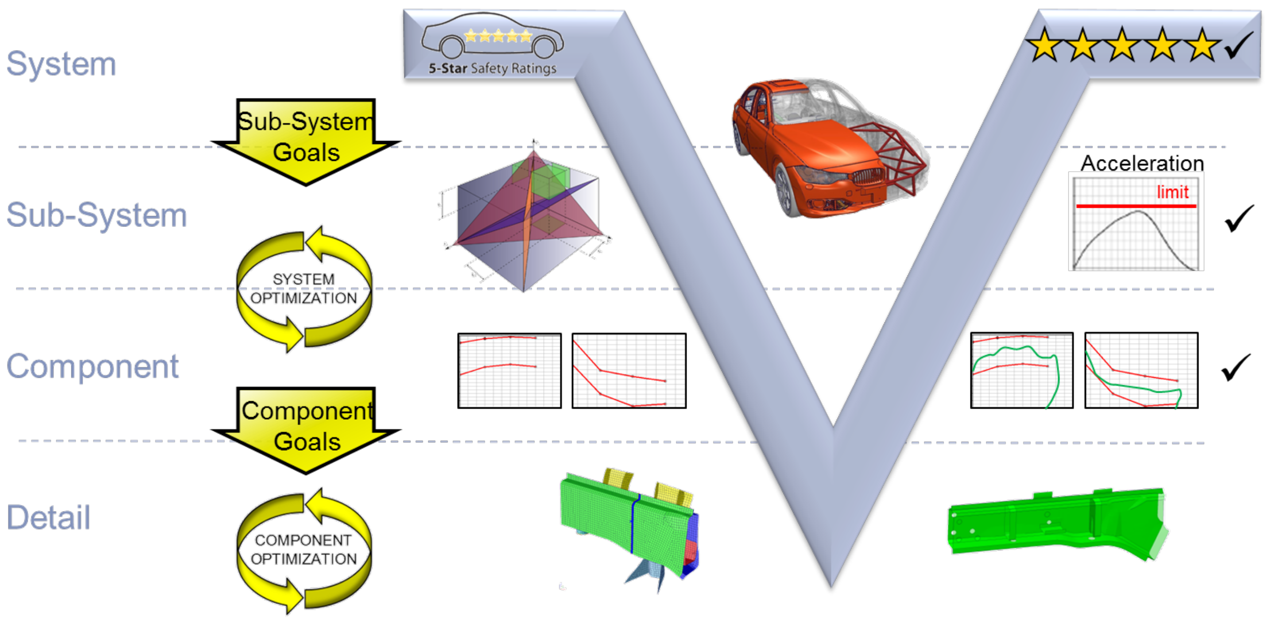


Figure 4.1: V-diagram from systems engineering for the development of a vehicle. Source [53].

For the V-diagram shown in Fig. 4.1, four hierarchical levels exist, being: system, sub-system, component and detail level. For the system level, a certain design requirement, such as a five star rating in crash safety, is established. From this requirement, sub-system goals are derived which allow for system optimization. Going down one level further, one arrives at component level goals which impose detailed requirements that are optimized on component level. According to Fender, the higher level problem is to derive a solution space which is as decoupled as possible [7]. In addition, the author states in his PhD thesis that the lower level problem is the design of a specific component in order to fulfill the component goal [7]. Ultimately, the main idea behind the V-diagram is to arrive at components which can be analyzed and optimized individually [7]. These optimized components form a sub-system and these sub-systems are combined to assemble the complete vehicle which fulfills all top level goals [7]. Referring to the example shown in Fig. 4.1, a five star rating in crash safety is the top level goal.

## 4.2 Concept of solution spaces

The concept of solution spaces can be applied for several engineering areas [7]. For the purpose of this thesis, however, the focus lies on passive safety design of passenger vehicles and therefore, in the remainder of the chapter, the principles are discussed with respect to crashworthiness of passenger vehicles.

### 4.2.1 Solution spaces for crashworthiness design

The idea of solution spaces for means of crashworthiness design goes back to the PhD thesis of Fender in which he states that the concept of a solution space can be thought of having a optimization problem in which the largest region in the parameter space is tried to be determined that fulfills the constraints. Within this region, all requirements are satisfied and therefore only feasible design solutions are obtained [7].

By following the principle of the V-diagram from systems engineering, the vehicle, thought of as a system, can be decoupled and optimization methods can therefore be applied on subsystem level. Having an optimized sub-system, a superior performing higher order system is obtained which also fulfills the top level requirement [7]. Finding the largest possible area of the parameters of interest (from now on called solution space), satisfying the postulates requirements, is the optimization problem of interest [7].

The solution space itself can be thought of a multidimensional parameter space in which only feasible design options are contained. For the case of a two dimensional solution space, the area is constrained by the lower and upper feasible design curve. All possible points between these curves can be thought of feasible design options. In the two dimensional case, the concept of a solution corridor can be introduced. The area constructed by the upper and lower curve is commonly described as force deformation corridor. Therefore, when speaking about two dimensional force deformation solution spaces in crashworthiness design, one commonly refers to them as force deformation solution corridors. Specifically, for component design in automobile applications, solution spaces are expressed as corridors [7].

The power of solution spaces comes from the fact that components which fall inside the solution space bounds also meet the higher level design goals, greatly helping in the crashworthiness design, especially at an early development stage. This means that components which are designed within the force deformation solution corridor is a valid approach to for obtaining higher level design goals, since these are implicitly fulfilled [7].

### 4.2.2 Importance of solution spaces for early stage crashworthiness design

The concept of solution spaces complements to a large extend with the V-diagram from systems engineering, presented in Section 4.1. Referring to the work of Fender [7], the goal of arriving at decoupled component requirements is rather difficult for crash design due to the nonlinearities and complex interactions of the system. However, applying the solution spaces approach, which takes nonlinearities into account, allows to decouple the system parameters on component level [7]. By determining force deformation solution corridors for structural components, it is possible to derive requirements on component levels at an early development stage which can be used before the detailed design phase is started [7].

### 4.2.3 Force deformation solution spaces for crash structures

By searching for the largest solution space of a certain parameter while complying with the constraints, one obtains a force deformation solution space for crash structures, as described earlier. In essence, one has to think of a corridor in the force deformation domain restraint by an upper and a lower force level in which a feasible, achievable and safe design is guaranteed. An example of force deformation solution spaces for crash structures is shown in Fig. 4.2.

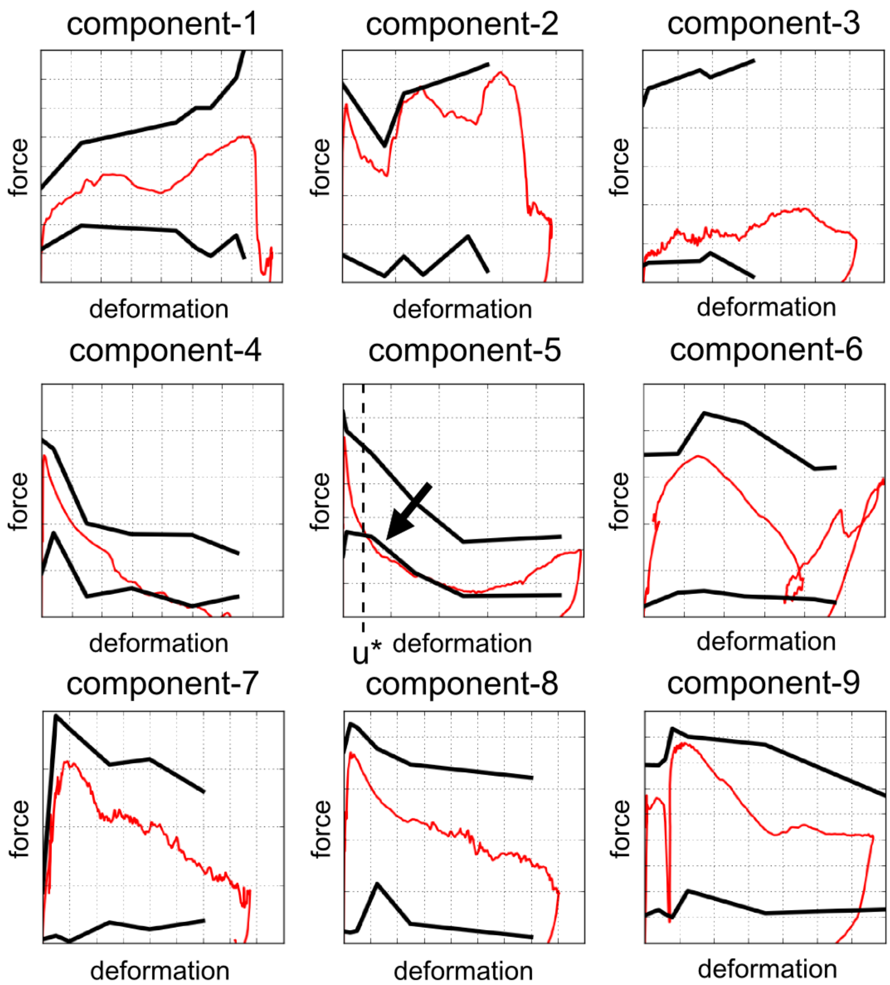


Figure 4.2: Force deformation corridors of structural components of a passenger vehicle. Source [63].

In Fig. 4.2, the force deformation corridors for nine structural components of a passenger vehicle are shown. The black lines in each graph illustrate the upper and lower bounds of the force which satisfy the requirements. The red curves in each graph show the design of the specific components. Therefore, when the red curve falls between the upper and lower bounds of the force deformation solution corridor, the particular component design fulfills the design goal.

## 4.3 Fundamental principles of solution spaces for crashworthiness design

Finding the largest possible solution space can be obtained by several iterative statistical methods, such as the Monte Carlo sampling method. As the Monte Carlo sampling method is used for finding the largest solution space for the grouped components in the small overlap crash test in this thesis, the following Section only describes the Monte Carlo sampling method [64].

### 4.3.1 Monte Carlo sampling method

Since the feasible domain of the solution space is unknown and it is opted to obtain the largest possible solution space for the particular component, statistical methods are used in order to determine the feasible solution space for crashworthiness design. For this matter, the so called Monte Carlo sampling method is used. The main reason behind this choice is the fact that in the Monte Carlo sampling method, the probability of obtaining a single sample point which falls outside the solution bound, i. e. an infeasible design, is equal to the ratio of infeasible volume to the sampled region, as stated by Fender [7].

The Monte Carlo sampling is a specific statistical sampling method and commonly used in optimization schemes. The basic definition of the Monte Carlo method is '... the art of approximating an expectation by the sample mean of a function of simulated random variables' [65]. Central to the Monte Carlo sampling method is the construction of a random process for a problem and performing a numerical experiment by sampling from a random number sequence of numbers with a prescribed probability distribution [66]. Generally speaking, Monte Carlo sampling follows the following four major steps [67]:

· Obtain the statistical properties of the input [67].
· Determine possible input groups which fulfill the statistical input properties [67].
· Perform a deterministic computation with the possible input groups [67].
· Statistically examine the outcome [67].

Referring to Doucet, de Freitag and Gordon, the main advantages of using Monte Carlo sampling methods is the strength to be independent on Gaussianity constrains [68]. However, a major limitation of the Monte Carlo sampling method is the poor performance in discrepancy, so the homogeneity of points distributed over the sampled region [7].

### 4.3.2 Objective function

For the thesis, the solution space is determined using an existing tool available at BMW AG. The search algorithm is based on the previously described Monte Carlo sampling method. Similar to other optimization schemes, such as linear integer programming or genetic algorithms, an objective function is used. An example of an objective function in a generalized form is given by Eq. 4.1 [64].

$$z = f(x_1, x_2, ..., x_p) \tag{4.1}$$

For the objective function, a threshold value, $z_c$, is defined for which $f(x) < z_c$ the outcome is feasible and for which $f(x) \geq z_c$ the outcome is infeasible [64]. Following this principle, one can differentiate between input variables that produce good outcome values and input values which produce bad outcome values. An example of such a solution space for parameters $x$ is given in Fig. 4.3.

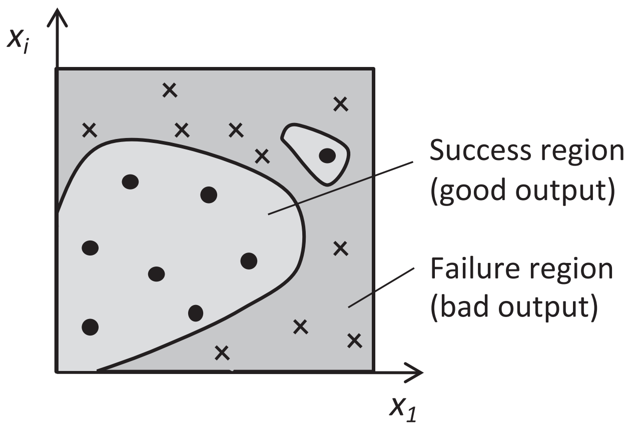


Figure 4.3: Feasible and infeasible design regions. Source [64].

As seen in Fig. 4.3, the outcome of the objective function describes a certain region which only consists out of feasible solutions. When the input variables are randomly chosen, the probability that a feasible outcome is obtained is fixed. Lehar and Zimmermann argue that in the early development stage of passenger vehicles, the distribution should be uniform [64]. Following this argument and using the Monte Carlo sampling method, the confidence interval can be estimated [64]. Lehar and Zimmermann determined in their work that for a failure probabilities which are between 1 to 10%, a confidence interval of ± 10% at a 95% confidence level can be obtained for a failure estimate by performing 100 simulations. This is an important outcome to reduce the number of trials when determining the solution bounds of certain components in passive safety development of passenger vehicles.

As with any optimization scheme, the choice of the objective function is of large importance. Of course, the choice itself is dependent on the type of problem. Often, the objective function requires a threshold value above or below which the outcome of the optimization is feasible. Solutions which fall outside of this region are not fulfilling the objective function and therefore are not considered to be valid. For the particular case of crashworthiness design, the objective functions can be derived from global vehicle parameters such as the required position of the A-Pillar with respect to the barrier at a certain time of the crash analysis, the rotation of the center of gravity (COG) of the vehicle at a certain time of the analysis and/or the remaining velocity or energy of the vehicle at the final time step. Other possible objective functions could contain a threshold value for the acceleration or the kinetic energy of the vehicle.

CHAPTER 5

# Numerical study on the most relevant structural components

In order to develop an insight into the kinematic behavior of the vehicle and to identify the most relevant structural components for crashworthiness when subjected to the small overlap crash test load-case, a numerical study with the FEA package Abaqus/Explicit is performed in this chapter. This investigation follows the bottom-up approach, where the influence of changes in the characteristics of the structural components on the response of the vehicle is analyzed. For the numerical study, two different FEM simulation crash models are used, being: a trolley model representing the main frontal structure of a vehicle of the BMW AG product range and a reduced full vehicle model which contains out of the components until the A-Pillar, representing a second vehicle of the BMW AG product range. The chapter is structured as follows. First, in Section 5.1, the methodology is provided, followed by the numerical study of the trolley model in Section 5.2. In Section 5.3, the results of the numerical study for the reduced full vehicle model are presented. Finally, in Section 5.4, the results of this chapter are discussed and reflected on.

## 5.1 Methodology

Since the approach for the numerical study of the two FEM crash simulation models is similar, the methodology is described first. The process is divided into five steps, being: the energy study, the determination of the output variables, the explanation and implementation of the measurement kit, the variation of parameters and the determination of the structural components of relevance. In the following, each of the five mentioned steps is described in more detail.

### 5.1.1 Energy study

In order to determine the most important structural components of the FEM crash simulation models, an energy study is performed. For this matter, an existing tool at BMW AG is used. The tool visualizes the accumulated strain energy of all elements of the crash simulation which are grouped into components. The post-processing is done with Animator 4, an animation tool for large FEM models [69]. In order to determine the strain energy of all elements, the output ALLIE in Abaqus/Explicit must be requested as a history output for all sections of the FEM crash simulation. Note that the output parameter ALLIE contains the strain energy of all elements during the simulation in Abaqus/Explicit. Specifically, the term ALLIE in Abaqus/Explicit is the summation of the recoverable strain energy, the energy dissipated by rate-independent and rate-dependent plastic deformation, the energy dissipated by viscoelasticity, the artificial strain energy, the energy dissipated by damage, the energy dissipated by distortion control and the fluid cavity energy [61].

The tool itself is started in the Animator 4 environment and requires the .odb file to be located in the same folder. Before running the script, one can specify the threshold value for the accumulated strain energy below which no components are shown. This is particularly useful for very detailed FEM simulation models, as non-structural components such as radiators, headlights and plastic covers should not be taken into account as structural components relevant for the small overlap crash test. After specifying the threshold value for the accumulated strain energy level, the tool reads in the .odb file and the components, grouped by their Property identifier (PID) number, are presented in a colored fashion based to their accumulated strain energy level. This allows to investigate which components take up the largest amount of cumulative strain energy for the given FEM crash simulation. However, the evaluation is performed at the final time step of the simulation and hence only the plastic energy is taken into account. Therefore, only the components which have a large plastic deformation are visualized by the tool. In addition, note, that the higher the area of the component, the larger the strain energy will be, as it is not looked at the strain energy density, but the accumulated total strain energy. Therefore, it can sometimes be the case that components are visualized with the tool which do have a large accumulated strain energy, but their strain energy density is rather low (a bonnet would be an example).

Depending on the outcome of the energy study using the existing tool at BMW AG and comparing them to the outcome of the literature study, see Chapter 2, the relevant structural components of the FEM vehicle model for the small overlap crash test are selected.

### 5.1.2 Output variables

Based on the description in Chapter 2, any vehicle subjected to the small overlap crash test load-case experiences either the rotational or lateral translational response or a combination of these. Note that only a distinction between the lateral and rotational response is done in the thesis, as the combination of the two responses is not that clearly distinguishable. The main goal of the numerical study is to identify the main relevant components having an influence on the vehicle's response during the small overlap crash test. Since the effect on the response of the vehicle of these components has to be quantitatively measured, output variables must be determined which monitor the response. These output variables describe the kinematics of the vehicle, the reaction forces of the barrier and the internal and kinetic energy of the model, as discussed in the following.

#### Kinematics of vehicle

The lateral translational response can be observed when monitoring the movement in the lateral direction over time. In addition, the longitudinal displacement over time is of interest, as it helps to distinguish between a rotational and lateral translational response. Therefore, the trajectory of the COG of the vehicle is monitored over the entire simulation. Specifically, this is achieved by monitoring the vehicle's COG x and y position over time. For the remainder of this chapter, the following coordinate systems are used. The global coordinate system is such that the x axis is aligned with the traveling direction of the vehicle (so from right to left). The global y axis is aligned with the flat surface of the barrier which is struck by the vehicle. The local coordinate system is aligned with the vehicle axis and located at the COG of the vehicle. So, if the vehicle rotates, the x axis is pointing along the axial direction of the vehicle and the local y axis is pointing along the lateral direction of the vehicle.

Note that it is assumed that the deformation and separation of the components of the vehicle is such that the position of the COG does not change with respect to its original position. Next to that, the rotational angle of the vehicle is measured with respect to time. This helps to classify the observed response of the FEM simulation model. The angle is determined by selecting two nodes of a component which shows no large deformations and is on the opposite to the impacting side of the vehicle. Generally, this is a structural component of the rocker of the vehicle, as it is relatively stiff and does not deform significantly. The angle is measured using the relative position of the two nodes towards each other, as shown in Eq. 5.1.

$$\theta(i) = \arctan\left(\frac{y_2(i) - y_1(i)}{\sqrt{(x_2(i) - x_1(i))^2 + (y_2(i) - y_1(i))^2 + (z_2(i) - z_1(i))^2}}\right) \tag{5.1}$$

In Eq. 5.1, $x(i)$, $y(i)$ and $z(i)$ are the coordinates of the two rocker nodes at the $i^{th}$ time step. Using Eq. 5.1, the rotational angle in the xy plane, so around the z axis of the COG of the FEM simulation model is determined. Note that the sign convention is such that a positive angle means that the car is rotating counter clockwise (CCW) when looking at the xy plane and when the vehicle travels from right to left. A negative angle designates a clockwise rotation of the vehicle (CW).

#### Reaction forces of the barrier

The reaction forces of the barrier are monitored in order to obtain an overview of the vehicle's response and the effect of changes of the structural components. Specifically, the output of the contact force

(CF) in Abaqus/Explicit, is measured in all three directions of the global axis system in order to obtain the reaction forces of the barrier. These reaction forces are then used in order to obtain an indication of the response of the vehicle. As the lateral translational response requires a certain amount of force in the lateral direction which forces the vehicle to glance-off the barrier, the corresponding reaction force curve should show this trend. Furthermore, by plotting the longitudinal reaction force over the assumed rigid body displacement in the global x direction of the vehicle, one obtains an indication if there is a so called springback behavior of the car. This occurs when the vehicles bounces back from the barrier, seen by a decrease in displacement in the local coordinate system when compared to the previous displacement. This is a clear evidence of a rotational response of the vehicle, as the vehicle is not able to pass the barrier. Due to these reasons, the reaction forces in the x and y direction of the barrier are monitored with respect to time.

**Internal and kinetic energy**

In order to have an overview of the energy dissipation due to the deformation and failure of the structural components, as well as of the remaining kinetic energy of the vehicle, the output variables ALLIE and ALLKE are monitored with respect to time, by requesting them as a history output. Note that the abbreviation ALLKE is used within the Abaqus/Explicit environment to describe the kinetic energy of the simulation model [61].

### 5.1.3 Monitoring of output variables

To monitor the described outputs variables in the Abaqus/Explicit FEM crash simulations, several adoptions have to be made on the evaluated FEM simulation models.

In order to retrieve the trajectory of the COG of the vehicle over time, a so called measurement kit is constructed. This measurement kit is created by setting up a new include file, build up from scratch. The include file contains the definition of an accelerometer attached to the location of the COG by means of a tie and connector construction. If there is no element in the close proximity of the COG, the node is placed on the location of the COG and attached to a stiff structure in the surrounding area by means of a rigid connection. Then the accelerometer is attached to a node of very small mass and inertia which is tied to the surrounding structure. For this accelerometer, a history output is defined for the position in all three directions. This is achieved by specifying the relative position element output CP (in all three directions) in the step section of the include file.

Following the same approach, the positions CP1, CP2 and CP3 are measured over time for two nodes lying on the stiff structural component of the rocker, located on the opposite of the impacting side of the vehicle. Using the position of the two nodes over time, the angle between can be computed using Eq. 5.1.

For measuring the barrier contact forces, the include file of the barrier model is added by the extension that for the node set containing the barrier nodes, the forces CF1, CF2 and CF3 are given as an history output for the simulation. The CF3 component, so the contact force in the global z coordinate system, is only given as an check for the simulation model, because is not relevant due to its magnitude compared to the other two forces, see Fig. 5.1.

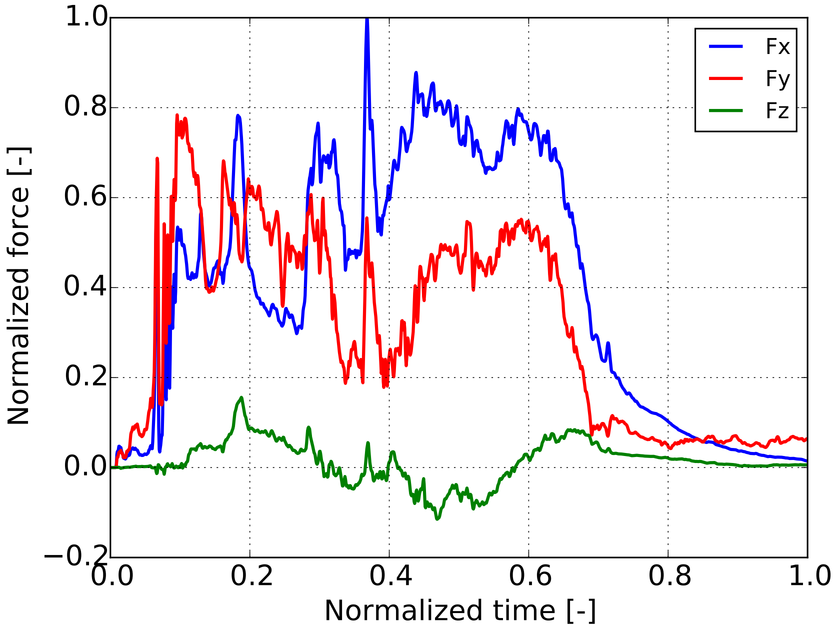


Figure 5.1: Normalized forces as a function of normalized time.

Looking at Fig. 5.1, it is indeed seen that the force component in the z direction is reasonably low and hence this force is not taken into account in the remainder of this chapter.

In order to retrieve the internal and kinetic energy of the simulation as an output, the include file containing the step definition of the simulation model is changed such that the outputs ALLIE and ALLKE are retrieved as history output for the simulation.

The main ideas behind the above mentioned procedure to monitor the output variables are the following. First of all, by creating the measurement kit which is used to monitor the output variables, the only include which needs to be changed for a new simulation is the measurement kit itself. This allows to automatize the process, since the output variables are always the same. Furthermore, by defining the output variables as an history output in the FEM simulation means that they are stored in the .odb file. Having the output stored in the .odb file not only increases the accuracy, but also allows to automatize the post-process of the results by using Python for reading the .odb file.

### 5.1.4 Variation of parameters

In order to evaluate the influence of the structural components on the vehicle's response, several parameters are changed. As mentioned previously, the most relevant structural components are determined by evaluating the performed energy study and comparing the outcome to the results obtained from the literature study. After knowing the most influential structural components, the wall thicknesses are changed for these structural components. The magnitude of the wall thickness is chosen according to the function of the component, as well as the desired change in behavior while accounting for manufacturing constraints (too low wall thicknesses are not possible). For example, a higher wall thickness for the crashbox does not necessarily mean that it is absorbing more energy, since the component does not deform in its desired mode anymore.

### 5.1.5 Determination of the structural components of interest

The final step consists of drawing conclusions of the numerical study on how important certain components are for the overall performance of the vehicle in terms of crashworthiness of the small overlap crash test and how they can influence the kinematic response of the car. This is done by evaluating the FEM simulation models with the changed wall thickness with respect to the output variables of interest. From the obtained change in the output variables, conclusions are drawn on the relevance of the structural components for the small overlap crash test load-case. Finally, the outcome is used as a starting point for developing the predictive kinematic model, since the relevant structural components, the required and expected force levels, as well as the expected kinematic behavior is known.

Due to the confidentiality agreement with BMW AG, the output variables in the numerical study are normalized using the formula shown in Eq. 5.2.

$$z_i = \frac{x_i - min(x)}{max(x) - min(x)} \tag{5.2}$$

In Eq. 5.2, $z$ is the new normalized value and $x$ is the output variable of interest at the $i^{th}$ time step, given in its original scale. If multiple output variables are plotted in graph, the maximum and minimum reference values are taken from the output variable which has the highest values compared to the other output variables.

As a final note, it is emphasized that in the remainder of the chapter, the images which illustrate the structure of the FEM simulation models are blurred due to the confidentiality agreement with BMW AG.

## 5.2 Trolley FEM simulation model

Nowadays, full vehicle FEM simulation models use as many as five million elements. In the automotive industry, it is common practice to compute these models using high performance cluster systems with multiple cores. However, even with these sophisticated methods, the computational time for a full vehicle FEM model can easily take more than one day to complete, especially when large deformations are occurring. Given the time constraint of the thesis, full vehicle FEM simulation models are very inconvenient to use for the numerical study. Therefore, simplified FEM simulation models are chosen. For the first numerical study, shown in this section, a trolley model of a passenger car is used.

### 5.2.1 Overview

Normally, a trolley model is used at an early development phase of a passenger vehicle to investigate and test the structural performance of the load carrying structural components for frontal crashes without having the necessity to build the complete vehicle. Basically, a trolley model is used in hardware testing where complete vehicles are crashed in crash test facilities. In order to investigate the hardware test beforehand, a FEM simulation model is often created of the trolley model.

A FEM simulation trolley model consists only out of the structural components in front of the firewall, without the unibody frame of the vehicle, the drive-train, the suspension, the head lamps, the body-shells, the wheels and the interior equipment, such as seats and steering wheel. The frontal structural parts are attached to a plate which is assembled to a trolley. The trolley model has a comparable mass with respect to the full vehicle model it is representing. In order to give an overview of the trolley model, an illustration of the FEM simulation model along with the barrier is shown in Fig. 5.2.

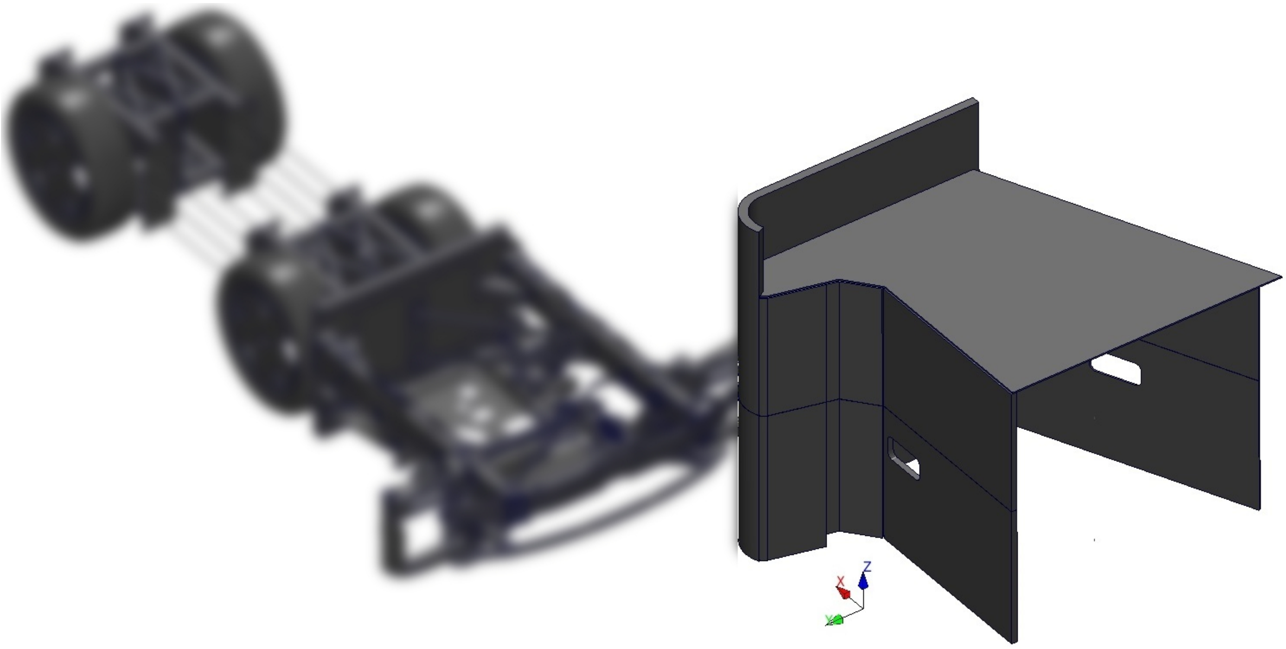

Figure 5.2: Isometric view of the trolley FEM simulation model.

As shown in Fig. 5.2, the trolley model consists out of the following structural components: upper and lower framerails, upper and lower crashboxes, upper and lower bumper, load specific components (radiator support frames), shear plate and supporting struts. These structural components are attached to a thick end plate which is the frontal part of the trolley assembly. In addition, the frontal axle of the trolley is attached using connectors to the rear axle of the trolley. In order to get a better overview of the trolley model, the top, the bottom, the side and the front view of the trolley model are shown in Fig. 5.3.

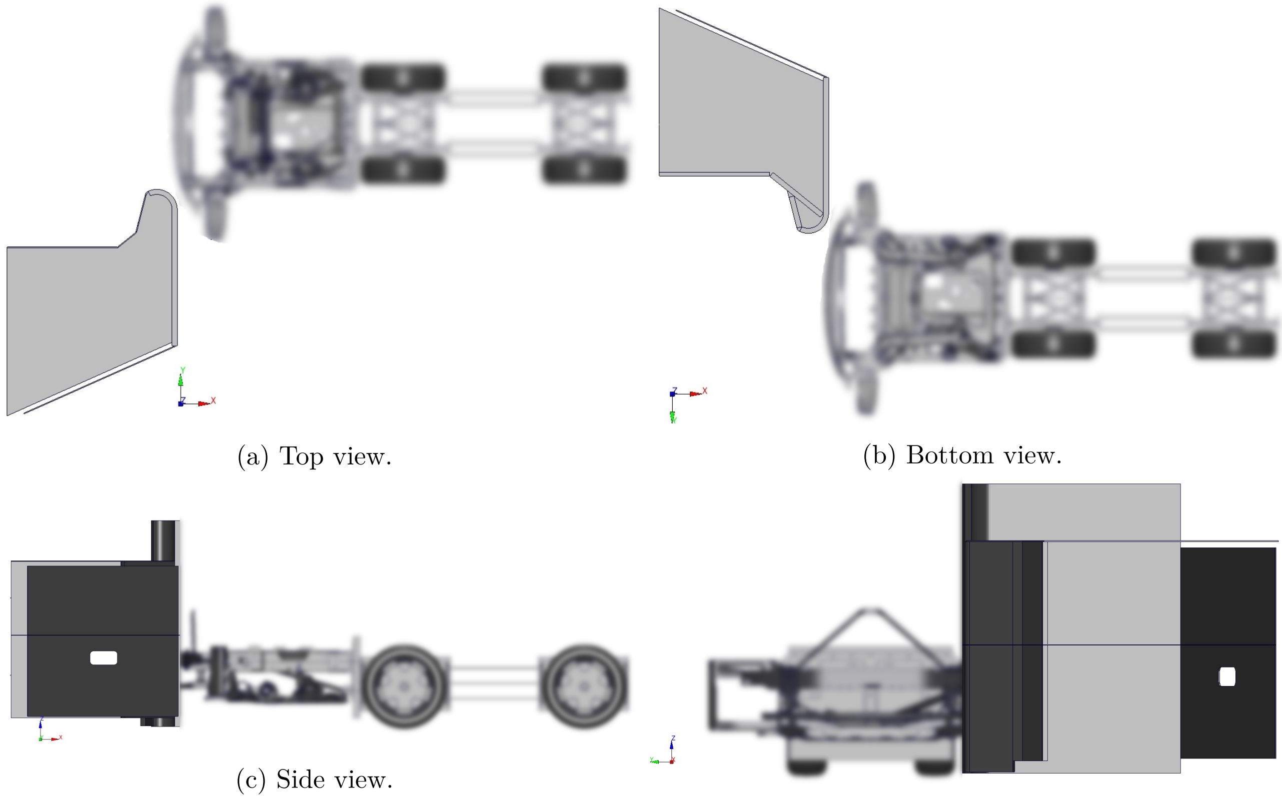

(a) Top view. (b) Bottom view.

(c) Side view. (d) Front view.

Figure 5.3: Overview of the trolley FEM simulation model.

Looking at Fig. 5.3, it becomes clear that the trolley model consists out of two major load paths. The first load path consist out of the upper structural components, being: upper bumper, crashbox and upper framerail. The second load path consists out of the lower structural components, which are: lower bumper, crashbox, radiator support frame, lower framerail and shear plate.

### 5.2.2 Energy study

In order to determine the most important structural components, an energy study is performed, as mentioned in the methodology section. Doing the energy analysis using the existing tool available at BMW AG with a threshold value of 1.4%, the following components are visualized, grouped by their PID and colored according to their value in accumulated strain energy level, see Fig. 5.4.

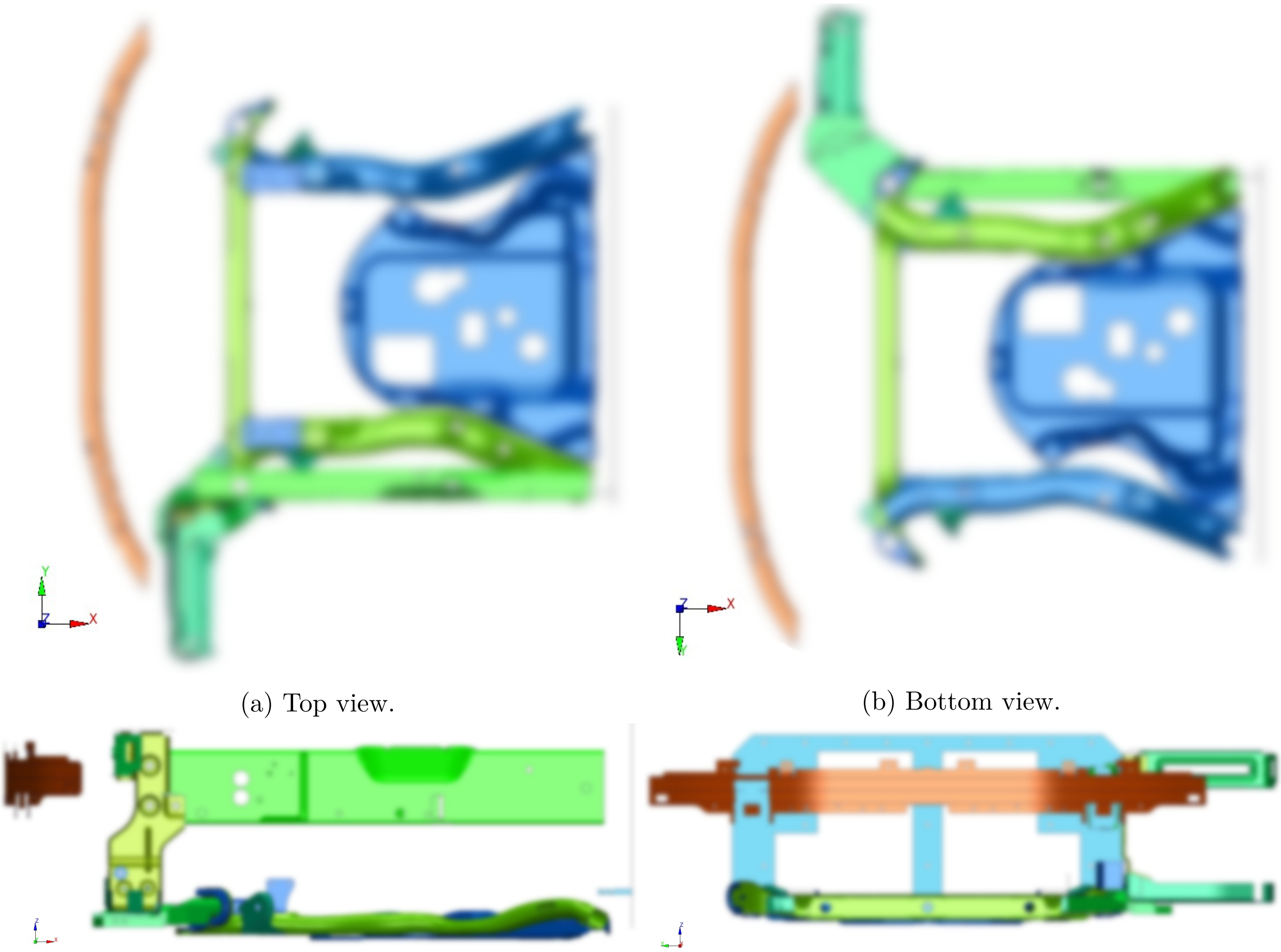

(a) Top view.

(b) Bottom view.

(c) Side view.

(d) Front view.

Figure 5.4: Result of the energy study of trolley FEM simulation model.

Note that in Fig. 5.4, the color blue indicates the lowest strain energy level and the color red indicates the highest strain energy level. Thus, when applying this color scheme for the energy, it can be seen that the upper bumper takes up most of the strain energy, followed by the lower and upper framerails, respectively. A smaller amount of strain energy is taken up by the shear plate, upper and lower crashbox and upper and lower framerail on the opposite of the impacted structure by the barrier. Therefore, referring to the energy analysis, shown in Fig. 5.4, the following components are identified as being most relevant for the small overlap crash test load-case:

- Upper and lower bumper.
- Upper and lower framerail.
- Upper and lower crashbox.
- Upper and lower strut.
- Radiator support frame.
- Connection between framerail and plate.

Note that due to the fact that the trolley model is only made out of structural components, the energy study basically complies with engineering judgment that almost all the components shown in the trolley

FEM simulation model are relevant for the small overlap crash test. However, since the approach is the same for all investigated FEM crash models, the energy study is done for completeness. Also, the energy investigation reveals that not all components shown in Fig. 5.3 are absorbing the strain energy to the same extend.

### 5.2.3 Output variables

In order to investigate the effect of changing the wall thickness of the most influential components on the strain energy, certain output variables must be established, as mention in Section 5.1. For the trolley model, the displacement of the COG in x and y, the angle of the trolley model, the reaction forces in x and y of the barrier, as well as the kinetic and internal strain energy are monitored as a function of simulation time.

### 5.2.4 Monitoring of output variables

The monitoring of the x and y position of the COG, as well as the angle of the COG, are performed using a measurement kit. The measurement kit is created as discussed in Section 5.1 and is added as an include file to the FEM simulation model.

### 5.2.5 Variation of parameters

Using the most relevant components of the trolley FEM simulation model for absorbing the energy during the small overlap crash test, five different simulation models are build, being the baseline, the weak, the strong bumper, the strong and the strong framerail variant. The idea behind this is to create the most extreme cases of the trolley FEM model which then serve as the upper and lower bounds of the values of the changeable parameters and find models which are in between. As mentioned in Chapter 2, any vehicle subjected to the small overlap crash test load-case of the IIHS experiences either the rotational or lateral translational response or a combination of the two. From engineering judgment, it becomes clear that a very strong and stiff structure should glance-off from the barrier and a weak and flexible structure should show large deformations and consequently rotate around the barrier. Therefore, by having a strong and weak variant of the trolley model should capture the two different response modes of the impact. Below, in Tab. 5.1, the changed parameters of the trolley model are summarized. Note that although the load-case is asymmetrical, the wall thicknesses of the components which have a left and a right side are changed to the same extend.

Table 5.1: Thickness ratios of structural components of the trolley FEM simulation model variants.

| *Component* | $\frac{t_{baseline}}{t_{baseline}}$ | $\frac{t_{weak}}{t_{baseline}}$ | $\frac{t_{strong\ bumper}}{t_{baseline}}$ | $\frac{t_{strong}}{t_{baseline}}$ | $\frac{t_{strong\ framerail}}{t_{baseline}}$ |
|---|---|---|---|---|---|
| Upper bumper | 1.0 | 6.7 | 6.7 | 4.0 | 3.3 |
| Lower bumper | 1.0 | 9.1 | 9.1 | 2.0 | 4.5 |
| Upper framerail | 1.0 | 0.2 | 1.2 | 2.0 | 1.2 |
| Lower framerail | 1.0 | 0.2 | 1.6 | 2.0 | 2.4 |
| Upper crashbox | 1.0 | 0.3 | 0.3 | 2.0 | 0.3 |
| Lower crashbox | 1.0 | 0.3 | 0.3 | 2.0 | 0.3 |
| Upper strut | 1.0 | 1.0 | 1.0 | 2.0 | 1.0 |
| Lower strut | 1.0 | 1.0 | 1.0 | 2.0 | 1.0 |
| Radiator support frame | 1.0 | 5.7 | 5.7 | 2.0 | 5.7 |
| Connection between framerail and plate | 1.0 | 1.0 | 1.0 | 2.0 | 1.0 |

As can be seen in Tab. 5.1, the components of the weak variant of the trolley model are changed such that the model has weak framerails and crashboxes. The thickness of the bumper and radiator support frame are increased for obtaining large deformations of the weak framerails and crashboxes which should force the complete structure to deform significantly. The intention is to let the trolley model rotate around the barrier with this variant. The strong variant is basically made twice as strong for all components, except for the upper bumper which showed the largest strain energy absorption in the energy study. This model should show an increased glancing-off behavior compared to the baseline model. The strong bumper variant is between the weak and strong variant and has an increased wall thickness for the upper and lower bumper. The last variant, the strong framerail variant, is basically a version to investigate the change in wall thickness for the lower framerails on the vehicle response, as this component showed a significant amount of internal strain energy, as shown in Fig. 5.4.

The reason for the non-uniform variation in thickness ratio of the weak variant comes from the fact that having the same ratio for all components leads to non-robust simulation results and abortions of the simulation process in Abaqus/Explicit. In addition, it was looked at the simulation and the deformation mechanisms of the structures and therefore, it was decided to make a weak and highly deformable crashbox.

### 5.2.6 Determination of structural components of interest

After performing the simulations of the five cases, the response is analyzed. For this, the output variables are investigated in more detail. First, the initial position of the models in the simulation are compared with the final position in the visualization software Animator A4, as shown in Fig. 5.5. Note that in Fig. 5.5, blue is the baseline model, red is the weak variant, green is the strong bumper variant, magenta is the strong variant and cyan is the strong framerail variant.

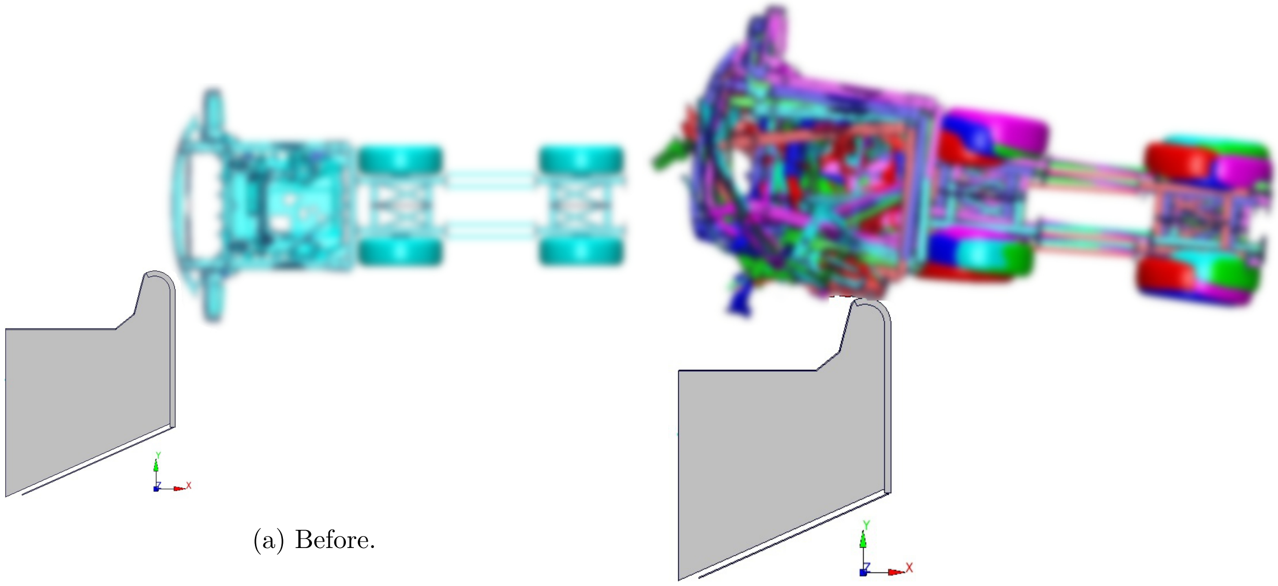

(a) Before.

(b) After.

Figure 5.5: Trolley FEM simulation model before and after impact.

As can be seen in Fig. 5.5, the strong variant glances-off the most. Next, comes the baseline model which also glances-off to a large extend. The strong framerail variant and the strong bumper variant show almost the same behavior, except for the fact that the strong bumper variant deforms more. The weak variant shows significant deformation of the frontal structure and the frontal structure itself rotates in the CCW direction. However, the trolley itself of the weak variant still does glance-off and rotates in the CW direction. Looking at the final position of the models, all variants of the trolley model glance-off from the barrier.

Next, it is looked at Fig. 5.6 where the normalized displacement in x and y are plotted over the normalized time.

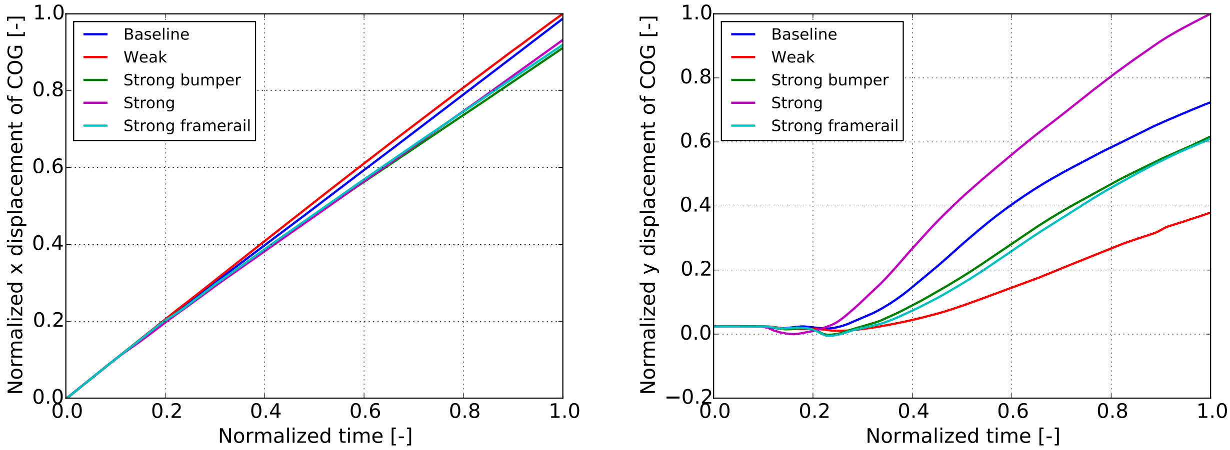


(a) Displacement in x.

(b) Displacement in y.

Figure 5.6: Normalized displacement as a function of normalized time of the trolley model.

From Fig. 5.6a, it can be seen that the deviation in x displacement not large. Although the displacement in y differs significantly for all models, see Fig. 5.6b, the displacement is still high enough for the variants to glance-off.

By investigating Fig. 5.7, a similar trend is observed. Here the normalized angle is plotted over normalized time.

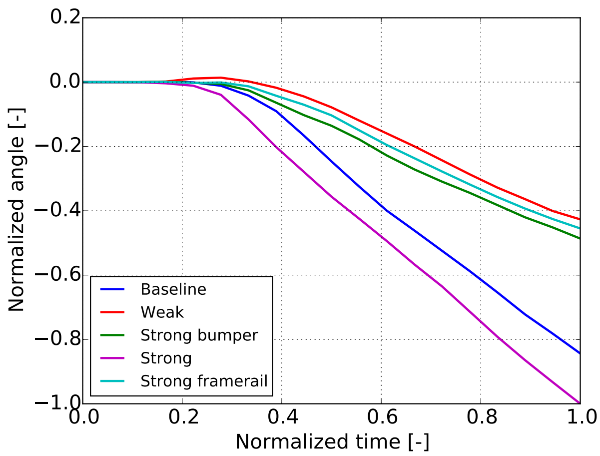


Figure 5.7: Normalized angle as a function of time of the trolley model.

In Fig. 5.7, it can be seen that the rotation of the trolley is negative at the final step in time of the simulation which means that the models rotate in a CW fashion. However, the weak variant first shows a small tendency to rotate CCW, seen by the small peak at 0.3 of normalized time in Fig. 5.7. However, the angle changes in sign after a value of 0.35 of normalized time.

Next, it is looked at the force in x and y as a function of time, shown in Fig. 5.8.

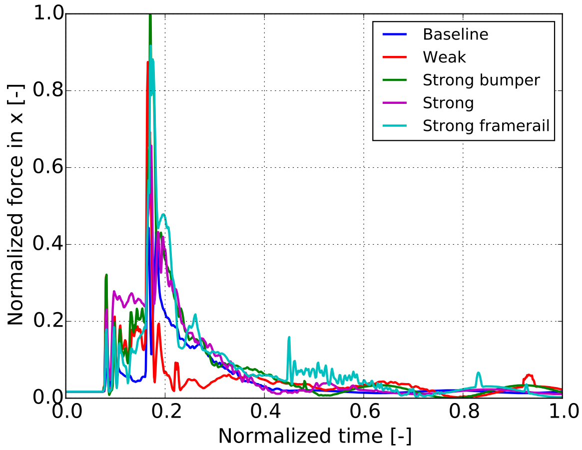


(a) Force in x.

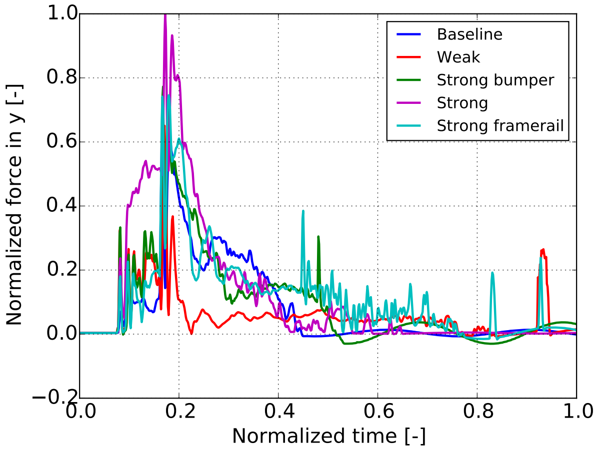


(b) Force in y.

Figure 5.8: Normalized force as a function of normalized time of the trolley model.

It is seen in Fig. 5.8a, that the force in x increases at 0.1 of normalized time, especially for the strong variant. Before that time, the models are not in contact with the barrier, resulting in a zero force level. At 0.2 of normalized time, the highest force level is observed for all five models, where the baseline model has the lowest peak at approximately 0.5 of the maximum observed force. After that peak, the force decreases quite rapidly and reaches a reasonable low level from 0.4 of normalized time onwards. In Fig. 5.8b, no force is observed until 0.1 of normalized time, as there is no contact with the barrier. Then all five models show an increase in force, where the force of the strong variant increases the most to the highest value at approximately 0.2 of normalized time. The weak variant shows the lowest force peak at that time value. After the peak, the force levels of all variants decrease to almost zero, only the strong framerail and strong bumper variant show some remaining force levels at 0.5 of normalized time.

In addition, the normalized x and y force as a function of normalized x displacement is investigated, as shown in Fig. 5.9.

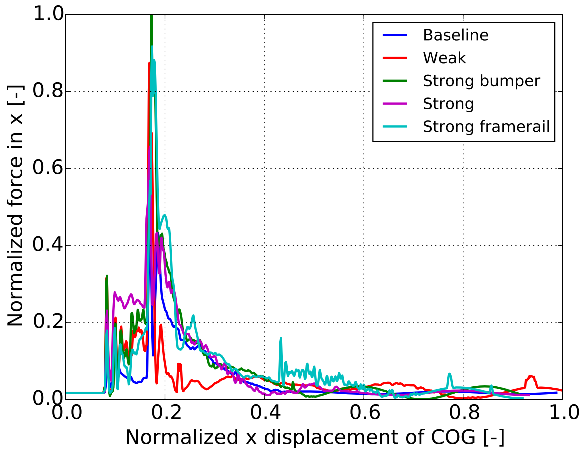


(a) Force in x.

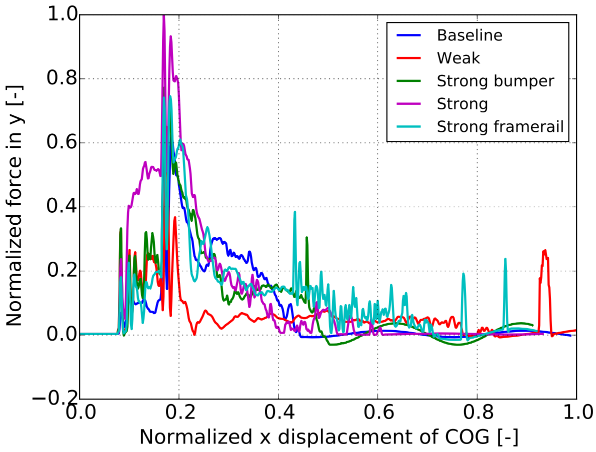


(b) Force in y.

Figure 5.9: Normalized force as a function of normalized x displacement of the trolley model.

Similar as observed for the forces as a function of time, the forces over normalized x displacement of the COG show the same trend. Looking at Fig. 5.9, no springback is seen for the five models.

Finally, it is looked at the normalized kinetic and internal energy of the models, as shown in Fig. 5.10.

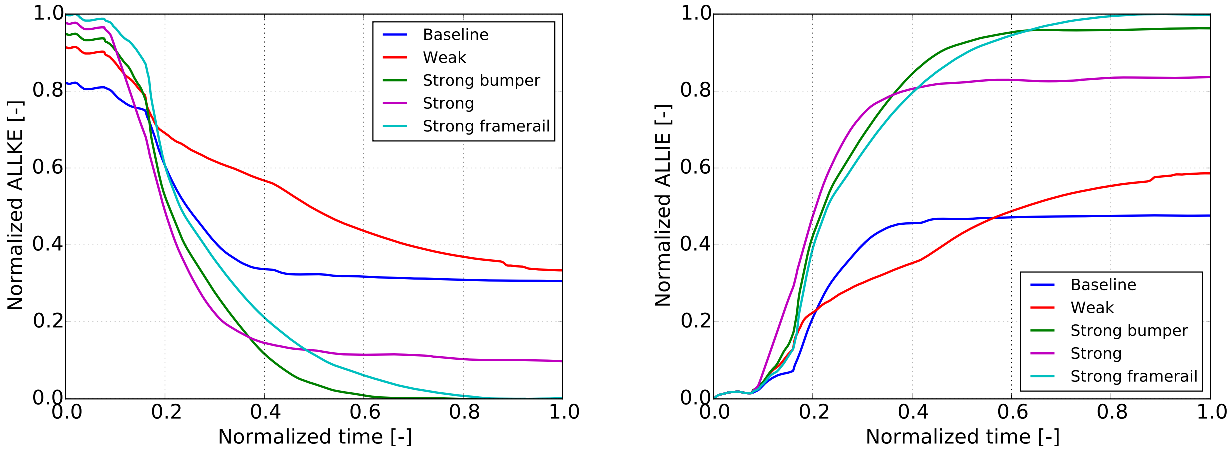


(a) Kinetic energy. (b) Internal energy.

Figure 5.10: Normalized energy as a function of normalized time of the trolley model.

From Fig. 5.10a it can be seen that the kinetic energy of the strong bumper, strong and strong framerail variants are reduced the most. The weak and baseline model have the highest remaining kinetic energy at the end of the simulation. The former three variants also show an 's' shape behavior in their kinetic energy over time. The latter two variants experience this phenomenon to a less amount.

Looking at the internal energy of the models shown in Fig. 5.10b, it can be seen that the strong bumper, strong and strong framerail variant have the highest internal energy level at the end of the simulation. The weak and baseline model end at a value of approximately half of the stiff variant.

### 5.2.7 Discussion of results

From the numerical study of the trolley FEM simulation model, several observations can be made.

On the one hand, it can be seen that the strong variant does glance-off the most, seen by the largest y displacement of the COG and the largest negative angle of the COG. This can be explained by the highest force level in y of the model. On the other hand, the weak variant does glance-off the least, seen by the smallest value in y displacement of the COG and the smallest value of the magnitude of the angle of the COG. Again, this behavior can be explained by investigating the force levels in x and y of the variant. For both the x and y force, the weak variant shows the smallest level of force.

Investigating the energy of the models, similar trends can be seen. Due to the small forces in x and y, but almost the same x displacement of the COG, the weak variant has the highest remaining kinetic energy. This means that although the structure does deform a lot, not much energy is dissipated, also seen by the internal energy where the among of energy at the final time step of the simulation is only half of the strong variant. This is also seen for the baseline model, which is too weak to take up a lot of deformation energy which is the reason for the relatively high remaining kinetic energy.

From the numerical study on the trolley model, it is seen that a higher y force increases the tendency of the trolley model to glance-off from the barrier. This is seen by the comparison of the strong bumper, strong and strong framerail models. The higher the y force is, the higher the lateral displacement of the COG of the model. Interestingly, the x force has a smaller effect of the response of the vehicle. However, this can also be the case due to the absence of structural parts such as the wheel and surrounding structure.

Although several components have been changed in thickness and their importance on the overall energy absorption have been found out, it becomes clear from the numerical study that changing the wall thickness in case of the trolley model is not sufficient to make the model experience another mode other than the glancing-off behavior. This might be because the trolley model is not detailed enough to represent the behavior of the real vehicle. It was tried to make the structure even weaker as done for the weak variant. However, this lead to non robust solutions and the even higher deformations resulted into abortions of the Abaqus/Explicit. In addition, making the wall thicknesses even lower, results in unfeasible design in terms of manufacturing constraints.

The response for all five cases is the same, being the glancing-off response. Therefore, it has been decided to use a different simplified FEM simulation model which is more detailed. It can be later proved that the wheel has a great influence in the x force component and therefore for the rotational response of the vehicle. However, the study revealed that indeed, as engineering judgment and intuition suggests, the forces in x and y must be balanced in order to achieve a certain behavior. This aspect will be discussed in a later part of the thesis, but it is a valuable insight. So in order to glance-off, the force in y should be sufficiently high. Similarly, in order to rotate around the barrier, it is expected that the force in x should be sufficiently high. But this could not been proven using the trolley FEM simulation model, as it experienced only one response mode to the small overlap crash test.

## 5.3 Reduced full vehicle FEM simulation model

As described in Section 5.2, often FEM crash simulation models with reduced complexity are used at an early development phase of the passive safety analysis in order to reduce development time due to reduced simulation time. Comparable to the concept of the trolley model, a reduced FEM model is used in this section in order to investigate the most relevant components of the vehicle's structure and their influence on the kinematics of the vehicle.

### 5.3.1 Overview

The reduced FEM simulation model is based on an existing FEM simulation model of a production vehicle at BMW AG. Analyzing crash test videos of current vehicles from BMW AG and also of competitor vehicles which are subjected to the small overlap crash test, it becomes clear that most of the deformation takes place at the front of the vehicle, as shown in Fig. 5.11.

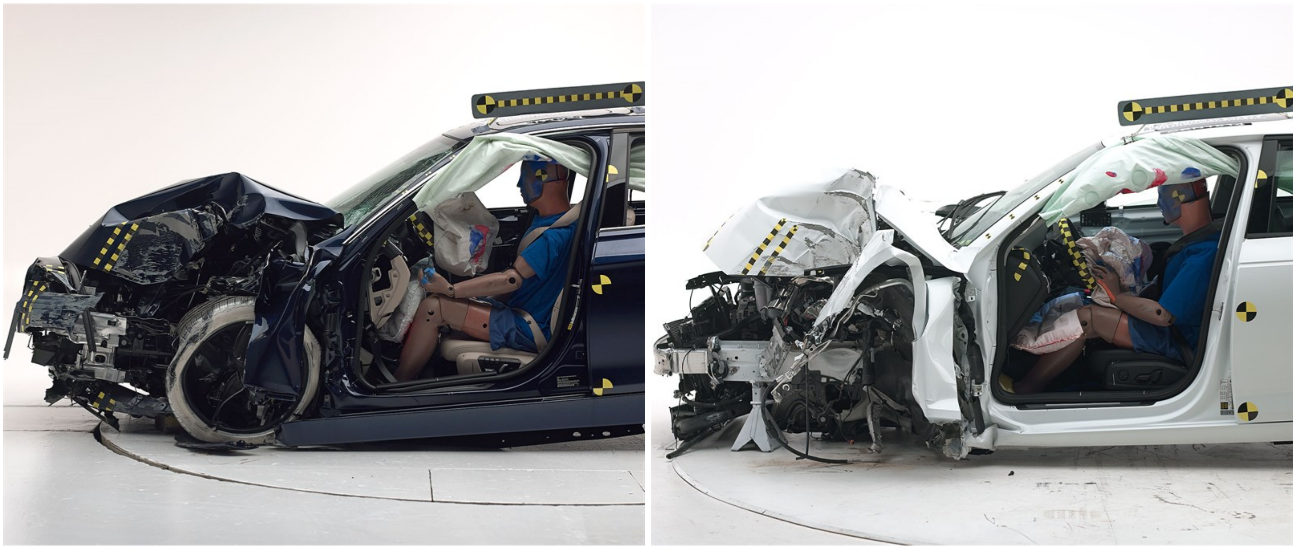

(a) BMW 3 Series. (b) Audi A4.

Figure 5.11: Deformation due to the small overlap crash test load-case. Source [70].

Specifically, when looking at Fig. 5.11, it can be observed that most of the deformation is occurring in front of the A-Pillar of the vehicle. Based on this observation, a reduced FEM simulation model is used in this section. Basically, all elements behind the A-Pillar are deleted. At the location of the COG, a node is added which has the mass and equivalent inertia of the deleted elements. The elements at the cutting plane are connected to the node using Multi-Point constraints (MPC). Note that a MPC in Abaqus/Explicit couples the nodes which are assigned to the MPC node using, in this case, a rigid connection. This means that the nodes related to the nodes at the cutting surface are related to the MPC node positioned at the COG via a direct link which is in this case rigid. This also means that everything after the A-Pillar is assumed to be rigid and non-deformable. In addition, the node containing the mass and equivalent mass moment of inertia of the deleted geometry is restrained to only move in the xy plane. To illustrate how the FEM model of the reduced simulation model looks like, an image of the model is shown in Fig. 5.12.

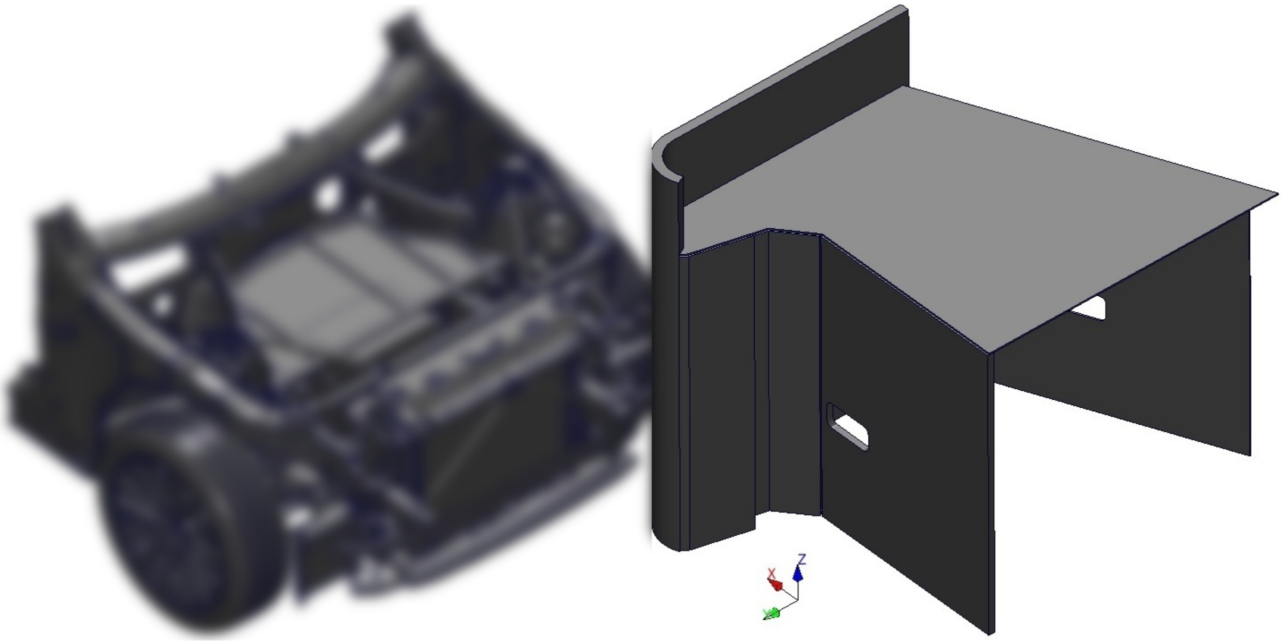


Figure 5.12: Isometric view of the reduced FEM simulation model.

From Fig. 5.12, it can be seen that the reduced FEM model is more representative of a real vehicle structure compared to the trolley FEM simulation model. However, some components are not included, for example no bonnet structure is present in the simulation model. For a clearer overview of the reduced FEM simulation model, the top, bottom, side and front view of the model are shown in Fig. 5.13.

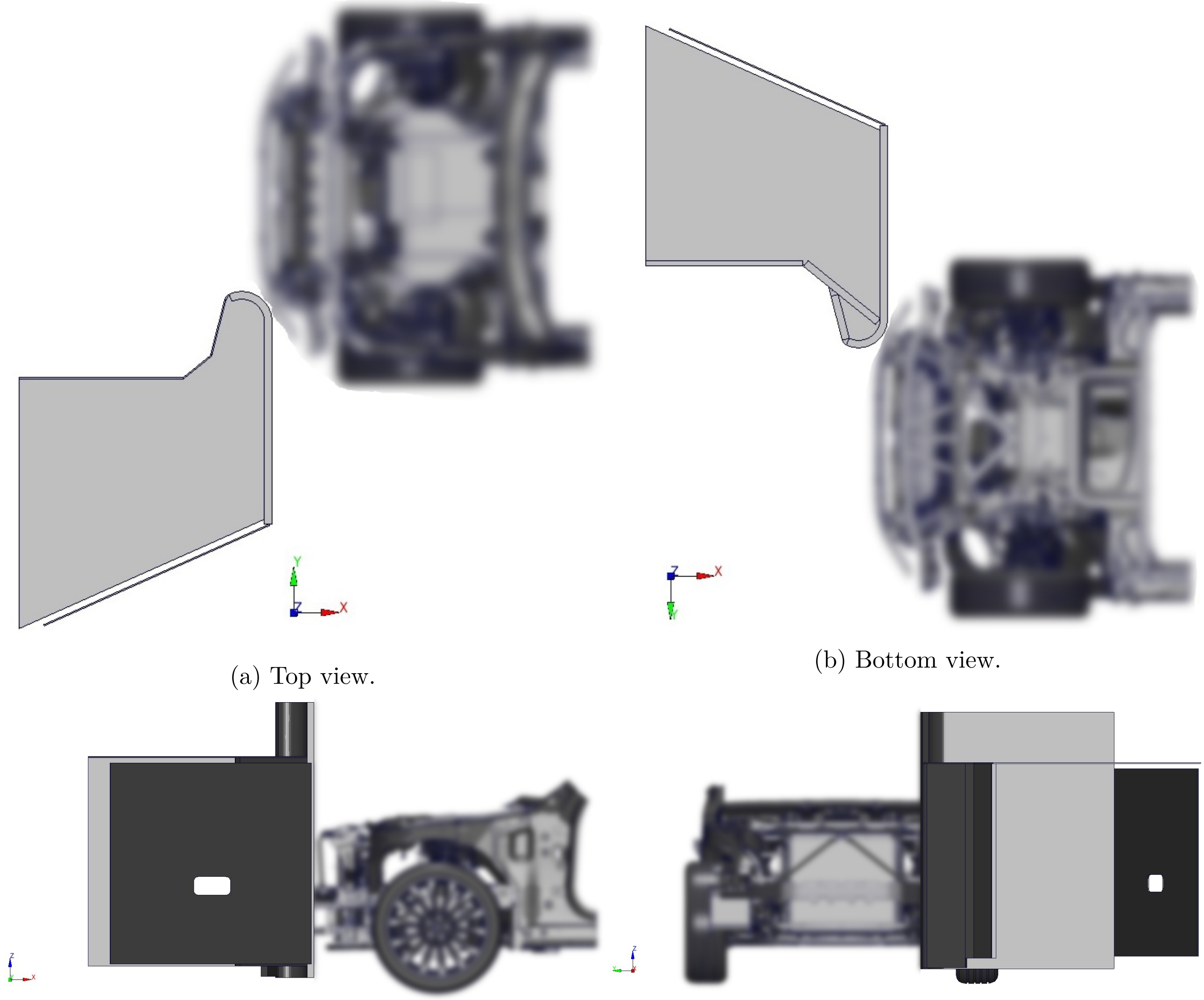

(a) Top view.

(b) Bottom view.

(c) Side view.

(d) Front view.

Figure 5.13: Overview of the reduced FEM simulation model.

Looking at Fig. 5.12 and at Fig. 5.13, it can be seen that besides the structural parts, also non-structural parts such as radiators, suspension assembly, steering assembly and wheels are included in the model. Also, it becomes clear that the distinction between the two load paths, represented by the trolley FEM simulation model, is not that generic, due to the presence of the wheel and surrounding structure.

### 5.3.2 Energy study

Similar to the trolley FEM simulation model, an energy analysis of the reduced FEM simulation model is performed. The cumulative internal strain energy of the model, with a threshold value of 0.75% in the available tool at BMW AG, reveals the following contour color plot of the component groups, as shown in Fig. 5.14.

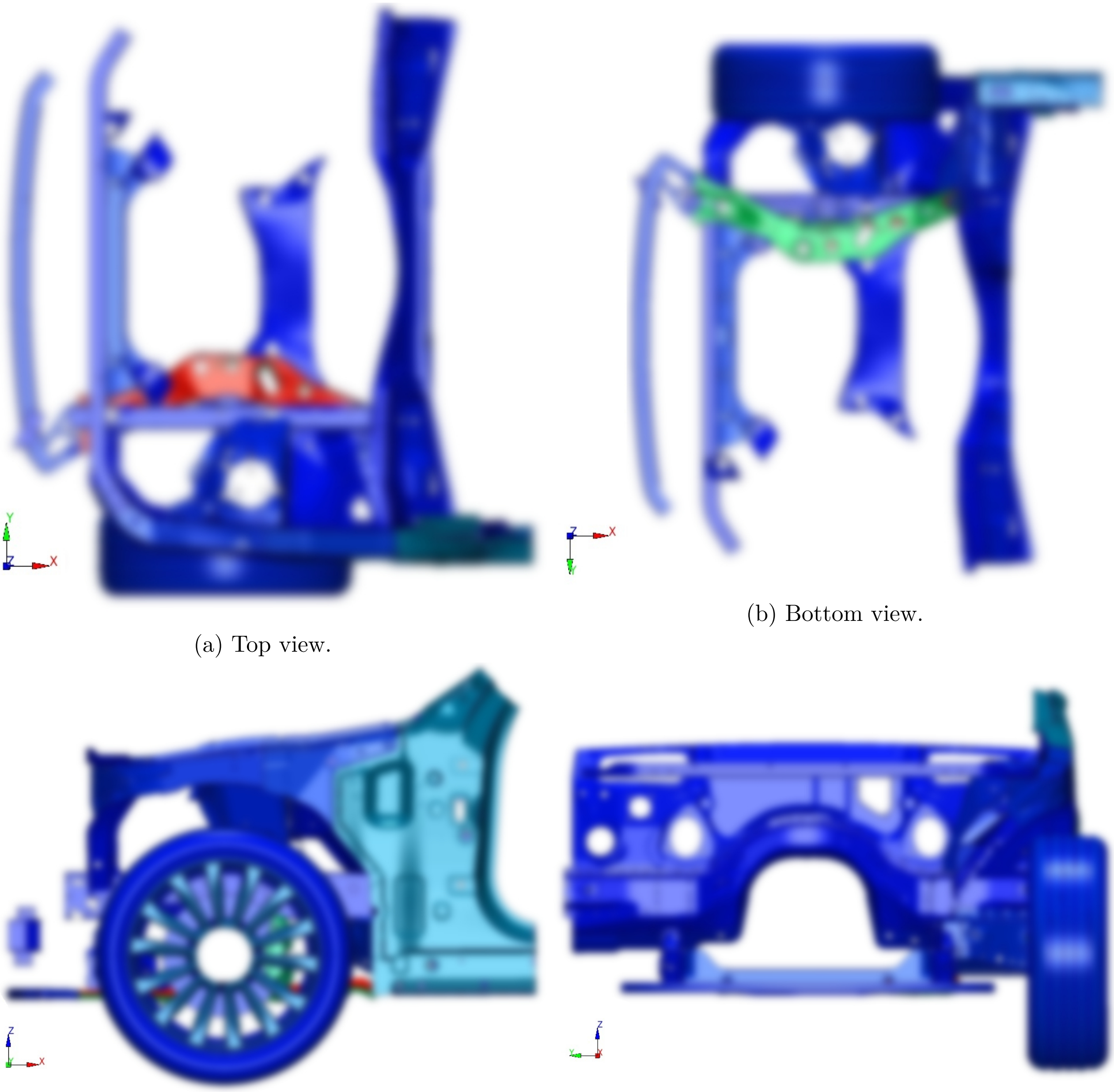

(a) Top view.

(b) Bottom view.

(c) Side view.

(d) Front view.

Figure 5.14: Overview of the energy study of FEM trolley model.

Looking at Fig. 5.14, it becomes clear that most of the strain energy is taken up by the lower framerail, colored in red and green in the top and bottom view, respectively. In addition, quite a large portion of the energy is taken up by the wheels, specifically the rims and brake disc, as well as the supporting structure of the A-Pillar. The remaining components show a similar strain energy level. Therefore, referring to Fig. 5.14, the following components are identified as being of vital importance for the reduced FEM simulation model subjected to the small overlap crash test load-case:

- Upper and lower bumper.
- Upper and lower framerail.
- Upper and lower crashbox.
- Shotgun.
- Springdome.
- Crashbar.
- Crossmembers.
- Shear plates.
- Truss structure.
- Wheel.

### 5.3.3 Output variables

Similar to the trolley model, output variables need to be defined in order to see the influence of the changed wall thicknesses of the most relevant components on the response of the vehicle. Basically, the same output variables as for the trolley FEM simulation model are chosen to monitor the response.

### 5.3.4 Monitoring of output variables

In order to monitor the output variables, a measurement kit is build up. The procedure is the same as for the trolley FEM simulation model, as described in Section 5.1.

### 5.3.5 Variation of parameters

The components which take up most of the deformation energy in terms of strain energy of the simulation are taken as the components which are changed in wall thickness. Comparable to the trolley FEM simulation model, the goal is to arrive at variants which are able to capture both responses. For the reduced FEM simulation model, this means that three models are chosen, the baseline model, the strong model variant and the weak model variant. An overview of the wall thicknesses of the three variants is given in Tab. 5.2. Note that although the load-case is asymmetrical, the wall thicknesses of the components which have a left and a right side are changed to the same extend, similar to the investigation done with the trolley FEM simulation model.

Table 5.2: Thickness ratios of structural components of reduced FEM simulation model variants.

| *Component* | $\frac{t_{baseline}}{t_{baseline}}$ | $\frac{t_{strong}}{t_{baseline}}$ | $\frac{t_{weak}}{t_{baseline}}$ |
|---|---|---|---|
| Upper bumper | 1.0 | 2.0 | 0.5 |
| Lower bumper | 1.0 | 2.0 | 0.5 |
| Upper framerail | 1.0 | 2.0 | 0.4 |
| Lower framerail | 1.0 | 2.0 | 0.8 |
| Upper crashbox | 1.0 | 2.0 | 0.5 |
| Lower crashbox | 1.0 | 2.0 | 0.4 |
| Shotgun | 1.0 | 2.0 | 1.0 |
| Spring dome | 1.0 | 2.0 | 1.0 |
| Crashbar | 1.0 | 2.0 | 0.4 |
| Crossmembers | 1.0 | 2.0 | 0.7 |
| Shear plates | 1.0 | 2.0 | 1.0 |
| Truss structure | 1.0 | 2.0 | 0.4 |

Similar to the investigation of the trolley FEM simulation model, the identified relevant components of the strong version of the FEM simulation model have wall thicknesses which are twice as thick compared to the baseline FEM simulation model. For the weak variant of the FEM simulation model, wall thickness ratios between 0.4 and 1 are used. The reason for the non-uniform variation in thickness ratios of the weak variant comes from the fact that having the same ratio for all components leads to non-robust simulation results and abortions of the simulation process in Abaqus/Explicit. Therefore, after changing the wall thicknesses for several simulation runs, the variants shown in Tab. 5.2 are used for the numerical study of the reduced FEM simulation model.

### 5.3.6 Determination of structural components of interest

Using the three different variants shown in Tab. 5.2 and the mentioned output variables, the influence of the changes on the response of the model is analyzed.

First, the response of the vehicle to the load-case, as seen in Animator 4 is inspected, see Fig. 5.15. Note that the blue model shown in Fig. 5.15 is the baseline model, the red model is the strong variant and the green model is the weak variant.

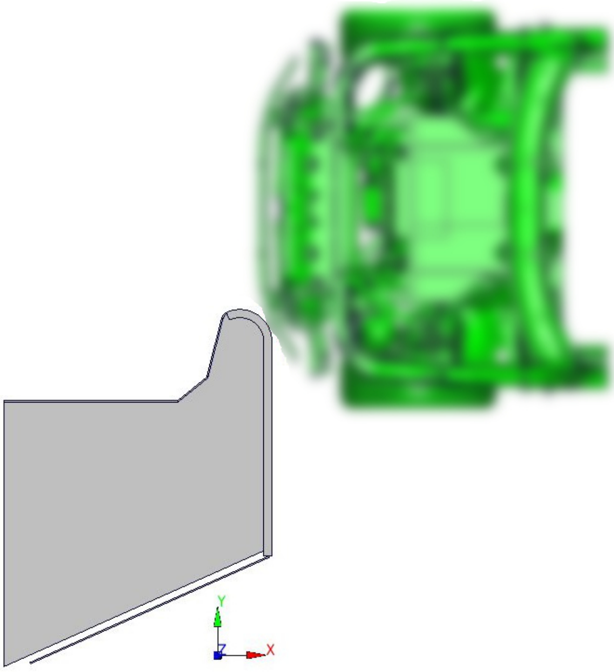


(a) Before.

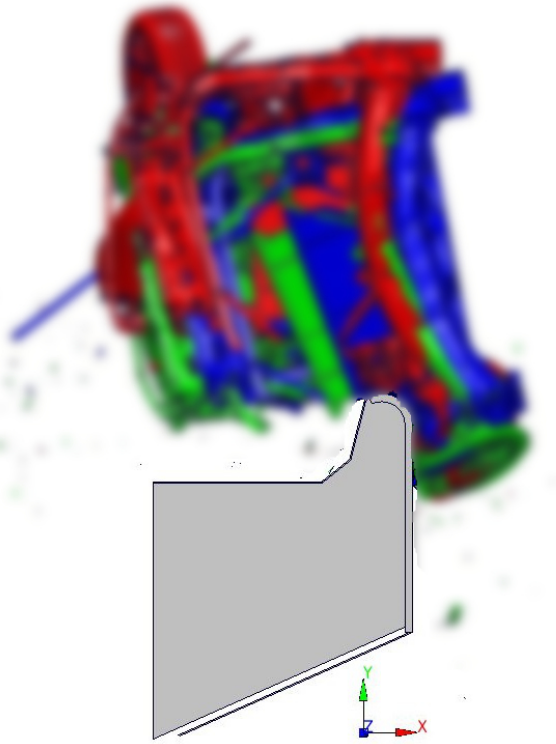


(b) After.

Figure 5.15: Reduced FEM simulation model before and after impact.

From Fig. 5.15, it is observed that all three variants do rotate around the barrier, but their angle differs significantly. The weakest variant shows the largest CCW rotation of the three models, followed by the baseline model. The strongest variant, almost did not rotate at all, but it also did not glance-off from the barrier.

In order to inspect the behavior in more detail, the displacement of the COG in x and y are analyzed, as shown in Fig. 5.16.

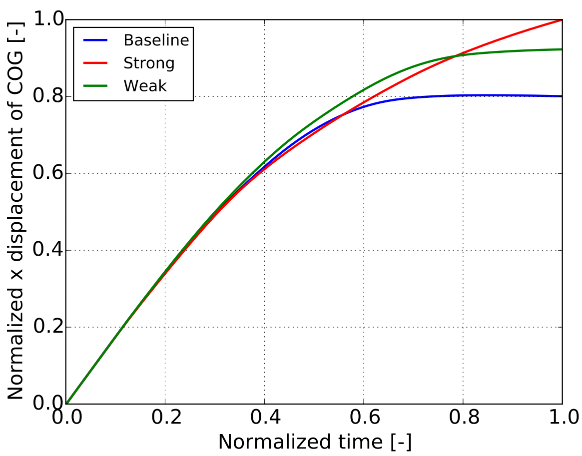


(a) Displacement in x.

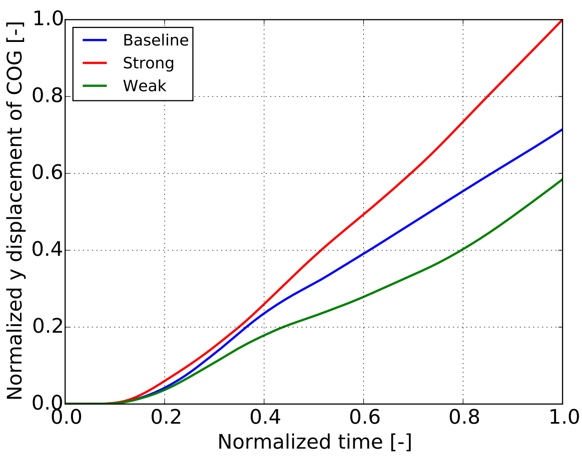


(b) Displacement in y.

Figure 5.16: Normalized displacement as a function of normalized time for the reduced model.

From Fig. 5.16a it becomes clear that the strong variants has the largest displacement in x while the baseline model as the lowest displacement in x over simulation time. In addition, for these two variants, at approximately 70%, respectively, 80% of the simulation time, no increase in displacement is observed for an increase in simulation time. Referring to Fig. 5.16b, a large difference can be seen between the strong variant compared to the weak variant. The graphs illustrates that the strong variant experiences the highest lateral displacement. The baseline model lies basically in between the two curves shown in

Fig. 5.16b. In addition, it is observed that the weak variant has the least amount of y displacement, followed by the baseline model.

Next, it is looked at the rotation of the model, as shown in Fig. 5.17.

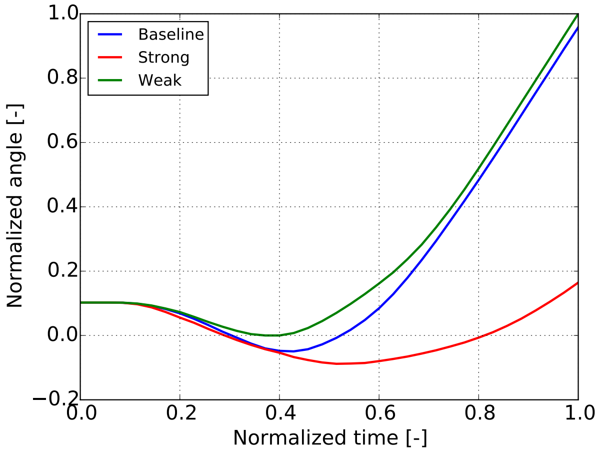


Figure 5.17: Normalized angle as a function of time of the reduced model.

In Fig. 5.17, the normalized angle of the reduced FEM simulation models are shown as a function of normalized time. Both, the weak and the baseline model have a similarly high CCW angle which is also seen by Fig. 5.15. The strong variant first shows CW rotation followed by a switch in sign and sub-sequentially a CCW rotation.

In the following, the forces in x and y as a function of time are investigated, se Fig. 5.18.

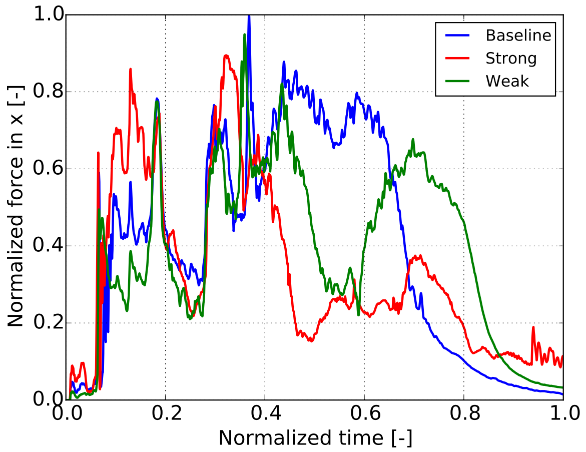


(a) Force in x.

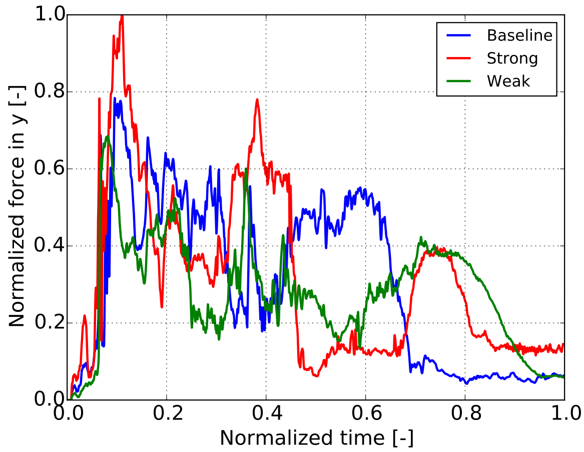


(b) Force in y.

Figure 5.18: Normalized force as a function of normalized time of the reduced model.

In Fig. 5.18a, two peaks in force level can be observed, at 0.17 and 0.38 of normalized time, respectively. The strong variant has the highest force level at the first peak, while the baseline model has the highest force level at the second peak. After the first peak, a large drop in force is seen. After the second force peak, the force of the weak variant decreases significantly. The weak variant shows the same behavior, except for an increase at 60% of simulation time The baseline model has a relatively constant x force level from 0.4 to 0.6 of normalized simulation time. At 0.8 of simulation time, all models have a low x force. The forces in y, shown in Fig. 5.18b show all a large force peak at 0.1 of simulation time, where the highest force level is observed for the strong variant, followed by the baseline and the weak variant. After that force peak, the y forces decrease to approximately half of the reached peak. For the baseline, the level stays relatively constant and drops to almost zero at 0.7 of simulation time. The strong variant shows two more peaks, one at 0.4 of normalized time and one at 0.7 of normalized time. The same can be seen for the weak variant, except for the fact that the force level is lower at the location of the peaks.

Next, it is looked at the normalized x and y force plotted over normalized displacement, as shown in Fig. 5.19.

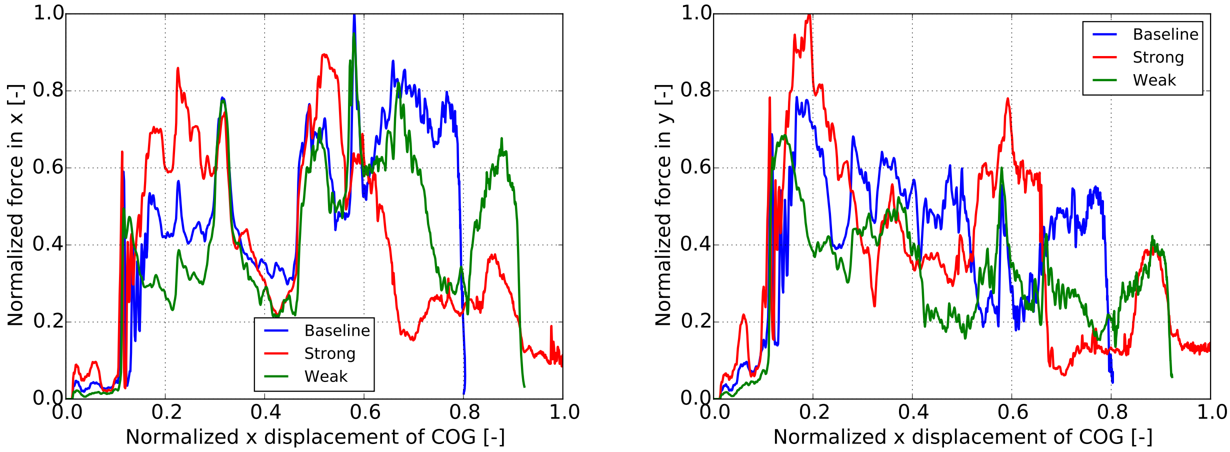


(a) Force in x.

(b) Force in y.

Figure 5.19: Normalized force as a function of normalized time for the reduced model.

Fig. 5.19 shows that the highest forces in y are obtained for the strong variant. Also, the first force peak in x is the highest for the strong variant. The highest force in x, however, is seen for the baseline and the weak variant. In addition, looking at Fig. 5.19a, springback is seen for the baseline and weak variant.

Finally, it is looked at the normalized kinetic and internal energy as a function of normalized time of the three simulation models, as shown in Fig. 5.20.

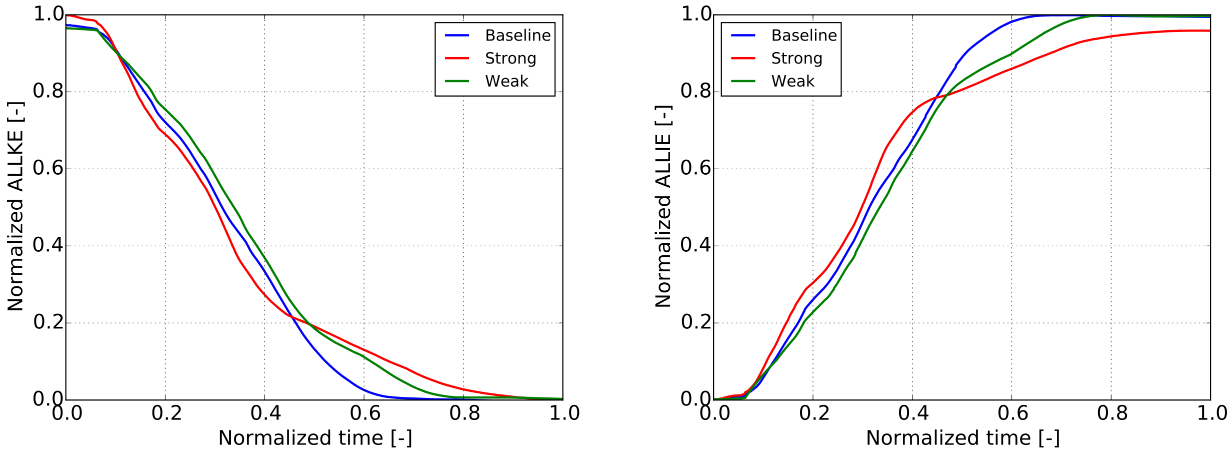


(a) Kinetic energy.

(b) Internal energy.

Figure 5.20: Normalized energy as a function of normalized time for the reduced model.

From Fig. 5.20a it can be seen that the strong variant requires more time to arrive at the lowest energy level compared to the other two models. For all three variants a decrease of the energy level to the lowest level is seen. The baseline model reaches the lowest level at 0.6 of simulation time, while the weak variant requires 0.8 of simulation time and the strong variant 0.9 of simulation time. Looking at Fig. 5.20b, it is observed that the strongest variant shows the lowest internal energy compared to the two other models. In addition, it is seen that the baseline model reaches the highest level at 0.65 of simulation time, where the weak model reaches this level at 0.7 of simulation time. Both, the weak and baseline model, have the highest internal energy level.

### 5.3.7 Discussion of results

At this point, several observations from the numerical study of the reduced FEM simulation model can be made.

First of all, none of the three FEM simulation models do glance-off and all of the three models exhibit the rotational response mode. However, the behavior is not exactly the same for all three models. The strong variant does show the largest tendency to eventually glance-off, seen by the highest displacement of the COG in y. In addition, the magnitude of the angle of the COG for the strong model is relatively small compared to the other two variants. Furthermore, it is observed that the weak variant shows the least tendency to glances-off, seen by the lowest displacement of the COG in y. The reason for this are the high y forces of the strong variant while the weak variant has the lowest y forces. The stiff components of the strong variant do transfer the highest forces, while the deformation is lower. This is seen by the lower internal energy.

The plots of the forces in x as a function of time show that after 0.17 and 0.38 of simulation time force peaks are occurring, followed by a significant drop. This shows the deformation of components, taking up a significant amount of force, followed by a drop due to the collapse of the load path. Looking at the y force, this phenomenon is seen most prominently for the strong variant where the large drop in force over time indicates the collapse of components.

Compared to the trolley FEM simulation model, the presence of multiple force peaks is explained by the fact that the reduced FEM simulation model is more detailed, as it includes the wheel assembly and the suspension. These two groups of components are seen in the two force peaks in x. These group of components help to rotate the reduced FEM simulation around the barrier. Due to the increased level of detail, it can be expected that the results obtained from the numerical study will be more accurate and more realistic when compared to the trolley model.

Investigating the energy level, similar trends are seen. The highest remaining kinetic energy is seen for the strong model which has the largest tendency to show a glancing-off behavior. However, the force level in y is too low to push the vehicle away from the barrier. Also, the largest peak for the baseline and weak variant show that these models do deform the most and dissipate the most energy.

From the numerical study of the reduced FEM simulation model, a tendency of required force levels in x and y is seen for obtaining a certain response. However, changing the wall thickness of the most important components is not sufficient to obtain a different response for the vehicle, as even the most extreme cases do not show a different behavior. It has also been tried to change the geometry of some structural components to influence the load paths, however the result is still the same. The fact that the simulation does fail when the wall thickness is too low or too high does not help in the process of the numerical investigation. Since the response is based on the combination of force levels in x and y, changing wall thicknesses of components is not a very efficient approach to obtain a different response mode of the vehicle.

## 5.4 Discussions and conclusions

The main idea of the numerical study was the identification of the most relevant components for the small overlap crash test and the impact on the response of the vehicle. Using two different FEM simulation models, being the trolley model and the reduced FEM simulation model, it was tried to identify these components and the relation to the response by changing the wall thicknesses of relevant components. The results have shown that this only possible to a limited extend. The reasons behind this are the following.

The geometry and nature of the load paths do only allow a certain increase and/or decrease in wall thickness, as otherwise multiple failure mechanisms do occur. The two investigated FEM simulations models have pre-described sets op components, some of which do not define a certain load path, but which are required to obtain a certain response. In addition, each change in wall thickness has an influence on the surrounding structure and the load transfer the surrounding structure. In order to obtain a detailed view on which component has which influence, a very large sampling size would be required. However, as performing a numerical study using very detailed FEM simulation models is not very robust, another method is required.

The main conclusion from the numerical study is that the first approach which is the bottom up approach where the investigation of the influence of a certain component on the response of the vehicle does not work satisfactorily. In order to obtain an idea of which components need which force level, a different method must be used. Therefore, it is concluded that a top-down approach is required in which the global kinematics of the vehicle are modeled. This kinematic model is then extended to multiple components. This is a strong promoter for developing a simplified kinematic model which is able to capture the kinematics of the vehicle sufficiently accurate and can be used to find force deformation solution spaces for achieving either one of the two mentioned behaviors of the vehicle.

CHAPTER 6

# Predictive kinematic model

Following the top down approach, this chapter deals with the development of the predictive kinematic model created for the small overlap crash test of the IIHS. The chapter is structured as follows. First, in Section 6.1, the motivation of having a simplified predictive kinematic model is discussed. Section 6.2 presents the methodology of the kinematic model along with the governing equations and working principles. Then, in Section 6.3, the model is extended by using multiple springs in order to represent several grouped structural components.

## 6.1 Motivation

As found out by the numerical study performed with the FEA program Abaqus/Explicit, the investigation of the most relevant structural components for the small overlap crash is a time consuming process when using detailed FEM crash simulation models. In addition, this process is only possible if a detailed FEM simulation model is available. Normally, at the early development phase of the passive safety development, this is not the case. In this early development phase, little information is known about the geometry of structural components and of the load paths. Since it is of special interest in the passive safety development to investigate the safety of the vehicle at the earliest possible phase of the development phase, other methods must be used. As discussed in the literature study in Chapter 2, developing a simplified model is commonly done in crashworthiness investigations. Therefore, having a simplified model which is as simple as possible and as complex as necessary which is able to predict the response of the vehicle is of large importance to enhance the safety of passenger vehicles.

A simplified predictive model allows to quickly asses structural changes and their influence on the kinematics of the vehicle. In addition, such a simplified predictive kinematic model does not require detailed information of the structure and the load paths. This is particularly helpful at the early development stage of a passenger vehicle where little information of the exact geometry is known. However, the earlier the information on a certain required force level for structural components, the better the outcome for the project in terms of cost, efficiency and performance. Therefore, being able to predict which force levels of the structural components are required is rather convenient. The real advantage of having an idea of what force levels are sufficient to obtain a certain response is the possibility to design in the early development phase accordingly. In addition, a predictive kinematic model allows to obtain results quickly and enables engineers to estimate the performance of the vehicle adequately.

Specifically, the idea becomes even more powerful when combining the simplified model with the concept of force displacement solution spaces, as presented by the work of Fender [7]. If the system can be divided into several subsystems (e. g. load paths and components), a set of uncoupled force-displacement solution spaces can be generated. Each of which can then the be defined as design targets for the responsible design department. According to the principles of the V-model, these individually designed subsystems do then fulfill the overall design goal when integrated to form the crash management system. Therefore, having an upper and lower bound for the local force levels in x and y as a function of deformation of the vehicle for the force deformation solution space, gives a certain design area in which a safe vehicle structure is guaranteed. Since the force deformation solution space tool is already available at BMW AG, the focus of this chapter lies in creating the simplified model which is able to predict the responses of a vehicle subjected to the small overlap crash test. First, the predictive kinematic model is explained using the simplest possible configuration as a proof of concept in Section 6.2 and is then extended to a more detailed level using grouped components in Section 6.3.

## 6.2 Methodology of predictive kinematic model for two springs

This section deals with the creation of the predictive kinematic model. The governing principle of the predictive model is based on a mass spring system to represent the model. First, an overview of the predictive model is given, followed by the mathematical formulation of the model. Next, the procedure of interpolating the force deformation curve is discussed and finally the simulation algorithm implemented into Python is presented.

### 6.2.1 Overview

The idea of the predictive kinematic model is derived from idealizing the problem with a mass spring system, commonly done in crashworthiness applications, as discussed in Chapter 2. The idealization of the small overlap crash using one mass and one spring is shown in Fig. 6.1.

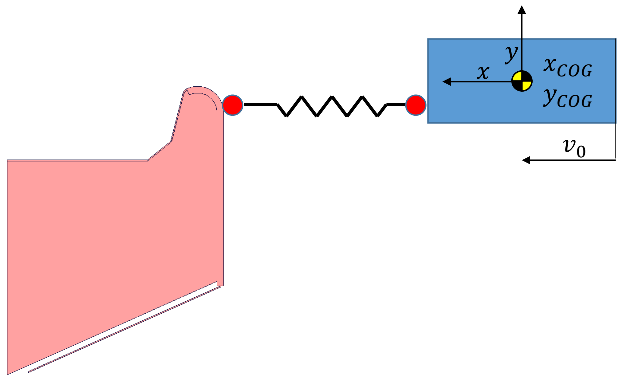


Figure 6.1: Idealization of the small overlap crash test using a mass spring system.

With the idealization shown in Fig. 6.1, the structural stiffness in local coordinate system is idealized with the spring shown in the illustration. The initial condition of the initial crash speed of 64.4 km/h is imposed on the mass. The mass and mass moment of inertia are related to the COG of the vehicle, shown in Fig. 6.1. The offset between the application point of the spring on the barrier and the vehicle's COG, forces the body to rotate. For modeling the rotation, rigid body dynamics mechanics is used, thus the rotational angle of the COG of the vehicle is a function of the moment due to the force which is not applied at the COG and the mass moment of inertia. However, the problem with having only one spring in x is the fact that no stiffness in the transverse direction is taken into account, as the spring is able to only transfer axial loads. Thus, in order to describe the stiffness of the vehicle in axial and transverse direction, at least two springs are required. The transverse forces originate from the geometry of the barrier, friction and geometry of the structural components, as observed in FEM simulation models. Note that it is important to denote the stiffness in the local coordinate system which is the coordinate system that moves with the vehicle, as otherwise the stiffness can not be related in a convenient way to structural components. Therefore a two springs system is considered in order to explain the working principle and the governing physics behind the predictive kinematic model.

By using a two spring mass system to represent the mechanics behind the problem, the following idealization is obtained for the predictive kinematic model, as shown in Fig. 6.2.

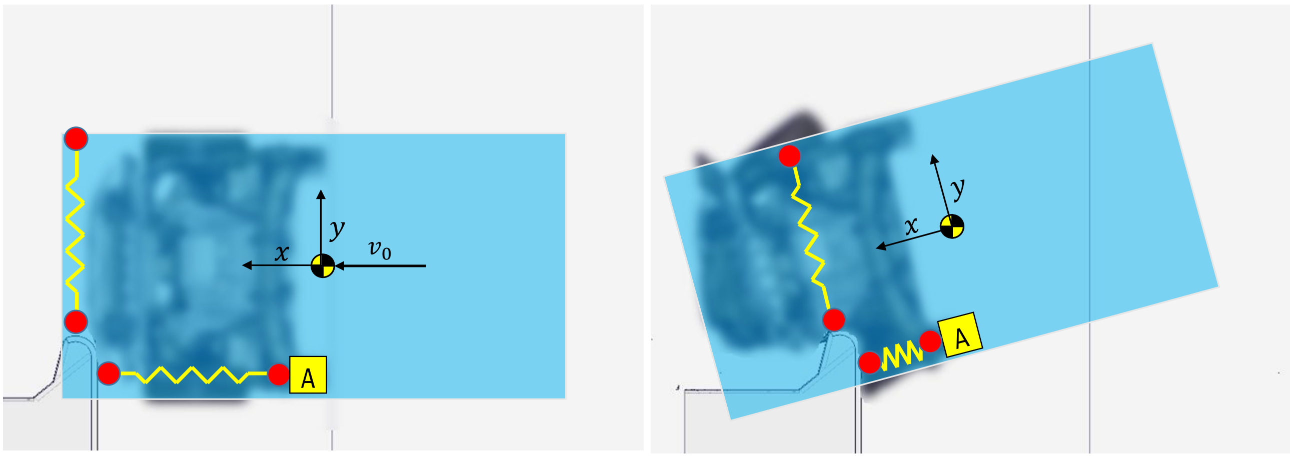


(a) Non-rotated state.

(b) Rotated state.

Figure 6.2: Overview of the predictive kinematic model using two springs.

As can be seen by Fig. 6.2, the predictive kinematic model consists out of two springs, each representing the stiffness in each of the two directions of the vehicle's coordinate system. The spring aligned with the x axis is attached to the A-Pillar of the vehicle and the spring aligned with the y axis is assumed to move by the same amount in the negative x direction in the local coordinate system as the spring in x compresses. Note that the springs do rotate with the coordinate system of the vehicle, so they are always aligned in the local x and y direction. The vehicle has the initial condition that the initial speed of 64.4 km/h is imposed on the COG of the vehicle. It is assumed that everything behind the A-Pillar can be assumed to be rigid, similar to the argumentation used in the numerical study, see Fig. 5.11. The consequence of this assumption is that the initial length of the spring in x is the maximum possible deformation length in front of the A-Pillar of the vehicle. The application point of the force on the barrier for determining the moment is assumed to be the projection point of the A-Pillar along the vehicle's x direction onto the barrier. In addition, it is assumed that the barrier is flat, so there is no arc connecting the horizontal surface with the vertical surface. Also note that it is assumed that no changes in mass and moment of inertia are occurring due to the deformation and separation of components during and/or after impact.

Summarized, the simplified predictive kinematic model uses the following input variables:

- Position of COG.
- Position of barrier.
- Mass of vehicle.
- Mass moment of inertia of vehicle.
- Location of spring. Note that this is the location of the A-Pillar.
- Initial velocity of vehicle.
- Force in x over x deformation in local coordinate system.
- Force in y over x deformation in local coordinate system.

The degrees of freedom of the model are the following:

- Displacement of COG in x.
- Displacement of COG in y.
- Rotation of the vehicle around the z axis of the COG of the vehicle.

The assumptions of the predictive kinematic model are summarized below:

- Force in lateral direction is related to the deformation of the spring in axial direction.
- Projection of axial spring attached to the A-Pillar onto the barrier is used to compute the deformation of the axial spring.
- Projection of axial spring attached to the A-Pillar onto the barrier is assumed to be the force application point for calculating the moment.

- The barrier is assumed to have no radius. This implies that the force application point in x does not move over time. In y direction however, the point does move.
- Effective force is interpolated from input spring characteristic at every time step.
- No change in mass moment of inertia over time.
- No change in mass over time.
- No friction of the tires is included.
- Only x and y forces are modeled. In the numerical study shown in Chapter 5, it was shown that the z component of the resultant force is rather small compared to the other two components, see Fig. 5.1. It is assumed that it has not a major influence on the considered planar movement in the xy plane.
- The vehicle is assumed to be rigid behind the yz cutting plane at the location of the A-Pillar.
- The friction is not explicitly modeled, but is taken into account when implementing the y force of the transverse spring.
- Once the spring in axial direction has no calculated projection point anymore, no force is transferred by the axial as well as the lateral spring to the vehicle, since the axial spring is not in contact anymore.

As the discussion in this section was rather general and it was intended to give an overview of the assumptions and general working principles, the following section deals with the detailed mathematical formulation of the predictive kinematic model using two springs.

### 6.2.2 Mathematical formulation

The derivation of the equation of motion (EOM) is best described by looking at the following idealization of the predictive kinematic model, as shown in Fig. 6.3.

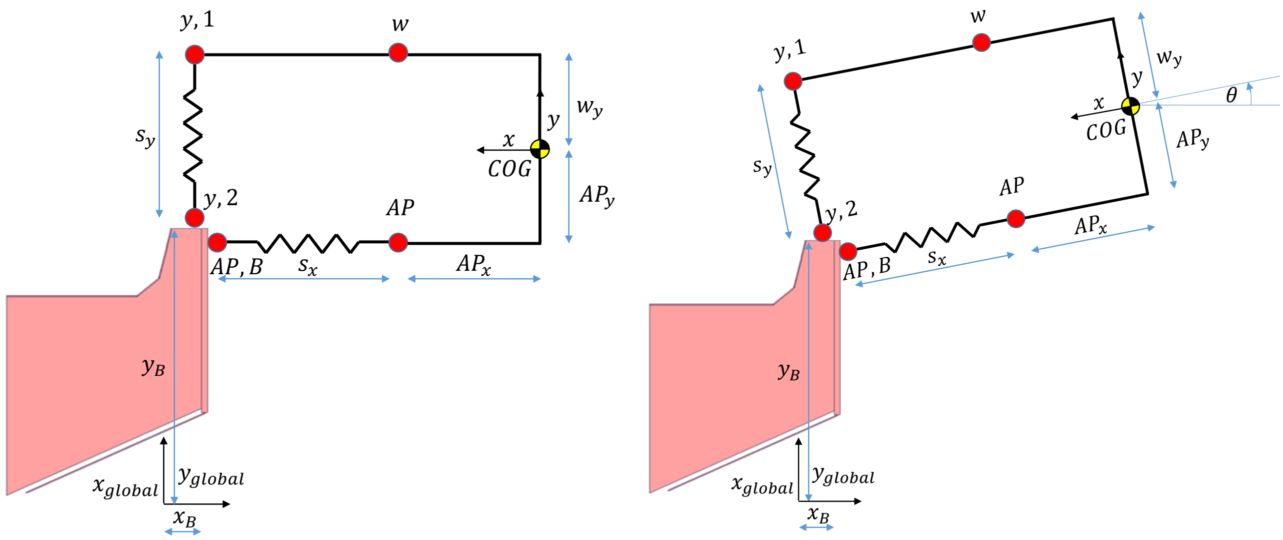


(a) Non-rotated state. (b) Rotated state.

Figure 6.3: Idealization of predictive kinematic model using two springs.

Note that in Fig. 6.3a, the configuration of the kinematic predictive model is in the non-rotated state while the configuration in Fig. 6.3b is in the rotated state. The EOM of the idealized system shown in Fig. 6.3, is given in Eq. 6.1.

$$\underline{\underline{M}}\ \underline{\ddot{q}} + \underline{\underline{K}}\ \underline{q} = \underline{F} \tag{6.1}$$

Where in Eq. 6.1, $M$ is the mass matrix of the vehicle, given by Eq. 6.2, $q$ is a vector containing the DOFs, shown in Eq. 6.3, $\ddot{q}$ is the second derivative of the DOFs, given by Eq. 6.4, and $K$ is the stiffness matrix of the vehicle, shown in Eq. 6.5.

$$\underline{\underline{M}} = \begin{bmatrix} m & 0 & 0 \\ 0 & m & 0 \\ 0 & 0 & I_{zz} \end{bmatrix} \tag{6.2}$$

$$\underline{q} = \begin{bmatrix} u_{x,COG} \\ u_{y,COG} \\ \theta \end{bmatrix} \tag{6.3}$$

$$\underline{\ddot{q}} = \begin{bmatrix} \ddot{u}_{x,COG} \\ \ddot{u}_{y,COG} \\ \ddot{\theta} \end{bmatrix} \tag{6.4}$$

$$\underline{\underline{K}} = \begin{bmatrix} k_x & 0 & 0 \\ 0 & k_y & 0 \\ 0 & 0 & k_\theta \end{bmatrix} \tag{6.5}$$

In order to determine the stiffness matrix in Eq. 6.1 the Lagrangian dynamics analysis, as proposed by Török, is used [71]. Using the Lagrangian analysis method, the EOM is obtained by taking the derivative of the kinetic and potential energy of the system with respect to its degrees of freedom. As mentioned in the previous section, the degrees of freedom are the displacement of the COG in x ($u_{x,COG}$), the displacement of the COG in y ($u_{y,COG}$) and the rotation of the COG around its z axis ($\theta$). Since the kinetic energy of the system is dependent on the movement of the COG in x and y, as well as the rotation of the COG around the z axis, the following equation is obtained for the kinetic energy, see Eq. 6.6.

$$T = \frac{1}{2} m \dot{u}_{x,COG}^2 + \frac{1}{2} m \dot{u}_{y,COG}^2 + \frac{1}{2} I_{zz} \dot{\theta}^2 \tag{6.6}$$

Looking at the idealization of the system in Fig. 6.3, it becomes clear that the potential energy of the system is due to the compression of the two springs and therefore the potential energy of the system is as follows, see Eq. 6.7. In this first approach the deformation of the spring in y is also investigated, however it will be determined later that it is not practical nor representative.

$$V = \frac{1}{2} k_x s_x^2 + \frac{1}{2} k_y s_y^2 \tag{6.7}$$

In Eq. 6.7, $s_x$ and $s_y$ are the deformations of the spring in x and y in the local coordinate system, respectively and $k_x$ and $k_y$ are the local stiffness of the springs in the x and y direction, respectively. The Lagrangian analysis gives the following equations for deriving the EOMs for the three degrees of freedom, as shown in Eq. 6.8.

$$\underline{L} = \begin{bmatrix} \frac{d}{dt}\left(\frac{\partial T}{\partial \dot{u}_{x,COG}}\right) - \frac{\partial T}{\partial u_{x,COG}} + \frac{\partial V}{\partial u_{x,COG}} \\ \frac{d}{dt}\left(\frac{\partial T}{\partial \dot{u}_{y,COG}}\right) - \frac{\partial T}{\partial u_{y,COG}} + \frac{\partial V}{\partial u_{y,COG}} \\ \frac{d}{dt}\left(\frac{\partial T}{\partial \dot{\theta}}\right) - \frac{\partial T}{\partial \theta} + \frac{\partial V}{\partial \theta} \end{bmatrix} \tag{6.8}$$

In order to solve this equation, the compression of the spring needs to be determined, for which the vector notation is used. First, let the position of the COG be given by Eq. 6.9.

$$\underline{r}_{COG} = \begin{bmatrix} x_{COG,0} + u_{x,COG} \\ y_{COG,0} + u_{y,COG} \\ 0 \end{bmatrix} \tag{6.9}$$

Where $x_{COG,0}$ and $y_{COG,0}$ are the initial x and y coordinates of the COG location and $u_{x,COG,0}$ and $u_{y,COG,0}$ are the displacements of the COG location. Looking at Fig. 6.3, the position of the A-Pillar can be determined as follows, see Eq. 6.10.

$$\underline{r}_{AP} = \underline{r}_{COG} + \begin{bmatrix} AP_x \cos(\theta) - AP_y \sin(\theta) \\ AP_x \sin(\theta) + AP_y \cos(\theta) \\ 0 \end{bmatrix} \tag{6.10}$$

Where in Eq. 6.10, $AP_x$ and $AP_y$ are the x and y distance from the COG to the location of the A-Pillar and $\theta$ is the rotational angle of the COG, see Fig. 6.3. The location of the projection of the A-Pillar onto the barrier is determined using Eq. 6.11.

$$\underline{r}_{AP,B} = \begin{bmatrix} x_B \\ \tan(\theta)x_B - r_{AP_x}\tan(\theta) + r_{AP_y} \\ 0 \end{bmatrix} \tag{6.11}$$

Note that in in Eq. 6.11, $x_B$ is the x distance to the barrier. Knowing the location of the contact point of the spring with the barrier and the location of the A-Pillar, the compression, $s_x$, of the spring is determined in using Eq. 6.12.

$$s_x = \left\| \underline{r}_{AP,B} - \underline{r}_{AP} \right\| \tag{6.12}$$

In a similar fashion, the compression of the spring in y is determined. For this, first the position $r_w$ is determined, see Eq. 6.13.

$$\underline{r}_w = \underline{r}_{COG} + \begin{bmatrix} AP_x\cos(\theta) - w_y\sin(\theta) \\ AP_x\sin(\theta) + w_y\cos(\theta) \\ 0 \end{bmatrix} \tag{6.13}$$

Where in Eq. 6.13, $w_y$ is the y distance from the COG location to the point $w$ in the local coordinate system. By investigating Fig. 6.3, the first pillar of the spring in y direction is computed using Eq. 6.14.

$$\underline{r}_{y,1} = \underline{r}_w + \begin{bmatrix} -s_x\cos(\theta) \\ -s_x\sin(\theta) \\ 0 \end{bmatrix} \tag{6.14}$$

For the computation of the second pillar of the spring in y direction, an auxiliary vector for the direction is first determined, as shown by Eq. 6.15. This vector gives the unit vector direction of the vectors $r_{y,1}$ and $r_w$ and it is pointing from $r_{y,1}$ to $r_w$, see Eq. 6.15.

$$\underline{v}_{r_{y,1}r_w} = \frac{\underline{r}_{y,1} - \underline{r}_w}{\left\| (\underline{r}_{y,1} - \underline{r}_w) \right\|} \tag{6.15}$$

Using the axillary vector $r_{y,1}$ to $r_w$, a vector $v_1$ is constructed. The vector $v_1$ points in the orthogonal direction to $z$ and the vector $v_{r_{y,1}r_w}$. Therefore, the vector $v_1$ points in the direction of the second pillar of the spring aligned with the local y axis.

$$\underline{v}_1 = \underline{v}_{r_{y,1}r_w} \times \begin{bmatrix} 0 \\ 0 \\ 1 \end{bmatrix} \tag{6.16}$$

Now the intersection point with the barrier is determined. For this, the following two equations are used, as shown in Eq. 6.17 and Eq. 6.18.

$$\underline{p}_1 + \underline{v}_a \cdot a = \underline{p}_3 \tag{6.17}$$

$$\underline{p}_2 + \underline{v}_b \cdot b = \underline{p}_3 \tag{6.18}$$

Where in Eq. 6.17 and Eq. 6.18 $p_1$ and $p_2$ are the coordinates of a point, $v_a$ and $v_b$ are unit vectors in the direction of $p_3$, $a$ and $b$ are the magnitudes of the vectors $v_a$ and $v_b$ and $p_3$ is the location of the intersection point of interest. By equating Eq. 6.17 with Eq. 6.18, the intersection can be found which is shown in the following.

For the current problem, this intersection can be found as follows. First a point on the y location of the horizontal flat surface of the barrier and on a negative x location is used and its corresponding vector is constructed. This vector $v_2$ shown in Eq. 6.19.

$$\underline{v}_2 = \begin{bmatrix} -10000.0 \\ y_B + 1000 + 150 \\ 0 \end{bmatrix} \tag{6.19}$$

The $y$ entry in $v_2$ is basically the width of the surface plus the arc of the barrier (as it is assumed to be flat) together with the location of the barrier $y_B$ with respect to the global coordinate system. Now the intersection can be found using the following two equations and vectors.

$$\underline{r}_{y,1} + \underline{v}_1 \cdot a = \underline{r}_{y,2} \tag{6.20}$$

$$\underline{v}_2 + \begin{bmatrix} 1 \\ 0 \\ 0 \end{bmatrix} \cdot b = \underline{r}_{y,2} \tag{6.21}$$

Combining Eq. 6.20 with Eq. 6.21 gives.

$$\underline{r}_{y,1} + \underline{v}_1 \cdot a = \underline{v}_2 + \begin{bmatrix} 1 \\ 0 \\ 0 \end{bmatrix} \cdot b \tag{6.22}$$

Rearranging Eq. 6.22 and multiplying both sides with the unit vector $e_1$ gives.

$$\underline{v}_1 \times \begin{bmatrix} 1 \\ 0 \\ 0 \end{bmatrix} \cdot a = (\underline{v}_2 - \underline{r}_{y,1}) \times \begin{bmatrix} 1 \\ 0 \\ 0 \end{bmatrix} \tag{6.23}$$

Rearranging yields the following result.

$$a = \frac{\left\| (\underline{v}_2 - \underline{r}_{y,1}) \times \begin{bmatrix} 1 \\ 0 \\ 0 \end{bmatrix} \right\|}{\left\| (\underline{v}_1) \right\|} \tag{6.24}$$

Using the vectors $r_{y,1}$ and $v_5$, along with the magnitude $a$, the length of the intersection point between the barrier and the second point of the spring is found.

$$\underline{r}_{y,2} = \underline{r}_{y,1} + \underline{v}_1 \cdot a \tag{6.25}$$

Using the two locations of the pillar points of the spring aligned with the local y axis, the length $s_y$ can be determined using Eq. 6.26.

$$s_y = \left\| (\underline{r}_{y,2} - \underline{r}_{y,1}) \right\| \tag{6.26}$$

Since the components of Eq. 6.7 and Eq. 6.6 are known, the components of the Lagrangian, see Eq. 6.8 can be determined. In the following, each of the derivatives of the Lagrangian analysis are provided.

$$\frac{d}{dt}\left(\frac{\partial T}{\partial \dot{u}_{x,COG}}\right) = m\ddot{u}_{x,COG} \tag{6.27}$$

$$\frac{\partial T}{\partial u_{x,COG}} = 0 \tag{6.28}$$

$$\frac{d}{dt}\left(\frac{\partial T}{\partial \dot{u}_{y,COG}}\right) = m\ddot{u}_{y,COG} \tag{6.29}$$

$$\frac{\partial T}{\partial u_{y,COG}} = 0 \tag{6.30}$$

$$\frac{d}{dt}\left(\frac{\partial T}{\partial \dot{\theta}}\right) = I_{zz}\ddot{\theta} \tag{6.31}$$

$$\frac{\partial T}{\partial \theta} = 0 \tag{6.32}$$

$$\frac{\partial V}{\partial \theta} = 0 \tag{6.33}$$

The derivative of $V$ with respect to $u_{x,COG}$ and $u_{y,COG}$ is not as trivial due to the multiple dependency of $s_x$ and $s_y$ on $u_{x,COG}$, as well as $u_{y,COG}$. Performing the derivative calculation using MATLAB, the following result is obtained for the derivative of $V$ with respect to $u_{x,COG}$.

$$\frac{\partial V}{\partial u_{x,COG}} = \Big[(x_B - x_{cog,0} - AP_x\cos(\theta) + AP_y\sin(\theta) - u_{x,COG})^2$$
$$+ (\tan(\theta)(-x_B + x_{cog,0} + AP_x\cos(\theta) - AP_y\sin(\theta) + u_{x,COG}))^2\Big]^{\frac{1}{2}} \tag{6.34}$$

Similarly, the analysis using MATLAB gives the following result for the derivative of $V$ with respect to $u_{y,COG}$.

$$\frac{\partial V}{\partial u_{y,COG}} = \frac{1}{\cos(\theta)}$$
$$(((\cos(\theta)(-y_B + 1000 + 150 + y_{COG,0} + w\cos(\theta)$$
$$+ (AP_x - ((x_B - x_{COG,0} - AP_x\cos(\theta) + AP_y\sin(\theta) - u_{x,COG})^2$$
$$+ (\tan(\theta)(-x_B + x_{COG,0} + AP_x\cos(\theta) - AP_y\sin(\theta) + u_{COG,x}))^2)^{\frac{1}{2}})\sin(\theta) + u_{COG,y})^2$$
$$+ (\sin(\theta)(-y_B + 1000 + 150 + y_{COG,0} + w\cos(\theta)$$
$$+ (AP_x - ((x_B - x_{COG,0} - AP_x\cos(\theta) + AP_y\sin(\theta) - u_{x,COG})^2$$
$$+ (\tan(\theta) - (x_B x_{COG,0} + AP_x\cos(\theta) - AP_y\sin(\theta) + u_{COG,x})))^2)^{\frac{1}{2}})\sin(\theta) + u_{COG,y})^2)^{\frac{1}{2}}) \tag{6.35}$$

As can be seen by Eq. 6.35, the term $\frac{\partial V}{\partial u_{y,COG}}$ is not practical for implementation and hence applying the Lagrangian analysis for determining the stiffness matrix is too inconvenient to do.

Instead, it has been decided to use the direct approach to solve the EOM which is shown in Eq. 6.36.

$$\begin{bmatrix} m & 0 & 0 \\ 0 & m & 0 \\ 0 & 0 & I_{zz} \end{bmatrix} \begin{bmatrix} \ddot{u}_{x,COG} \\ \ddot{u}_{y,COG} \\ \ddot{\theta}_z \end{bmatrix} = \begin{bmatrix} F_x(s_x) \\ F_y(s_x) \\ M_z(s_x) \end{bmatrix} \tag{6.36}$$

Eq. 6.36 is solved by taking the inverse of the mass matrix, as shown in Eq. 6.37.

$$\begin{bmatrix} \ddot{u}_{x,COG} \\ \ddot{u}_{y,COG} \\ \ddot{\theta}_z \end{bmatrix} = \begin{bmatrix} m & 0 & 0 \\ 0 & m & 0 \\ 0 & 0 & I_{zz} \end{bmatrix}^{-1} \begin{bmatrix} F_x(s_x) \\ F_y(s_x) \\ M_z(s_x) \end{bmatrix} \tag{6.37}$$

In order to calculate the moment, the global forces from the springs are used. This is done by using the rotation matrix, shown in Eq. 6.38.

$$\underline{\underline{R}} = \begin{bmatrix} \cos(\theta) & -\sin(\theta) \\ \sin(\theta) & \cos(\theta) \end{bmatrix} \tag{6.38}$$

Thus the global forces are determined using the following relation, as shown in Eq. 6.39.

$$\underline{F}_{global} = \underline{\underline{R}} \begin{bmatrix} F_{x,local} \\ F_{y,local} \end{bmatrix} \tag{6.39}$$

Using the global forces, the moment $M_z$ is calculated as follows, see Eq. 6.40.

$$M_z = F_{x,global}(r_{COG_y} - r_{AP,B_y}) - F_{y,global}(r_{COG_x} - x_B) \tag{6.40}$$

Knowing the second derivatives of the DOFs in Eq. 6.37, the DOFs of interest are computed using the central difference scheme, as introduced in Chapter 3.

$$u_{x,COG}^{t+\Delta t} = \ddot{u}_{x,COG}\Delta t^2 + 2u_{x,COG}^{t} - u_{x,COG}^{t-\Delta t} \tag{6.41}$$

$$u_{y,COG}^{t+\Delta t} = \ddot{u}_{y,COG}\Delta t^2 + 2u_{y,COG}^{t} - u_{y,COG}^{t-\Delta t} \tag{6.42}$$

$$\theta^{t+\Delta t} = \ddot{\theta}\Delta t^2 + 2\theta^{t} - \theta^{t-\Delta t} \tag{6.43}$$

Note that the problem is initialized using the given velocity of the crash test and the chosen time step to determine the first displacement $u_{x,COG}(\Delta t)$, see Eq. 6.44.

$$u_{x,COG}(\Delta t) = v_0 \Delta t \tag{6.44}$$

### 6.2.3 Interpolation of force deformation curve

As stated previously, the forces in x and y over x deformation are an input for the model. As the predictive model uses a certain time step which can have a different resolution than the pre-described force deformation characteristics of the spring, the force deformation curve is interpolated in order to find the corresponding force level for the calculated deformation. As there are some special cases which need to be accounted for, a certain algorithm has been created.

As the forces in x and y have an influence on the deformation and rotation of the model, the correct interpolation is of vital importance. From the discussion of the previous chapter, it can be the case that the model either experiences a glance-off behavior or a rotational behavior. For the former, no force for an increase in deformation should be obtained after passing the barrier and for the latter, after the point of maximum deformation of the axial spring, the deformation decreases and hence there are two force levels for a certain deformation, as shown in Fig. 6.4.

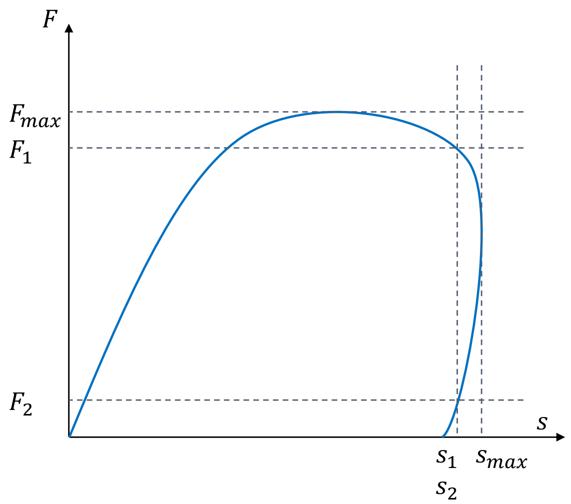


Figure 6.4: Force deformation curve.

Looking at Fig. 6.4, it can be seen that at the deformation value $s_1$ which is equal to the deformation value $s_2$, two different force levels, $F_1$ and $F_2$, are obtained. In addition, it has to be accounted for the cases that the force level exceeds the maximum force and for the case when the deformation exceeds the maximum deformation $s_{max}$. This can be the case when the input given as such is not achievable with the selected parameters and therefore the curve is not matched exactly. The same can happen when a slightly different mass or mass moment of inertia is selected.

In order to account for these cases, the following procedure is implemented into Python. First of all, the force deformation curve is split into two segments. The first segment of the curve goes until the maximum of the displacement $s_{max}$ and the second segment goes from $s_{max}$ until the end of the curve. This is shown in Fig. 6.5 where the green portion of the curve represents the first segments and the orange portion of the curve represents the second segment.

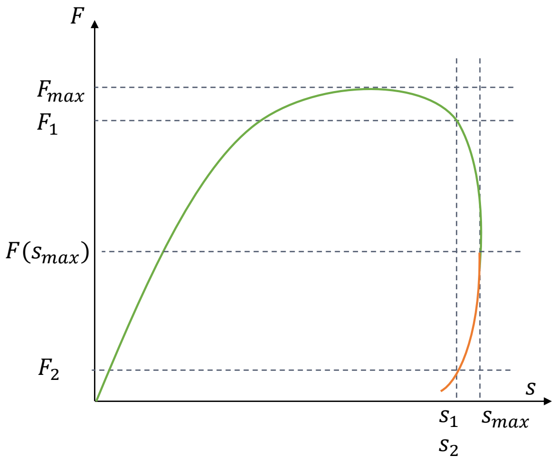


Figure 6.5: Force deformation curve divided into two segments.

Next, the traveling direction of the length of the axial spring in the local coordinate system is determined at every time step. This is done by checking the value of the local deformation of the axial spring and by subtracting the value of the previous time step from the current value. If this value is positive, the vehicle is traveling in the same direction. If this is not the case, the vehicle is traveling in the opposite direction and hence has bounced back from the barrier. This direction value is defined by Eq. 6.45.

$$dir(t) = s_L(t) - s_L(t - \Delta t) \tag{6.45}$$

Note that $s_L$ is the deformation of the spring and determined by subtracting the current value of the length of the spring of the original un-deformed length of the spring, see Eq. 6.46.

$$s_L(t) = s_x(0) - s_x(t) \tag{6.46}$$

In order to do the interpolation, the following process is performed. First it is checked if the deformation $s$ is smaller than the maximum value $s_{max}$ and if the direction value, shown by Eq. 6.45 is positive. If this is the case, the force deformation curve is just interpolated. If however, the deformation $s$ is larger than $s_{max}$, but the direction is still positive, the force level at the maximum deformation ($s_{max}$) is taken as input value for the interpolation. Now, if the direction is not positive, the second segment of the force deformation curve is taken. If now the deformation is larger than the lowest value of the deformation at the new portion of the curve the new portion of the curve is just interpolated. If this is not possible, the maximum force value is taken. If the deformation is smaller than the minimum in the second segment of the force deformation curve and it is not possible to interpolate anymore, the force level is set to zero. This is done since the vehicle has no contact with the barrier anymore.

### 6.2.4 Simulation process

The equations shown in the previous section are written in a Python script which is discussed in this section. Basically, the algorithm of the program is the following.

1. Read input.
2. Initialize mass matrix, deformation vector, force vector.
3. Check if current time is less than the specified simulation time.
4. Calculate position vector of the vehicle's COG and of the spring aligned with the x axis of the local coordinate system.
5. Interpolate the local forces in x and y using the deformation value of the spring in local x and the described interpolation algorithm scheme.
6. Rotate forces from local coordinate system to global coordinate system.
7. Determine moment around vehicle's COG using global forces, position of COG and projection point of A-Pillar on the barrier.
8. Solve for DOFs using the direct approach.
9. Use central difference scheme to compute new values of DOF.
10. Add time increment to current time.

As described in the list, the program in Python works in the following way. First, the required input parameters are read. Then the mass matrix, deformation vector and force vectors are initialized. Then, with a while loop, the simulation process is started where at every time step it is checked if the final specified simulation time has been reached. If the loop is entered the first time, the displacement is calculated using Eq. 6.44. If not, the position vectors of the COG and locations of the pillars of the axial spring are calculated, as shown in the previous section. With the position vectors known, the compression of the axial spring is computed. Next, the forces in x and y are interpolated using the compression value of the axial spring and the algorithm described previously. The forces are then rotated using the angle of the vehicle (in the first time step the angle is zero) to the global coordinate system. Using the global forces, the moment around the COG is computed with the moment arm known from the force application point determined in the vector calculation and the location of the COG. Then the vector $\ddot{q}$, containing the second derivative of the DOFs, is computed using Eq. 6.37. Next, the vector $q$ which contains the DOFs, is calculated using the central difference scheme, shown in Eq. 6.41, Eq. 6.42 and Eq. 6.43. With the new displacements in x and y of the COG and the new rotational angle of the COG, a new iteration loop in the while loop is computed.

## 6.3 Methodology of predictive kinematic model for multiple springs

The kinematic model shown in the previous section is only able to represent the overall stiffness in the x and y direction aligned with the local coordinate system of the vehicle. Since the model is created in order to combine it with an optimization using Monte Carlo sampling with the main aim of finding force deformation corridors of grouped structural components, the predictive kinematic model is extended in this section.

### 6.3.1 Overview

Similar to the previous section, first an overview of the predictive kinematic model using multiple springs is given, see Fig. 6.6. Note that for the sake of visualization, the lower pillar points of the springs in the y direction are not directly on top of the corresponding springs in x direction.

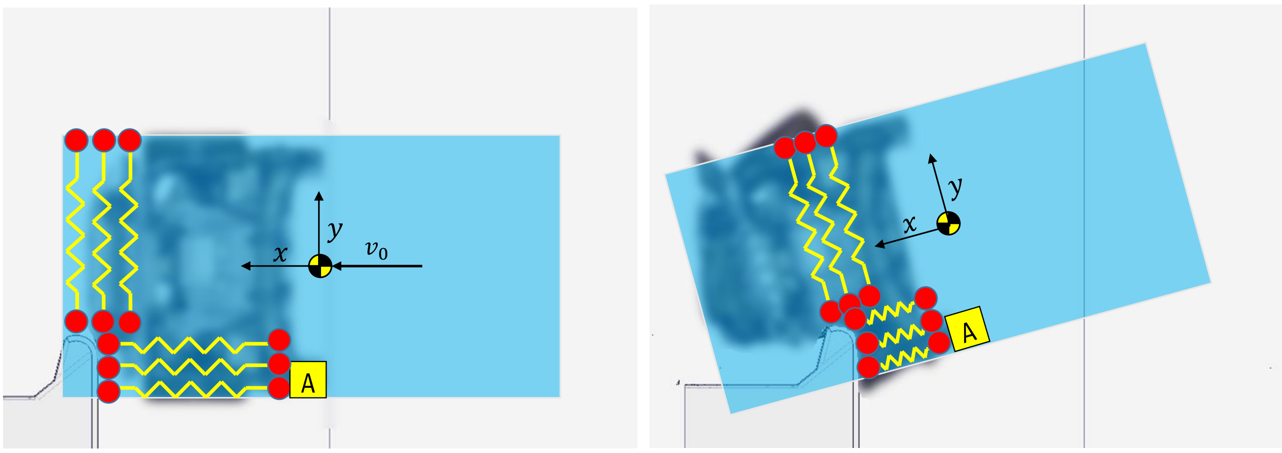


(a) Non-rotated state. (b) Rotated state.

Figure 6.6: Overview of the predictive kinematic model using multiple springs.

As illustrated in Fig. 6.6, the kinematic predictive model consist now out of multiple springs in x and y. Similar to the two springs model, one spring is still attached to the A-Pillar. However, multiple springs in the y direction in case of axial springs and x direction in case of transverse springs are used. Also, although in Fig. 6.6 only the springs in the xy plane are shown, multiple springs on the same y, but different z location can be used in case of axial springs and multiple springs on the same x location, but different z location can be used in case of transverse springs. However, the different z location does not introduce a moment around the x or y axis, as the movement of the COG is considered to be only in the xy plane. The different locations in z are used in order to represent different components. Note that two springs are always coupled together, so one lateral spring is always coupled with one axial spring.

Summarized, the following input variables are used for the predictive kinematic model using multiple springs:

- Position of COG.
- Position of barrier.
- Mass of vehicle.
- Mass moment of inertia of vehicle.
- Location of springs. Note that one spring must be located at the A-Pillar.
- Initial velocity of vehicle.
- Forces in x of springs.
- Forces in y of springs.
- Local deformation of springs in axial direction.

The degrees of freedom of the model are the following:

- Displacement of COG in x.
- Displacement of COG in y.
- Rotation of the vehicle around the z axis of the COG of the vehicle.

Similar to the predictive model consisting out of two springs, several assumptions are made for the predictive kinematic model using multiple springs. The assumptions made on top of the already mentioned assumptions for the previous kinematic model are given below:

- At least one spring must be located at the A-Pillar to determine if the vehicle has glanced-off.
- The summation of forces of the springs is equal to the reaction force of the barrier.
- If there is no projection point of the axial spring with the surface of the barrier in y, the spring does not transfer any forces anymore. This is basically like a switch which differentiate between an active and inactive spring.
- Equal distribution of springs in x and y.

The mathematical formulation of the predictive model using multiple springs is discussed in the following section.

### 6.3.2 Mathematical formulation

The governing EOM of the predictive model using multiple springs is explained best by looking at the idealization of the vehicle shown in Fig. 6.6. Again, note that for the sake of visualization, the lower pillar points of the springs in the y direction are not directly on top of the corresponding springs in x direction. This means that $P4_1$ should lie exactly on $P2_1$, $P4_2$ on $P2_2$ and $P4_3$ on $P2_3$.

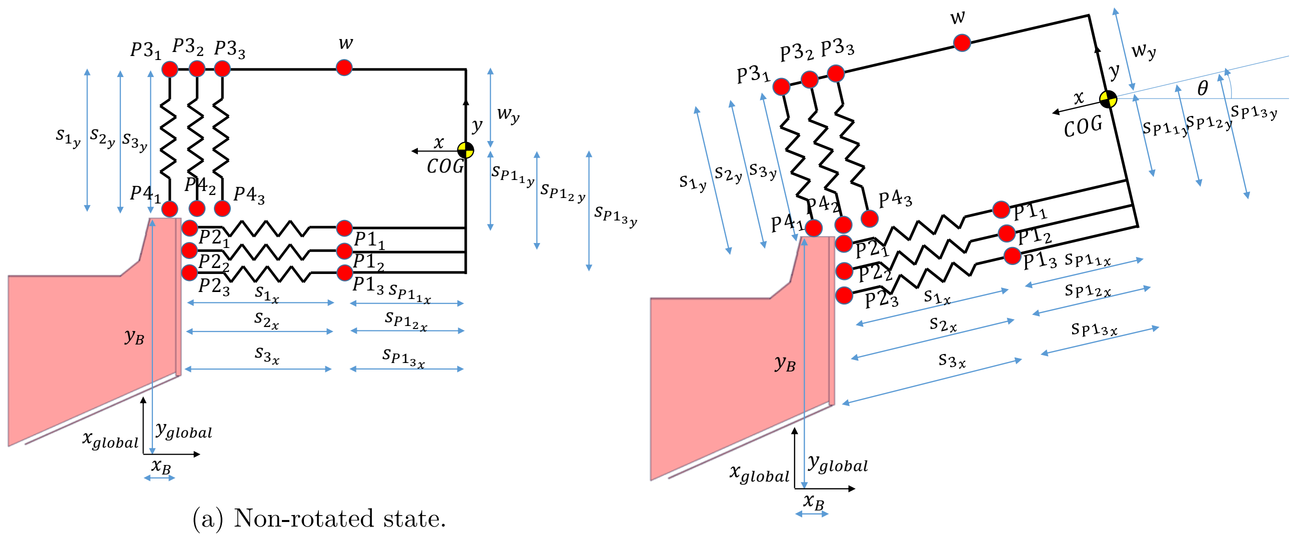


(a) Non-rotated state.

(b) Rotated state.

Figure 6.7: Idealization of predictive kinematic model using multiple springs.

Note that the model is also able to represent multiple springs in the xz plane, as discussed previously. However, the springs are always located in the xy plane and only take up forces in the x and y direction, so no forces in z are represented by the springs and the moment is not affected by the z position of the springs. Nevertheless, these force are negligible anyways, as discussed the numerical investigation of the small overlap crash test, see Chapter 5. Similarly to the previous section, the governing equations for the system are given in the following. Note that the principle is shown for three springs axial and three lateral springs, but the principle holds for any number of springs.

The position of the COG is computed using Eq. 6.9. However, for each spring, the first pillar point of the axial spring is determined as follows, see Eq. 6.47.

$$\underline{r}_{P1_1} = \underline{r}_{COG} + \begin{bmatrix} s_{P1_{1_x}} \cos(\theta) - s_{P1_{1_y}} \sin(\theta) \\ s_{P1_{1_x}} \sin(\theta) + s_{P1_{1_y}} \cos(\theta) \\ 0 \end{bmatrix} \tag{6.47}$$

Similarly, the first pillar point of the two remaining axial springs are determined using Eq. 6.48 and Eq. 6.49.

$$\underline{r}_{P1_2} = \underline{r}_{COG} + \begin{bmatrix} s_{P1_{2_x}} \cos(\theta) - s_{P1_{2_y}} \sin(\theta) \\ s_{P1_{2_x}} \sin(\theta) + s_{P1_{2_y}} \cos(\theta) \\ 0 \end{bmatrix} \tag{6.48}$$

$$\underline{r}_{P1_3} = \underline{r}_{COG} + \begin{bmatrix} s_{P1_{3_x}} \cos(\theta) - s_{P1_{3_y}} \sin(\theta) \\ s_{P1_{3_x}} \sin(\theta) + s_{P1_{3_y}} \cos(\theta) \\ 0 \end{bmatrix} \tag{6.49}$$

The location of the projection of the axial springs onto the barrier are determined using Eq. 6.50, Eq. 6.51 and Eq. 6.52.

$$\underline{r}_{P2_1} = \begin{bmatrix} x_B \\ \tan(\theta) x_B - r_{P1_{1_x}} \tan(\theta) + r_{P1_{1_y}} \\ 0 \end{bmatrix} \tag{6.50}$$

$$\underline{r}_{P2_2} = \begin{bmatrix} x_B \\ \tan(\theta) x_B - r_{P1_{2_x}} \tan(\theta) + r_{P1_{2_y}} \\ 0 \end{bmatrix} \tag{6.51}$$

$$\underline{r}_{P2_3} = \begin{bmatrix} x_B \\ \tan(\theta) x_B - r_{P1_{3_x}} \tan(\theta) + r_{P1_{3_y}} \\ 0 \end{bmatrix} \tag{6.52}$$

Knowing the location of first and second pillar point of the axial springs, the compression $s_{1_x}$, $s_{2_x}$ and $s_{3_x}$ of the axial springs are determined in using Eq. 6.53, Eq. 6.54 and Eq. 6.55.

$$s_{1_x} = \left\| \underline{r}_{P2_1} - \underline{r}_{P1_1} \right\| \tag{6.53}$$

$$s_{2_x} = \left\| \underline{r}_{P2_2} - \underline{r}_{P1_2} \right\| \tag{6.54}$$

$$s_{3_x} = \left\| \underline{r}_{P2_3} - \underline{r}_{P1_3} \right\| \tag{6.55}$$

The global forces are determined as follows, see Eq. 6.56, Eq. 6.57 and Eq. 6.58.

$$\underline{F}_{1_{global}} = \underline{\underline{R}} \begin{bmatrix} F_{1_{x,local}} \\ F_{1_{y,local}} \end{bmatrix} \tag{6.56}$$

$$\underline{F}_{2_{global}} = \underline{\underline{R}} \begin{bmatrix} F_{2_{x,local}} \\ F_{2_{y,local}} \end{bmatrix} \tag{6.57}$$

$$\underline{F}_{3_{global}} = \underline{\underline{R}} \begin{bmatrix} F_{3_{x,local}} \\ F_{3_{y,local}} \end{bmatrix} \tag{6.58}$$

Using the global force, the moment $M_z$ is calculated, using Eq. 6.59.

$$
\begin{aligned}
M_z = & F_{1_{global_x}}(r_{COG_y} - r_{P21_y}) - F_{1_{global_y}}(r_{COG_x} - x_B) \\
& + F_{2_{global_x}}(r_{COG_y} - r_{P22_y}) - F_{2_{global_y}}(r_{COG_x} - x_B) \\
& + F_{3_{global_x}}(r_{COG_y} - r_{P23_y}) - F_{3_{global_y}}(r_{COG_x} - x_B)
\end{aligned} \tag{6.59}
$$

### 6.3.3 Interpolation of force deformation curve

The force deformation curves of the different springs are each interpolated individually. Specifically, each spring in x and corresponding spring in y have their own deformation of the axial spring and corresponding curve. The interpolation itself is done using the same algorithm, as described in the previous section.

### 6.3.4 Simulation process

The equations shown in the previous section are written in a Python script which is discussed in this section. The simulation process itself is quite similar to the algorithm for two springs. However, due to the presence of multiple springs, the algorithm gets a bit more complicated. Basically, the algorithm of the program is the following.

1. Read input.
2. Initialize mass matrix, deformation vector, force vector.
3. Check if current time step is less than final time step.
4. Calculate position of COG.
5. Calculate position vectors of location points of springs.
6. Check if springs are still in contact with the barrier.
7. Interpolate forces in x and y using the deformation values of the corresponding axial spring and the described interpolation algorithm scheme.
8. Rotate forces from local coordinate system to global coordinate system.
9. Determine moment around vehicle's COG using global forces and position of COG.
10. Solve for DOFs using the direct approach.
11. Use central difference scheme to compute new values of DOF.
12. Add time increment to current time.

The algorithm implemented into Python works in the following way. As a first step, the input parameters are read and stored. In the next step, the mass matrix, deformation vector and force vectors are initialized. Next, a while loop is started in which at every time step it is checked if the final specified simulation time has been reached. When the loop is entered the first time, the displacement is calculated using Eq. 6.44. If the loop is not entered for the first time, the position vectors of the COG and locations of the pillars of the axial spring are calculated, as shown in the previous section. With the position vectors known, the compression of the axial springs are calculated. Next, the forces in x and y in the local coordinate system are interpolated using the compression values of the axial springs and the algorithm described previously. The forces are then rotated using the angle of the vehicle to the global coordinate system. Using the global forces, the moment around the COG is computed with the moment arm from each spring computed from the force application points determined in the vector calculation and the location of the COG. Then the vector $\ddot{q}$, containing the second derivative of the DOFs, is computed using Eq. 6.37. Next, the vector $q$ which contains the DOFs, is calculated using the central difference scheme, shown in Eq. 6.41, Eq. 6.42 and Eq. 6.43. With the new displacements in x and y of the COG and the new rotational angle of the COG, a new iteration loop in the while loop is entered.

CHAPTER 7

# Verification and validation of the predictive kinematic model

As with any simplified model which is used to predict the behavior of a real life physical problem, several assumptions must be made. Often, this has the consequence that simplified models are never as accurate as the real life physical problem they are modeling. The same holds for the predictive kinematic model presented in Chapter 6. As mentioned, several assumptions and simplifications are made in the development of the model. Thus, in order to determine the validity and accuracy of the model, it is of vital importance to perform verification and validation measures of the predictive kinematic model which is done in this chapter. First, in Section 7.1 the process of verification of the predictive model is described. Then the validation process is shown in Section 7.2.

## 7.1 Verification of predictive kinematic model

In order to verify the predictive kinematic model, the program implemented into the Python script is checked if there are any syntax and spelling mistakes. Furthermore, all functions are investigated individually and their outputs are checked as well. In addition, the input for the predictive kinematic model is changed such that the resulting output can be inspected and checked if it complies with engineering judgment and results seen in the numerical study. On the one hand, for example, if the local x force of the spring is increased, while all other parameters are the same, the axial movement of the COG of the vehicle should decrease. Similarly, the rotational angle should increase in the CCW direction for this case. On the other hand, when increasing the local y force of the spring and keeping all other input variables constant, the vehicle should glance-off more. This would mean that the lateral movement of the COG of the vehicle should increase.

Several of these cases have been checked with the predictive kinematic model and the result is indeed as expected. Therefore, it is assumed that the predictive kinematic model is verified.

## 7.2 Validation of predictive kinematic model

As the verification alone is not enough to check if the model complies with reality, a validation process must be performed which is done in this section. The validation of the predictive kinematic model is performed using three different configurations of the model consisting out of two springs, 18 springs and 80 springs. The reason for increasing the number of springs is that it is expected to converge towards the results obtained by the FEM simulation. Following the argumentation of the previous chapter, using more springs would increase the accuracy in terms of force application point on the barrier. For each of the different configurations of the predictive kinematic models, three different vehicle models of the BMW AG product line are used. The first vehicle is a sports utility vehicle (SUV), the second one is a mid-size sedan and the third vehicle is a sports car. For each vehicle model, two different full vehicle FEM crash simulation models are used, one which has the lateral translational response and one which has the rotational response. The reason behind the three different vehicles, each with two different responses, is that of checking a broad range of applications of the predictive kinematic model. If the predictive kinematic model is able to match the responses of these three vehicle models, a broad range of applicability is guaranteed. Thus, for each configuration of the predictive kinematic model (two, 18 and 80 springs), six variants are used for the validation.

The structure of this section is the following. First, the methodology of the validation is explained in Subsection 7.2.1. Then, the validation using the two springs configuration of the predictive model is discussed in Subsection 7.2.2. Next, in Subsection 7.2.3, the validation is done for the 18 springs configuration followed by the validation using the 80 springs configuration in Subsection 7.2.4. Finally, the results are combined in a table and it is reflected on the outcome in Subsection 7.2.5.

### 7.2.1 Methodology

As the validation processes of the three different configurations of the predictive kinematic model are similar, the methodology is described centrally in this Subsection. First, the appropriate output variables are determined. Then, the description of the determination of the mass, mass moment of inertia and COG location is given. Next, the creation of the measurement kit is described, followed by the explanation of the barrier force analysis, necessary for the validation when using more than two springs. Finally, the used method to measure the error of the output variables is presented.

#### Output variables

In order to quantitatively compare the kinematics of the vehicle obtained by the predictive kinematic model in comparison to the kinematics obtained by the full vehicle FEM simulation models, output variables need to be determined that can be compared with each other. For the validation, the response mode of the prediction is compared to the FEM simulation model. This is done by comparing the displacement of the COG of the vehicle in x and y in the global coordinate system. In addition, the rotational angle of the COG around the z axis is compared between the kinematic predictive model and the full vehicle FEM crash simulation models. Note that all output variables are normalized, using the same principle as described in Chapter 5 using Eq. 5.2.

#### Determination of the COG location

As the full vehicle FEM simulation models do include the barrier and the road on which the vehicle is traveling on, the value of the mass, mass moment of inertia and the location of the COG in the .pre file of the FEA analysis program Abaqus/Explicit are not of the vehicle solely. Therefore, for all six full vehicle FEM simulation models, the barrier and the road include files are removed and a datacheck run is performed. From the resulting .pre file, the location of the COG, the mass and the mass moment of inertia are retrieved and used for the validation purposes.

#### Measurement kit

The output variables described in the previous subsection are already an output of the predictive kinematic model. In order to obtain these variables from the full vehicle FEM simulation models, a measurement kit is added as an include to the simulation. Similar to the procedure described in Chapter 5, the measurement kit is created. Specifically, three nodes are created where the first one lies exactly on the position of the center of gravity, obtained using the procedure described previously. The two latter nodes are located on a structural part of the rocker opposite to the impacting side of the vehicle. These nodes are used for measuring the angle of the vehicle. On the nodes, connector elements are created and a very small mass and inertia are added on the nodes. Then, accelerometers are placed on the connectors in order to obtain the output variables CP1, CP2 and CP3 which are the coordinates of the COG in x, y and z, respectively. The two nodes located on the rocker are tied to the neighboring nodes using the tie definition in Abaqus/Explicit. Finally, the node located on the cog is attached to the tunnel structure of the vehicle using a rigid connector, as this structural component does not deform much which has been observed in the FEM simulation models.

#### Barrier force analysis

In order to determine the local x and y force for the springs, the contact forces of the barrier are analyzed. From the contact forces of the barrier, given in the global coordinate system, the local forces taken up by the springs are obtained. In order to be able do that, the field output contact force (CFORCE) consisting out of the contact normal force (CNORMF) and the frictional shear force (CSHEARF) must be retrieved from the analysis [61]. For this, the include of the barrier must be changed for all six full vehicle FEM simulation models. Here, the surface output CFORCE must be given as a field output for all surface nodes of the barrier. The surface nodes of the barrier are selected using the program Automatic net generation for structural analysis (ANSA) [72] and are then stored as a node set in the barrier include. With the changed barrier include, the six full vehicle FEM simulation models are simulated in Abaqus/Explicit in order to be able to retrieve the output CFORCE.

Once the simulations of the six FEM vehicle models are finished, the contact force is obtained in the post-processing. For this matter, the post-processing is performed using Python and Animator 4. The reason for this combination is that the output variable CFORCE is only given in the .odb file of the result. Therefore, the CFORCE value can only be retrieved when opening the .odb file with Animator 4. However, since the barrier contact force must be assigned according to the movement of the springs, a script, written in Python, is created. Since the Animator 4 environment is such that the syntax for every action performed in Animator 4 is shown, it is possible to create a session file with the specific tasks Animator 4 has to perform. This means that a session file can be written using Python and the resulting syntax is stored in a session file which is read and executed by Animator 4. In the following, the exact procedure of determining the force each spring takes up is described.

First, the .odb file is opened and the functions CNORMF and CSHEARF are loaded. Next, all elements which have no significant force level are deleted. Then, all nodes with a sufficient force level are selected. These nodes are then stored into a group and their coordinates are stored. Now the script loops over all states of the simulation. For each state, the function values, so CNORMF and CSHEARF are stored for each node. This procedure is done for all three components of CNORMF and CSHEARF, thus six times in total. Now that the function values as a function of time and the location of each node of the barrier are known, the force level must be assigned to the number of springs. For assigning the force levels to the springs, the barrier is divided into patches, depending on the number of springs. As the lateral springs are related to the axial springs and take up the local y force, the patches are determined by the projection of the axial springs onto the barrier. As the spring moves over time, the patches change over time. In order to account for this change in position, the movement and rotation of the COG of the vehicle are read from the .odb file of the simulation. Knowing these values as a function of time, the projection point of the springs at each time step can be determined using Eq. 6.9, Eq. 6.10 and Eq. 6.11. Using the projection values on the barrier, the barrier is divided into patches. This is done by taking the mid distance between two springs as the boundary of the spring. Note that in order for the algorithm to work, if multiple springs are used in the z direction, these springs must have the same y location. An example how the patches move over time for the case of a 18 springs configuration of the predictive kinematic model, as a result of the moving springs over time, is given in Fig. 7.1.

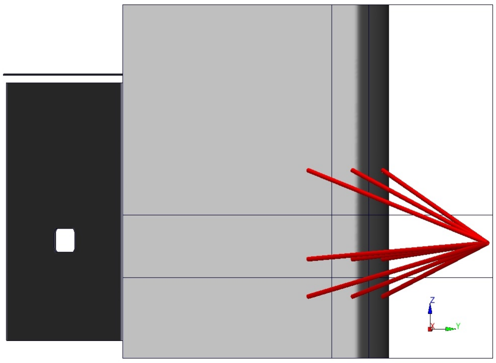

(a) Front view initial.

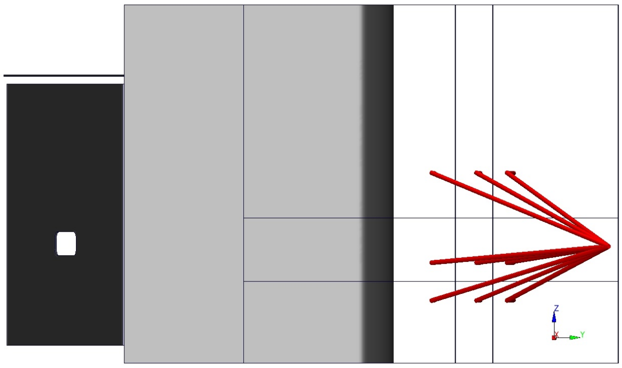

(b) Front view final.

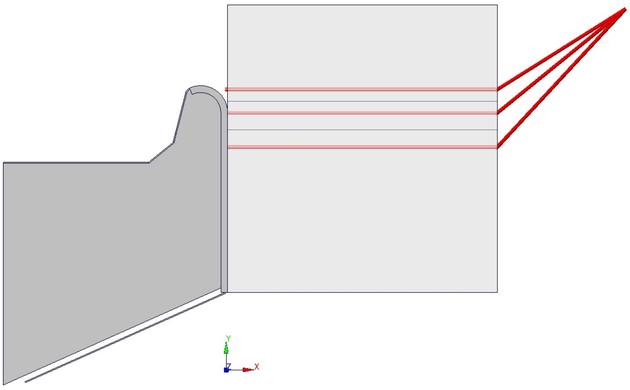

(c) Top view initial.

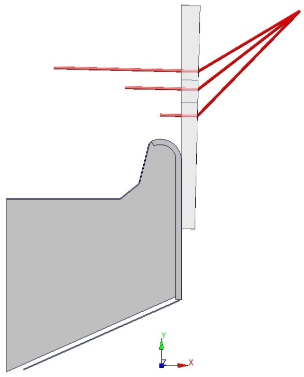

(d) Top view final.

Figure 7.1: Overview of patches on barrier for 18 springs and glance-off concept.

Note that in Fig. 7.1, a glance-off concept is shown. Similarly, for a rotational concept, the following patches are obtained for a 18 springs configuration of the predictive kinematic model, see Fig. 7.2.

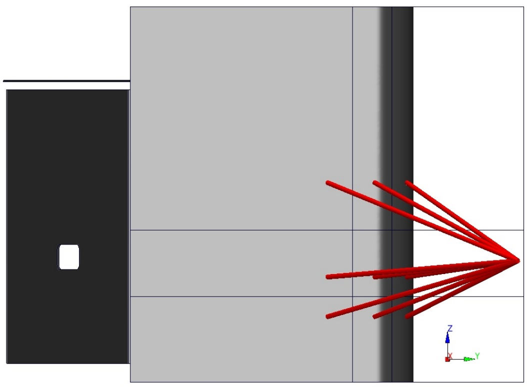

(a) Front view initial.

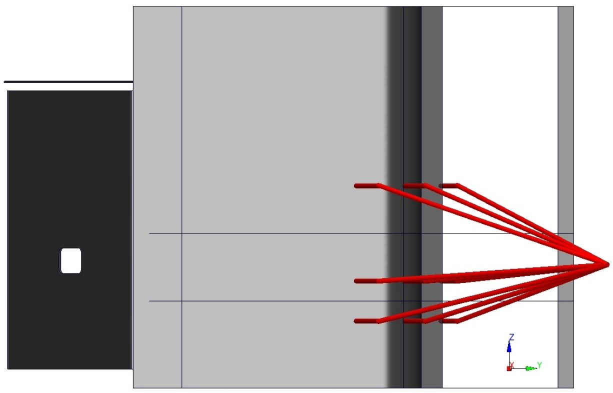

(b) Front view final.

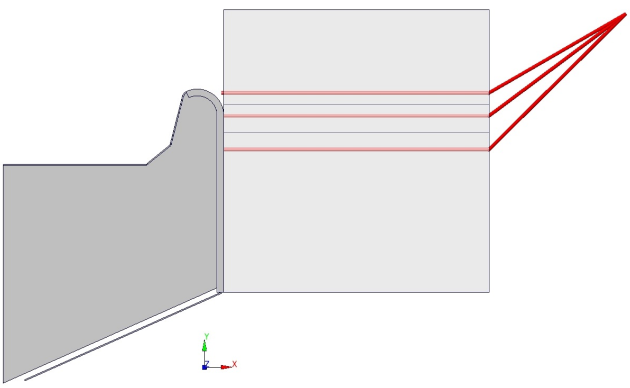

(c) Top view initial.

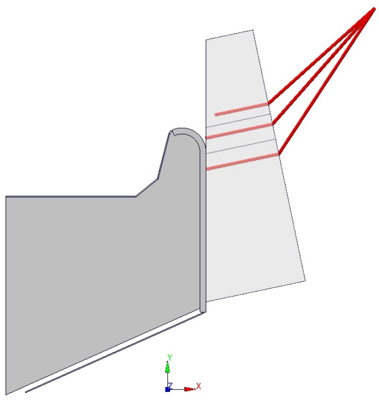

(d) Top view final.

Figure 7.2: Overview of patches on barrier for 18 springs and rotational concept.

From Fig. 7.1 and Fig. 7.2, it can be clearly seen that the patches move over time. Thus in order to find the corresponding force from the stored nodes along with their function values over time, the data must be assigned in the correct way. This is performed in Python by determining the boundaries of every spring at every time step. Knowing the values of the boundaries, for each spring it is looped through the nodes with the function values and if the node lies within the boundaries the value is added to the CNORMF and CSHEARF value of the spring. Finally, after doing that for all springs, the local forces of the spring are determined using the rotational matrix and the CNORMF and SHEARF values. Summarized the barrier analysis follows the following algorithm.

1. Read CNORMF function from .odb file.
2. Loop over all states.
3. Delete nodes which have no significant CNORMF value.
4. Select nodes with sufficient force level on barrier.
5. Store coordinates of nodes along with CNORMF value.
6. End loop when all states are looped through.
7. Loop over all time steps.
8. Obtain vehicle's COG movement and rotational value of COG.
9. Compute projection point of springs onto barrier.
10. Determine boundaries (patches/boxes) of springs of barrier.
11. Store coordinates of boundaries along with time step.
12. Increase time step.
13. Obtain nodes which fall inside the boundaries of each spring.
14. Using the nodes, assign CNORMF values to each spring.
15. Sum up CNORMF values of each spring.
16. Determine forces in x and y of each spring in the local coordinate system.
17. Store resulting forces.

**Mean absolute error of response variables**

As the error between the kinematic predictive model relative to the full vehicle FEM simulation models must be measured to form a judgment in terms of accuracy, an objective measure is required to evaluate the output variables. As discussed previously, the output variables are the displacement of the COG in x and y, as well as the rotational angle of the vehicle around the COG, all in the global coordinate system. As there is the possibility that some of the output variables can be zero or can change in sign (in case of the angle), the mean absolute error (MAE) is taken instead of the mean relative error (MRE). The formula to determine the MAE is shown in Eq. 7.1 [73].

$$MAE = \left[ \frac{1}{n} \sum_{i=1}^{n} |P_i - O_i| \right] \tag{7.1}$$

In Eq. 7.1, $n$ are the number of points, $P_i$ is the $i^{th}$ predicted value and $O_i$ is the $i^{th}$ observed value [73]. All three output variables are compared to the FEM simulation with Eq. 7.1 in order to determine how accurate the predictive kinematic model is. Note that the number of the sampling points $n$ must be the same for the predictive kinematic model and the result of the FEM simulation. Therefore, in cases when the step size of the time is not the same of the two models, the data is first filtered before the MAE is determined using Eq. 7.1.

### 7.2.2 Validation of predictive kinematic model with two springs

Using the procedure described in the methodology section, the two springs configuration of the predictive kinematic model is validated. As the barrier does not need to be divided into patches, the local forces of the springs are just obtained from the reaction forces of the barrier, rotated to the local coordinate system using the rotation matrix. These measured forces are used as an input for the predictive kinematic model. Note that for all the plots in this Subsection and the following Subsections, the blue curves present the results obtained by the FEM crash simulation models and the red curves represent the results determined with the predictive kinematic model. Finally, note that in all plots the value obtained for the MAE is given, calculated using Eq. 7.1.

**SUV**

First, the result of the SUV FEM simulation model compared with the predictive kinematic model using two springs in total, one in the local x and and one in the local y direction, is investigated for a glance-off concept, see Fig. 7.3.

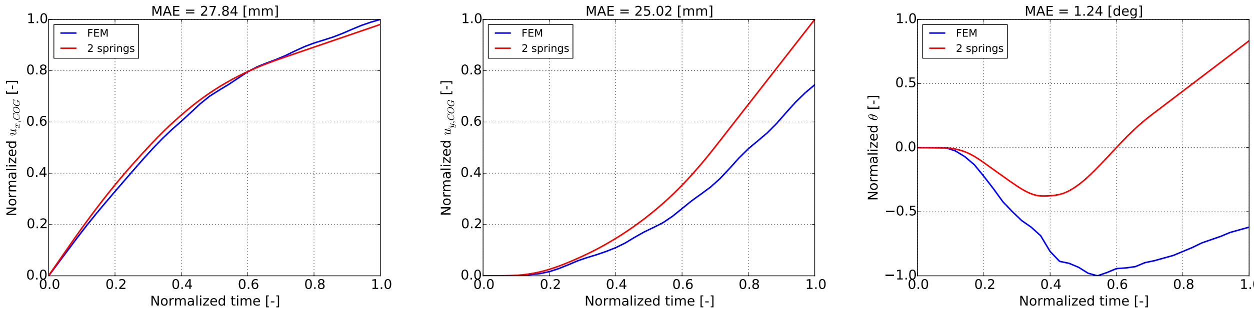


(a) COG displacement in x. (b) COG displacement in y. (c) COG rotation.

Figure 7.3: Model using two springs compared to SUV FEM model with glance-off concept.

From Fig. 7.3, it can be seen that the displacement of the COG in x is estimated very well with the predictive kinematic model with a MAE of 27.8 mm. The curve representing the y displacement of the COG shows a similar trend compared to the FEM simulation of the SUV model, however, above 30% of simulation time, the displacement value diverges from the reference value, resulting in an MAE of 25 mm. The angle shows initially a similar trend, but deviates with increasing simulation time, resulting in a MAE of 1.2 degrees. Note, however, that the plots are normalized and although the relative error might be reasonably high, the absolute error might not be, as seen in the plots.

The rotational behavior of the SUV vehicle is shown in Fig. 7.4.

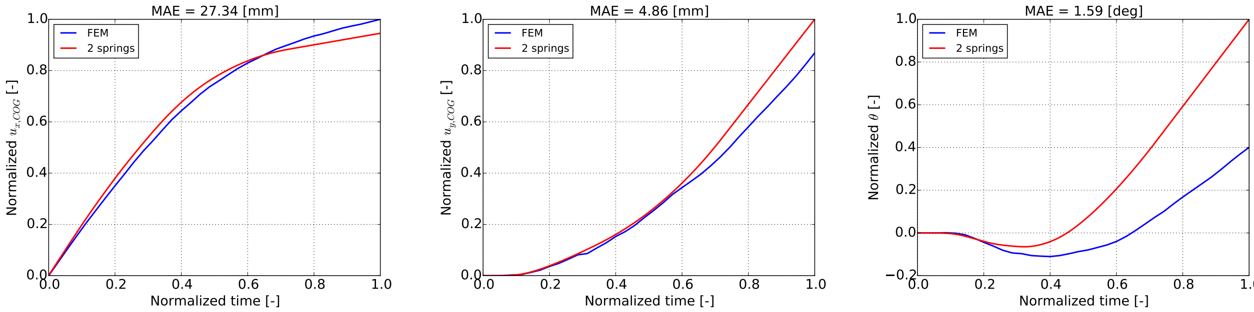


(a) Displacement in x of COG. (b) Displacement in y of COG. (c) Rotation of COG.

Figure 7.4: Model using two springs compared to SUV FEM model with rotational concept.

From Fig. 7.4 it can be seen that the accuracy of the prediction of the COG x displacement is relatively similar compared to the glance-off concept where a MAE of 27.3 mm is obtained. However, the prediction for the y displacement of the COG is better, with a MAE of 4.86 mm. Especially until 0.6 of normalized time, the prediction is very accurate, as seen in Fig. 7.4b. After that point, the two curves diverge. The angle shows again a similar trend and, in contrast to the glancing off model of the SUV, the sign of the angle is also correct. The value for the MAE is relatively similar, namely 1.6 degrees.

**Mid-size sedan**

Now, it is looked at the validation of the predictive model using two springs and a mid-size sedan FEM vehicle model. The response of both models to the glance-off variant of the mid-size sedan is shown in Fig. 7.5.

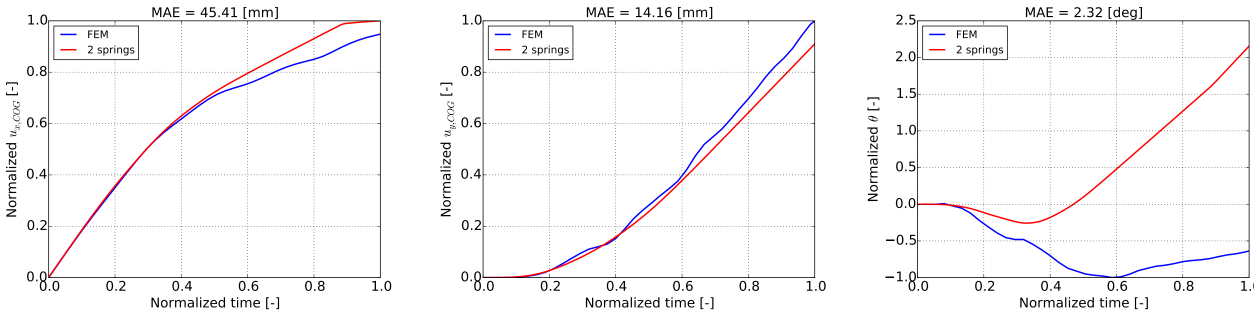


(a) Displacement in x of COG. (b) Displacement in y of COG. (c) Rotation of COG.

Figure 7.5: Model using two springs compared to mid-size sedan FEM model with glance-off concept.

From Fig. 7.5 it can be seen that good correlations between the x and y displacement of the COG are obtained with the predictive kinematic model. Specifically, the MAE for these two output variables are 45.3 and 14.2 mm, respectively. Especially when looking at the x displacement of the COG, a good prediction until 0.5 of the normalized simulation time is obtained. The angle shows, similar to the SUV model, a similar trend at the start of the simulation, but then it increases significantly compared to the FEM simulation, leading to a MAE of 2.3 degrees.

In the following, the rotating response of the mid-size sedan is investigated, as provided in Fig.7.6.

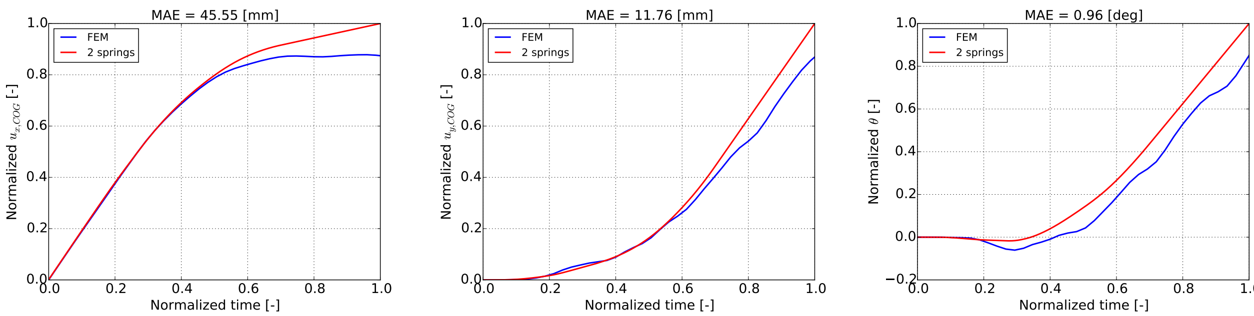


(a) Displacement in x of COG. (b) Displacement in y of COG. (c) Rotation of COG.

Figure 7.6: Model using two springs compared to mid-size sedan FEM model with rotational concept.

Again, a good prediction is obtained for the y displacement of the COG of the vehicle, leading to a value of the MAE of 11.8 mm. The x displacement prediction of the COG is relatively close, especially until 0.5 of the simulation, but then it starts to deviate where a value of 45.6 mm is obtained for the MAE. In addition, the prediction of the angle is close to the FEM simulation and the same shape of the curve is obtained. The value of the MAE for the angle is 1 degree.

### Sports car

For the sports car, first, it is looked at the glancing-off behavior of the sports car to the small overlap crash, simulated with both models, as presented in Fig. 7.7.

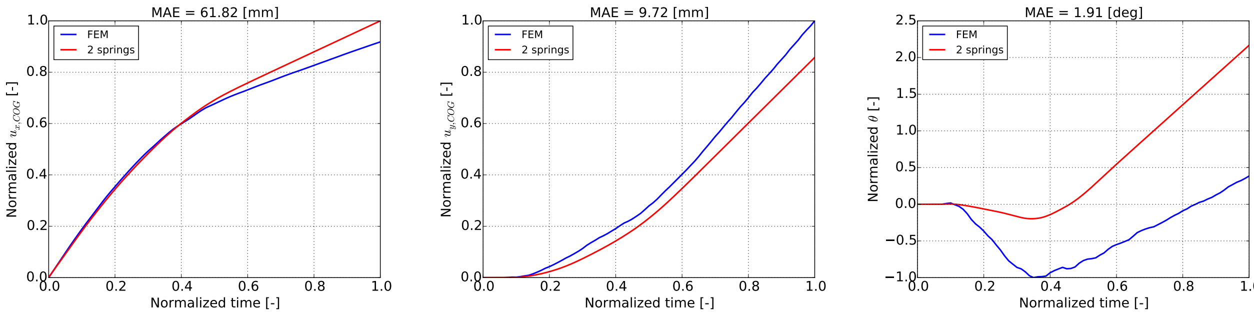


(a) Displacement in x of COG. (b) Displacement in y of COG. (c) Rotation of COG.

Figure 7.7: Model using two springs compared to sports car FEM model with glance-off concept.

Again, the x and y displacement of the COG are predicted reasonably well with the predictive kinematic model. The values of the MAE are 61.8 and 9.7 mm respectively. The angle shows a similar trend as well, but deviates in value from the FEM simulation. For the angle a MAE of 1.9 degrees is obtained.

The comparison for the two models for the rotational response of the sport car is shown in Fig. 7.8

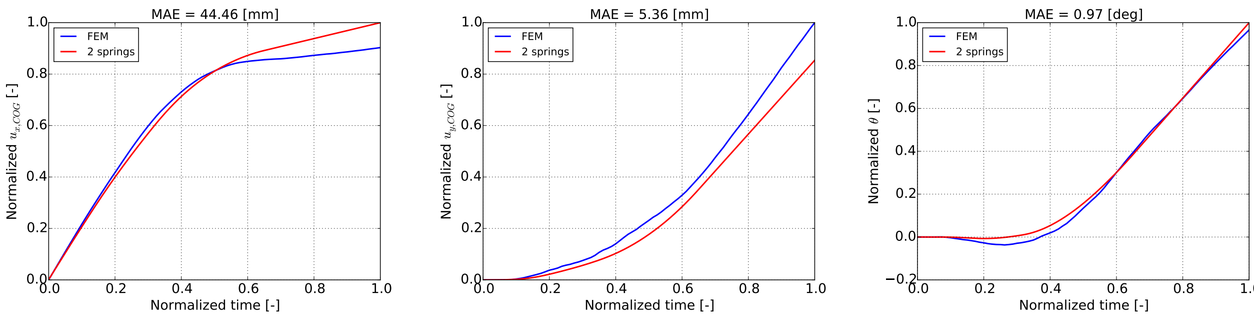


(a) Displacement in x of COG. (b) Displacement in y of COG. (c) Rotation of COG.

Figure 7.8: Model using two springs compared to sports car FEM model with rotational concept.

For all three response variables, a reasonably good fit with the FEM simulation data is obtained. For the x and y displacement of the COG values of 44.5 and 5.36 mm for the MAE are obtained. The angle has a good fit with the FEM simulation data and a value of 1 degree for the MAE is obtained.

### Discussion

The predictive kinematic model using a two springs configuration has been validated using six different models where for each variant three output variables are looked at.

For the x displacement of the COG, the smallest MAE is obtained for the SUV model, followed by the mid-size sedan model and the sports car. The smallest MAE error for the y displacement of the COG is observed for the sports car, followed by the mid-size sedan and the SUV. For the angle, it is observed that the prediction is better for models which glance-off compared to models which rotate. The same holds for a large extend for the y displacement of the COG and to a smaller extend for the x displacement of the COG. When looking back to the FEM simulation models, it can be seen that the rotational variants do experience some deformation behind the A-Pillar location which is not accounted for by the predictive kinematic model. This explains the difference between the x and y displacement after a certain amount of simulation time.

Although the MAE is relatively low for the three output variables, the prediction of the angle, however, was not as accurate as desired. This can be explained by the fact that the angle of the COG is a result of the moment around the COG. As the moment is not only influenced by the forces in x and y, but also by the moment arm, the location of the force application point is of large importance. For the predictive kinematic model, the force application point is the projection of the axial spring onto the surface of the barrier. For a two springs configuration, this projection is influenced to a large extend by the assumed location of the axial spring. The position of the A-Pillar thus has a large role, as its projection point on the barrier along the vehicle's contour is taken as the force application point. Thus depending on where this point is taken, the results differ substantially. When using multiple springs, the benefit does not only lie in the opportunity to design the grouped components according to the necessary force levels, but also in the more accurate force application point. This can be explained by the fact that it is not only one point anymore, but determined by each spring individually. This should give more accurate results in terms of the moment and hence of the angle of the COG.

### 7.2.3 Validation of predictive kinematic model with 18 springs

In this section, the validation of the predictive model using 18 springs is performed. Again, six different FEM simulation variants are looked at and for each variant, three output variables are investigated.

#### SUV

First it is looked at the glancing-off behavior of the SUV model, as shown in Fig 7.9.

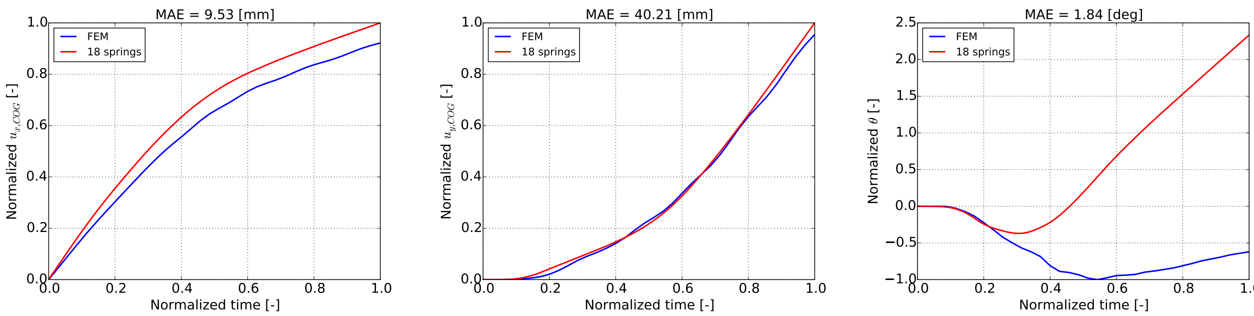


(a) Displacement in x of COG. (b) Displacement in y of COG. (c) Rotation of COG.

Figure 7.9: Model using 18 springs compared to SUV FEM model with glance-off concept.

From Fig. 7.9, a reasonably good match for the x and y displacement of the COG with the reference curve is observed where the values for the MAE are 9.5 and 40.2 mm, respectively. The prediction of the angle until 20% of the simulation is arguably exact, deviates from then on until the end of the simulation time and switches in sign. The value of the MAE for the angle is 1.8 degrees.

Next, it is looked at the rotational concept of the SUV model, as provided in Fig. 7.10.

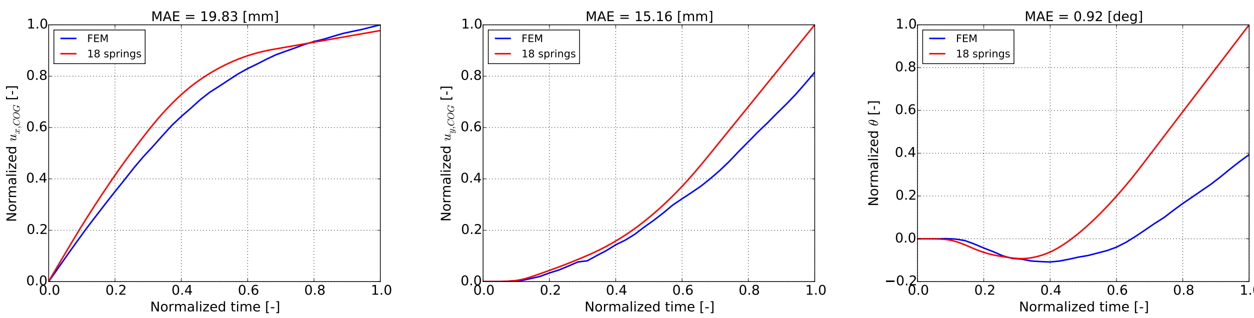


(a) Displacement in x of COG. (b) Displacement in y of COG. (c) Rotation of COG.

Figure 7.10: Model using 18 springs compared to SUV FEM simulation with rotational concept.

Again, the x and y displacement of the COG show good agreement with the FEM simulation result, resulting in a MAE of 19.83 mm and 15.16 mm. For the y displacement of the COG, a relatively good agreement between the two curves until 0.5 of the normalized simulation time is seen. The rotational angle initially shows a good fit with the FEM simulation, however, it diverges as the simulation progresses. The MAE value for the rotational angle is 0.9 degrees.

**Mid-size sedan**

In the following, it is looked at the mid-size sedan variant, as provided in Fig. 7.11 for the glancing-off behavior.

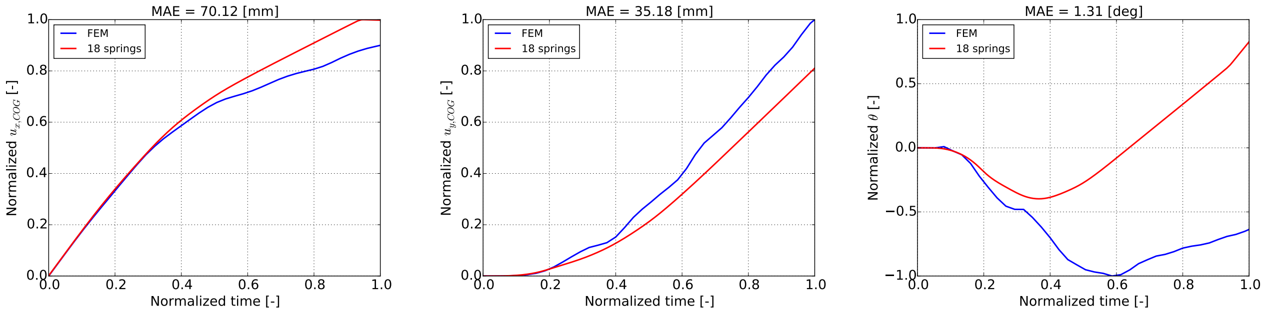


(a) Displacement in x of COG. (b) Displacement in y of COG. (c) Rotation of COG.

Figure 7.11: Model using 18 springs compared to mid-size sedan FEM model with glance-off concept.

The approximation of the x displacement of the COG shows a good correlation with the FEM simulation data until 30% of simulation time, after which the prediction deviates from the simulation, leading to a MAE of 70.1 mm. The y displacement of the COG shows almost the same shape, with a slight offset, resulting in a MAE of 35.18 mm. The rotational angle initially shows the same sign as the FEM simulation, but then after 60% of the simulation time, the result of the predictive model diverges from the FEM simulation. The value of the MAE for the rotational angle is equal to 1.3 degrees.

Next, it is looked at the rotational response of the mid-size sedan, shown in Fig. 7.12.

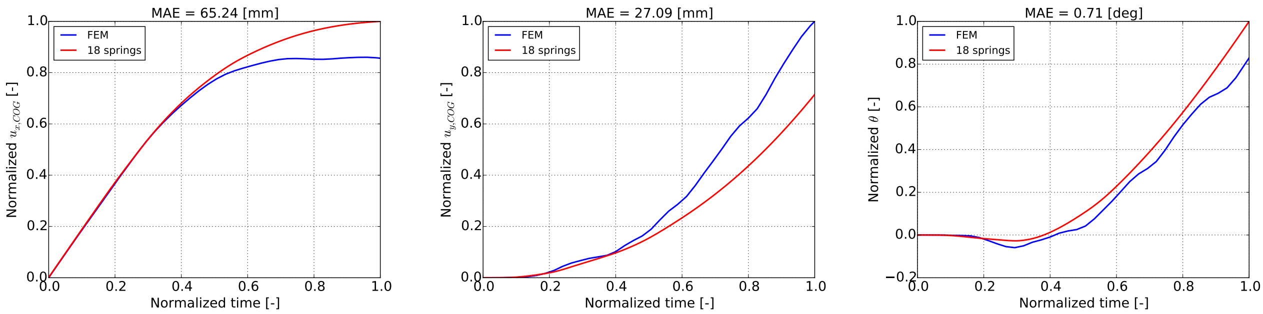


(a) Displacement in x of COG. (b) Displacement in y of COG. (c) Rotation of COG.

Figure 7.12: Model using 18 springs compared to mid-size sedan FEM model with rotational concept.

From Fig. 7.12, a relatively accurate prediction of the x displacement of the COG is observed until 0.5 of the normalized simulation time, after which the prediction is getting worse, resulting in a MAE value of 65.24 mm. Similarly, the prediction of the y displacement is reasonably good until 0.4 of normalized simulation time, after which the predictive model under-predicts the y displacement of the COG. The MAE for the y displacement of the COG is equal to 27.09 mm. The angle shows a good correlation with the FEM simulation data throughout the simulation time, leading to a MAE of 0.71 degrees.

**Sports car**

In the following, the glancing-off variant of the sports car is investigated, see Fig. 7.13.

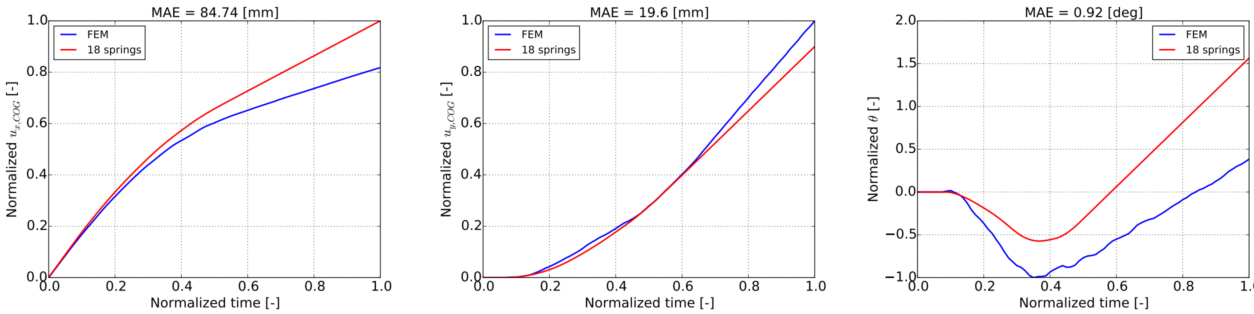


(a) Displacement in x of COG. (b) Displacement in y of COG. (c) Rotation of COG.

Figure 7.13: Model using 18 springs compared to sports car FEM model with glance-off concept.

In Fig. 7.13, the x displacement of the COG is predicted reasonably good until 0.4 of normalized simulation time, after which it is over-predicted. For the x displacement of the COG, the two curves show the same trend and no large deviation is observed. The MAE values of the two response variables are 84.74 and 19.6 mm, respectively. The angle prediction shows the same shape, however due to the offset between the two curves, a MAE of 0.92 is observed.

Next, the rotating variant of the sports car is investigated, see Fig. 7.14.

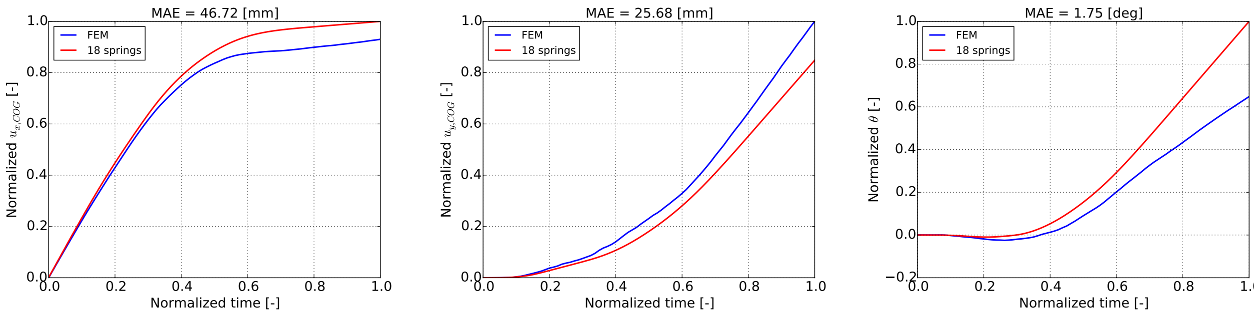


(a) Displacement in x of COG. (b) Displacement in y of COG. (c) Rotation of COG.

Figure 7.14: Model using 18 springs compared to sports car FEM model with rotational concept.

Until 0.4 of normalized simulation time, the prediction of the kinematic model is reasonably well for the x displacement of the COG, after which an over-prediction is seen, leading to a MAE of 46.72 mm. The y displacements of the COG for the FEM simulation and the predictive kinematic model show the same shape, although the predictive kinematic model is under-predicting the the target data a bit. This means that a value of 25.68 mm is obtained for the y displacement of the COG. The angle shows a similar shape compared to the FEM simulation data, only after 0.4 of normalized simulation time, the predictive model seems to over-predict the rotational angle. The resulting value for the MAE is equal to 1.75 degrees.

**Discussion**

Now that the six variants of the FEM simulation models have been compared to the results obtained with the predictive kinematic model using 18 springs some observations can be made.

Similar to the two springs configuration, the smallest MAE values are obtained for the SUV, followed by the sports car and the mid-size sedan. For the y displacement of the COG, the prediction is the best for the sports car, followed by the SUV and the mid-size sedan. Similar to the previous case, the offset for the x and y displacement of the COG can be explained by looking at the FEM simulation, where some deformation of the structure behind the A-Pillar occurs.

Comparing the 18 springs configuration to the two springs configuration, the angle prediction is better when using more springs. This confirms the previous argumentation that more springs leads to a better approximation in force application point. In the next Subsection, it is seen if it is possible to be more accurate in terms of predicting the rotational angle by using 80 springs for the predictive kinematic model.

### 7.2.4 Validation of predictive kinematic model with 80 springs

Finally, the validation is performed using the predictive kinematic model with 80 springs. First, it is looked at the SUV variant, followed by the mid-size sedan and the sports car.

#### SUV

The results for the three output variables as a function of time for the glancing-off behavior of the SUV model are shown in Fig. 7.15.

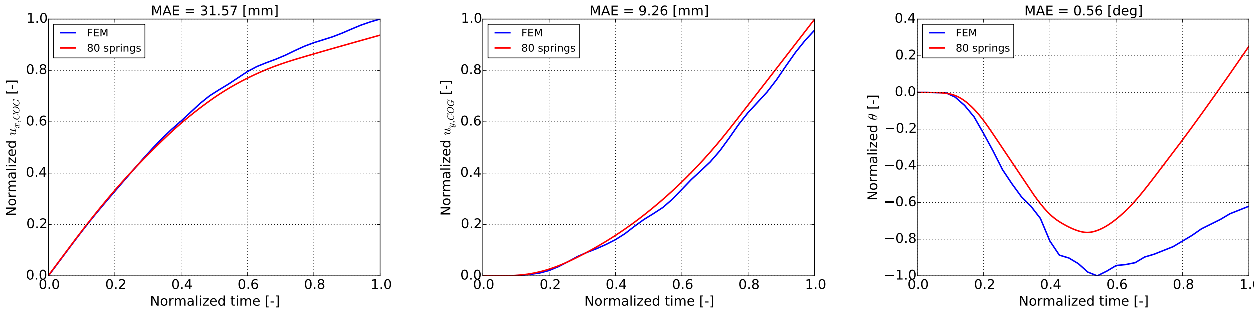


(a) Displacement in x of COG. (b) Displacement in y of COG. (c) Rotation of COG.

Figure 7.15: Model using 80 springs compared to SUV FEM model with glance-off concept.

From Fig. 7.15, it can be seen that the prediction of the kinematic model is reasonably accurate for the x and y displacement of the COG, where values of 31.57 and 9.26 mm are obtained for the MAE. The angle shows also a good agreement for the first 0.4 simulation time. However, then the curve deviates from the FEM result, resulting in a MAE value of 0.56.

Next, is is looked at the rotational response of the SUV FEM model, as shown in Fig. 7.16.

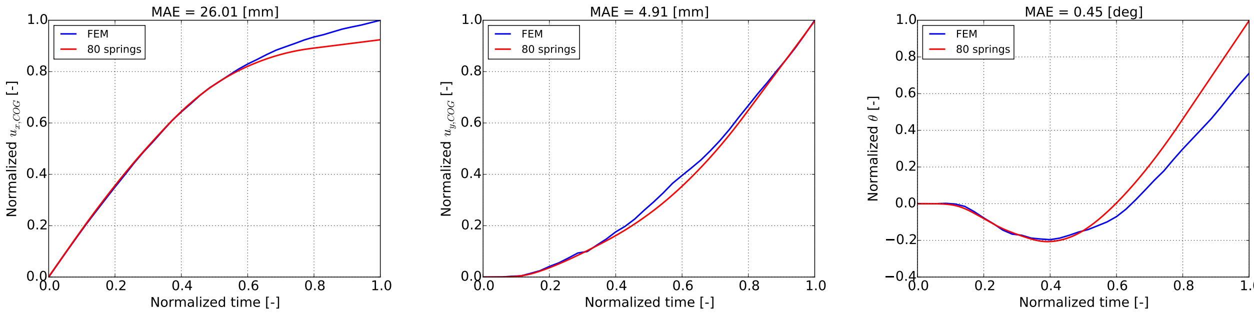


(a) Displacement in x of COG. (b) Displacement in y of COG. (c) Rotation of COG.

Figure 7.16: Model using 80 springs compared to SUV FEM model with rotational concept.

When looking at Fig. 7.16, it can be seen that the fit of the three output variables is reasonably well. For the displacement in x of the COG, the fit is accurate until 0.6 of simulation time, after which the predictive kinematic model under-predicts the FEM simulation, leading to a MAE of 26.01 mm. For the y displacement of the COG, the two curves almost lie on top of each other, resulting in a MAE of 4.91 mm. The angle of the COG is estimated reasonably well, especially until 0.4 of the normalized simulation time. After that point, the predictive kinematic model over-predicts the rotational angle where a value of 0.45 degrees is obtained for the MAE.

#### Mid-size sedan

The results for the glancing-off variant of the mid-size sedan model are provided in Fig. 7.17.

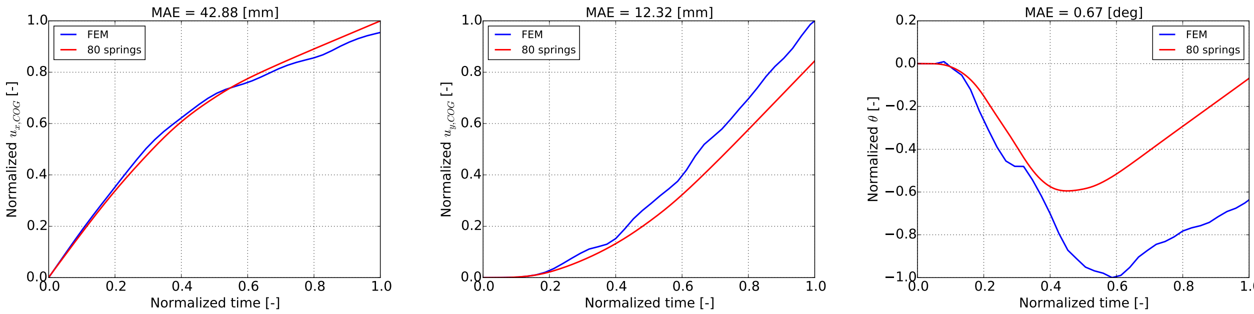


(a) Displacement in x of COG.
(b) Displacement in y of COG.
(c) Rotation of COG.

Figure 7.17: Model using 80 springs compared to mid-size sedan FEM model with glance-off concept.

Again, the agreement between the predictive kinematic model and the x, as well as y displacement of the COG are rather good, where the MAE values are 42.88 and 12.32 mm, respectively. The predicted angle has the same sign and a value of 0.67 degrees is obtained for the MAE.

Next, it is looked at the rotational variant of the mid-size sedan FEM simulation model, see Fig. 7.18.

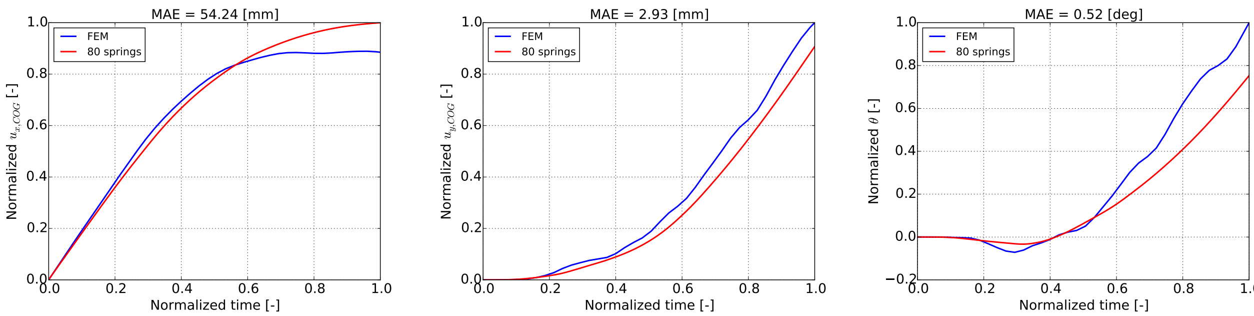


(a) Displacement in x of COG.
(b) Displacement in y of COG.
(c) Rotation of COG.

Figure 7.18: Model using 80 springs compared to mid-size sedan FEM model with rotational concept.

The displacement in x of the COG is over-predicted from 60% of the complete simulation time onwards, before which the fit is reasonably well. The y displacement of the COG shows also a relatively good accuracy, although the predictive kinematic model under-predicts the y displacement. The values of the MAE are 54.24 and 2.93 mm, respectively. The rotational angle of the predictive kinematic model shows a similar shape compared to the FEM simulation data and is not far off until 0.5 of the normalized simulation time. The MAE value for the angle is 0.52 degrees.

**Sports car**

Finally, it is looked at the sports car variant. Specifically, the glancing-off behavior of the sport car FEM simulation is investigated, as shown in Fig. 7.19.

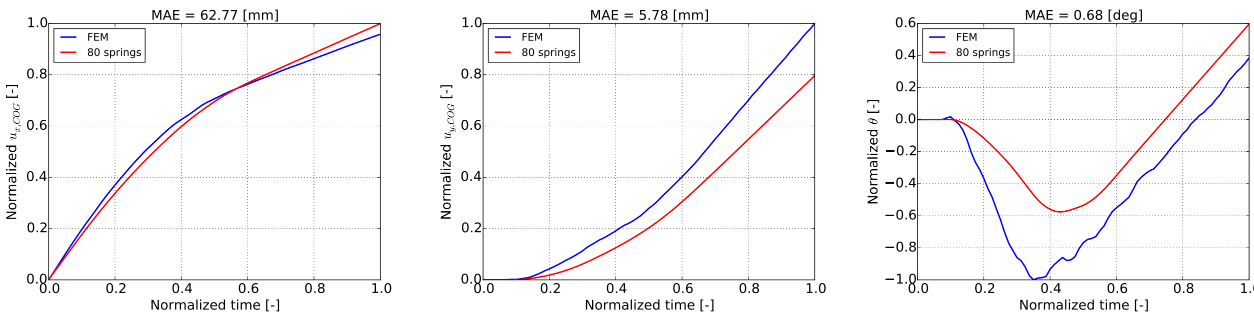


(a) Displacement in x of COG.
(b) Displacement in y of COG.
(c) Rotation of COG.

Figure 7.19: Model using 80 springs compared to sports car FEM model with glance-off concept.

The x displacement of the COG shows not much deviation from the FEM simulation, resulting in a MAE of 62.77 mm. The y displacement of the COG is under-predicted, as is the angle of the COG. These two output variables have a value of 5.78 mm and 0.68 degrees for the MAE. However, the shape of the curves are relatively comparable to the benchmark.

Finally, it is looked at is the sports car variant with the rotational concept which is predicted using an 80 springs configuration, see Fig. 7.20.

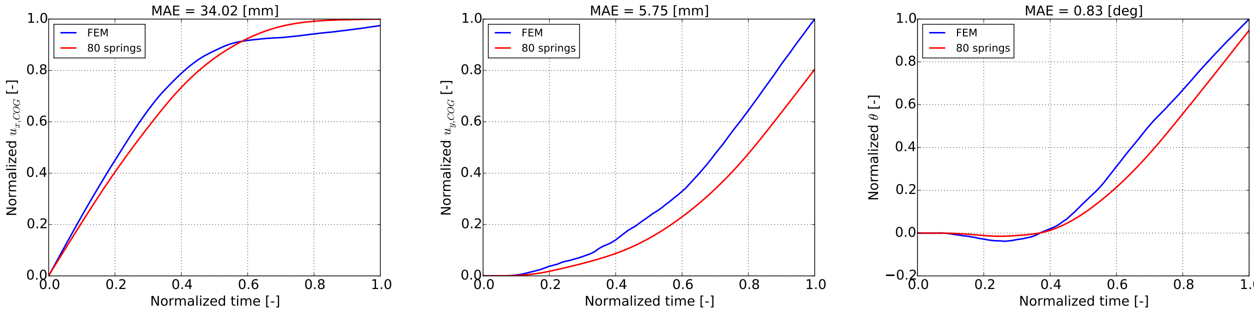


(a) Displacement in x of COG. (b) Displacement in y of COG. (c) Rotation of COG.

Figure 7.20: Model using 80 springs compared to sports car FEM model with rotational concept.

Looking at Fig. 7.20, it can be seen that the general shape of the curves which represent the three output variables are very similar to the FEM simulation. However, in terms of x displacement of the COG over time, the value is first under-predicted and then, approximately at 0.55 of normalized simulation time, the value of x displacement of the COG is over predicted, leading to a MAE value of 34.02 mm. For the y displacement of the COG, the curve lies below the FEM simulation, but the trend is the same and the MAE value is equal to 5.75 mm. The angle, shown in Fig. 7.20c, is approximated quite well using the 80 springs configuration of the predictive kinematic model, resulting into a value of 0.83 degrees for the MAE.

**Discussion**

From the 80 springs configuration of the predictive kinematic model, several observations are made.

As expected, using more springs results into more accurate predictions of the rotational angle of the COG. This seems to be intuitive, since more springs distribute the force location point along the barrier and since each spring has allocated the force from the barrier obtained by the barrier analysis, the force application point is estimated more accurately. In addition, compared to the 18 springs configuration, the prediction of the x and y displacements of the COG are more accurate in terms of MAE.

Similar to the previous argumentation, the offset in the x and y displacement of the COG can be explained by deformations observed in the structure behind the A-Pillar of the FEM simulation models.

Overall, the 80 springs configuration proves that by using more springs, also the approximation of the angle gets better.

### 7.2.5 Summarized results and discussion

In order to obtain a quantitative measure of how well the predictive model estimates the kinematic response of the vehicle, the MAE, determined using Eq. 7.1, is shown in Tab. 7.1 for all six variants compared to the FEM simulation models. Note that for all responses of the six variants, the three different configurations of the predictive kinematic model are plotted together in the Appendix for means of visualization and comparison between the different models.

Table 7.1: Mean absolute error of output variables.

| *Variant* | *# of springs* | $u_{x,COG}$[mm] | $u_{y,COG}$[mm] | $\theta$[deg] |
|---|---|---|---|---|
| SUV glance-off | 2 | 27.84 | 25.02 | 1.24 |
| SUV glance-off | 18 | 9.53 | 40.21 | 1.84 |
| SUV glance-off | 80 | 31.57 | 9.26 | 0.56 |
| SUV rotation | 2 | 27.34 | 4.86 | 1.59 |
| SUV rotation | 18 | 19.83 | 15.16 | 0.92 |
| SUV rotation | 80 | 26.01 | 4.91 | 0.45 |
| Mid-size sedan glance-off | 2 | 45.41 | 14.16 | 2.32 |
| Mid-size sedan glance-off | 18 | 70.12 | 35.18 | 1.31 |
| Mid-size sedan glance-off | 80 | 42.88 | 12.32 | 0.67 |
| Mid-size sedan rotation | 2 | 45.55 | 11.76 | 0.96 |
| Mid-size sedan rotation | 18 | 65.24 | 27.09 | 0.71 |
| Mid-size sedan rotation | 80 | 54.24 | 2.93 | 0.52 |
| Sports car glance-off | 2 | 61.82 | 9.72 | 1.91 |
| Sports car glance-off | 18 | 84.74 | 19.6 | 0.92 |
| Sports car glance-off | 80 | 62.77 | 5.78 | 0.68 |
| Sports car rotation | 2 | 44.46 | 5.36 | 0.97 |
| Sports car rotation | 18 | 46.72 | 25.68 | 1.75 |
| Sports car rotation | 80 | 34.02 | 5.75 | 0.83 |

Looking at Tab. 7.1, several observations can be made. First of all, it becomes clear that, in terms of averaged absolute values, the predictive kinematic model does not deviate a lot from the FEM simulation model. The largest MAE values for the three output values are 84.74 mm and 40.21 mm for the x and y displacement of the COG respectively and 2.32 degrees for the rotational angle.

Next, it can be seen when looking at the angle of the COG, the more springs are used the better the approximation of the FEM simulation is. For the x displacement of the COG, $u_{x,COG}$, the picture is not that clear. For three out of six variants, the best approximation of the FEM simulation is obtained using 80 springs. However, only for one case, the SUV rotation response, the configuration of the predictive kinematic model using 18 springs provides the smallest error. For the remaining two cases, the configuration using two springs provided the best results. Similarly, for the displacement in y of the COG, three variants using 80 springs provide the best result in terms of smallest MAE. Nevertheless, it should be noted that the overall values for the MAE of the displacement in x and y are rather small for all variants and all configurations of the predictive kinematic model. Also, it should be underlined that the location of the springs has an important influence on the result. This explains why the 18 springs model is not necessarily better than the two springs model. As the projection point of the springs are used for assigning the forces, choosing the right location is an important step in using the predictive kinematic model. Thus when the force application point does not move much in time and the approximation of taking only the A-Pillar projection onto the barrier is correct, rather good results are obtained with the two springs configuration of the predictive model.

Summarized, it can be noted that the predictive kinematic model, despite being an approximation and idealization, is able to predict the response of the vehicle and therefore can be assumed to be validated. Especially when looking at the magnitude of the MAE in comparison with the overlap width of the vehicle with the barrier, the accuracy of the model is really good. For a normal vehicle of approximately 1.8 m width, this would give an overlap width with the rigid barrier of 450 mm. From Tab. 7.1 it can be seen that the largest MAE value for the y displacement of the COG is 40.21 mm which is approximately 9% of the total overlap width. Finally, it should be noted that the most critical point in the prediction of the kinematics is the time when the A-Pillar of the vehicle reaches the barrier, as this determines if the vehicle glances-off or rotates around the barrier. Since this moment in time is before the end of the simulation, the error should be even smaller than the worst case previously mentioned, meaning that the accuracy of the model is relatively good, especially when used in the early development phase where little information about the exact geometry is known anyways.

The verification and validation of the model are important steps, since having a verified and validated model is a prerequisite for generating force deformation solution spaces of grouped structural components which is presented in the next chapter of the thesis.

# CHAPTER 8

## Force deformation solution corridors obtained with the predictive kinematic model

In this chapter, the force deformation solution corridors obtained with the predictive kinematic model are presented. First, in Section 8.1, the methodology is discussed. Then, the results of the force deformation solution corridors for a two springs and a ten springs configuration of the predictive model are shown in Section 8.2, 8.3, 8.4, 8.5, 8.6 and 8.7, respectively. Finally, in Section 8.8, a summary on the results is presented.

## 8.1 Methodology

First, a generic description for obtaining the force deformation solution corridors for the small overlap crash test is presented in this section. Note that the theory behind the force deformation corridors is presented in Chapter 4. The methodology section is divided into the description of the inputs, the description of the constraint variables and the description of the pre-processing.

### 8.1.1 Inputs

Basically, the force deformation solution space tool at BMW AG requires the following inputs.

- Upper and lower design bounds of the forces in x and y in the local coordinate system.
- Definition of the deformation pillar points of the axial springs.
- Objective/constraint functions in order to evaluate if the outcome is a feasible design.
- Predictive kinematic model script which has a certain required syntax for the outcome file.
- Number of sampling points.
- Number of steps in the exploration and consolidation phase.

With the help of the inputs and settings, the working principles and the reasoning behind the choices is explained in the following.

The upper and lower bounds of the solution space must be implemented, as the tool searches withing these design bounds for feasible design options. The design bounds are obtained from setting achievable and realistic local x and y force levels. Realistic and achievable in the sense that not every force level can be obtained at any deformation length. For example, during the first portion of the deformation, the amount of achievable stiffness and strength of components which are in contact with the barrier is limited. The forces at the first portion of the deformation are due to the deformation of bumpers, headlamps and radiators. These components are not able to carry high loads and hence the upper force levels can not be arbitrarily high. Then, after some significant amount of deformation, the wheel is in contact with the barrier, representing a component with high force levels and therefore the upper design bound of the local force in x and y can be increased for the design space. The start and end value of deformation for each spring is derived from the location of the represented component in the vehicle respectively.

### 8.1.2 Constraint variables

The optimizer tool at BMW AG uses so called constraint variables in order to determine which sampling points are feasible design solutions. For obtaining the force deformation solution spaces, the following constraint variables, as listed below, are used.

- $s_L$.
- $AbWAP$.
- $AbWP$.

The three constraints $s_L$, $AbWAP$ and $AbWP$ are defined in Eq. 8.1, Eq. 8.2 and Eq. 8.3.

$$s_L = \text{final length of the most outboard spring} \tag{8.1}$$

$$AbWAP = \frac{\text{y movement of A-Pillar with respect to original location}}{\text{overlap between barrier and vehicle}} \tag{8.2}$$

$$AbWP = \frac{\text{y movement of projected A-Pillar location on barrier with respect to original location}}{\text{overlap between barrier and vehicle}} \tag{8.3}$$

The choice of these three constraints is explained by the fact that it is desirable to obtain force deformation solution corridors for each of the two possible responses of the vehicle subjected to the small overlap crash. It is important to emphasize that the constraints do not enforce the tool to optimize towards a certain response, rather the response is categorized with these constraints. The optimization itself is the maximization of the width of the corridors. In the following, the three constraint variables are explained in more detail by describing the responses obtained by the variables.

**Rotating and glancing-off response**

For the case that there is no preference on the response of the vehicle, the constraint $s_L$ is taken. The variable $s_L$ is taken as a constraint due to the following reason. As the spring is located at the A-Pillar, a spring of zero length at the end of the simulation would mean that the complete structure would have been deformed until the A-Pillar. However, for this model, it is not wanted to have intrusions until the A-Pillar, but rather until some chosen point before that. Therefore, some remaining length of the spring at the end of the simulation must be imposed as constraint for finding the force deformation solution space corridors. This constraint is such that the value of $s_L$ must be larger than the distance between the A-Pillar location and the firewall. By imposing this constraint for the optimization tool, the outcome will be force deformation solution corridors which have no intrusions into the passenger compartment, so all solutions are feasible designs in terms of crashworthiness. However, no distinction is made between the rotational and glancing-off response of the vehicle and therefore both responses are possible design options in the solution space.

**Rotating response**

For obtaining the rotating response, the value of $AbWP$ should be smaller than 1. This would mean that the A-Pillar of the vehicle does not pass the barrier. Note, however, that this does only hold if the rotational angle of the vehicle is less than 90 degrees. As any intrusions into the passenger compartment are not allowed, the constraint of $s_L$ is imposed as well. This would then give force deformation solution corridors for the rotational response concept for the small overlap crash.

**Glancing-off response**

In order to obtain the glancing-off behavior, $AbWAP$ and $AbWP$ should be both larger than 1. This would mean that the A-Pillar does pass the barrier. The reason for using both the projection and the position of the A-Pillar is the following. It could be the case that the A-Pillar does pass the barrier, even though the vehicle does not. This is the case when the vehicle almost glanced-off and a large positive (so CCW) angle is observed. The rotation increases the y movement of the A-Pillar, but the lateral displacement of the COG does not increase. In addition, it has been investigated that the $AbWP$ constraint delivers more robust solutions for positive angles where the $AbWAP$ constraint devlivers more robust solutions for negative angles. On top of these constraints, the $s_L$ constraint is used as well, in order to avoid any intrusions into the passenger compartment. This optimization would then give as an output force deformation solution corridors which follow the glancing-off design principle.

### 8.1.3 Pre-processing

In order to obtain the force deformation solution corridors, the optimization tool at BMW AG calls the predictive kinematic model script. The script must be programmed such that it generates after each run an .out file in which the values of the calculated objective variables using the input selected by the optimizer are stored. The values of three objective variables are read by the optimizer in order to check if the sampling point is a feasible design.

In order to set up the optimization, the amount of sampling points of the Monte Carlo sampling method must be chosen. As discussed in Chapter 4, 100 sampling points would be sufficient for failure probabilities which are between 1 to 10% and while having a confidence interval of $\pm$ 10% at a 95% confidence level [64]. However, after performing the first optimizations, this value was increased to 200 in order to ensure convergence and in order to increase the confidence interval. Also, the tool requires the number of performed exploration and consolidation steps. For these values, it has been found out that 100 steps are conservative enough in order to obtain results which are converged.

The constant input for the predictive kinematic model is stored in a configuration file where the mass, mass moment of inertia, location of COG, location of nodes to measure the angle off the vehicle, name of the run and location of the springs are stored. When using only two springs, the location of the axial spring must be at the location of the A-Pillar, as discussed in Chapter 6. When using more than two springs, the location of the springs must be such that they represent the grouped components in an accurate matter. The location of the springs for the ten springs configuration of the predictive kinematic model is discussed in Section 8.5.

Using these settings, the solution corridors are determined using a two spring configuration of the kinematic model and a ten spring configuration of the predictive kinematic model. As for each configuration, three different cases are determined with the optimization, six runs in total are performed using the BMW AG optimizer tool. In the following Sections, the resulting force deformation solution spaces are presented.

## 8.2 Force deformation corridors with two springs kinematic model

In this section, the force deformation corridors with no preference on the response mode obtained with the two springs predictive kinematic model are presented.

### 8.2.1 Input parameters

For starting the optimization, the mass of the vehicle, mass moment of inertia, location of COG, location of spring and the location of nodes for obtaining the angle of the vehicle are stored in the configuration file. The deformation length of the spring in the x direction is discretized using nine discretization points. For each of these discretization points a lower and an upper bound is given for the x and y force respectively.

### 8.2.2 Optimization parameters

For this optimization, it is not looked at a specific response of the vehicle. Instead, the limitation of the intrusion into the passenger compartment is set as an constraint. Therefore, the constraint variable is that $s_L$ must be larger than the distance between the location of the spring and the firewall. The number of sampling points is set to 200 and the steps in the exploration and consolidation phase are set to 100.

### 8.2.3 Force deformation corridors

Using the specified input and optimization parameters, the following force deformation corridors are obtained, as shown in Fig. 8.1. Note that the blue lines in the plots indicate the upper and lower force level bounds used at the nine discretization points for the deformation of the axial spring. In addition note that although the boundaries have the same shape, this does not necessarily mean that both curves have the same values. The jump after a normalized deformation of 0.2 is due to the possible increase in force by using stiffer and stronger components. As a final note, due to the constraint of the final deformation length of the spring ($s_L$), the last discretization point of the deformation of the axial spring is not achieved by the vehicle. Therefore, the last portion of the curve from 0.8 of normalized deformation onwards should be interpreted with care. This comes from the fact that the optimizer tool tries to maximize the area of the force deformation solution space as much as possible and hence larger design spaces are possible in this region.

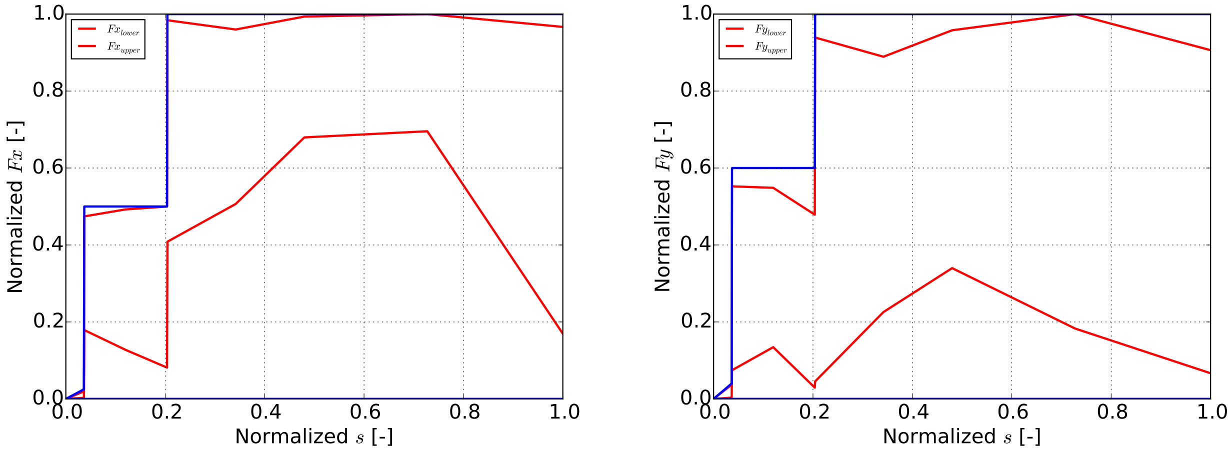


(a) $F_x$.

(b) $F_y$.

Figure 8.1: Force deformation corridors of predictive kinematic model with two springs.

Comparing the boundaries for the upper and lower force level for the x force in Fig. 8.1a with the obtained solution, it can be seen that after 0.2 of normalized deformation, the lower force level increases rapidly to almost 70% of the maximum normalized achievable force. The upper force level is almost at the maximum achievable force level. Looking at Fig. 8.1b, it can be seen that the upper force level is slightly lower than given by the upper design boundary. In addition, the lower force level is relatively low compared to the upper force level (maximum of 30% of normalized maximum achievable force level).

### 8.2.4 Discussion

The results obtained for the force deformation solution spaces with the constraint of the axial spring that no intrusion into the occupant compartment is guaranteed, complies with engineering judgment, as the minimum force in x is reasonably high. This high level of x force is required in order to ensure that the intrusion is not too large. As the constraint does not pre-describe the model which response is preferred, the predictive kinematic model has either the possibility to obtain a glancing-off or rotating response mode. The former can be achieved by a high y force and low x force while the latter can be achieved by using a high x force and low y force.

## 8.3 Rotational response force deformation corridors with two springs kinematic model

In this section, the force deformation corridors using the two springs configuration for a rotational concept is presented.

### 8.3.1 Input parameters

Similar to the previous optimization, the input parameters must be implemented. The same values for the mass of the vehicle, mass moment of inertia, location of COG, location of spring and the location of nodes for obtaining the angle of the vehicle are used. The same number of discretization points for the deformation length of the spring is implemented.

### 8.3.2 Optimization parameters

In contrast to the previous optimization, it is looked at a specific response of the vehicle, being the rotational response. Therefore, the constraint variables are the constraint that $s_L$ must be such that no intrusion in the passenger compartment occurs. In addition, the value for $AbWP$ must be smaller than 1. The same number of sampling points is used and the same number of steps in the exploration and consolidation phase is used.

### 8.3.3 Force deformation corridors

With these values for the input and optimization, the following two force deformation curves for the local x and y force are obtained, see Fig 8.2.

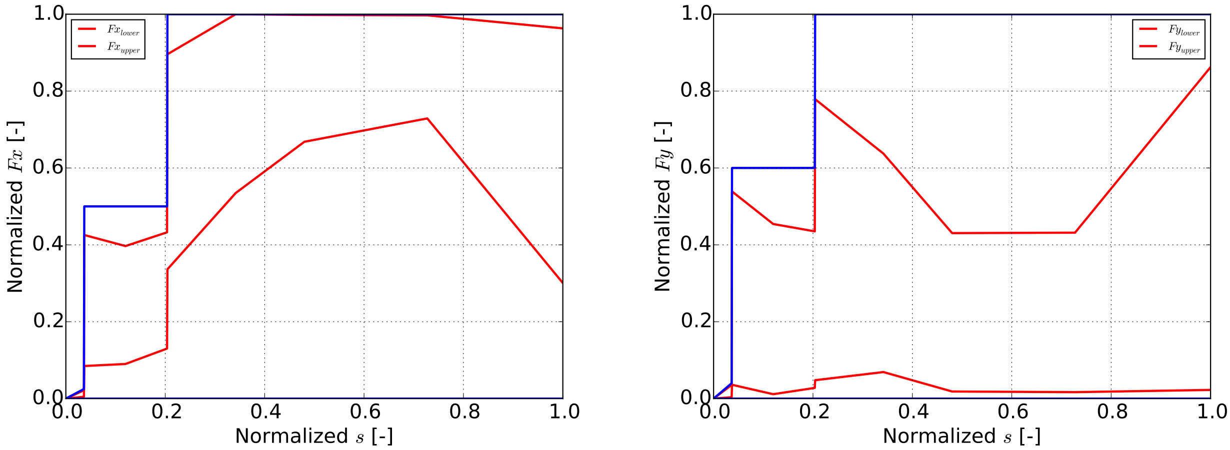


(a) $F_x$.

(b) $F_y$.

Figure 8.2: Force deformation corridors of kinematic model with two springs for rotational response.

From Fig. 8.2a, it can be seen that the lower level for the x force increases rapidly after a normalized deformation of 0.2 to approximately 0.7 of normalized force in x. The upper force level in x is almost at the maximum allowable level. Looking at Fig. 8.2b, it is observed that the lower force level in y is almost at 0. The upper force level does increase after 0.2 of normalized deformation length, but then decreases to approximately 0.4 of the maximum allowable level.

In order to see the influence of the constraint on having a rotational response of the vehicle on the force deformation corridor, the force deformation corridor using the $s_L$ constraint is plotted together with the force deformation corridor using the $s_L$ and $AbWP$ constraints, see Fig 8.3.

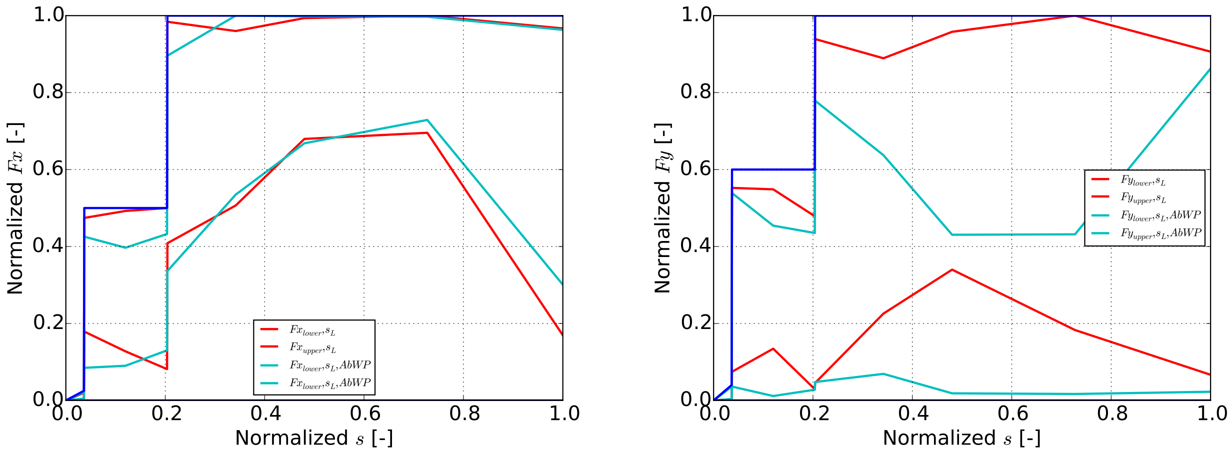


(a) $F_x$.

(b) $F_y$.

Figure 8.3: Comparison of force deformation corridors of two springs model for rotational response.

Looking at Fig. 8.3a, the upper and lower bounds for the local x force are at a comparable level. However, the upper and lower levels for the y force are reduced, as shown in Fig. 8.3b. In addition, it can be seen that the upper boundary of the y force is much more restrictive compared to the previous solution, resulting in a lower area of the solution space for the y force.

### 8.3.4 Discussion

As the vehicle's response is the rational response for the optimization shown in this section, a high level for x force should be observed and low forces in y. The results obtained in this section comply with engineering judgment, as the vehicle should not glance-off and hence, the force in y should be small which is observed by Fig 8.2. Especially, the comparison to the previous case shows that a low force in y is sufficient for obtaining feasible design solutions. The high force in x comes from the constraint variable $s_L$.

## 8.4 Glancing-off response force deformation corridors with two springs kinematic model

This section provides the force deformation corridors using the two springs configuration for a glancing-off concept.

### 8.4.1 Input parameters

Similar to the previous optimization, the same input parameters are used. Thus the same values for the mass of the vehicle, mass moment of inertia, location of COG, location of spring and the location of nodes for obtaining the angle of the vehicle are stored in the configuration file. The deformation length of the spring in the x direction is discretized using nine support points. For each of these support points realistic and achievable lower and upper force levels are given for the x and y force.

### 8.4.2 Optimization parameters

In this Section, it is looked at the glancing-off response of the vehicle. Therefore, the constraint variables are such that the value of $s_L$ avoids any intrusion into the passenger compartment and the values for $AbWAP$ and $AbWP$ are larger than 1. The same number of sampling points is used and the same number of steps in the exploration and consolidation phase is used.

### 8.4.3 Force deformation corridors

The obtained force deformation corridors for the glancing off response are shown in Fig. 8.4

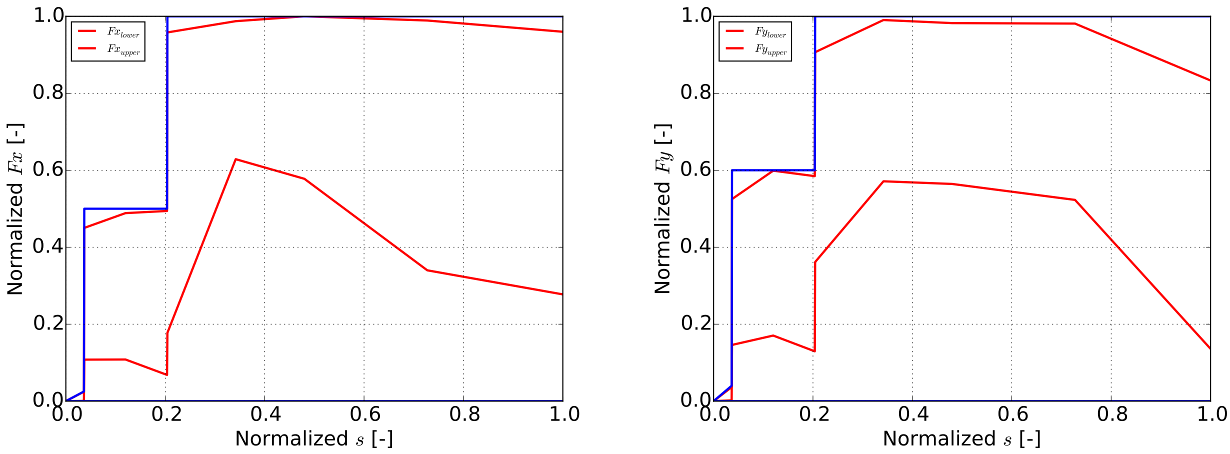


(a) $F_x$. (b) $F_y$.

Figure 8.4: Force deformation corridors of kinematic model with two springs for glancing-off response.

In Fig. 8.4a it can be seen that the constraints require a lower force level in x of 0.6 of the maximal force. The upper force level in x is almost at the maximum allowable level. The y force levels, shown in Fig. 8.4b, are such that the higher level is close to the maximum allowable, while the lower force level is at a level of 60% of the maximum force level from 0.2 of normalized displacement onwards.

The result becomes more clear when looking at the combined result, so that of the optimization using only $s_L$ and of the optimization using $s_L$, $AbWAP$ and $AbWP$ shown in Fig. 8.5.

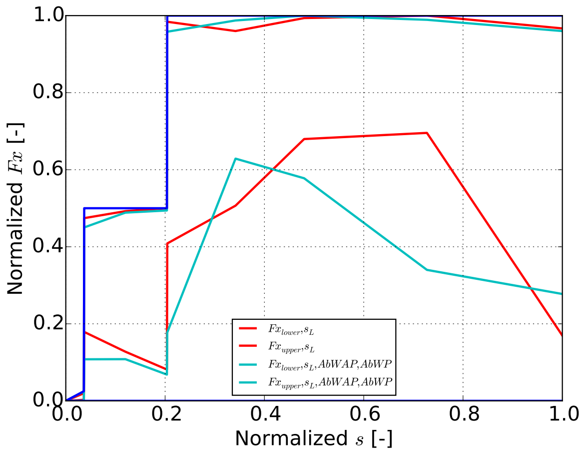


(a) $F_x$.

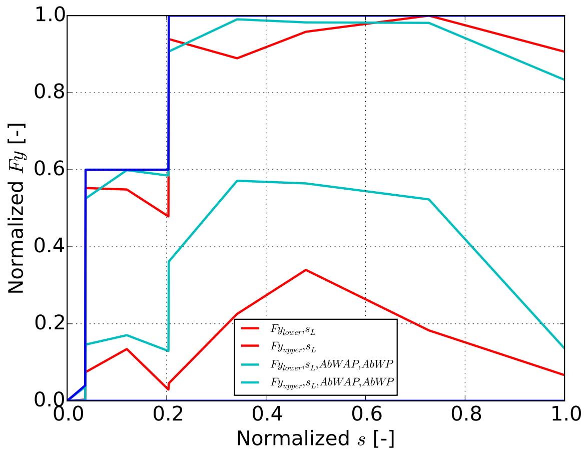


(b) $F_y$.

Figure 8.5: Comparison of force deformation corridors of two springs model for glancing-off response.

Here it can be seen that the upper force level in x is almost the same, see Fig. 8.5a. The lower force level in x is relaxed, making the force deformation corridor larger. The highest force level for the local y force is almost the same as well, see Fig. 8.5b. However, the lowest level for the y force is significantly higher when compared to the optimization using only the $s_L$ constraint, making the corridor width smaller.

### 8.4.4 Discussion

The result shown in this section are also expected, since the certain force in y is required in order to push the vehicle in the lateral direction and force it to glance off. This can be seen by the significantly higher lower y force level shown in Fig. 8.5b compared to the previous optimization. In addition, the width of the local y force deformation corridor is reduced, emphasizing the importance of the y force for the glancing-off response. The relatively comparable x force levels are due to the constraint of $s_L$ which is relatively strict in terms of x force and thus requires a certain x force.

## 8.5 Force deformation corridors with ten springs kinematic model

Since the results obtained from the optimization tool at BMW AG do comply with engineering judgment, the same constraints are used for the predictive kinematic model using ten springs in order to represent groups of components and determine the force deformation corridors for these components. The force deformation corridors with the ten springs kinematic model should not only be seen as allowable force levels as such, but also as a proof of concept of the idea of obtaining force deformation solution spaces for grouped components. Before running the optimization, first the placement of the springs and hence the grouping of components has to be performed. From investigating several FEM crash simulations in Animator 4 and analyzing them with the energy tool from BMW AG, similar to the numerical study, and referring to the findings of the literature study, five groups of components have been identified to be of importance. These are the following:

· Wheel and surrounding structure.
· Shotgun and surrounding structure.
· Lower framerail and surrounding structure.

· Upper framerail and surrounding structure.
· Springdome and surrounding structure.

As can be seen by the list mentioned above, the divisions of components are on a higher hierarchical level than originally done in the bottom up approach shown in Chapter 5. This complies with the realization that important components, for example the wheel, are not scalable through changes in wall thicknesses.

Note that due to the nature of the predictive kinematic model, the components must be grouped in order to obtain a force deformation corridor for them. The division is such that each spring in axial direction is assigned a box. Inside this box, all components are assigned to the spring. This is shown in Fig. 8.6. Note that due to confidentiality issues, only the boxes can be shown without the structure of the vehicle.

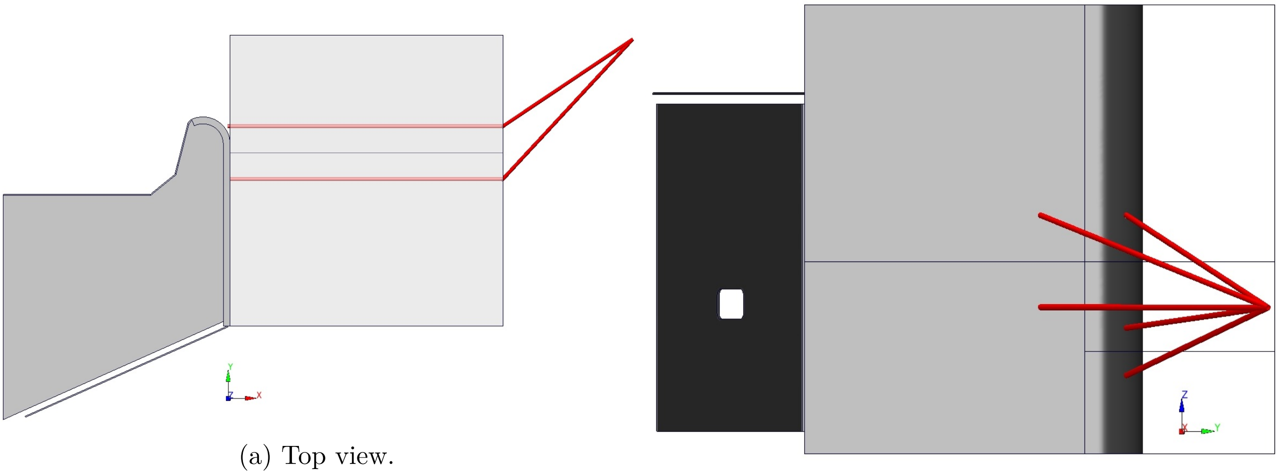

(a) Top view.

(b) Front view.

Figure 8.6: Boxes to determine the grouped components.

When looking at Fig. 8.6b, the principle of dividing the structure is shown. At the lower left box, the wheel and the surrounding structure is located. The shotgun and the surrounding structure are assigned to the upper left box. The lower right box contains the lower framerail and surrounding structure, while the middle right box contains the upper framerail and surrounding structure. The upper right box contains the springdome and other surrounding structures. Recall that the box moves over time and due to the deformation of the components, it is possible that some components of one group cross the boundaries of their assigned box.

### 8.5.1 Input parameters

The input parameters are the mass of the vehicle, mass moment of inertia, location of COG and the location of nodes for obtaining the angle of the vehicle. These input parameters are stored in the configuration file. The locations of the axial springs, as shown Fig. 8.6, are implemented as well into the configuration file. As the discretization points of the deformation of all springs in the axial direction are different, the values are obtained from looking at the geometry of the vehicle in Animator A4. From this observation, it has been decided that each spring has then three discretization points for the deformation of the spring.

### 8.5.2 Optimization parameters

The constraint in this optimization is that the value of the constraint variable $s_L$ is such that no intrusion in the occupant compartment is allowed. Similar to the previous case for the two spring configuration, this constraint is used to obtain force deformation solution spaces which only contain feasible design solutions. This means for the response, so rotational or glancing-off response, that there is no preference. The number of sampling points is equal to 200 and 100 steps in the exploration and consolidation phase are used.

### 8.5.3 Force deformation corridors

The optimization resulted in the following force deformation corridors for the five grouped components. Note that the plots are normalized in the following way. For the five groups of components, the x force levels are normalized to the highest observed force level for the five groups of components. The same is done for the y force levels. The deformation $s$ is normalized for each group of components for the geometrical length of the load path.

First, the result is shown for the x and y forces of the grouped components around the wheel, see Fig. 8.7.

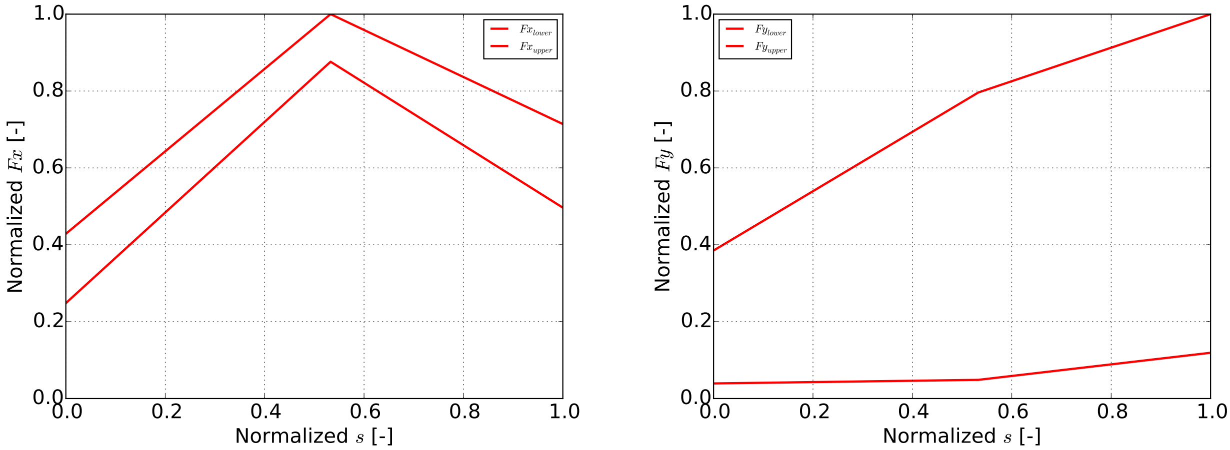


(a) $F_x$. (b) $F_y$.

Figure 8.7: Force deformation solution corridors for the wheel.

Here, it can be seen on the one hand that the width of the force deformation corridor in x is rather small. On the other hand, the force deformation corridor in y allows a larger width with respect to the design space boundaries. Especially, the lower level of the local y force is very low.

The force deformation solution space for the shotgun is shown in Fig. 8.8.

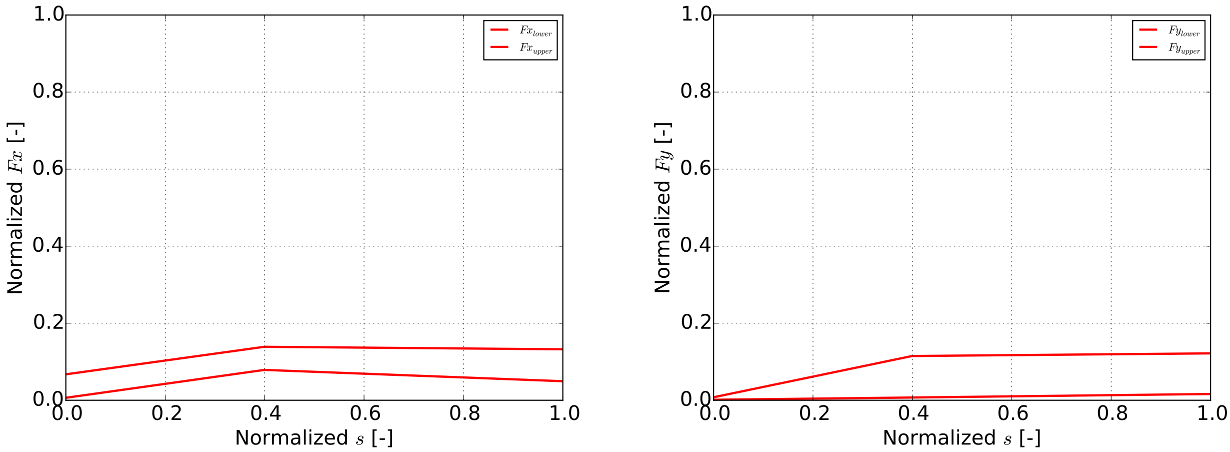


(a) $F_x$. (b) $F_y$.

Figure 8.8: Force deformation solution corridors for the shotgun.

In Fig. 8.8a, an increase in required x force over deformation length is observed. In addition, the component requires a lower bound of local x force of approximately 0.1 of normalized force. The local force in y requires a rapid increase in force and stays then relatively constant at a level of 0.1 of normalized y force, see Fig. 8.8a.

Next, it is looked at the lower framerail, as provided in Fig. 8.9.

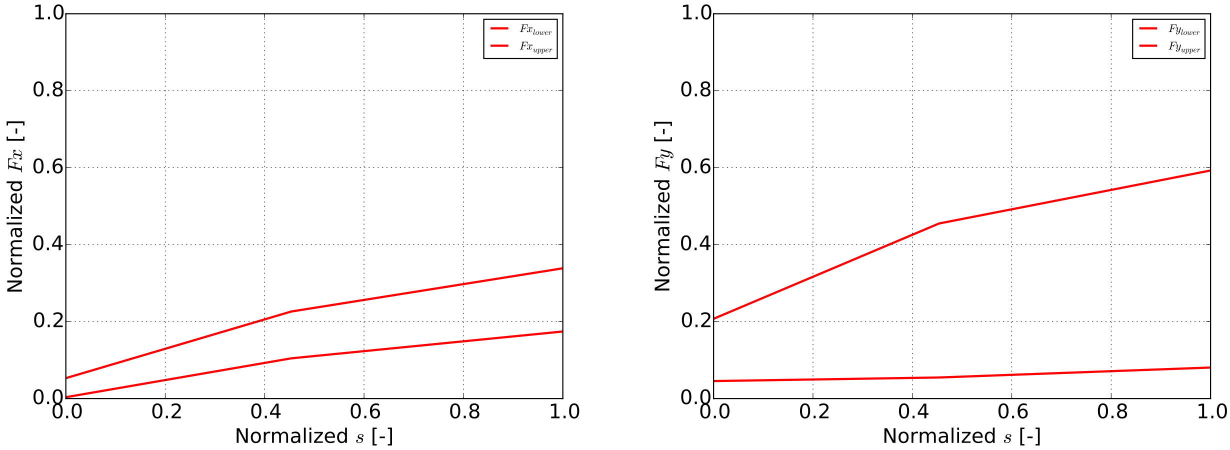


(a) $F_x$. (b) $F_y$.

Figure 8.9: Force deformation solution corridors for the lower framerail.

The lower level in x for the lower framerail increases to almost 0.35 of normalized x force. The overall width of the corridor is relatively small as well, shown in Fig. 8.9a. The local y force shows a similar trend, as observed for the shotgun, compare Fig. 8.9a with Fig. 8.9b, although the upper force level in y is almost five times as high.

Next, it is looked at the groups of components of the upper framerail, shown in Fig. 8.10.

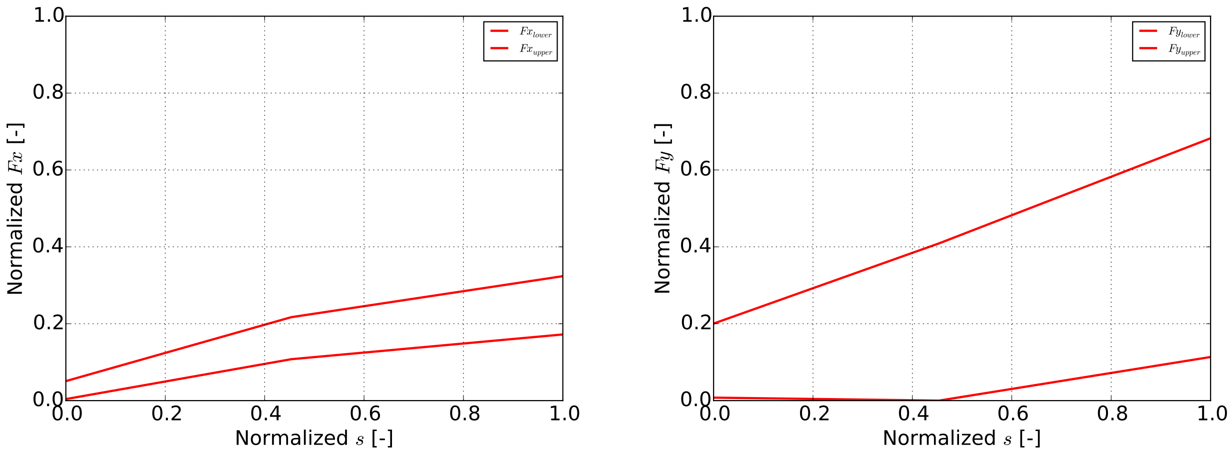


(a) $F_x$. (b) $F_y$.

Figure 8.10: Force deformation solution corridors for the upper framerail.

In Fig. 8.10a, almost the same force deformation corridor is obtained for the upper framerail (compare to Fig. 8.9a). The lower level of the local y force of the upper framerail is almost zero at the first part of the deformation, but then increases to a value of 0.1 of maximum force level. The upper force level of the local y force increases from 0.2 to 0.7 of normalized y force over the complete deformation length.

Finally, it is looked at the groups of components in the proximity of the springdome, see Fig. 8.11.

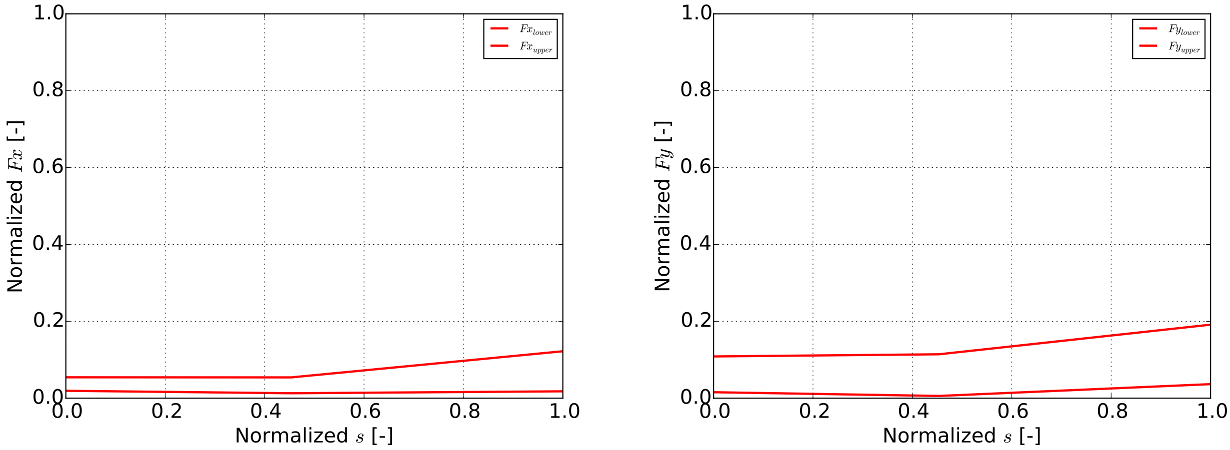


(a) $F_x$. (b) $F_y$.

Figure 8.11: Force deformation solution corridors for the springdome.

For both the x and y force, the lower required levels are relatively low. In addition, both curves shown in Fig. 8.11a and Fig. 8.11b show a similar trend in terms of required upper force level, but are relatively low as well. The values are at 0.1 and 0.2 of normalized force in x and y, respectively.

### 8.5.4 Discussion

From the force deformation plots of the five grouped components, several observation can be made.

First of all, it can be clearly seen that not all components have the same influence and importance for the small overlap crash test. For example, the grouped components around the wheel do have a small width of the corridor, meaning that the design space is not large and that the wheel must be able to deliver the highest load. This can be seen when looking at the abscissa of both plots shown in Fig. 8.7, where the maximum value is 1 for both the x and y force.

In addition, the local x and y force of the upper and lower framerail show very similar force deformation corridors. Especially, the x force levels are relatively similar. Also, it can be seen that the lower bound of the local y force of the shown components is relatively similar and quite low. Observed by the magnitude of the force levels, the grouped components around the springdome and the shotgun have the lowest observed force levels.

Compared to observation made in crash tests, FEM simulations and energy studies, it seems intuitively correct that the grouped components around the wheel take up the most load. The components which take also a significant portion of the load are the upper and lower framerail, where the y force levels of the lower framerail are higher. It is emphasized that the solution must be seen as a proof of concept.

The solutions obtained for the components comply with the solutions obtained for the two springs configuration where a relatively high required force in x is observed compared to the force in y.

## 8.6 Rotational response force deformation corridors with ten springs kinematic model

In this section, the optimization using ten springs is performed for obtaining force deformation solution corridors for the rotational response.

### 8.6.1 Input parameters

The same input parameters for the mass, mass moment of inertia, location of COG and nodes for obtaining the angle of the vehicle as described in the previous Section are used. The same discretization points for the deformation of the springs are used and the locations of the springs are the same.

### 8.6.2 Optimization parameters

On top of the constraint $s_L$ which is chosen such that no intrusion into the occupant compartment occurs, the same constraint for obtaining a rotational response shown in Section 8.3 is used, so $AbWP$ should be smaller than 1. Further, the same amount of sampling points for the Monte Carlo sampling is used and the same number of steps is used.

### 8.6.3 Force deformation corridors

The force deformation corridors for the grouped components around the wheel are shown in Fig. 8.12. Note that the force deformation curves shown in cyan are compared to the previous case which are shown in red. Recall that the previous case only had the constraint for the final length of the spring located at the A-Pillar and thus no preference on the response of the vehicle. The force deformation corridors for only the rotational response is shown in the Appendix.

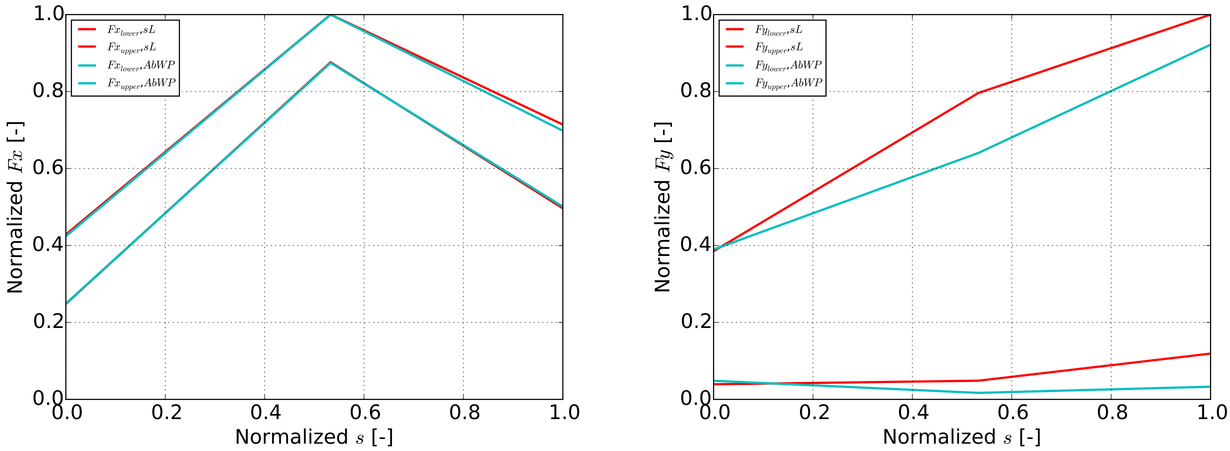


(a) $F_x$. (b) $F_y$.

Figure 8.12: Force deformation solution corridors of the wheel for rotating response.

Compared to the grouped components of the wheel in the previous case, the rotational response requires almost the same upper and lower force levels in x, see Fig. 8.12a. For the local y force, the upper bound of the force is lowered, as well as the lower bound, see Fig. 8.12b, increasing the width of the corridor.

Next, the grouped components around the shotgun are investigated, as shown in Fig. 8.13.

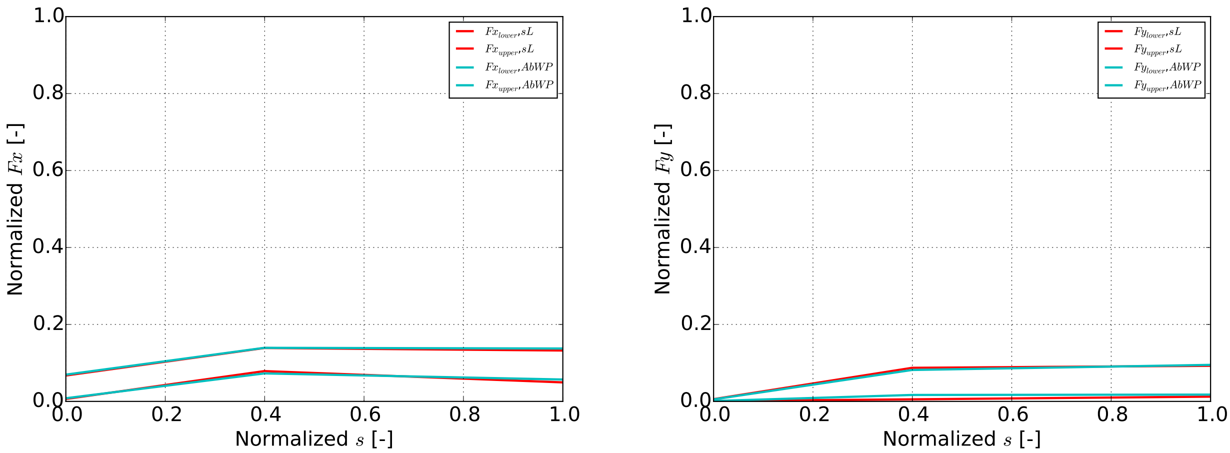


(a) $F_x$. (b) $F_y$.

Figure 8.13: Force deformation solution corridors of the shotgun for rotating response.

Looking at Fig. 8.13a, the force deformation corridor is almost the same, except that the upper force level in x is slightly larger and the lower force level is lower. In case of the y force, the force deformation corridor is smaller, however, the results are reasonably similar.

The force deformation corridor for the grouped components around the lower framerail are shown in Fig. 8.14.

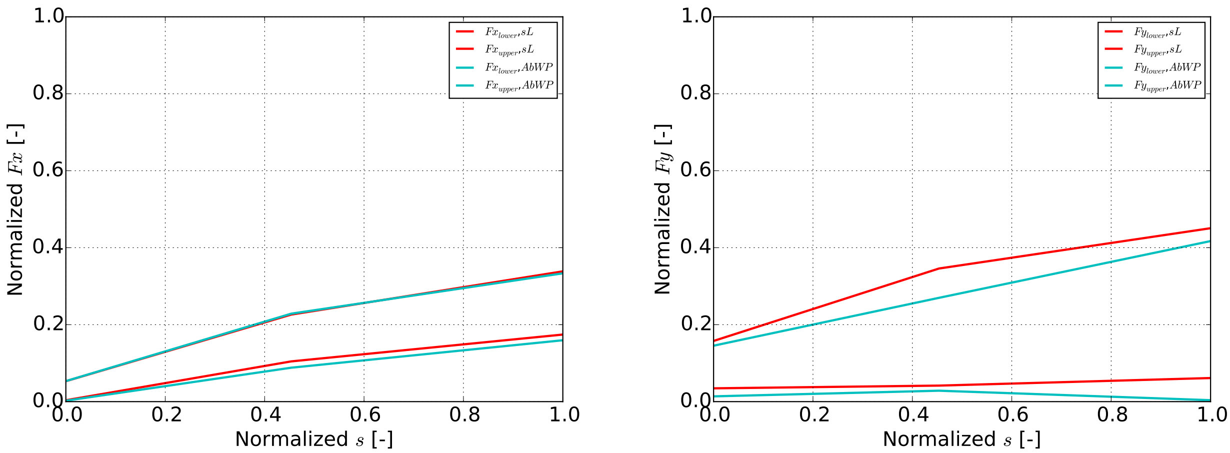


(a) $F_x$.

(b) $F_y$.

Figure 8.14: Force deformation solution corridors of the lower framerail for rotating response.

A similar trend is seen for the upper and lower x forces, however the lower level is lower, see Fig. 8.14a. The y force, shown in Fig. 8.14b, requires smaller forces, although the width of the corridor is almost the same.

The force deformation corridor for the grouped components of the upper framerail are shown in Fig. 8.15.

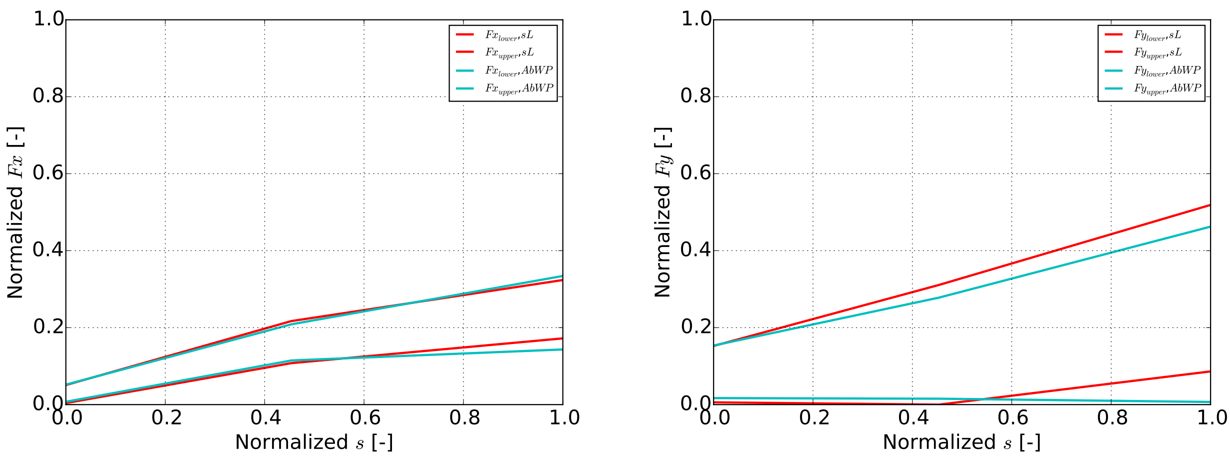


(a) $F_x$.

(b) $F_y$.

Figure 8.15: Force deformation solution corridors of the upper framerail for rotating response.

The corridor for the force in x shows not a large difference when looking at Fig. 8.15a. The force of the upper framerail shows a similar trend as before, except for the fact that the lower required force does not change over deformation and the higher bound is reduced compared to the previous case.

Finally, it is looked at the force deformation corridors of the components in the proximity of the springdome, see Fig. 8.16.

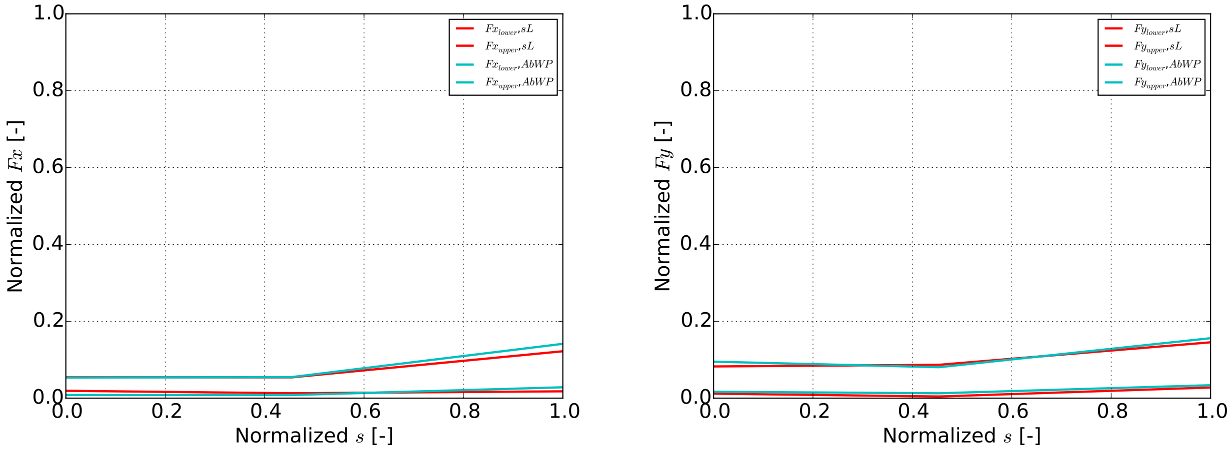


(a) $F_x$. (b) $F_y$.

Figure 8.16: Force deformation solution corridors of the springdome for rotating response.

Although the upper x force level until 0.5 of normalized deformation is relatively the same, the higher force level is at a higher specified level, see Fig. 8.16a. In terms of local y force, as shown in Fig. 8.16b, the upper and lower force levels do not deviate significantly from the previous case.

### 8.6.4 Discussion

From the optimization of the ten springs configuration of the predictive kinematic model for obtaining force deformation corridors for a rotational response, similar solutions are obtained as for the x force deformation corridors where no specification on the response is made. This result is comparable to the two springs configuration where the results obtained for the optimization using only $s_L$ and $AbWP$ and $s_L$ are relatively the same in terms of x force levels.

Looking at all five grouped components, it can be observed that the upper bound for the y force is lowered. Especially for the grouped components around the wheel this trend can be seen. These results do also comply with the results obtained with the two springs approach.

## 8.7 Glancing-off response force deformation corridors ten springs kinematic model

In this section, the optimizer tool at BMW AG is used for a ten springs configuration of the predictive kinematic model in order to obtain force deformation solution corridors for the five grouped components for a glancing-off concept.

### 8.7.1 Input parameters

Again, the same input parameters for the mass, mass moment of inertia, location of COG and nodes for obtaining the angle of the vehicle as described in the previous Section are used. The same discretization points for the deformation of the springs are used and the locations of the springs are the same.

### 8.7.2 Optimization parameters

In addition to the constraint $s_L$ for restricting any intrusion into the occupant compartment, the same constraint for obtaining a glancing-off response shown in Section 8.4 is used, so both $AbWAP$ and $AbWP$ should be larger than 1. Also, the same amount of sampling points for the Monte Carlo sampling is used and the same number of steps is selected.

### 8.7.3 Force deformation corridors

Similar to the previous section, first the result obtained for the grouped components in the proximity of the wheel is shown, as provided in Fig 8.17.

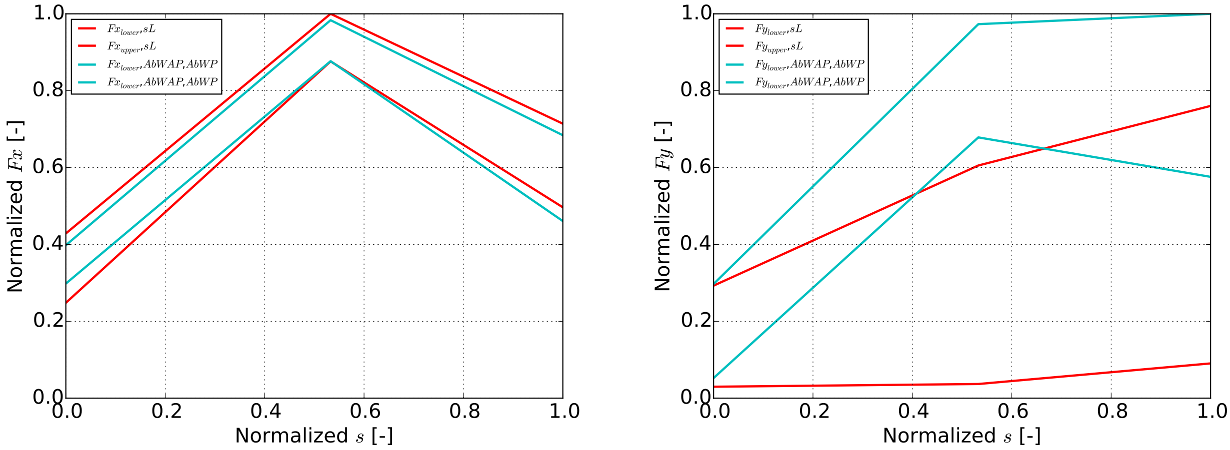


(a) $F_x$.    (b) $F_y$.

Figure 8.17: Force deformation solution corridors of wheel for glancing-off response.

Although the shape of the force deformation corridor in x is the same, the force levels of the upper bound are slightly lower, see Fig. 8.17a. But overall, the force is reasonably comparable. Looking at Fig. 8.17b, a significant higher force level in y is observed over the deformation of the spring when compared to the optimization using only the constraint $s_L$. In addition, the width of the corridor is smaller.

Next, it is looked at the grouped components around the shotgun, as presented in Fig. 8.18.

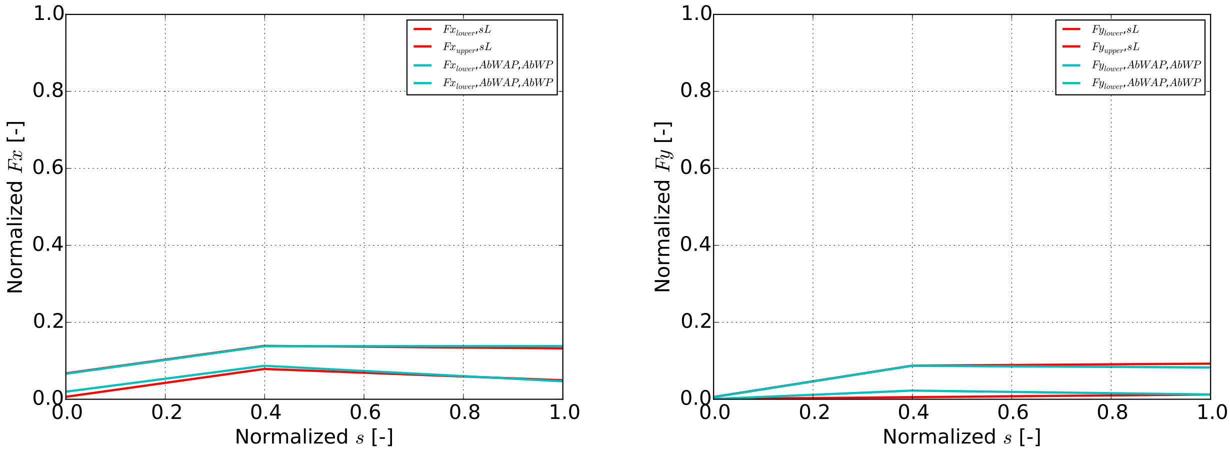


(a) $F_x$.    (b) $F_y$.

Figure 8.18: Force deformation solution corridors of shotgun for glancing-off response.

In Fig. 8.18a, a similar shape is found for the local x force. In addition, the width is slightly lower of the force deformation corridor. The y force shows again a higher lower bound, see Fig. 8.18b.

The force deformation corridors for the lower framerail are shown in Fig. 8.19.

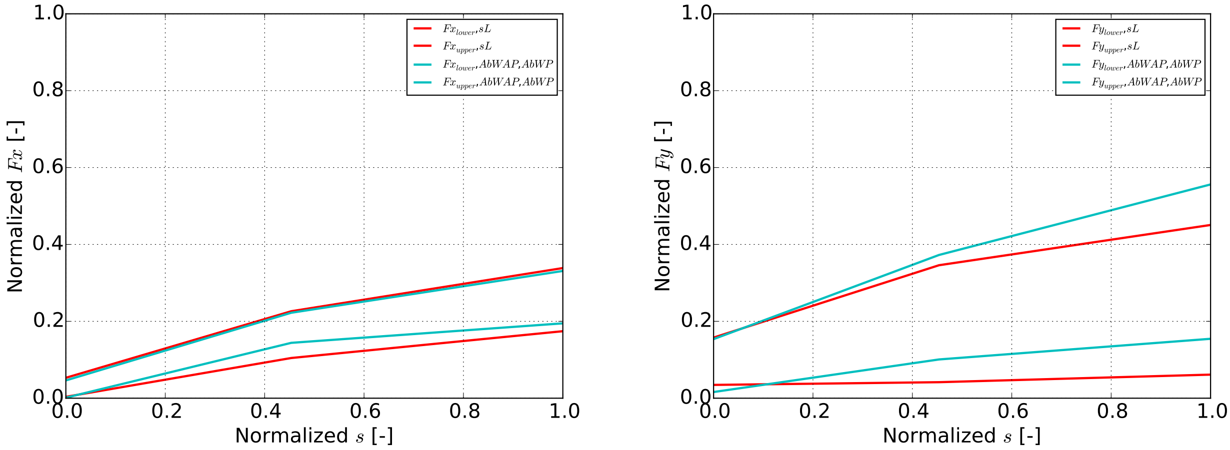


(a) $F_x$.

(b) $F_y$.

Figure 8.19: Force deformation solution corridors of lower fraimerail for glancing-off response.

The upper force level in x is almost the same, see Fig. 8.19a. However, the lower force level is increased, resulting in a smaller corridor for the lower framerail. The upper bound of the local y forces, shown in Fig. 8.19b, is higher compared to the previous case. The same holds for the lower bound of the y force level.

Next it is looked at the upper framerail, shown in Fig. 8.20.

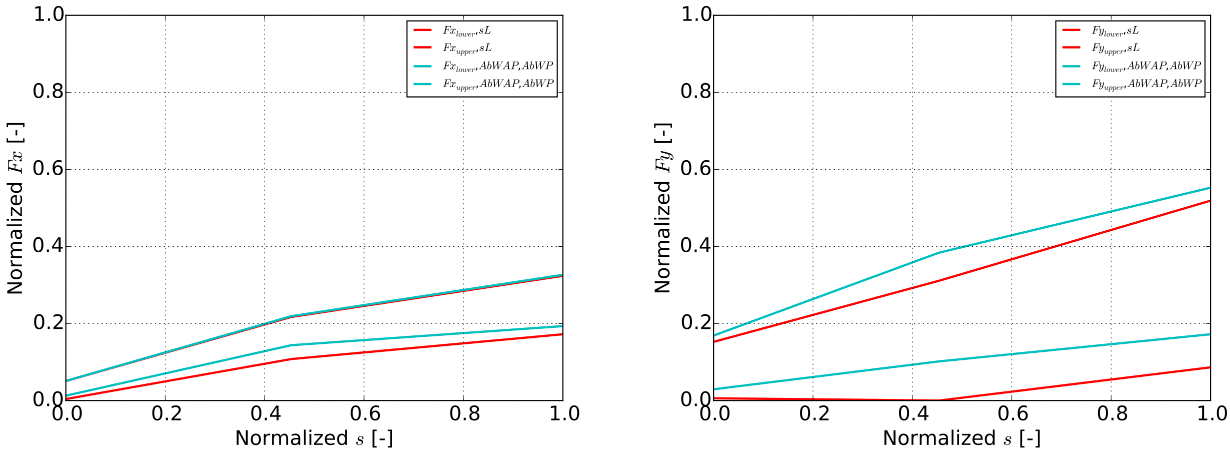


(a) $F_x$.

(b) $F_y$.

Figure 8.20: Force deformation solution corridors of upper fraimerail for glancing-off response.

Compared to the lower framerail, the upper framerail force deformation corridors show almost the same shape and magnitude, see Fig. 8.20a and Fig. 8.20b. For the x force levels, it can be seen that higher lower force bounds are obtained. In addition, the lower, as well as the higher force level in y are higher for the glancing-off response.

Finally, it is looked at the components around the springdome, see Fig. 8.21.

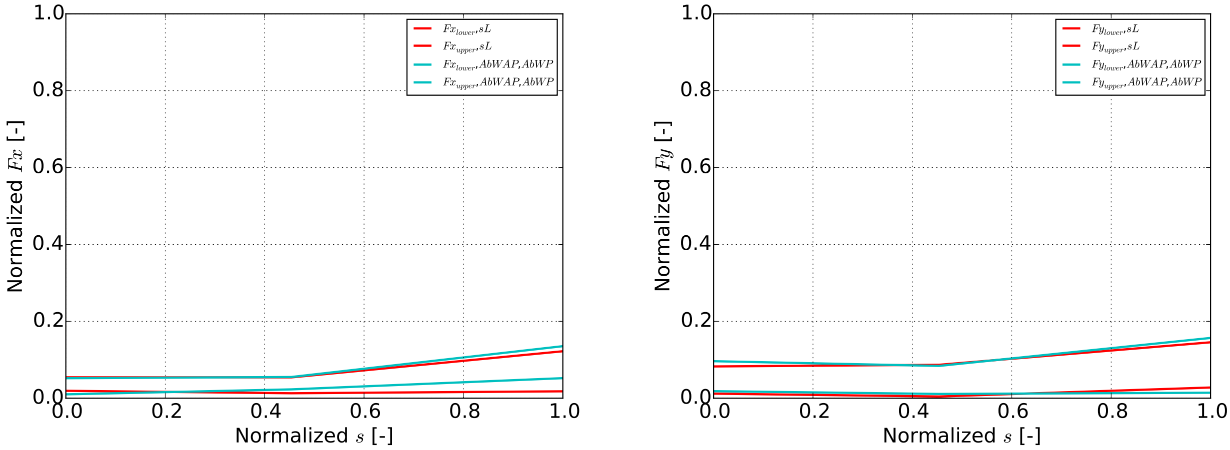


(a) $F_x$.

(b) $F_y$.

Figure 8.21: Force deformation solution corridors of springdome for glancing-off response.

In Fig. 8.21a, the upper force level in x is almost the same. The lower force level shows a larger value compared to the previous case, except for the start of the deformation. The forces in y show a similar trend than before, see Fig. 8.21b with no significant changes in the magnitude of the upper and lower force level bounds.

### 8.7.4 Discussion

From the force deformation corridors for the glancing-off behavior obtained with the predictive kinematic model using ten springs, several observations can be made.

First of all, it can be seen that the grouped components around the wheel show the largest force levels in x and y. Comparing the solution with the previous solution where the only constraint is the restriction of the length of the spring ($s_L$), a significant higher force level in y is observed. Similar trends are seen for the upper and lower framerail where an increase in y force is observed. The results do comply with the two springs configuration case, where a higher y force is required for glance-off. In addition, the same trend is seen that the x force levels are relatively comparable to the optimization where only the value of the length of the spring ($s_L$) is taken as constraint.

Furthermore, it can be seen that the most relevant groups of components are the wheel, upper and lower framerail, shotgun and then the springdome, similar to the findings of the previous section.

## 8.8 Summarized results and discussions

In this section, the results for the force deformation solution spaces are elaborated on. First, it is focused on the results of the two springs configuration, followed by the ten springs configuration.

### 8.8.1 Two springs configuration

The three different results obtained with the two springs configurations show that with the use of the predictive kinematic model and the stochastic tool described earlier, it is possible to find solution spaces for the force deformation characteristics of the springs.

The obtained results do comply with intuition and engineering judgment. Specifically, when relating the observation to the numerical study, a similar trend is seen between the relation of x and y forces and the response of the vehicle. A high x force with a relatively low y force results in a rotating response while a high y force and a low x force results in a glancing-off response, as seen in this chapter.

As with any optimization and simulation, several limitations are observed. First of all, the limited amount of discretization points results in a linear interpolation between the force values at these points, resulting in the showed force deformation solution space corridors. In addition, the choice of upper and lower force levels requires experience and has an influence on the outcome of the result. Overall, however, the predictive model is able to deliver solution space corridors in which feasible design options are found which then can be used at an early phase of the development of a passenger vehicle.

### 8.8.2 Ten springs configuration

The results obtained with the ten springs configuration should be understood as a proof of concept. The x and y force deformation solution corridors for the three cases showed that the developed method works. The tendency of the highest upper and lower force levels for the five grouped components comply with the insights obtained with the numerical study.

However, there are some drawbacks when using the method. As discussed previously, the movement of the box of each axial spring determines the assigned force. Investigating FEM simulations, it can be seen that it is generally hard to distinguish which components should belong to which group. The fact that the boxes move over time due to the moving vehicle makes this division even harder. On top of that, as there is no experience in grouping the components together, much thought should be put in this step. Similar to the two springs configuration, the choice of discretization points is crucial as the load paths are defined in the x direction in the predictive model.

Nevertheless, it should be emphasized that the results obtained with the ten springs configuration do show a similar trend to the two springs configuration and can therefore be understood as a proof of concept.

# CHAPTER 9

## Discussions and conclusions

This chapter presents a critical discussion of the results obtained in the thesis and of the main conclusions on the performed work. In particular, the focus of the discussions and the conclusions is with respect to the research objective shown in the introduction of the thesis.

As with any numerical study and simplified model, the used methods rely on certain assumptions. Note that some of the aspects discussed in this chapter were previously mentioned in the thesis, but nevertheless, these aspects are combined in this chapter. The discussion and conclusions are done individually on three main topics, being: the numerical study, the development of the predictive kinematic model and the obtained force deformation solution spaces. Specifically, the structure of the chapter is the following. First, it is reflected on the outcome of the numerical study, shown in Section 9.1. Next, in Section 9.2, the results of the predictive kinematic model are critically discussed. Finally, in Section 9.3, the outcome of the force deformation solution spaces are reflected on.

## 9.1 Numerical study

First of all, it should be discussed that the energy tool which is used in the energy study, uses the accumulative internal energy at the final time step of the simulation and therefore the plastic energy of each component in each time step of the simulation. Hence it does not take the energy due to elastic deformation into account. However, the structural components which take up a large amount of elastic energy, can also be of importance, but these are not taken into account in the energy study.

In addition, the numerical study of the two FEM simulation models proved that there is a strong correlation between x and y forces and the response modes of the model subjected to the small overlap crash test. On the one hand, for obtaining the rotational response, large x forces and low y forces are required. On the other hand, for obtaining the lateral translational response, low x forces and large y forces are required.

Referring to the trolley FEM simulation model, it can be concluded that modeling the small overlap crash test is not sufficient with only the main frontal structural parts being present and without the wheel assembly and surrounding structure. The fact that the wheels of the trolley are not located on the same position of the vehicle it represents, does also lower the accuracy in terms of vehicle dynamics. The main reason for the discrepancy is that the mass moment of inertia of the trolley FEM simulation model is not the same as the mass moment of intertia of the vehicle it represents.

Concerning the reduced full vehicle FEM simulation model, the restriction that the vehicle can only move in a planar fashion may not be according to reality. However, investigating the z force in relation to the x and y forces, this is a reasonable assumption. The assumption that after the A-Pillar a MPC constraint is used to rigidly couple the elements with the MPC node, however, is simplifying the result to a certain extend. Although no large deformations are observed behind the A-Pillar, even very small deformations do influence the monitoring process of the COG node.

In addition, it is concluded that changing the wall thicknesses of the relevant structural components is not sufficient in determining the influence of a certain component on the response of the vehicle subjected to the small overlap crash. This can be explained by the fact that the two investigated

FEM simulations models have pre-described sets of components, some of which do not define a certain load path, but which are required to obtain a certain response. Furthermore, each change in wall thickness of a certain structural component has an influence on the surrounding structure and on the load transfer of the surrounding structure. Also, it should be noted that the wheel is not scalable through changes in the wall thickness.

In order to obtain a detailed view on the influence of the relevant components on the response to the small overlap crash, a very large sampling size would be be required. However, as performing a numerical study using very detailed FEM simulation models is not very robust and given the time constraint of the thesis, it is concluded that the bottom up approach is working not as satisfactorily as desired, at least in terms of the scope of the thesis.

## 9.2 Predictive kinematic model

For the creation of the predictive kinematic model, it has been assumed that the barrier is flat. This is an approximation of the contour of the barrier and hence implies that the projection point of the axial spring is not entirely correct for the curved section of the barrier. However, note that the maximum difference between the curved contour and the flat assumed contour is 150 mm. In addition, it is important to mention that the curved section is rather small compared to the straight section (150 mm compared to 1000 mm).

Another point of interest is the assumption that everything behind the A-Pillar is assumed to be rigid. However, the validity of this assumption does not have been tested on all vehicle models available at BMW AG.

Furthermore, the change of mass and mass moment of inertia over time is not modeled by the predictive kinematic model resulting in a deviation from reality. Also, since the forces in z are not taken into account by the predictive kinematic model and only planar movement is considered, a small reduction in accuracy is observed.

Next, it should be noted that the time step used in the predictive kinematic model follows the central difference scheme which is known to have its limitations in terms of accuracy. This could been increased by investigating different time integration schemes and evaluate their performance on the accuracy.

For the configurations of the predictive kinematic model which uses more than two springs, the process of assigning the components to the boxes needs some point of discussion. The boundaries of the boxes move depending on the movement of the COG in the x and y direction. Depending on the deformation and the movement of the components inside a certain box, it can be the case that some of the grouped components fall outside of their assigned boundaries during the simulation time. Furthermore, it is underlined that the location of the springs is of importance, as it determines which groups of components are located inside the box and where the projection point of the spring of consideration on the barrier is located. Nevertheless, when comparing the grouped components used in this thesis for obtaining the force deformation solution corridors with the generic load paths presented in Chapter 2, good correlation is observed.

The validation of the predictive kinematic model has been done using three different full vehicle FEM simulation models, each with two different responses. For these models, a good correlation for the three output variables (displacement of COG in x and y direction and rotational angle of the COG around the z axis) is observed in terms of MAE. However, it should be noted that although the three full vehicle models are very different, not all vehicle models of the BMW AG product line were looked at during the validation. Furthermore, the FEM simulation models used for validation purposes, use a measurement kit for measuring the movement of the COG location during the simulation. Due to the nature of the definition of the measurement kit, it could be the case that the node used for the rigid connection is prone to deformations.

Furthermore, note that the predictive kinematic model is developed solely for the small overlap crash test, so no investigations have been done on other frontal crashes, such as the full frontal or the moderate overlap crash.

Finally, it should be pointed out that the predictive kinematic model, despite its limitations and simplifications, is able to reasonable predict the kinematic response of a broad range of passenger vehicles to the small overlap crash test. This has been done with six FEM simulation variants where the MAE is reasonably small given the overlap length of the vehicle with respected to the barrier compared to the MAE of the COG y movement. Specifically, when looking at the angle of the COG compared to the FEM simulation models, the MAE of the predictive kinematic model is negligible.

## 9.3 Force deformation solution spaces

For obtaining the force deformation solution spaces with the predictive kinematic model using a two springs configuration and a ten springs configuration, a sampling size of 200 set points was used. This number of points was used, as a lower number resulted into non-robust solutions where the force deformation solution corridor width was too small due to the small sampling size. As discussed in Chapter 4, the poor performance in homogeneity of points distributed over the sampled region is often observed when using a Monte Carlo sampling. Thus in order to avoid this for all force deformation solution spaces, a large sampling size was used.

The step size also needs some point of discussion. The used number was selected by investigating the converge of the optimizer used at BMW AG. As a starting point, a value of 50 was used for the step size. After performing the first optimization, it has been seen that the solution was not converged sufficiently. As a consequence, the step size was sub-subsequently increased and a value of 100 was sufficient for all the optimizations shown in this thesis, as the solution converged slightly before the 100 steps.

Another point of interest is the correct use of the discretization points for the force deformation solution spaces. This can only be done by assuming the location of the main components, or by using a previous full vehicle FEM simulation model as reference.

In addition, the choice of constraints is of importance. For example, in this thesis only a lower value is used for the constraint $s_L$. However, it could also be thought of using a restriction on a upper value of $s_L$ in order to limit the deceleration of the occupants. This is due to the fact that without the constraint on the upper value of $s_L$, solutions which have a high force in the x direction are also allowed.

Furthermore, it is stressed again that the force deformation solution spaces for the grouped components obtained with the ten springs configuration of the predictive kinematic model should be understood as a proof of concept, directly underlining that the research objective is achievable with the top down approach.

Finally, it should be discussed that the outcome of the force deformation spaces using the predictive kinematic model is very useful for the early phase of passive safety development of passenger vehicles. The obtained force deformation corridors, especially on the grouped components level, give the responsible design departments the required force levels for the components as a function of deformation for which it can be assured that a safe response to the small overlap crash is obtained.

# CHAPTER 10

## Recommendations

As the thesis project had limited resources in terms of time, some recommendations are made in this chapter for future research. Similar to the previous chapter, the recommendations are grouped into three main aspects, being: the numerical study, shown in Section 10.1, the development of the predictive kinematic model, presented in Section 10.2, and the obtained force deformation solution spaces, discussed in Section 10.3.

### 10.1 Numerical study

The numerical study shown in this thesis makes use of an energy analysis to determine the most relevant components of the investigated FEM simulation models. However, the considered energy is only the plastic strain energy, as the accumulated internal energy is taken at the final time step of the simulation which does not include the elastic part of the energy. Therefore, a recommendation for future research would be to look at the plastic, as well as the elastic energy taken up by the components.

Another point of interest is the improvement of the parameters of interest. In this numerical study, only the wall thicknesses of the components were changed. A recommendation for future research would be to also change parameters like the speed of the vehicle, the overlap width of the barrier, the mass and the mass moment of inertia of the vehicle.

Finally, it is recommended to use a FEM simulation model in Abaqus/Explicit which is very robust and not prone to abortion when changes in wall thickness for the structural components are made or geometrical changes of the components are made.

### 10.2 Predictive kinematic model

For the predictive kinematic model, some enhancements are recommended in order to increase the accuracy of the output.

A first recommendation would be to model the contour of the barrier with the arc, instead of assuming this surface to be flat, resulting into more accurate results.

In addition, as described in Chapter 6 and mentioned in Chapter 9, the central difference scheme is used to solve the system of equations of the EOM. Incorporating different time integration schemes into the predictive kinematic model, such as the Runge-Kutta scheme, would possibly increase the accuracy.

Furthermore, it is recommended to develop a generic way of assigning the components to a certain spring. The algorithm to draw the design boundaries is of special interest for further investigation and therefore left for future research.

In addition, a recommendation would be to validate the predictive kinematic model with hardware tests of passenger vehicles for the small overlap crash.

Moreover, as the predictive kinematic model is only working on component level, it is left for future research to extend the model such that single components can be modeled by this approach.

Finally, including springs in the z direction as well and hence extending the predictive kinematic model to a 3D simulation model would increase the accuracy of results and is therefore left as recommendation for future work.

## 10.3 Force deformation solution spaces

For the force deformation solution spaces, it is recommended to define a generic approach for obtaining the discretization points used for the deformation values of each spring for the force deformation solution spaces.

In addition, it is recommended to use more discretization points along with more sampling points and number of steps to obtain a benchmark case. However, given the scope of the thesis, this is left as future work.

Finally, the investigation of more constraint variables and selecting their appropriate values could be an interesting future research subject.

# Bibliography


[1] Association for Safe International Road Travel. Annual Global Road Crash Statistics. `http://asirt.org/initiatives/informing-road-users/road-safety-facts/road-crash-statistics`, 2015. Consulted on July 29, 2016.

[2] World Health Organization. Global status report on road safety 2015. `http://www.who.int/violence_injury_prevention/road_safety_status/2015/en/`, 2015. Consulted on July 29, 2016.

[3] World Health Organisation. Global status report on road safety 2013. `http://www.who.int/violence_injury_prevention/road_safety_status/2013/en/`, 2013. Consulted on July 29, 2016.

[4] C. Hobbs. The need for improved structural integrity in frontal car impacts. In *Proceedings of the 21st International Technical Conference on the Enhanced Safety of Vehicles*. National Highway Traffic Safety Administration Washington, DC, 1991.

[5] M. Lindquist, A. Hall, and U. Björnstig. Car structural characteristics of fatal frontal crashes in Sweden. *International journal of crashworthiness*, 9(6), 2004.

[6] Insurance Institute for Highway Safety. Small overlap crash test overview. `http://www.iihs.org/`, 2016. Consulted on July 29, 2016.

[7] J. H. W. Fender. *Solution Spaces for Vehicle Crash Design*. PhD thesis, TU Munich, Shaker Verlag, Munich, 2014.

[8] J. A. C. Ambrosio. *Crashworthiness: Energy management and occupant protection*, volume 423. Springer, 2014.

[9] Insurance Institute for Highway Safety. Small overlap frontal crashworthiness evaluation. `http://www.iihs.org/`, 2016. Consulted on July 29, 2016.

[10] B. C. Mueller, A. S. Brethwaite, D. S. Zuby, and J. M. Nolan. Structural Design Strategies for Improved Small Overlap Crashworthiness Performance. *Stapp Car Crash Journal*, 58:145, 2014.

[11] X. Da Silva and N. Parera. Forces Involved in Small Overlap Crash. In *Proceedings of the European Automotive Congress EAEC-ESFA 2015*, pages 105–116. Springer Internal Publishing, 2016.

[12] P. Du Bois, C. C. Chou, B. B. Fileta, T. B. Khalil, A. I. King, H. F. Mahmood, H. J. Mertz, J. Wismans, P. Prasad, and J. E. Belwafa. *Vehicle crashworthiness and occupant protection*. American Iron and Steel Institute, Southfeld, Michigan, 2004.

[13] World Health Organization. *Manual of the international statistical classification of diseases, injuries, and causes of death*, volume 2. World Health Organization, 1975.

[14] C. P. Sherwood, J. M. Nolan, and D. S. Zuby. Characteristics of small overlap crashes. In *Proceedings of the 21st International Technical Conference on the Enhanced Safety of Vehicles*, pages 1–7. National Highway Traffic Safety Administration Washington, DC, 2009.

[15] G. Jost, R. Allsop, and A. Ceci. Ranking European Union progress on car occupant safety. Technical report, European Transport Safety Council, 2014.

[16] A. K. Lund. 50 years of progress: Where do we go from here? Edmunds' Safety Conference: Truly Safe? Washington, DC, 2011.

[17] International Traffic Safety Data, Analysis Group, Organization for economic cooperation, and development. Road safety annual report 2015. Technical report, International Traffic Safety Data and Analysis Group, 2015.

[18] M. Svensson and J. Bärgman. Vehicle and traffic safety. Division of vehicle safety. Department of Applied Mechanics. Chalmers University of Technology, Gothenburg, Sweden, 2014.

[19] M. Lindquist, A. Hall, and U. Björnstig. Real world car crash investigations - A new approach. *International journal of crashworthiness*, 8(4):375–384, 2003.

[20] Z. Wei, H. R. Karimi, and K. R. Robbersmyr. A Model of Vehicle-Fixed Barrier Frontal Crash and Its Application in the Estimation of Crash kinematics. In *24th International Technical Conference on the Enhanced Safety of Vehicles (ESV)*, number 15-0161, 2015.

[21] P. Zhu, F. Pan, W. Chen, and S. Zhang. Use of support vector regression in structural optimization: Application to vehicle crashworthiness design. *Mathematics and Computers in Simulation*, 86:21–31, 2012.

[22] J. Lenard, A. Morris, E. Tomash, J. Nehmzow, D. Otte, L. Cant, M. Maddak, G. Vallet, H. Ebbinger, and J. Bernes. PENDANT: a European crash injury database. In *2nd Expert Symposium on Accident Research, Hannover, Germany*, 2006.

[23] J. J. Hallman, N. Yoganandan, F. A. Pintar, and D. J. Maiman. Injury differences between small and large overlap crashes. In *Annals of Advances in Automotive Medicine/Annual Scientific Conference*, volume 55, page 147. Association for the Advancement of Automotive Medicine, 2011.

[24] J. Iraeus and M. Lindquist. Influence of vehicle kinematic components on chest injury in frontal-offset impacts. *Traffic injury prevention*, 15(sup1):S88–S95, 2014.

[25] T. Kikuchi, T. Nakao, T. Watanabe, H. Saeki, and T. Okabe. An investigation of injury factors concerning drivers in vehicles involved in small-overlap frontal crashes. *SAE International Journal of Passenger Cars-Mechanical Systems*, 5(2):801–806, 2012.

[26] C. P. Sherwood, B. C. Mueller, J. M. Nolan, D. S. Zuby, and A. K. Lund. Development of a frontal small overlap crashworthiness evaluation test. *Traffic injury prevention*, 14(sup1):s128–s135, 2013.

[27] P. Scullion, R. M. Morgan, P. Mohan, C. D. Kan, K. Shanks, W. Jin, and R. Tangirala. A reexamination of the small overlap frontal crash. In *Annals of Advances in Automotive Medicine/Annual Scientific Conference*, volume 54, page 137. Association for the Advancement of Automotive Medicine, 2010.

[28] S. Yadav and S. K. Pradhan. Investigations into Dynamic Response of Automobile Components during Crash Simulation. *Procedia Engineering*, 97:1254–1264, 2014.

[29] P. T. L. Nguyen, J. Y. Lee, H. J. Yim, S. B. Lee, and S. J. Heo. Analysis of vehicle structural performance during small-overlap frontal impact. *International Journal of Automotive Technology*, 16(5):799–805, 2015.

[30] X. Sen, Y. Jikuang, and Z. Zhihua. Research and optimization of crashworthiness in small overlap head-on collision. In *Measuring Technology and Mechatronics Automation (ICMTMA), 2013 Fifth International Conference on*, pages 854–857. IEEE, 2013.

[31] C. Thomas. The role of the vehicle structure in reducing injuries in small overlap crashes. In *International Automotive Body Congress*. Curran Associates Inc., Red Hood, NY, 2011.

[32] W. Pawlus, H. R. Karimi, and K. G. Robbersmyr. Development of lumped-parameter mathematical models for a vehicle localized impact. *Journal of mechanical science and technology*, 25(7):1737–1747, 2011.

[33] M. M. Kamal. Analysis and simulation of vehicle to barrier impact. Technical report, SAE Technical Paper, 1970.

[34] M. Huang. *Vehicle crash mechanics*. CRC press, 2002.

[35] A. Deb and K. C. Srinivas. Development of a new lumped-parameter model for vehicle side-impact safety simulation. *Proceedings of the Institution of Mechanical Engineers, Part D: Journal of Automobile Engineering*, 222(10):1793–1811, 2008.

[36] National Highway Traffic Safety Administration. NHTSA. `http://www.nhtsa.gov/`, 2016. Consulted on July 29, 2016.

[37] W. Pawlus, H. R. Karimi, and K. G. Robbersmyr. Mathematical modeling of a vehicle crash test based on elasto-plastic unloading scenarios of spring-mass models. *The International Journal of Advanced Manufacturing Technology*, 55(1-4):369–378, 2011.

[38] R. C. Hibbeler. *Engineering mechanics*. Pearson education, 2001.

[39] R. R. Mc Henry. Analysis of the dynamics of automobile passenger-restraint systems. In *Proceedings: American Association for Automotive Medicine Annual Conference*, volume 7, pages 207–249. Association for the Advancement of Automotive Medicine, 1963.

[40] C. H. Kim. *Development of simplified models for automotive crashworthiness simulation and design using optimization*. PhD thesis, The University of Iowa, 2001.

[41] K. Schweizerhof, L. Nilsson, and J. O. Hallquist. Crashworthiness analysis in the automotive industry. *International journal of computer applications in technology*, 5:134–156, 1992.

[42] K. J. Bathe. *Finite element procedures*. Prentice Hall, Pearson Education, Inc., 2006.

[43] M. Ruess. Nonlinear Structural Modeling. Aerospace Structures and Computational Mechanics. Faculty of Aerospace Engineering. Delft University of Technology, Delft, The Netherlands., 2013.

[44] W. Abramowicz. Macro Element Method in Crashworthiness of Vehicles. *Crashworthiness - Energy Management and Occupant Protection*, pages 1–53, 2001.

[45] P. Hora. Principles of Nonlinear Finite Element Methods. Institute of Virtual Manufacturing. Department of Mechanical and Process Engineering. Swiss Federal Institute of Technology Zurich, Zurich, Switzerland, 2012.

[46] P. Drazetic, E. Markiewicz, and Y. Ravalard. Application of kinematic models to compression and bending in simplified crash calculations. *International journal of mechanical sciences*, 35(3):179–191, 1993.

[47] D. J. Inman. *Engineering vibrations*. Prentice Hall, 2009.

[48] T. Gholami, J. Lescheticky, and R. Pabmann. Crashworthiness simulation of automobiles with ABAQUS/Explicit. In *Proceeding of Abaqus Users' Conference, Munich*, 2003.

[49] W. Abramowicz and K. Takada. The macro element method in crashworthiness calculations-the state-of-the-art and the future. *Zeszyty Naukowe Instytutu Pojazdów/Politechnika Warszawska*, (4/71):5–22, 2008.

[50] Virtual Crash Studio. Impact desing. Impact Design Europe. `http://www.impactdesign.pl/index.php`, 2016. Consulted on July 29, 2016.

[51] J. M. Alexander. An approximate analysis of the collapse of thin cylindrical shells under axial loading. *The Quarterly Journal of Mechanics and Applied Mathematics*, 13(1):10–15, 1960.

[52] L. Lasek, D. Bohm, and V. Schindler. Vehicle layout tools for the early stage of the development process. In *Proceedings of the 21st International Technical Conference on the Enhanced Safety of Vehicles*, pages 24–26. VPD Conference, Munich, Germany, 2005.

[53] J. Fender, F. Duddeck, and M. Zimmermann. On the calibration of simplified vehicle crash models. *Structural and Multidisciplinary Optimization*, 49(3):455–469, 2014.

[54] I. K. Mc Ivor. Modeling and simulation as applied to vehicle structures and exteriors. In *Vehicle Safety and Research Integration Symposium, Rep. No. DOT HS-820*, volume 306, pages 5–18, 1973.

[55] C. H. Kim and J. S. Arora. Nonlinear dynamic system identification for automotive crash using optimization: A review. *Structural and Multidisciplinary Optimization*, 25(1):2–18, 2003.

[56] J. M. Chang, T. Tyan, M. El-Bkaily, J. Cheng, A. Marpu, Q. Zeng, and J. Santini. Implicit and Explicit Finite Element Methods for Crash Safety Analysis. Technical report, SAE Technical Paper, 2007.

[57] Ted Belytschko, Wing Kam Liu, Brian Moran, and Khalil Elkhodary. *Nonlinear finite elements for continua and structures*. John Wiley & Sons, 2013.

[58] Rao Venkateswara Dukkipati. *Matlab for mechanical engineers*. New Age Science, 2009.

[59] LSTC Inc and DYNAmore GmbH. LS-DYNA Support. LS-Dyna. `http://www.dynasupport.com/tutorial/ls-dyna-users-guide/time-step-size`, 2016. Consulted on July 29, 2016.

[60] Ted Diehl. Using ABAQUS Cohesive Elements to Model Peeling of an Epoxy-bonded Aluminum Strip: A Benchmark Study for Inelastic Peel Arms. In *2006 ABAQUS Users' Conference*, 2006.

[61] Abaqus 6.13. Abaqus Documentation. Simulia. `http://129.97.46.200:2080/v6.13/books/usb/default.htm`, 2015. Consulted on July 29, 2016.

[62] L. Song, J. Fender, and F. Duddeck. A Semi-Analytical Approach to Identify Solution Spaces for Crashworthiness in Vehicle Architectures. In *24th International Technical Conference on the Enhanced Safety of Vehicles (ESV)*, number 15-0183, 2015.

[63] J. Fender, L. Graff, H. Harbrecht, and M. Zimmermann. Identifying key parameters for design improvement in high-dimensional systems with uncertainty. *Journal of Mechanical Design*, 136(4), 2014.

[64] M. Lehar and M. Zimmermann. An inexpensive estimate of failure probability for high-dimensional systems with uncertainty. *Structural Safety*, 36:32–38, 2012.

[65] E. C. Anderson. Monte Carlo Methods and Importance Sampling. Statistical Genetics. University of California, Berkeley, 1999.

[66] John Hammersley. *Monte carlo methods*. Springer Science & Business Media, 2013.

[67] S. Paltani. Monte Carlo Methods. Data Center for Astrophysics. Astronomical Observatory of the University of Geneva, Geneva, Switzerland, 2010.

[68] Arnaud Doucet, Nando De Freitas, and Neil Gordon. An introduction to sequential Monte Carlo methods. In *Sequential Monte Carlo methods in practice*, pages 3–14. Springer, 2001.

[69] GNS-Gesellschaft für Numerische Simulation mbH . Animator 4. GNS mbH. `http://gns-mbh.com/animator.html`, 2015. Consulted on July 29, 2016.

[70] Insurance Institute for Highway Safety. IIHS Technical data. `https://techdata.iihs.org/`, 2016. Consulted on July 29, 2016.

[71] Josef S Török. *Analytical Mechanics: With an Introduction to Dynamical Systems*. John Wiley & Sons, 2000.

[72] Dassault Systems. ANSA. 3DS Simulia. `http://www.3ds.com/products-services/simulia/products/tosca/structure/ansa/`, 2015. Consulted on July 29, 2016.

[73] Cort J Willmott and Kenji Matsuura. Advantages of the mean absolute error (MAE) over the root mean square error (RMSE) in assessing average model performance. *Climate research*, 30(1):79–82, 2005.

In the following, the results for the output variables for the validation of all three FEM vehicle models, each with two different response modes, using two springs, 18 springs and 80 springs for the predictive kinematic model are shown.

### SUV

In Fig. A.1, the results for the response using the three different configurations of the predictive kinematic model are shown and compared to the SUV FEM simulation model which experiences the glancing-off response.

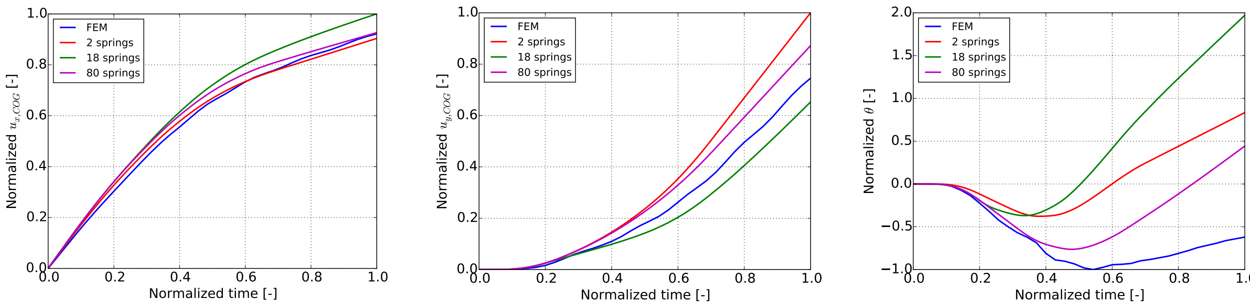


(a) COG displacement in x. (b) COG displacement in y. (c) COG rotation.

Figure A.1: Kinematic model compared to SUV FEM model with glance-off concept.

In Fig. A.2, the results for the response using the three different configurations of the predictive kinematic model are shown and compared to the SUV FEM simulation model which experiences the rotational response.

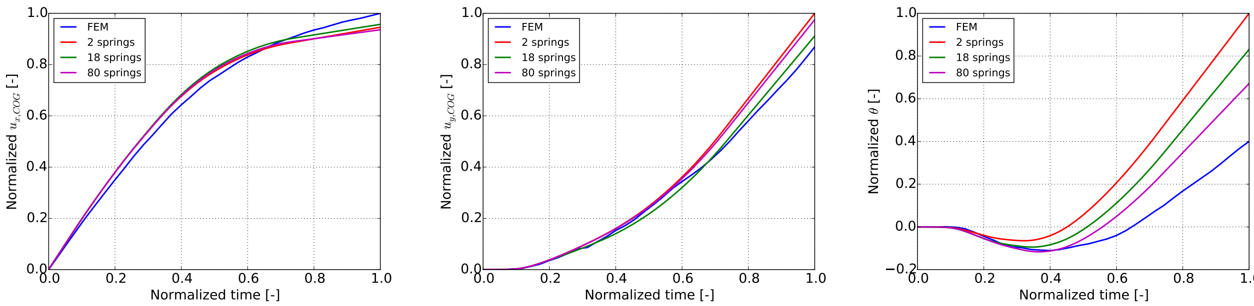


(a) COG displacement in x. (b) COG displacement in y. (c) COG rotation.

Figure A.2: Kinematic model compared to SUV FEM model with rotational concept.

### Mid-size sedan

In Fig. A.3, the results for the response using the three different configurations of the predictive kinematic model are shown and compared to the mid-size sedan FEM simulation model which experiences the glancing-off response.

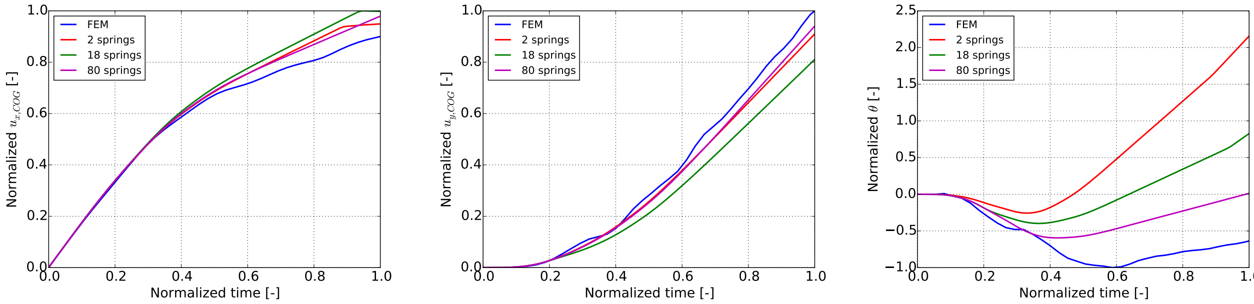


(a) COG displacement in x. (b) COG displacement in y. (c) COG rotation.

Figure A.3: Kinematic model compared to mid-size sedan FEM model with glance-off concept.

In Fig. A.4, the results for the response using the three different configurations of the predictive kinematic model are shown and compared to the mid-size sedan FEM simulation model which experiences the rotational response.

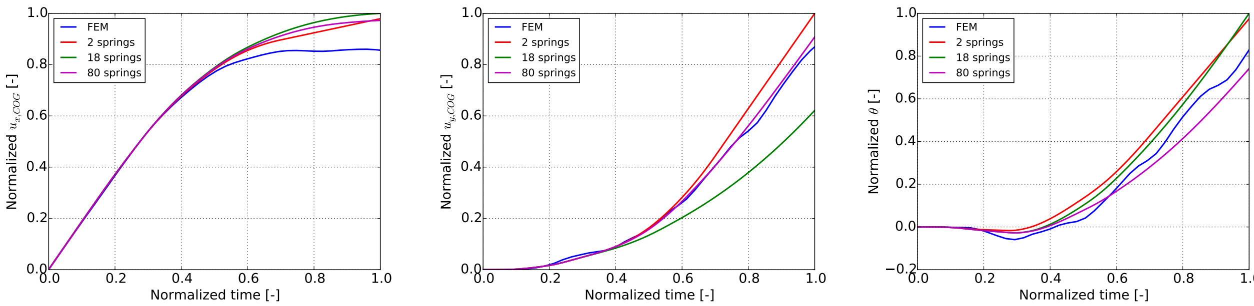


(a) COG displacement in x. (b) COG displacement in y. (c) COG rotation.

Figure A.4: Kinematic model compared to mid-size sedan FEM model with rotational concept.

**Sports car**

In Fig. A.5, the results for the response using the three different configurations of the predictive kinematic model are shown and compared to the sports car FEM simulation model which experiences the glancing-off response.

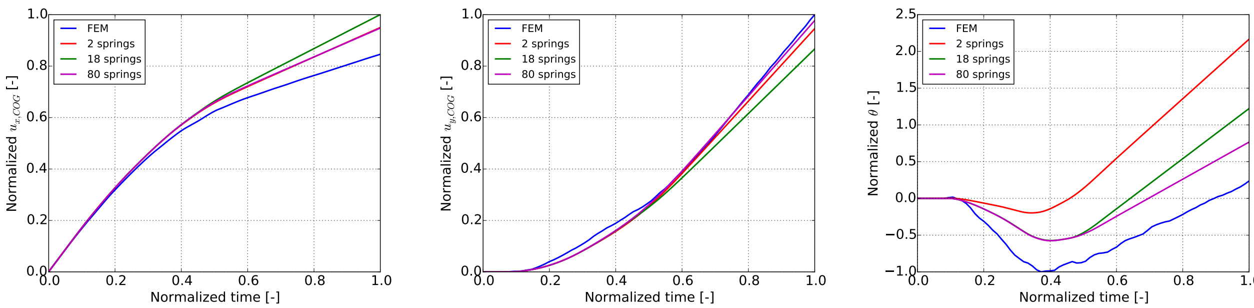


(a) COG displacement in x. (b) COG displacement in y. (c) COG rotation.

Figure A.5: Kinematic model compared to FEM sports car model with glancing-off concept.

In Fig. A.6, the results for the response using the three different configurations of the predictive kinematic model are shown and compared to the sports car FEM simulation model which experiences the rotational response.

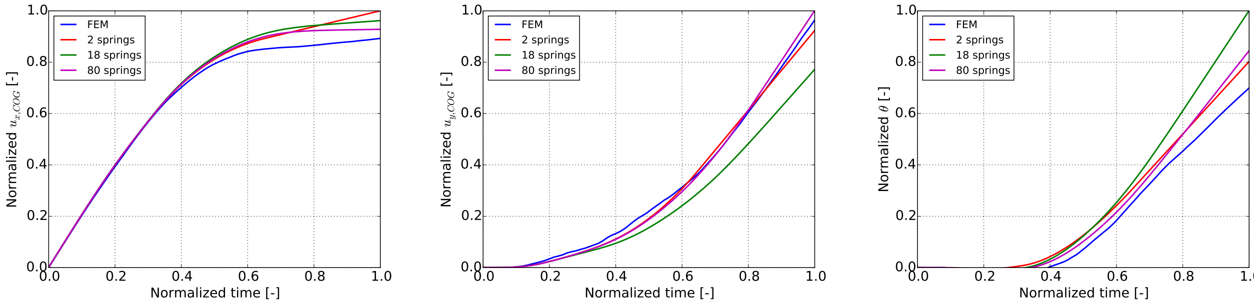


(a) COG displacement in x.

(b) COG displacement in y.

(c) COG rotation.

Figure A.6: Kinematic model compared to FEM sports car model with rotational concept.

# Appendix B - Force deformation solution corridors for ten springs configuration of predictive kinematic model

In the following, the force deformation solution corridors for a ten springs configuration of the predictive kinematic model are shown for a rotational response and a glancing-off response.

**Rotating response using constraints $s_L$ and $AbWP$**

The force deformation solution corridors of the grouped components of the wheel for the rotational response are shown in Fig. B.1.

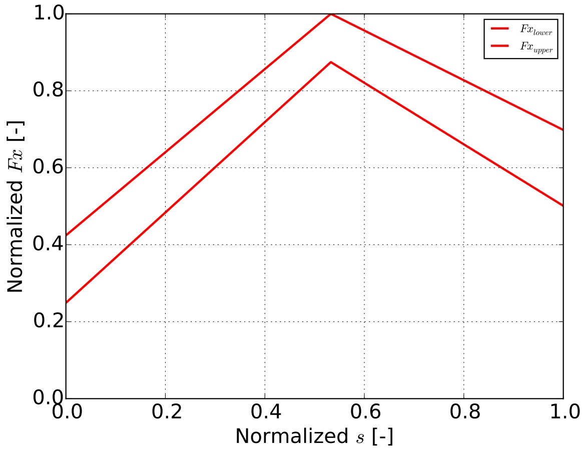


(a) $F_x$.

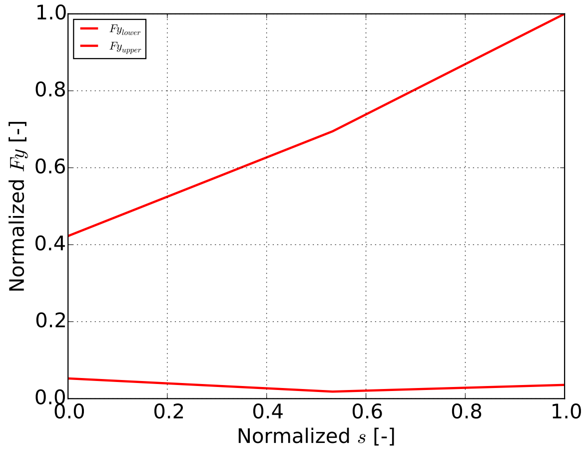


(b) $F_y$.

Figure B.1: Force deformation solution corridors of wheel for rotational response.

The force deformation solution corridors of the grouped components of the shotgun for the rotational response are shown in Fig. B.2.

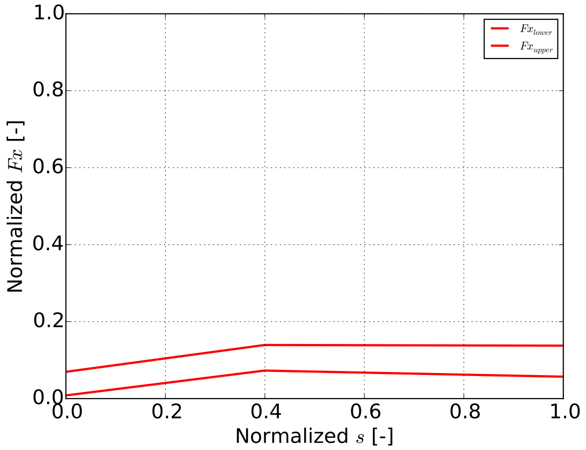


(a) $F_x$.

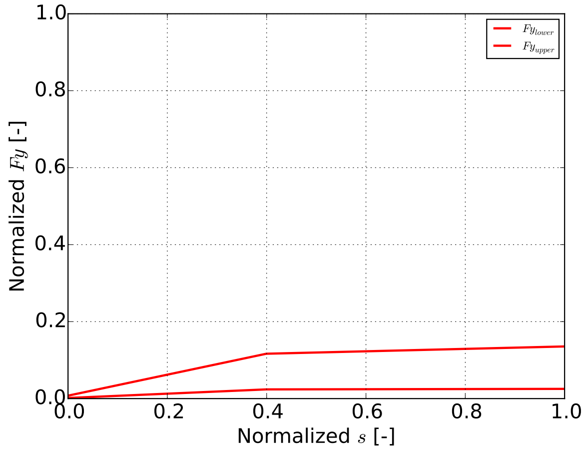


(b) $F_y$.

Figure B.2: Force deformation solution corridors of shotgun for rotational response.

The force deformation solution corridors of the grouped components of the lower framerail for the rotational response are shown in Fig. B.3.

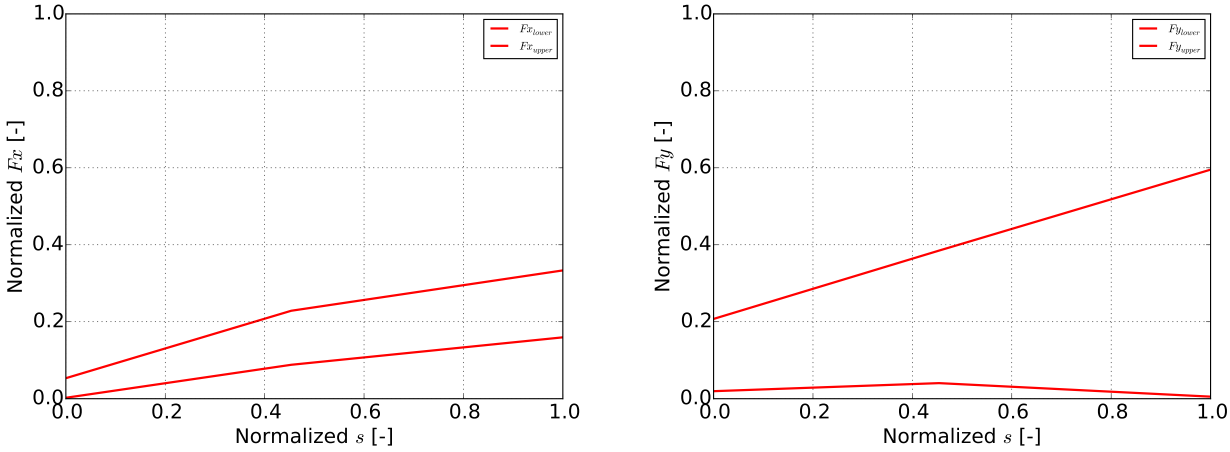


(a) $F_x$. (b) $F_y$.

Figure B.3: Force deformation solution corridors of lower framerail for rotational response.

The force deformation solution corridors of the grouped components of the upper framerail for the rotational response are shown in Fig. B.4.

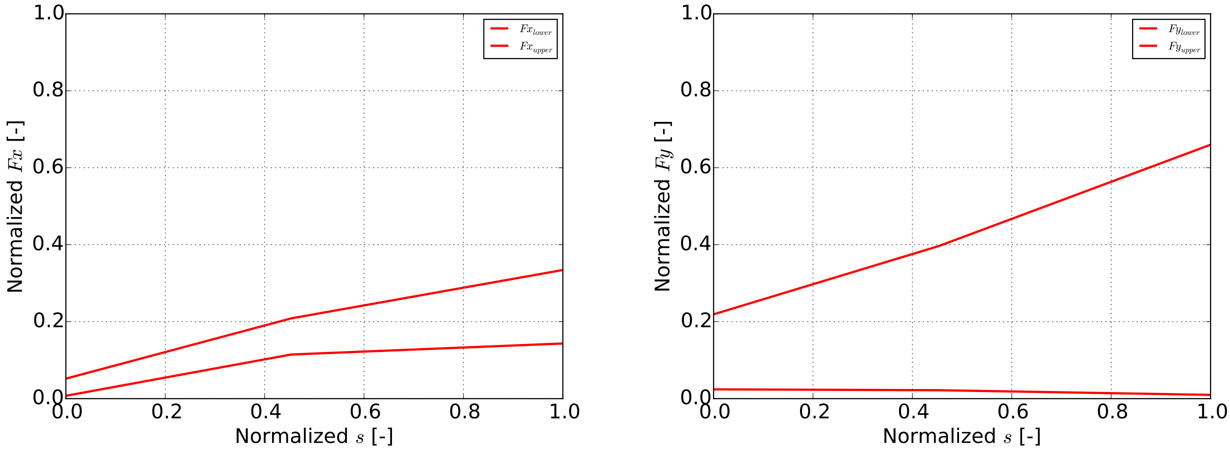


(a) $F_x$. (b) $F_y$.

Figure B.4: Force deformation solution corridors of upper framerail for rotational response.

The force deformation solution corridors of the grouped components of the springdome for the rotational response are shown in Fig. B.5.

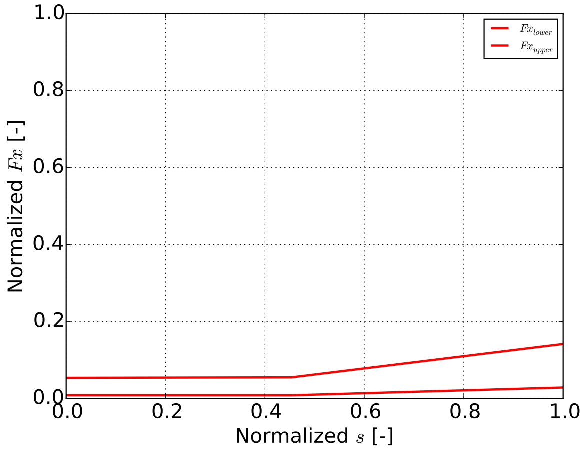


(a) $F_x$.

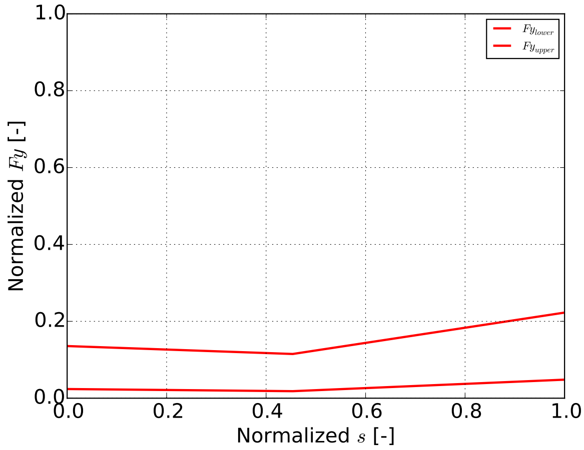


(b) $F_y$.

Figure B.5: Force deformation solution corridors of springdome for rotational response.

**Glancing-off response with constraints** $s_L$**,** $AbWAP$ **and** $AbWP$

The force deformation solution corridors of the grouped components of the wheel for the glancing-off response are shown in Fig. B.6.

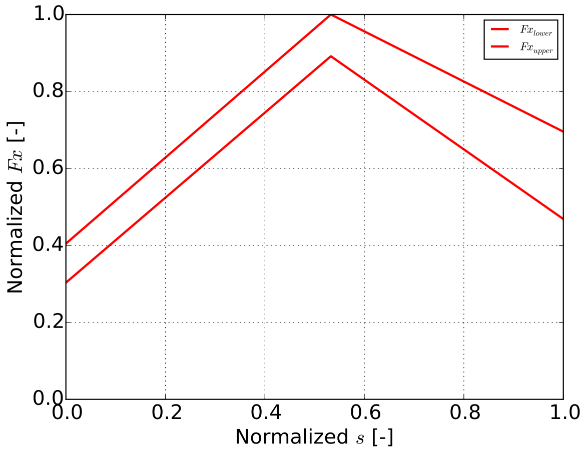


(a) $F_x$.

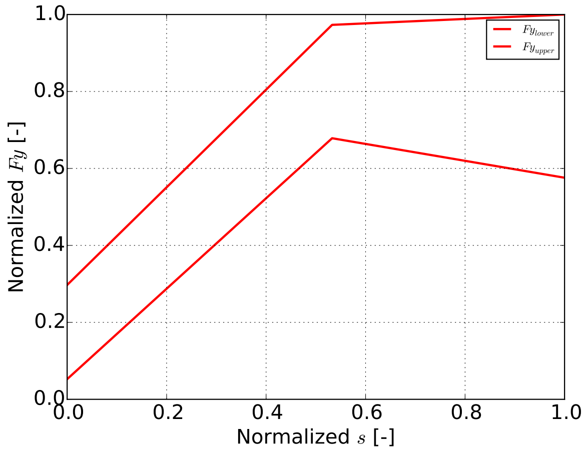


(b) $F_y$.

Figure B.6: Force deformation solution corridors of wheel for glancing-off response.

The force deformation solution corridors of the grouped components of the shotgun for the glancing-off response are shown in Fig. B.7.

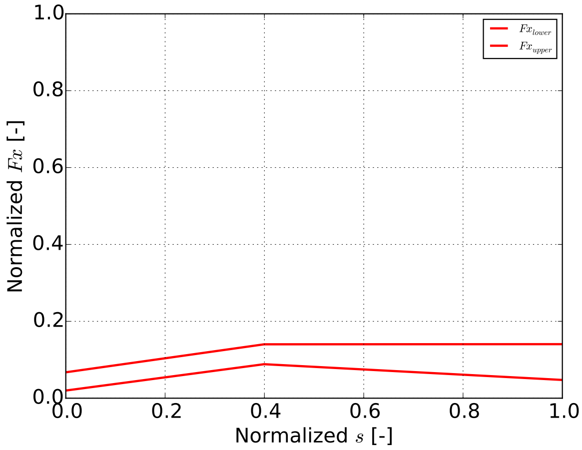


(a) $F_x$.

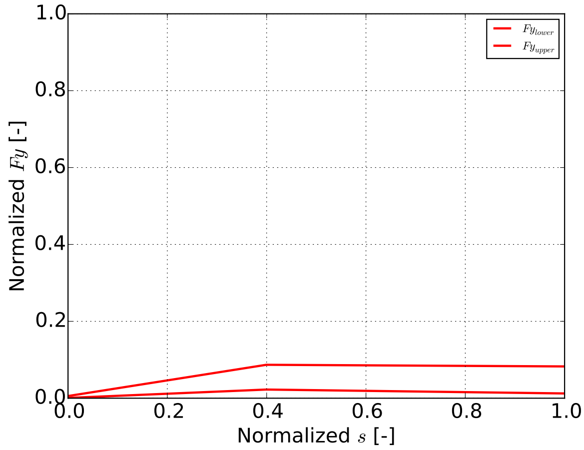


(b) $F_y$.

Figure B.7: Force deformation solution corridors of shotgun for glancing-off response.

The force deformation solution corridors of the grouped components of the lower framerail for the glancing-off response are shown in Fig. B.8.

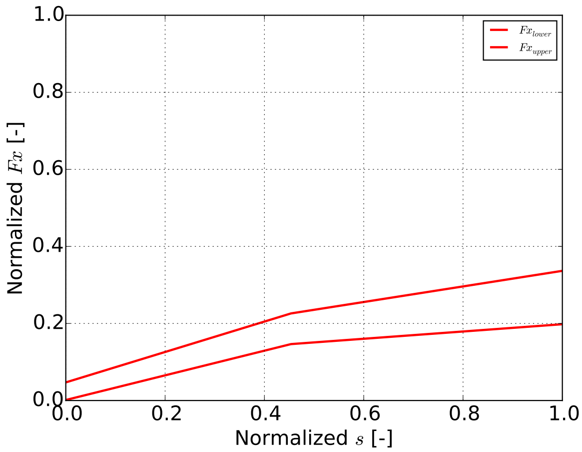


(a) $F_x$.

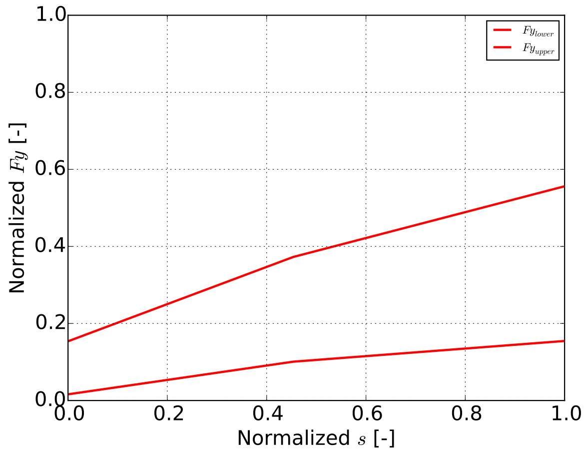


(b) $F_y$.

Figure B.8: Force deformation solution corridors of lower framerail for glancing-off response.

The force deformation solution corridors of the grouped components of the upper framerail for the glancing-off response are shown in Fig. B.9.

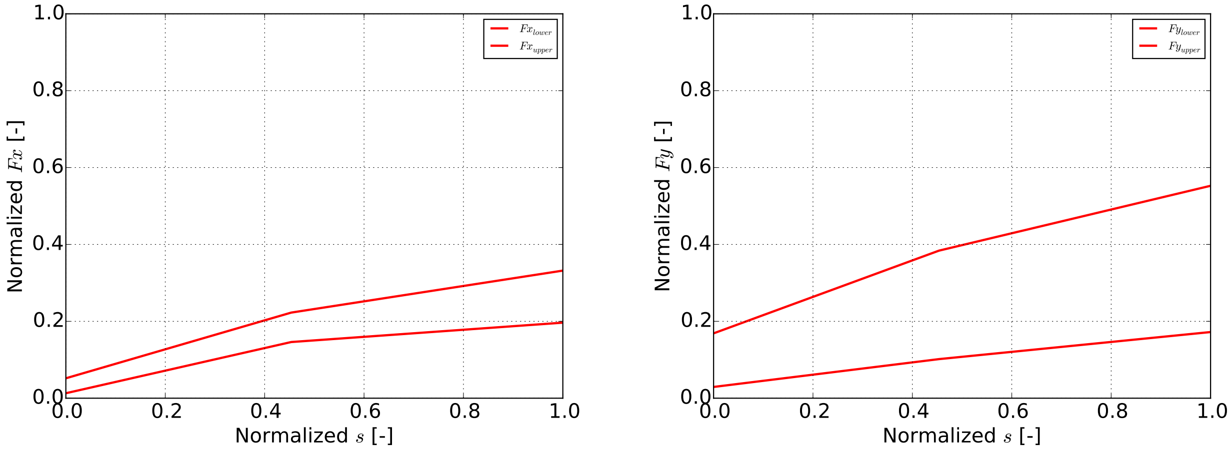


(a) $F_x$. (b) $F_y$.

Figure B.9: Force deformation solution corridors of upper framerail for glancing-off response.

The force deformation solution corridors of the grouped components of the springdome for the glancing-off response are shown in Fig. B.10.

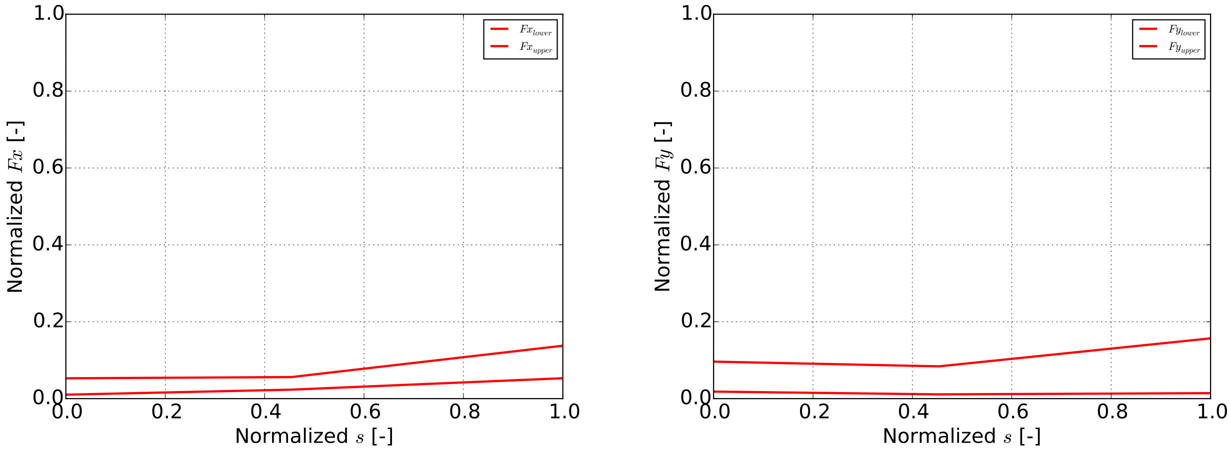


(a) $F_x$. (b) $F_y$.

Figure B.10: Force deformation solution corridors of springdome for glancing-off response.

Elastoplastic collapse element models, 12

Finite element method simulations, 14
Force deformation solution spaces, 27

Hybrid model simulations, 17

load paths, 8
Lumped mass models, 11

Macro element method simulations, 15
Monte Carlo sampling method, 27

Predictive kinematic model, 53

Reduced full vehicle FEM simulation model, 42
Research objective, 2
Response modes, 6
Rigid multibody models, 12

Small overlap crash, 4
Structural components of passenger vehicles, 7

Time integration scheme, 20
Trolley FEM simulation model, 34

V-model, 25
Visual Crash Studio, 15